



Ntala, Chara (2020) Immune profiling of the tumour microenvironment in prostate cancer. PhD thesis.

<https://theses.gla.ac.uk/81660/>

Copyright and moral rights for this work are retained by the author

A copy can be downloaded for personal non-commercial research or study, without prior permission or charge

This work cannot be reproduced or quoted extensively from without first obtaining permission in writing from the author

The content must not be changed in any way or sold commercially in any format or medium without the formal permission of the author

When referring to this work, full bibliographic details including the author, title, awarding institution and date of the thesis must be given

Enlighten: Theses

<https://theses.gla.ac.uk/>
research-enlighten@glasgow.ac.uk

Immune profiling of the tumour microenvironment in prostate cancer

Dr Chara Ntala MBBS, MSc

**Submitted in fulfilment of the requirement for the Degree of
Doctor of Philosophy (PhD)**

July 2020

Beatson Institute for Cancer Research

Institute of Cancer Sciences

College of Medical, Veterinary and Life Sciences

University of Glasgow

Abstract

Prostate cancer is the most common cancer among men in the UK and is characterised by large biological and clinical heterogeneity. There is an urgent need for better-personalised patient stratification, for example in accurately identifying patients with regional lymph node metastasis. Nodal involvement negatively impacts on patient survival outcomes and the current pre-operative staging tools to determine the need for extended pelvic lymph node dissection at time of radical prostatectomy are far from precise. The primary tumour immune microenvironment influences tumour immune editing and therefore disease progression. The primary aim of this research was to investigate the *in situ* phenotype of prostate cancer tumour infiltrating immune cells and determine their potential as biomarkers for regional lymph node involvement and further explore possible underlying mechanisms for their distribution.

The discovery tissue microarray comprised of index lesions from 94 patients undergoing radical prostatectomy and pelvic node dissection (50 with and 44 without histologic evidence of pelvic nodal disease respectively, referred to as LN+ and LN- thereafter). Two multiplex immunofluorescence panels were optimised to comprehensively characterise the immune microenvironment: (1) The macrophage and B cell panel includes CD68, CD163, CD20, AE1/3 (PanCK) and DAPI and (2) The T lymphocytic panel assays for CD4, CD8, FoxP3, PD-1, AE1/3 and DAPI. The macrophage (CD68, CD163+), T (CD8+, CD4+) and B (CD20+) cell immune cell subpopulations within the malignant epithelium and associated stroma were measured and correlated to the nodal status. Stromal infiltration by M1-like macrophages (CD68+CD163-) ($p=0.047$), CD8 effector (CD8+FoxP3-PD-1-) ($p=0.008$) and CD4 effector (CD4+FoxP3-PD-1-) T cells ($p=0.0003$, Mann Whitney test) were lower in LN+ patients. Stromal CD4 effector immune cell density remained a statistically significant independent predictor of lymph node spread in multivariate regression analysis (OR= 0.15, $p=0.004$). Additionally, in an independent validation cohort of 184 radical prostatectomy specimens, stromal CD4 effector immune cell density predicted the presence of nodal metastasis (OR=0.26, $p=0.0004$). Addition of stromal CD4 effector T cell density to currently used clinicopathological factors, namely T stage, PSA level, Gleason score and percentage of tumour positive cores, improved the predictive accuracy of current

nomograms (from 63.5% to 76.8%, $p < 0.0001$). Tumour infiltrating immune cells did not however correlate with common molecular alterations of prostate cancer such as ERG overexpression and *PTEN* deletion.

Transcriptomic analysis (by HTG EdgeSeq) of the tumour microenvironment was performed to assay 1,041 host immune response related genes. Surprisingly, I did not observe significant differences in the expression levels of adhesion molecules or chemokines (common regulators of immune cell migration) between LN+ and LN- cases. Instead, there was significant upregulation ($FC > 1.5$, adj p value < 0.05) of extracellular matrix components (collagen I, collagen III, fibronectin 1) in LN+ tumours, suggesting increased extracellular matrix fibrosis to be associated with reduced T lymphocytic infiltration and tumour immune evasion. Increased collagen III and fibronectin 1 protein expression were confirmed in LN+ patients. Collagen I had increased density score (by second generation harmonic), but not overall abundance, in LN+ patients, eluding to a disorganised stroma with increased cross-linking and elongated fibres.

B7-H3 is a newly discovered member of the B7 family of immune checkpoint molecules with both immune and non-immune functions. I investigated the relationship of B7-H3 to the tumour microenvironment as well as its non-immune functions in prostate cancer. Contrast to PD-1, high B7-H3 expression correlated with worse clinicopathological patient features: higher T stage ($p < 0.0001$), perineural invasion ($p = 0.01$) and lymph node spread ($p = 0.0006$). Furthermore, there was significant decrease in migration and invasion *in vitro* following suppressed B7-H3 expression in multiple human prostate cancer cell lines. RNA sequencing identified extracellular space chemotactic cytokines and their receptors to be highly downregulated genes in PC3M cells with B7-H3 knocked out. Future experiments will investigate the mechanistic downstream pathways of this phenotype and further evaluate the role of B7-H3 in metastasis *in vivo*.

Data presented in this thesis reveal differences in the immune infiltrates, particularly CD4 effector (CD4+FoxP3-PD-1-) T cells between LN+ and LN- patients. Prospective clinical studies are needed to test the predictive value of stromal CD4 effector T cell density in diagnostic prostatic biopsies for regional nodal disease. The role of increased extracellular matrix components in determining tumour immune infiltrates also warrants additional research.

Table of Contents

Immune profiling of the tumour microenvironment in prostate cancer.....	1
Abstract.....	2
List of Tables.....	8
List of Figures.....	9
Acknowledgement.....	11
Author's Declaration.....	12
Definitions/Abbreviations.....	13
Chapter 1 Introduction.....	15
1.1 Prostate cancer.....	15
1.1.1 Prostate pathology.....	15
1.1.2 Prostate cancer epidemiology.....	15
1.1.3 Prostate cancer progression and clinical management.....	16
1.1.4 Prostate cancer clinical challenges.....	17
1.1.5 Radical prostatectomy and extended lymph node dissection.....	18
1.1.6 Molecular Taxonomy of Prostate cancer.....	19
1.1.7 Stratification of prostate cancer molecular subtypes using immunohistochemistry.....	20
1.2 Tumour microenvironment.....	21
1.2.1 Tumour stromal microenvironment.....	21
1.2.2 Tumour immune microenvironment.....	21
1.2.3 Prostate cancer immune microenvironment.....	27
1.3 Multiplex immunofluorescence as a tool for immune cell characterisation	31
1.4 B7-H3 immune checkpoint molecule.....	34
1.4.1 Immune function of B7-H3.....	34
1.4.2 Non- immune function of B7-H3.....	36
1.4.3 B7-H3 immune checkpoint in prostate cancer.....	38
Chapter 2 Materials and methods.....	40
2.1 Reagents.....	40
2.2 Solutions and buffers.....	40
2.3 Human tissue.....	41
2.3.1 Construction of intermediate/high risk discovery primary prostate cancer tissue microarray.....	41
2.3.2 Validation intermediate/high risk primary prostate cancer tissue microarray.....	42
2.3.3 Low risk primary prostate cancer tissue microarray.....	43
2.3.4 Benign prostatic hyperplasia tissue microarray.....	43
2.4 Chromogenic immunohistochemistry.....	43

2.4.1	Chromogenic immunohistochemistry protocol	44
2.4.2	Dual CD4-FoxP3 chromogenic immunohistochemistry protocol	45
2.4.3	HALO scoring	45
2.4.4	ERG, PTEN, Ki67 scoring	46
2.4.5	Histoscoreing	47
2.5	In situ hybridisation for CXCL14	47
2.6	Second generation harmonic image acquisition and analysis for determination of collagen quantity and quality	47
2.7	Multiplex immunofluorescence	48
2.7.1	Optimisation steps for multiplex immunofluorescence panel development	48
2.7.2	Automated multiplex immunofluorescence staining and image acquisition	51
2.7.3	Multiplex immunofluorescence analysis	53
2.8	Gene expression analysis of formalin fixed paraffin embedded tissue using HTG EdgeSeq Precision Immuno-Oncology Panel	56
2.8.1	Sample preparation	57
2.8.2	Library preparation	57
2.8.3	Library quantification and Normalisation	57
2.8.4	Sequencing	58
2.8.5	Data analysis	58
2.9	<i>In vitro</i> experiments	58
2.9.1	Cell Culture and Cell Storage	58
2.9.2	Protein extraction	59
2.9.3	Western Blot	59
2.9.4	RNA extraction and cDNA preparation	60
2.9.5	Quantitative Polymerase chain reaction (qPCR)	60
2.9.6	Transient silencing transfection using Lipofectamine RNAiMAX	61
2.9.7	Generation of stable cell clones with reduced levels of B7-H3 expression	62
2.9.8	<i>In vitro</i> Growth Assay	62
2.9.9	<i>In vitro</i> apoptosis assay	63
2.9.10	<i>In vitro</i> colony formation assay	63
2.9.11	<i>In vitro</i> transwell migration assay	64
2.9.12	<i>In vitro</i> scratch wound healing assay	64
2.9.13	<i>In vitro</i> invasion assay	65
2.9.14	RNA sequencing	65
2.10	Statistical methods	66
Chapter 3	Immune profiling of prostate cancer tumour microenvironment in the context of lymph node metastasis	67

3.1	Validation of multiplex immunofluorescence assay	68
3.1.1	Correlation between mIF and DAB chromogenic IHC	69
3.1.2	Co-localisation of markers	69
3.2	Immune profiling of the discovery TMA cohort.....	71
3.2.1	Clinical characteristics of lymph node discovery TMA	71
3.2.2	Immune profiling of intermediate and high risk prostate cancer patients.....	72
3.2.3	Immune cell densities and ratios in discovery cohort patients with vs without lymph node metastasis.....	75
3.2.4	Correlations between immune cell densities.....	76
3.2.5	Immune cell densities and clinicopathological characteristics	77
3.3	Immune profiling of Validation cohort	79
3.3.1	Clinical characteristics of Validation cohort (Validation TMA).....	79
3.3.2	Immune profiling of validation cohort patients in the context of lymph node metastasis.....	80
3.4	Prognostic value of tumour stromal CD4 effector T cells for lymph node metastasis.....	82
3.5	Prognostic value of stromal CD4 effector T cells in survival	83
3.6	Prostate cancer common genetic alterations are not associated with immune cell infiltration	84
3.6.1	Molecular characteristics in primary tumours of patients with vs without lymph node metastasis.....	86
3.6.2	ERG, PTEN and Ki67 are not associated with immune cell infiltration	87
3.6.3	Combining PTEN and stromal CD4 effector T cells in predicting lymph node metastasis does not improve prognostic value	89
3.7	Optimisation of dual CD4-FoxP3 Immunohistochemistry	91
3.8	Exploration of stromal CD4 effector T cells in low risk prostate cancer patients	92
3.8.1	Low risk prostate cancer cohort.....	92
3.8.2	Stromal CD4 effector T cells are not associated with survival in low risk prostate cancer patients.....	93
3.9	Translation of stromal CD4 effector T cells detection in the clinical setting.....	93
3.9.1	Staining of prostate cancer diagnostic biopsies.....	93
3.10	Concluding summary.....	96
Chapter 4	Phenotyping of prostate cancer using a targeted gene expression panel	102
4.1	Post-sequencing quality control	103
4.2	Extracellular matrix components genes are upregulated in prostate cancer patients with nodal metastasis	105

4.3	Extracellular matrix components are increased and disorganised in prostate cancer patients with lymph node metastasis	106
4.4	Exploratory investigation of cancer associated fibroblast markers (CXCL14 and FAPa) in prostate cancer patients with nodal metastasis.....	110
4.5	Concluding summary	112
Chapter 5	B7-H3 and prostate cancer	117
5.1	B7-H3 is overexpressed in prostate cancer and associated with worse clinicopathological features.....	118
5.1.1	B7-H3 staining of human tissue.....	118
5.1.2	High B7-H3 expression is associated with worse clinicopathological features in intermediate and high risk prostate cancer patients	120
5.1.3	B7-H3 expression inversely correlates with immune cell infiltration	122
5.2	Transient silencing of B7-H3 expression in prostate cancer cell lines ..	122
5.2.1	Transient loss of B7-H3 expression does not affect prostate cancer cell growth or apoptosis <i>in vitro</i>	123
5.2.2	Transient loss of B7-H3 expression reduces prostate cancer cell migration <i>in vitro</i>	124
5.2.3	Transient loss of B7-H3 expression reduces PC3M cell invasion <i>in vitro</i>	127
5.3	Generation of stable knock out (KO) B7-H3 clones of PC3M and C4-2 cell lines	128
5.4	Stable knock out (KO) of B7-H3 does not affect survival and proliferation of PC3M cells	129
5.5	Stable knock out (KO) of B7-H3 reduces prostate cancer cell migration and invasion <i>in vitro</i>	130
5.6	RNA sequencing and metacore pathway analysis reveals extracellular space cytokines are decreased in B7-H3 deficiency	131
5.6.1	Differentially expressed genes from RNA sequencing validate in PC3M cells	133
5.7	Concluding summary	135
Chapter 6	Discussion and future directions	137
6.1	Identification and validation of novel TME signature to identify patients with nodal metastasis.....	137
6.2	B7-H3 checkpoint molecule immune function insights.....	138
6.3	Future directions in tumour immune profiling	139
6.4	Concluding summary	141
Appendices	142
List of References	173

List of Tables

Table 1 Summary of studies characterising human primary prostate cancer immune microenvironment	30
Table 2 Commonly used reagents	40
Table 3 Working solutions and buffers	41
Table 4 Antibodies used for chromogenic immunohistochemistry	44
Table 5 Multiplex immunofluorescence panels developed and used for staining	52
Table 6 Primers and probe pairs used	61
Table 7 List of siRNA sequences	62
Table 8 Clinical and histopathological characteristics of discovery TMA of patients with (LN+) and without lymph node metastasis (LN-)	72
Table 9 Immune cell densities of intermediate and high-risk patients included in the Discovery cohort	73
Table 10 Summary of discovery cohort immune cell densities stratified according to lymph node status.....	76
Table 11 Macrophage and B cell densities of discovery cohort stratified by clinicopathological parameters.....	78
Table 12 CD4 T cell densities of discovery cohort stratified by clinicopathological parameters	78
Table 13 CD8 T cell densities of discovery cohort stratified by clinicopathological parameters	79
Table 14 Clinicopathological characteristics of the validation cohort	80
Table 15 Summary of validation cohort immune cell densities stratified according to lymph node status.....	81
Table 16 Multivariate regression analysis of stromal CD4 effector T cells with standard of care clinicopathological factors commonly used for the prediction of nodal metastasis.....	82
Table 17 Molecular features of discovery cohort according to their lymph node status.....	87
Table 18 Immune cell densities of discovery cohort stratified by ERG status....	88
Table 19 Immune cell densities of discovery cohort stratified by PTEN status ..	88
Table 20 Immune cell densities of discovery cohort stratified by Ki67 score	89
Table 21 Multivariate regression analysis of PTEN status with standard of care clinicopathological factors commonly used for the prediction of nodal metastasis	90
Table 22 Differentially expressed genes in patients with vs without lymph node metastasis (LN+ vs LN-).....	106

List of Figures

Figure 1 Multiplex immunofluorescence with tyramide signal amplification method	33
Figure 2 Multiplex immunofluorescence staining workflow	49
Figure 3 Manual multiplex immunofluorescence staining optimisation.....	51
Figure 4 Multiplex immunofluorescence analysis workflow	54
Figure 5 Multiplex immunofluorescence cell phenotyping	56
Figure 6 Photographs of representative examples of validation from IHC and H&E (bottom panels), uniplex and multiplex IF (top panels) in tonsil tissue.....	68
Figure 7 Representative examples of co-localisation of the cell markers	70
Figure 8 Spatial distribution of CD4 effector T cells (CD4+ FoxP3- PD-1-) in intermediate and high risk prostate cancer patients	74
Figure 9 Clinical impact of stromal CD4 effector T cells in lymph node metastasis	83
Figure 10 Clinical impact of stromal CD4 effector T cells in survival.....	84
Figure 11 Representative images of ERG, PTEN and Ki67 staining	86
Figure 12 Clinical impact of PTEN and stromal CD4 effector T cells in lymph node metastasis	91
Figure 13 Optimisation of dual CD4- FoxP3 immunohistochemistry.....	92
Figure 14 Stromal CD4 effector T cells in low risk prostate cancer.....	93
Figure 15 Staining of prostate cancer diagnostic biopsies with dual CD4-FoxP3 immunohistochemistry.....	95
Figure 16 Post sequencing quality controls	104
Figure 17 Extracellular matrix components staining	108
Figure 18 Enhanced collagen I, collagen III and fibronectin 1 in patients with lymph node metastasis	110
Figure 19 CXCL14 and FAPa expression in prostate cancer patients with nodal metastasis	112
Figure 20 B7-H3 staining of human prostatic tissue and pelvic lymph nodes....	119
Figure 21 High B7-H3 expression is associated with lymph node metastasis	120
Figure 22 High B7-H3 expression is associated with worse clinicopathological features.....	121
Figure 23 Transient silencing of B7-H3 in prostate cancer cell lines	123
Figure 24 Transient loss of B7-H3 expression does not affect prostate cancer cell growth or apoptosis <i>in vitro</i>	124
Figure 25 Transient loss of B7-H3 expression reduces prostate cancer cell migration in a transwell Boydon chamber assay	125
Figure 26 Transient loss of B7-H3 expression reduces prostate cancer cell migration shown by scratch wound assay	126
Figure 27 Transient loss of B7-H3 expression reduces PC3M prostate cancer cell invasion shown by inverted transwell Boydon chamber assay	127
Figure 28 Generation of stable B7-H3 knock out (KO) clones of PC3M and C4-2 cells	129
Figure 29 Stable knock out (KO) of B7-H3 does not affect survival and proliferation of PC3M cells.....	130
Figure 30 Stable knock out (KO) of B7-H3 reduces prostate cancer cell migration and invasion <i>in vitro</i>	131
Figure 31 Metacore pathway analysis	133
Figure 32 Differentially expressed genes from RNA sequencing validate in PC3M cells	134

Figure 33 Differentially expressed genes from RNA sequencing do not validate in C4-2 cells 135

Acknowledgement

Firstly, I would like to thank Professor Hing.Y. Leung for his guidance, support and mentorship during my PhD. It has been a pleasure being a member of his team and has enabled me to develop personally and professionally. I would also like to thank my second supervisor, Dr Leo Carlin for his encouragement and guidance throughout my studies.

I am grateful to all current and previous members of R08 for introducing me to wet lab work, guiding me and providing technical advice whenever I needed it. This work would have been impossible without the valuable help of our collaborators, Dr John Le Quesne, Professor George Thalmann and Professor David Berman and their teams.

I would also like to thank my partner and family for their patience and continuous support during these past three years.

This clinical fellowship was funded by Cancer Research UK

Author's Declaration

I declare that this thesis is the result of my own work unless otherwise stated and that it has not been submitted previously for a higher degree in any institution.

Definitions/Abbreviations

PCa- Prostate cancer
 PIN- Prostatic Intraepithelial neoplasia
 PSA- Prostatic specific antigen
 RP- Radical prostatectomy
 ADT- Androgen deprivation therapy
 mCRPC- metastatic Castration Resistant Prostate Cancer
 IHC- Immunohistochemistry
 FISH- Fluorescence in situ hybridisation
 PCR- Polymerase chain reaction
 PTEN- Phosphate and tension homolog located on chromosome 10
 TME- Tissue microenvironment
 ECM- Extracellular matrix
 MDSC- Myeloid derived suppressor cell
 DC- Dendritic cell
 TAM- Tissue associated macrophage
 MHC- Major histocompatibility complex
 FoxP3- Forkhead box P3
 Th- T helper
 TCR- T cell receptor
 APC- Antigen presenting cell
 PD-1- Programmed cell death protein 1
 H&E- Haematoxylin and eosin stain
 mIF- multiplex Immunofluorescence
 PDAC- Pancreatic ductal adenocarcinoma
 TIL- Tumour infiltrating lymphocyte
 FFPE- Formalin-fixed, paraffin-embedded
 DAB- 3,3'-Diaminobenzidine
 MSI- Multispectral imaging
 HRP- Horseradish peroxidase
 Ig- Immunoglobulin
 NK- Natural killer cell
 TRAMP- Transgenic adenocarcinoma mouse prostate
 CART- Chimeric antigen receptor T cells
 NSCLC- Non-small cell lung carcinoma
 ACCC- Antibody-dependent cellular cytotoxicity
 TREML2- Triggering receptor expressed on myeloid cell-like transcript 2
 MMP- Matrix metalloproteinase
 TIMP- Tissue inhibitor of metalloproteinase
 EMT- Epithelial to mesenchymal transition
 VEGF- Vascular endothelial growth factor
 SRT- Salvage radiation therapy
 TURP- Transurethral resection of the prostate
 NPP- Nuclease protection probe
 BSA- Bovine serum albumin
 PNI- Perineural invasion
 OS- Overall survival
 RFS- Relapse-free survival
 DPX- Dibutylphthalate polystyrene xylene
 IF- Immunofluorescence
 sIF- singleplex Immunofluorescence

HDR- Homology directed repair
TBS- Tris buffered saline
TBST- Tris buffered saline and tween
PBS- Phosphate buffered solution
ATCC- American Type Culture Collection
DMSO- Dimethyl sulphoxide
KO- Knock-out
ROC-Receiver operating curve
AUC- Area under the curve
PanCK- Pancytokeratin
GEMM- Genetically engineered mouse models
CXCL14- Chemokine (C-X-C motif) ligand 14
QC- Quality criteria
RSD- Relative standard deviation
FN- Fibronectin
LOX- Lysyl oxydase
PCA- Principal component analysis

Chapter 1 Introduction

1.1 Prostate cancer

1.1.1 Prostate pathology

The prostate gland is part of the male reproductive system. Histologically, it comprises of prostatic glands and connective tissue, ensheathed by a fibromuscular layer referred to as capsule (1). The glandular component is composed of ducts and acini of luminal cells overlying basal epithelial cells and scant scattered neuroendocrine cells (1). The luminal cells contribute to a wide variety of secretions for the seminal fluid, including prostatic-specific antigen (PSA) (1, 2). The connective tissue is composed of stromal fibroblasts, immune cells, nerves, vascular and lymphatic vessels and muscle fibres. All those components can give rise to malignancy but the majority of cancers arising in the prostate are prostatic acinar adenocarcinomas, commonly referred to as prostate cancer (1, 2).

The precursor lesion of prostate cancer is prostatic intraepithelial neoplasia (PIN), which consists of cytologically atypical and abnormally proliferating luminal epithelial cells that retain an underlying layer of basal cells (2). Prostate cancers have a wide spectrum of histological appearances, ranging from poorly differentiated tumours without glandular architecture to well differentiated tumours, morphologically similar to benign glands (1, 2). The key feature is the loss of basal cell layer underlying the luminal cells. The vast majority of patients have multifocal disease, with multiple tumour foci across the entire prostate gland (1). Apart from architectural changes, prostate cancer cells also exhibit cytological abnormalities, such as nuclear enlargement, prominent nucleoli and mitoses (1), which along with immunohistochemical stains are used by pathologists for prostate cancer diagnosis.

1.1.2 Prostate cancer epidemiology

Prostate cancer (PCa) is the most common cancer in males in the UK, with approximately 48,600 new diagnoses each year (3). Currently, one in six males will be diagnosed with prostate cancer in their lifetime (4), and the incident rate is projected to rise even more by 2035 (3). This rise in diagnoses can be at

least partly attributed to advancing population age and increasing PSA testing (2, 5). Prostate cancer is also the second most frequent cause of cancer death in males the UK, with around 12,000 deaths in 2017 (6). The incidence and mortality rates of PCa are similar in other developed countries, including the United States (5).

The most decisive factor for patient prognosis and survival is how advanced the tumour is, i.e. the stage of PCa at diagnosis. Patients with stages I and II have prostate tumours confined within the prostate gland, whereas patients with stage III have prostate tumours that have spread beyond the prostate (2). Stage IV prostate tumours have spread to organs outside the prostate (and seminal vesicles) and/or have regional nodal and/or distant metastatic deposits (2). In the UK, more prostate cancer patients are diagnosed at an early stage (up to 63% diagnosed at stage I or II), in which their tumour is still localised in the prostate (4). However, this is lower in Scotland, where only 56% of new diagnoses are at an early stage, the rest 44% of newly diagnosed patients have locally advanced (stage III) or metastatic disease (stage IV) (4). Advancing age, race and a family history of PCa are the only established risk factors for PCa, there is no clear link to any modifiable risk factors that could aid prevention of the disease (2, 4).

1.1.3 Prostate cancer progression and clinical management

PCa is characterised by clinical heterogeneity, ranging from indolent disease that can safely be observed to an aggressive, lethal course (5, 7). Key to the effective management of this heterogeneous disease is early risk stratification (8). Newly diagnosed PCa is assessed using a combination of radiological cancer staging (cTNM stage), PSA level and histological characteristics of prostatic biopsies including Gleason score (2, 8). The Gleason scoring system is based on the tumour architecture, assigning a primary pattern for the most prevalent grade and a secondary pattern for the second most prevalent grade. These grades range from 1 to 5, 1 being well-differentiated glands with nodular circumscription and 5 being very poorly differentiated tumours with a non-glandular pattern (2). The Gleason score derives from the addition of those two grades. Additional histological markers currently used to predict tumour behaviour include perineural invasion and percentage of tumour in biopsy cores (tumour quantification) (2).

For organ confined or locally advanced disease at the time of diagnosis, there are guidelines on patient management according to low (PSA <10 ng/ml and Gleason score <7 and cT1-T2a), intermediate (PSA 10-20 ng/ml or Gleason score =7 or cT2b) and high risk status (PSA ≥20 ng/ml or Gleason score >7 or cT2c-T4) (2, 8). In men diagnosed with lower risk, treatment options include active surveillance, radical prostatectomy (RP) or radiation therapy (2, 8). Patients with higher risk disease can be offered RP with or without extended lymph node dissection, radiation therapy as well as androgen deprivation therapy (ADT) (2, 8).

Some patients are diagnosed with advanced/metastatic disease or subsequently develop disease relapse following primary treatment with ADT (4, 7). ADT and chemotherapy are standard therapies for metastatic PCa. Suppression of the androgen receptor pathway has evolved from the traditional surgical or pharmacological castration to newer pharmacological agents, such as enzalutamide and abiraterone acetate, which target the androgen receptor or androgen enzymatic biosynthesis respectively (2). Chemotherapy with docetaxel or carbazitaxel (with significant risks of toxicities) can extend the life expectancy of PCa patients but only by a few months (2, 7). Patients inevitably develop resistant disease despite treatments and metastatic castration resistant PCa (mCRPC) remains an incurable disease.

1.1.4 Prostate cancer clinical challenges

Even though prostate cancer mortality rates are falling over the last decade (6), there are two main clinical areas in need of improvement. Firstly, there is an urgent need for better patient stratification in order to prevent over- or under-treatment of PCa patients (7). Gleason scoring, PSA levels and tumour quantification are valuable tools for deciding disease management but they cannot adequately distinguish indolent from aggressive tumours. Additional prognostic markers are urgently needed to more effectively guide clinical decision making, for example in accurately stratifying patients that would benefit from extended lymph node dissection at the time of radical prostatectomy.

The second clinical unmet need is the paucity of therapeutic options for late stage mCRPC (2, 7). In other cancer types there has been significant advancement in cancer immunotherapy, which harnesses the body's intrinsic immune responses against the tumour (9). Sipuleucel-T, an autologous personalised immunotherapy focused on patient's own dendritic cell maturation against specific antigens, was the first immunotherapy agent approved for mCRPC (9). However the high cost and modest survival benefits have prevented its widespread adaptation to the clinic (9). Other immunotherapy approaches, such as immune checkpoint inhibitors, have so far been disappointing in PCa. It is possible that better patient selection and understanding of the key mechanisms that promote immunosuppression in prostate cancer would improve the efficacy of immunotherapy.

1.1.5 Radical prostatectomy and extended lymph node dissection

Radical prostatectomy (open, laparoscopic or robotic) is an established curative option for patients with early PCa (8). It involves the removal of the entire prostate gland and seminal vesicles alongside sufficient surrounding tissue in order to obtain a negative surgical margin (2, 8). This procedure can be accompanied by an extended pelvic lymphadenectomy in higher risk patients (2, 8). This includes removal of more than 10 regional lymph nodes overlying the external and common iliac artery and vein, medial and lateral to the internal iliac artery, and within the obturator fossa (2, 10, 11). Even though extended lymph node dissection is necessary for accurate staging and therapeutic benefit (12) it does not come without patient complications and economic burden associated with extended operation time and hospitalisation (10). Approximately 20% of patients develop such complications, which include lymphocele, deep vein thrombosis, pelvic haematoma, fever, acute urinary retention, pulmonary embolism and ureteral injury (10, 13).

It is challenging for urological surgeons to make personalised patient decisions regarding extended lymph node dissection due to the heterogeneity of high-risk patients (7, 11). Currently preoperative nomograms based on clinical and histological parameters are used, the most popular being the Briganti nomogram (11). This is based on pre-operative PSA level, clinical stage, biopsy Gleason score and the percentage of positive cores (11). Even though this is considered

relatively accurate, it undeniably results in a significant portion of patients unnecessarily undergoing nodal dissection (2, 11). The prevalence of pathological confirmation of lymph node metastasis in patients undergoing nodal dissection ranges from 1 to 26% (10-13). Since extended pelvic lymph node dissection is considered for each patient with intermediate or high-risk disease undergoing radical prostatectomy, it is evident that better prognostic biomarkers for this procedure are urgently needed.

1.1.6 Molecular Taxonomy of Prostate cancer

During the past decade, the understanding of PCa genomics has progressed substantially (14). It is increasingly recognised that the clinical heterogeneity observed in patients can be attributed to the wide array of genomic aberrations observed in PCa. About 50% of primary prostate cancer are characterised by juxtaposition of androgen regulated gene *TMPRSS2* and *ETS* family genes (15). The most commonly involved member of the *ETS* family is the transcription factor *ERG* (46%), but also *ETV1* (8%), *ETV4* (4%) and *FLI1* (1%) (15). These fusions of androgen regulated gene promoters and oncogenes are collectively the most common genetic alterations in PCa and are mostly mutually exclusive (14, 15). Whole genome sequencing revealed that these fusions are caused by a complex genetic rearrangement called ‘chromoplexy’, in which multiple chromosome segments are randomly severed and re-joined with frequent DNA deletions at their junction points (2).

Tumours that lack *ETS* fusions commonly have mutually exclusive mutations of *SPOP* (11%), *FOXA1* (3%) and *IDH* (1%) genes (15). The 26% of remaining PCa tumours were genomically heterogeneous and are driven by yet unknown specific genetic or epigenetic aberrations (15). These mutations of primary PCa, alongside *ETS* fusions and are both clonal, early events in PCa oncogenesis (14, 15). They are followed by a wide array of subclonal changes that provides survival benefit and proliferative advantage to the cancer cells. Phosphatase and tensin homolog (*PTEN*) genomic inactivation acts as a negative regulator of the PI3K-AKT pathway and occurs in up to 40% of CRPC (16). *PTEN* loss has been repeatedly associated with worse clinical outcome and metastatic disease (17, 18). PI3K-AKT pathway aberrations are frequently attributed to *PTEN* inactivation and occur in up to 40% of primary tumours (1) and 49% of CRPC (16).

They contribute to PCa progression by activating target genes that promote cancer cell growth and proliferation (19). Somatic aberrations of DNA repair genes occur in approximately 12% of CRPC and include genes involved in homologous recombination, such as *BRCA1/2* and mismatch repair (16, 20). The incidence of mutations affecting cell cycle genes varies significantly between primary (5%) (21) and advanced CRPC (21-55%) (16, 20) and include deletions of tumour suppressor genes *p53*, *RB1*, *CDKN1*, *CDKN2A/B*, and *CDKN2C*, and amplifications of oncogenes *CDK4* and *CCND1*. Lastly, in CRPC, the most frequent aberrations were found in the androgen receptor (AR) pathway (71%), implying that these tumours still depend on AR signalling (20).

Summarising, there is a refined classification of PCa subtypes based on genetic alterations. Interestingly, different genetic backgrounds of PCa have been shown to influence the immune composition of the tumour microenvironment *in vivo* via different chemokine expression patterns (22) and inactivation of mismatch repair genes have been strongly associated with increased CD8 T cell infiltration in patient tumours (23). Also, pro-inflammatory cytokines produced by immune cells result in oxidative stress which has been linked to *TMPRSS2-ETS* gene fusions via DNA breaks (24). However, the overall reciprocal interactions between different genetic alterations and tumoural immune cell composition is far from clear. Better understanding of these relationships would potentially contribute to the identifications of novel prognostic as well as predictive biomarkers for personalised immunotherapies.

1.1.7 Stratification of prostate cancer molecular subtypes using immunohistochemistry

The commonest genetic alteration of PCa is the juxtaposition of *TMPRSS2* and the transcription factor *ERG* by chromoplexy (15). As a result of this translocation, the expression of *ERG* becomes regulated by androgens and is therefore overexpressed in prostatic epithelium. *ERG* overexpression assessed by immunohistochemistry (IHC) has been successfully validated as a surrogate for *TMPRSS2-ERG* translocation, with concordance between *ERG* IHC and Fluorescence in situ hybridisation (FISH) or quantitative polymerase chain reaction (PCR) above 95% (17, 25-27). Using IHC for detection of genetic alterations is less

expensive and time-consuming than FISH as well as more easily transferable into the current clinical pathology workflow setting.

PTEN inactivation is a subclonal event that occurs frequently in PCa and has been repeatedly associated with worse clinical outcome and metastatic disease (17, 28-30). Interestingly, it is more frequently concomitant with *ERG* fusion cancers (19). Detection of *PTEN* loss by immunohistochemistry has been well established in previous reports and is comparable to the previously gold standard FISH detection (17, 18, 31). Even though *PTEN* is most frequently lost by large gene deletions that are detected by FISH (16, 32), less frequent genomic alterations, such as gene mutations, small insertions/deletions and epigenetic silencing (16, 32) can be detected with IHC only. Also, because *PTEN* loss is commonly heterogeneous in primary prostate tumours (18) using FISH detection for gene deletion can be technically challenging and screening for focal loss with IHC can be advantageous. Therefore, assessing *PTEN* expression by IHC is a robust and advantageous approach.

1.2 Tumour microenvironment

1.2.1 Tumour stromal microenvironment

In cancer, the growth of tumour cells is driven by activation of oncogenic drivers and inactivation of tumour suppressors (33). However, these aberrantly proliferating epithelial cells are not in isolation. They depend on reciprocal interactions with their surrounding stromal compartment, the tumour microenvironment (TME) (33, 34). The TME comprises of several different non-malignant cells, such as fibroblasts, endothelial cells, pericytes and immune cells situated within extracellular matrix (ECM) (34). Crosstalk between cancer cells and TME can enhance or inhibit tumourigenesis, invasion and metastasis (34).

1.2.2 Tumour immune microenvironment

Tumour immune microenvironment is a decisive factor in tumour initiation and progression. Immune cells can provide tumour promoting as well as tumour

suppressive signals on epithelial cells via cell contact or secreted molecules (35, 36). The interaction between cancer and immune cells is called cancer immunoediting and encompasses the consecutive phases of tumour elimination, equilibrium and tumour escape (36). During tumour elimination the host immune system successfully eradicates developing tumours. If tumour cells survive the elimination process they enter into an equilibrium phase, in which the immune system continues to contain tumour cells without fully eliminating them. Escape is signified by the expansion of tumour cells, overcoming the immune system (36). The balance between the effectiveness of the immune response and the mechanisms adopted by tumours to evade immune recognition and destruction determines the overall results (35).

All solid tumours, including prostate cancer, contain different types of infiltrating immune cells that operate in conflicting ways, antagonising as well as promoting cancer progression (33). There are currently three main tumour immune microenvironment phenotypes that are driven by different biological mechanisms and are clinically relevant (35, 37). Firstly, the immune inflamed phenotype, also known as ‘hot’ tumours, are characterised by increased immune cell infiltration within tumour epithelial cells and surrounding stroma. These include immune suppressive cells, such as CD4 T regulatory cells and myeloid-derived suppressor cells as well as CD4 and CD8 effector cells expressing exhaustion markers, such as programmed cell death 1 (PD-1) (35). This profile suggests the presence of a pre-existing anti-tumour immune response that has been halted, most likely due to immunosuppression within the TME (35, 37).

Secondly, the immune excluded phenotype is also characterised by immune cell infiltration, however these do not penetrate the epithelial cells but are instead retained within the tumour-associated stroma (35, 37). This phenotype suggests a pre-existing anti-tumour response that has become ineffective due to the retention of immune cells away from the target epithelial cells. The limited immune cell migration through the tumour stroma can be attributed to altered chemokine milieu or mechanical barriers and is responsible for this immune phenotype’s tumour eradication failure (35, 37). Lastly, the immune desert phenotype is characterised by a paucity of immune cell infiltration within the tumour parenchyma and surrounding stroma. This is the result of absence of pre-

existing tumour immunity, with a lack of generation of anti-tumour specific T cells. The immune excluded and immune desert phenotypes are also known as 'cold' tumours (35, 37).

All immune cell types may be found within the tumour immune microenvironment. These include macrophages, myeloid derived suppressor cells (MDSCs), dendritic cells (DCs), B cells, CD4 helper and CD8 T lymphocytes being the most commonly encountered. These immune cells can be located within the tumour parenchyma, stroma or in organised tertiary lymphoid structures (37, 38). Innate immune cells (macrophages, MDSCs, DCs) are the first line of defence against tumour antigens, and can also exert immune suppressive functions in order to maintain tissue homeostasis. DCs are key players that take up antigens and migrate to lymphoid organs where they present their antigens to T lymphocytes, functioning as a link between innate and adaptive immunity (39). Following priming and activation, these lymphocytes can produce an efficient antigen specific response against tumour cells. However, there are also effector lymphocytes with immune suppressive abilities such as regulatory T cells (39).

1.2.2.1 Macrophages and myeloid derived suppressor cells

Macrophages are abundant immune cells of the TME, characterised by high plasticity that allows them to shape their phenotype in response to the surrounding environmental cues (38). On the one end of the spectrum, tumour associated macrophages (TAM) can be M1-like or 'classical' TAMs that secrete pro-inflammatory cytokines, can present tumour antigens and have a pro-inflammatory and tumouricidal role. On the other end, M2-like or 'alternative' TAMs can secrete anti-inflammatory cytokines (IL-4, IL-10, and TGF β) playing an immunosuppressive role, promoting angiogenesis and favouring tumour progression (38). In reality, TAMs comprise different populations that often share features of both those two phenotypes which can change as tumour progresses (40).

Myeloid derived suppressor cells are a heterogeneous population of myeloid lineage cells that can be immunosuppressive within the tumour microenvironment (38, 39). They consist of monocytes, granulocytes and immature myeloid cells which suppress T cytotoxic cells (39, 40).

1.2.2.2 Dendritic cells

DCs are professional antigen presenting cells that are necessary for lymphocyte priming and activation. Tissue resident DCs capture antigens, process them and transfer them to draining lymph nodes, where they present them to lymphocytes (38). Alternatively, soluble antigens are transferred to the lymph node resident DCs via lymph fluid and are captured there (38). DCs present the captured antigens on major histocompatibility complex (MHC I and MHC II) molecules to T cells, resulting in the priming and activation of naive T cell responses against the cancer-specific antigens. Finally, the now activated effector T cells leave the regional lymph node and migrate to the tumour site (41). In cancer patients, this process is perturbed as tumour antigens may not be detected as foreign, effector T cells can be inhibited from infiltrating the tumour or factors within the TME can suppress the effector cells that are produced (41).

1.2.2.3 Lymphocytes

T and B lymphocytes are adaptive immune cells that can exert cell-mediated and humoral antigen specific immunity respectively (39). T cells mainly comprise of CD8 and CD4 helper T cells. Both subtypes are initially naïve T cells that differentiate into effector T cells in secondary lymphoid organs (38). CD8 T effector cells are largely cytotoxic CD8 T cells in the TME. They contain cytotoxic granules with perforin and granzyme B, which are released on interaction with target cells leading to their destruction by direct lysis (42). CD8 regulatory T cells are also encountered with much lower frequency. CD8 as well as CD4 regulatory T cells inhibit anti-tumour immune response by cell contact dependent mechanisms and producing immunosuppressive cytokines (IL-10 and TGF β) (38). They are characterised by expression of nuclear forkhead box P3 (FoxP3) (43).

CD4 helper T cells comprise of a constantly expanding list of Th (T helper) subsets according to their transcriptional profiles, cytokine secretion and biological function (43). Apart from regulatory T cells, Th1 and Th2 polarised CD4 T cells play key roles in cancer immunoediting. CD4 Th1 T cells secrete inflammatory cytokines, such as IL2 and INF γ , promoting CD8 cytotoxic and innate immune cell cytotoxicity as well as antigen presentation (43, 44). In

contrast, Th2 CD4 T cells secrete immunosuppressive cytokines, such as IL4 and enhance T cell anergy and the tumour promoting activity of M2-like macrophages (44, 45). The functional orientation of CD4 helper T cells within the tumour microenvironment can favour a pro- or anti-tumourigenic immune response. Lastly, B cells are critical for humoral immunity, produce immunoglobulins and paracrine factors that can influence neighbouring immune cells (43).

1.2.2.4 Immune checkpoints

The adaptive immune system is able to recognise and respond to a variety of antigens. To ensure a tight balance is maintained between eradicating harmful pathogens and maintaining self-tolerance, T cell activation is finely tuned by two independent signals. The first signal is provided by the binding of T cell receptor (TCR) to the MHC upon recognition of an antigen. The second one, which is antigen independent, is provided by members of the B7 superfamily that are expressed on antigen presenting cells (APCs), which bind to their receptors on T cells and regulate immune responses by either co-stimulating or co-inhibiting them (44).

Programmed death 1 (PD-1) is a transmembrane glycoprotein expressed on lymphocytes, DCs and activated monocytes that generates inhibitory signals and suppresses activity of T cells upon binding with its programmed death ligands, PD-L1 or PD-L2 (35). PD-L1 is expressed on a variety of cell types, including tumour cells and immune cells whereas PD-L2 is expressed mainly on dendritic cells in normal tissues (35). PD-L1 can be autonomously expressed by tumour cells under the influence of oncogenic signalling pathways, known as 'innate immune resistance' (46). Alternatively, PD-L1 upregulation can be a result of 'adaptive immune resistance' in response to pro-inflammatory cytokines in order to protect tumour cells from CD8 cytotoxic T cell lysis and escape immunosurveillance (46) .

1.2.2.5 Tumour immune microenvironment as a prognostic and predictive biomarker

There is evidence that the immune reaction taking place at the primary tumour site has a significant impact on the course of the disease (38, 47). In colorectal cancer patients, increased CD8 T cell infiltration at the tumour invasive margin

has reproducibly been associated with improved clinical outcome, supplementing, if not superseding, the conventional TNM staging (48-51). These observations have been expanded to gene expression analyses of human samples and *in vivo* models in order to investigate the functional relationships of different immune cell types in colorectal cancer, highlighting CD4 follicular helper and B cells as key players collaborating in the adaptive immune cell defence against tumour progression, via specific mediators such as CXCL13 (52). In renal cancer, higher percentage of infiltrating natural killer (NK) cells and CD4 T cells with Th1 orientation were associated with better survival (53). In another renal cancer study using multiplex immunofluorescence (mIF) panels, increased CD4 regulatory T cells and PD-1 expressing CD8 T cells within the tumour centre and invasive margin respectively were associated with worse survival (54). In a large diffuse large B cell lymphoma study, low CD3 T cell infiltration was associated with a lower anti-tumour response expression signature and had an unfavourable prognostic impact. Also, tumour cells expressing PD-L1 and PD-1 expressing T cells had adverse prognostic impact only in patients with high T-cell infiltration in close proximity to each other, suggesting a possible exhausted anti-tumour immune reaction in those patient (55).

The importance of immune contexture is underscored not only by the abundance of immune infiltrates but also by its spatial context. In pancreatic ductal adenocarcinoma (PDAC), the spatial distribution of cytotoxic CD8 T cells in proximity to cancer cells correlated with improved patient survival (56). This highlights the importance of spatial distribution as when CD8 T cells are restricted from the tumour centre they are not associated with better outcomes (56, 57), even when they are located at the tumour margin or within the stroma. Poor infiltration of CD8 cells was associated with an immunosuppressive microenvironment comprising of regulatory lymphocytes, M2-like polarised macrophages, PD-L1 positive tumour cells and cancer associated fibroblasts (57). The same has been observed in breast cancer patients, where a significant proportion of cases with dense NK and lymphocytic infiltrates contained areas with large distances between immune cells and tumour cells, suggesting a low chance of direct contact and therefore interaction with those cytotoxic effector immune cells (58). A study focusing on macrophage heterogeneity in gastric cancer using mIF and gene expression analysis showed that the abundance of

specific macrophage subpopulations and their proximity to tumour cells were key for predicting outcome, suggesting that direct contact and/or paracrine mediators are important for their function (59).

Tissue immune profiling is becoming an important tool for identifying predictive markers for response to immunotherapy as well as other treatments. In breast cancer, specific lymphocyte immune cell infiltration (CD3 T cells, CD8 cytotoxic T cells, CD20 B cells) has predicted better response to neo-adjuvant chemotherapy and trastuzumab (60-62). In chronic myeloid leukaemia, combining the proportion of CD4 helper T cells and PD-1+TIM3⁻ CD8 T cells in the bone marrow with clinical parameters improved the prediction of remission after tyrosine kinase inhibitor therapy (63). In melanoma patients, characterising the in situ tumour profile using seven immune markers could successfully predict the generation of tumour infiltrating lymphocytes (TILs) for autologous adoptive T cell therapy (64). In another study, tumours with myeloid dominated tumour immune composition were associated with CD8 T cell exhaustion and poor response to neo-adjuvant GVAX vaccination in PDAC patients (65).

It is obvious that the exact composition as well as spatial organisation of the immune tissue microenvironment is critical to building and maintaining an effective antitumor immune response (35, 39). Therefore characterising the exact immune cell composition, functional orientation, tissue density and localisation within tumour regions is crucial for elucidating how the immune microenvironment affects cancer development and progression. Furthermore, those features may be associated with patient prognosis and response to therapies (35, 38, 47).

1.2.3 Prostate cancer immune microenvironment

Relative to other cancer types described above, the characterisation of primary PCa tumour immune microenvironment has been challenging with conflicting results. A detailed summary of the studies on human PCa immune microenvironment is presented in Table 1. The reason for their inconsistent results lays partly on the study of limited immune cell types (macrophages or limited lymphocytic subpopulations), different specimens used (tissue

microarrays or whole sections), variable methodologies for protein detection (IHC or immunofluorescence), visual quantification assessment (inter and intra observer variability), small patient cohorts and measurement of disparate outcomes. In addition, very few studies have integrated tumour molecular subtyping in relation to immune cell infiltration (25, 66).

The presence of inflammatory cells in the prostate is well documented (67). PCa is generally considered to have a relatively immunologically 'cold' microenvironment compared to other solid tumour types. However spatial distribution and functional orientation are emerging as more important features than the mere quantification of immune cells. Interestingly, a recent study using deep learning computational analysis on haematoxylin and eosin (H&E) slides from TCGA patients, showed that even though PCa was not among the highest immune infiltrated cancers it had distinctive structural patterns reflecting the nature of immune responses (68).

The macrophage presence in primary PCa has been investigated in several studies with inconsistent results regarding patient survival outcomes (69-73). Part of the literature has shown a negative impact of macrophage density to patient survival (69, 72). High macrophage density was also predictive of a shorter relapse-free survival after ADT (72) and PCa specific death (69). On the contrary, high macrophage infiltration has been predictive of prolonged disease-free survival (73) or has resulted in no difference in patient outcomes (70, 71). These studies have been limited by the absence of uniform patient treatment and small sample sizes, making it difficult to draw definitive conclusions on the significance of macrophages in prostate cancer. One consistent finding is that macrophage infiltration is increased in PCa when compared to normal prostate (70, 72, 73), however its clinical significance in PCa progression and survival remains unclear.

There is evidence that prostate cancer induces recruitment of lymphocytes into the prostate microenvironment but information regarding precise biological functions and their potential reciprocal interactions with tumour cells are very limited (67). T regulatory cells are increased in blood as well as tumour tissues of PCa patients and have confirmed *in vitro* immunosuppressive potential (74-76). Interestingly, CD8 T regulatory cells are also present in PCa TME with cell

contact dependent suppressive function (77). Another functionally important observation showing negative immune regulatory activity was the expression of PD-1 on PCa infiltrating CD8 T lymphocytes (75, 78). These CD8 T cells were oligoclonal and antigen driven, suggesting a functional inhibition or exhaustion of CD8 T lymphocytes (78). The PD-1 ligand PD-L1 is however rarely expressed on prostate cancer tumour cells (79, 80), suggesting that prostate cancer cells do not impact on immune cells directly via PD-1/PD-L1 pathway.

Lymphocytic infiltration of primary PCa is often increased and perturbed compared to normal prostate tissue (67) but its prognostic implication remains elusive. One of the largest cohort studies found that patients with either high or very low numbers of intratumoural CD3 T lymphocytes, but not B-lymphocytes, had a shorter relapse-free survival (66). Similarly, poor survival outcomes were observed in patients with tumours containing high CD4 (81) and intratumoural CD3 and CD8 T lymphocytic infiltration (82), while other studies had opposite findings (83, 84). Part of the literature has also shown that high FoxP3 T regulatory T cell infiltration was associated with shorter disease free survival (85) and increased risk of dying of PCa specific death (86). More recently, effector CCR4 expressing T regulatory cells were identified as the subpopulation associated with poor survival outcomes (87). The effect of TILs in PCa cancer development is complex and their prognostic value may depend on factors beyond density, such as specific immune subtype, spatial localisation and functional orientation.

Tumour infiltrating immune cells have previously been identified as prognostic and predictive biomarkers in several cancers (38), however in PCa further research is necessary. The contradicting results highlight the need for studying well defined patient cohorts with similar disease stage, risk status and treatments in order to obtain meaningful results. Furthermore, investigation of different immune cell subsets, taking into consideration their spatial organisation and phenotype combined with high-throughput digital quantification will lead to a robust characterisation of PCa tumour immune microenvironment. Multiplex immunofluorescence (mIF) with tyramide signal amplification (TSA) is a suitable methodology for gaining a better understanding of immune-epithelial cell interactions.

First Author, Year	Number of cases studied	Immune marker	Tissue used	Quantification	Association with clinicopathological parameters	Association with clinical outcomes
Macrophage studies						
Shimura, 2000 (73)	81	CD68	Whole RP sections	Visual	Patients with high MΦ had higher T stage and LN metastasis	Patients with high MΦ had longer RFS
Nonomura, 2011 (72)	71	CD68	PCa biopsies	Visual	Patients with high MΦ had higher T stage and GS	Patients with high MΦ had shorter RFS
Gollapudi, 2013 (70)	537	CD68	TMA	Visual	Patients with high MΦ had higher GS	No association with RFS
Lanciotti, 2014 (71)	93	CD68, CD163	Whole RP sections	Visual	Patients with high M2-like MΦ had more frequently EPE	No association with RFS
Erlandsson, 2019 (69)	592	CD163	TMA	Digital	Patients with high MΦ had higher GS	Patients with high MΦ had increased PCa-specific death
Lymphocytic studies						
McArdle, 2004 (81)	80	CD4	Whole RP sections	Visual	None	Patients with high CD4 T cells had shorter PCa-specific survival
Fox, 2007 (88)	146	FoxP3	TMA	Visual	None	No association with RFS
Flamminger, 2012 (66)	2,144	CD3	TMA	Visual	Patients with high CD3 T cells had increased ERG expression	Patients with very high or low CD3 lymphocytes had shorter RFS
Flamminger, 2013 (85)	2,002	FoxP3	TMA	Visual	Patients with high T regulatory cells had higher T stage	Patients with high regulatory T cells had shorter RFS
Davidsson, 2013 (86)	735	CD4+ FoxP3+	TMA	Visual	None	Patients with high CD4 regulatory T cells had increased odds of PCa-specific death
Ness, 2014 (82)	535	CD8, CD3	TMA	Visual	None	Patients with high CD3 and CD8 T cell had shorter RFS
Woo, 2014 (84)	53	CD20	Whole RP sections	Digital	None	High risk PCa patients with high B cells had significantly shorter RFS
Watanabe, 2019 (87)	75	FoxP3+ CCR4+	Whole RP sections	Visual	Patients with high CCR4+Tregs had higher T stage and GS	Patients with high CCR4+ regulatory T cells had shorter RFS and OS

Table 1 Summary of studies characterising human primary prostate cancer immune microenvironment

RP=Radical prostatectomy, MΦ= macrophages, RFS= relapse free survival, GS=Gleason score, EPE=extra-prostatic extension, PCa=prostate cancer, OS=overall survival

1.3 Multiplex immunofluorescence as a tool for immune cell characterisation

The understanding of spatial cellular composition and heterogeneity of tissues in cancer provides vital insights about the biology and clinical progression of the disease. Thus, it is imperative to have effective and reliable tools to detect different immune cell subtypes within tumour samples. Flow cytometry successfully evaluates a large number of markers, however the lack of morphology information and inability to use on archival tissue pose significant limitations. The gold standard method for in situ protein detection is chromogenic immunohistochemistry (IHC) on formalin-fixed paraffin-embedded (FFPE) tissues with is followed by visual assessment of antibody reactivity using 3,3'-Diaminobenzidine (DAB) or equivalent stains. This approach, although widespread and relatively cheap has its limitations.

The information that can be obtained from traditional IHC is confined to a low number of markers per tissue section, usually limiting the classification of immune cells to up to two markers, e.g. CD4+ FOXP3+ regulatory cells. Furthermore, this information is obtained from consecutive tissue sections, making it difficult to relate cells to each other and more importantly using unnecessarily precious clinical tissue. This approach cannot resolve mixtures of chromogens if the target antigens spatially overlap to reliably study co-localisation. Its assessment remains challenging, as it is time consuming, subjective, often poorly reproducible and dependent on the experience of the observer (89). This is done by using binary (positive versus negative), tiered (0, 1+, 2+, and 3+) or semi quantitative (Histo-score) scoring systems, which are unable to discern subtle differences of protein expression and provide only rough estimates of immune cell counts (90). In order to dissect the biological processes that take place and deliver more accurate patient stratification and prognosis, tumours need to be characterised more comprehensively, combining cellular information with intact spatial context of the surrounding microenvironment.

Multiplex immunofluorescence (mIF) has been a great asset in immune profiling of the tumour microenvironment because it overcomes the limitations of traditional chromogenic IHC (91). The benefits of multiplexing lie in collecting maximal information from a single tissue section - it allows the simultaneous

examination of 5 or more different biomarkers (92). Therefore, cell populations can be classified accurately and their spatial associations and frequency of marker co-expression can be determined (92). A key component for the success of this technology is pairing the multiplex fluorescence staining with multispectral imaging (MSI). Using a 'spectral library', MSI separates overlapping fluorophore spectra (including auto fluorescence) enabling accurate fluorophore quantitation for each marker on a FFPE samples. In addition, sophisticated software (i.e. InForm) have been developed for these type of image outputs and can be incorporated for an automated analysis workflow.

We used the tyramide system amplification (TSA) methodology, in which the primary antibody binds to the antigen of interest, which is then bound to a horseradish peroxidase (HRP)-conjugated secondary antibody to the host species. With the addition of tyramide-fluorophore system, HRP activates the fluorophore and tyramide binds to tyrosine residues on or immediately around the epitope through covalent bonds (92). This allows for heat mediated removal (stripping) of primary and secondary antibodies whereas the fluorophore remains bound to the tissue allowing staining with more pairs of primary-secondary antibodies of the same species (Figure 1) (92). In this way, several antibodies of the same species can be used, simplifying the protocol requirements. Furthermore, fluorescent signals are more amenable to quantitation because of their linear and additive nature and relatively well-defined emission spectra. This linear responsiveness allows for more objective and reproducible intensity quantitation (92). Finally, TSA methodology is ideal for detection of low abundance targets, like scarce immune subpopulations present.

While this technique is providing many benefits compared to traditional IHC it is essential to follow extensive optimisation and be aware of possible pitfalls. Firstly, all antibodies used need to be validated with conventional chromogenic staining and confirm sensitivity and specificity of the staining. The fluorophores used need to be chosen carefully so that they have minimal bleed through. Each antibody needs to be paired with the optimal fluorophore based on the signal intensity and signal/noise ratio. As a general rule, low abundance targets are best paired with the brightest fluorophores. Finally, the optimal sequence in which the antibodies will be added has to be determined. Repetitive rounds of

heating can compromise the integrity of some antigens and weaken the fluorophore signal. Therefore, most sensitive targets and fluorophores impacted the least by microwaving should be added early on. Lastly, it is good practice to compare singleplex with multiplex staining in order to account for ‘antigen sheltering’, whereby existing tyramide-fluorophore deposits may preclude subsequent deposition of tyramide-fluorophores if their target is located in their vicinity (92).

The mIF methodology has robustly been validated in mouse (93, 94) and in a larger extent in human FFPE tissues in previous studies (91, 95-97). It has gradually progressed from manual to automated staining to become less time consuming and avoid the risk of human error leading to staining variability (98, 99). Additionally, previous work has confirmed its reliability showing a high correlation between mIF and other established methodologies, such as conventional chromogenic IHC (91, 97, 98, 100, 101) or flow cytometry (65, 93). More recent studies have expanded the capabilities of this method, increasing the number of markers up to 12 (65), using whole-slide tissue imaging and analysis (102) and combining fluorescent with chromogenic staining (102, 103).

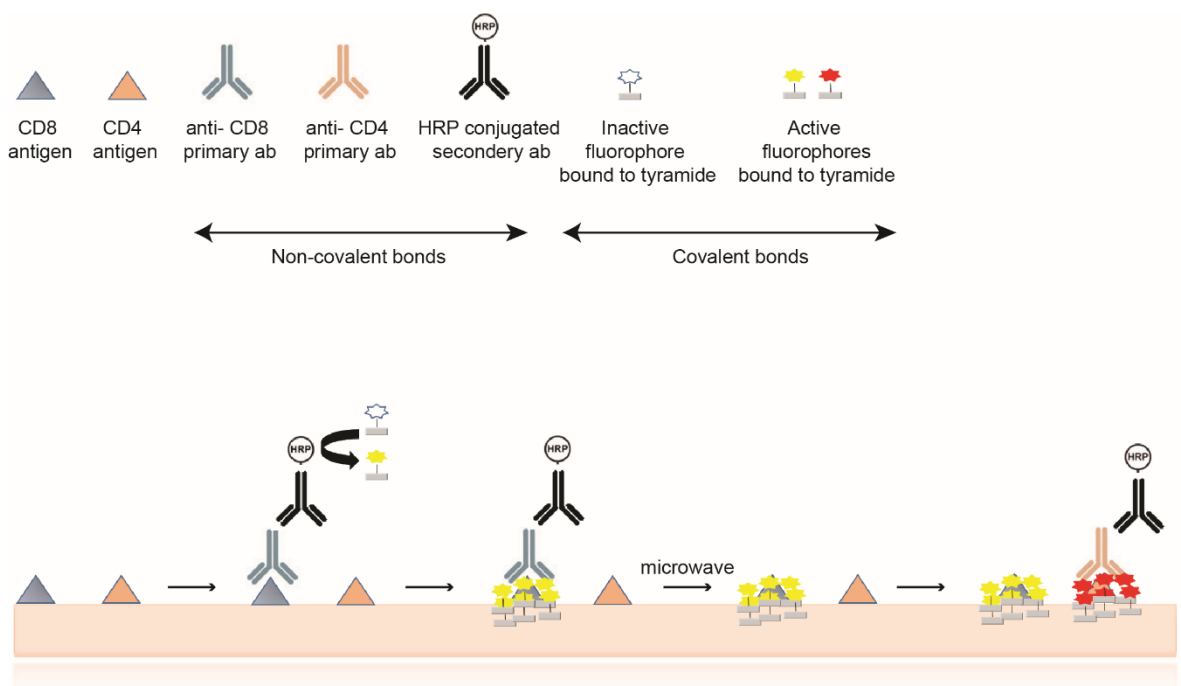


Figure 1 Multiplex immunofluorescence with tyramide signal amplification method

The multiplex immunofluorescence using tyramide signal amplification methodology lies in the covalent bonds developing between tyramide and tissue that allow for heat induced removal of the non-covalently bound primary and secondary antibodies. Iterative rounds of staining allow for the visualisation of up to seven markers on the same tissue section.

1.4 B7-H3 immune checkpoint molecule

1.4.1 Immune function of B7-H3

As a new member of the B7 superfamily, B7-H3 (CD276) was first identified in 2001 (104). It is a type I transmembrane protein that contains an immunoglobulin (Ig) extracellular domain, a transmembrane domain and a short intracellular domain. Its expression can be induced on mature dendritic cells, T cells, B cells, macrophages, monocytes and natural killer cells (104, 105). Whilst B7-H3 protein expression is limited in normal tissues (106), it is overexpressed in different types of tumours, including PCa, pancreatic and breast cancer (107-109), making it a promising target for immunotherapies. Further research has confirmed that there are two main isoforms, 2Ig-B7-H3 and 4Ig-B7-H3, being the dominant forms in mouse and human respectively (105). Human 4Ig-B7-H3 structure is the result of an exon duplication that contains two immunoglobulin-like V and C domains, whereas 2Ig-B7-H3 contains a single V and C domain (110, 111).

B7-H3 was initially reported to function promoting the TCR mediated CD4 and CD8 T cell proliferation and inducing IFN- γ production (104, 105). In a lymphoma mouse model, injection of B7-H3 expressing plasmid into the tumour, resulted in a complete regression of 50% of tumours which was dependent on cell mediated cytotoxic CD8 T and NK anti-tumour immune response (112). In an orthotopic colon cancer murine model, intratumoural injection with adenovirus expressing mouse B7-H3 resulted in a reduction of tumour size and metastatic foci. Treated mice had significantly higher IFN- γ producing tumour specific CD8 T cells (113). Another study showed that in a transgenic adenocarcinoma mouse prostate (TRAMP) model, ablation of B7-H3 led to an increased tumour burden and regulatory T cell infiltration (114).

Although initially reported to function as a co-stimulator of T cell response, mainly from *in vivo* studies, the current body of evidence strongly supports the role of B7-H3 as a co-inhibitor, contributing to immune cell evasion. With

regards to murine B7-H3, mice treated with a blocking anti- B7-H3 antibody showed decreased growth of PDAC (108), melanoma and lymphoma (115), which depended on the cytotoxicity of NK and CD8⁺ T cells (108, 115). A study using pancreatic and lung syngeneic mouse models showed improved anti-tumour immunity with anti-B7-H3 blockade that was orchestrated by CD8 cytotoxic T cells (116). In a recent study chimeric antigen receptor T cells (CART) targeting 2Ig and 4Ig B7-H3 isoforms was developed. Targeting PDAC, ovarian and neuroblastoma *in vitro* reduced tumour proliferation via increase of the cytolytic activity and IFN- γ and IL-2 release (117). Validating this in *in vivo* orthotopic and metastatic xenograft models, as well as patient derived xenografts, confirmed that administration of CART B7-H3 controlled tumour growth (117).

Accumulating evidence also indicates that human B7-H3 acts as a co-inhibitory factor of immune responses. A study investigating the consequences of B7-H3 and T cell interaction using different experimental conditions showed that B7-H3 negatively regulated naïve and activated T cells, reduced IL-2, Th1 and Th2 cytokine production (118). Another study showed DCs isolated from non-small cell lung cancer (NSCLC) patients had upregulated B7-H3 and reduced T cell proliferation in mixed lymphocyte reactions compared to healthy controls (119). In neuroblastoma, B7-H3 expressed at the tumour cell membrane was shown to exert a protective role from NK cell mediated lysis by interacting with a still undefined inhibitory receptor expressed on NK cells. A bispecific anti-CD3 x anti-B7-H3 antibody armed with activated T cells was synthesised recently (120) and showed increased cytotoxicity against human cancer cells *in vitro* and *in vivo*, at least partly due to increased IFN- γ , TNF- α and IL-2 secretion (120, 121). B7-H3 was also used as a target of antibody-drug conjugate therapy that exhibited potent tumouricidal and anti-metastatic activity in human lung, cancer and breast human tumour xenografts targeting tumour and tumour vasculature (106). Another humanised anti-B7-H3 (MGA271) IgG1 monoclonal antibody showed potent antibody-dependent cellular cytotoxicity (ADCC) *in vitro* and in xenografts against a variety of B7-H3 expressing tumours (122). MGA271 is currently under evaluation in a phase I study for several B7-H3 expressing tumours, including PCa (123).

In summary, while initially B7-H3 immune function was controversial, current consensus supports its classification as a co-inhibitory molecule of T-cell activity. It is conceivable that the contradicting results may be due to interactions with both inhibitory and stimulatory receptors, therefore the co-stimulatory or co-inhibitory effect could prevail depending on the experimental system used. There is the possibility that B7-H3 may interact with different affinities to several receptors and exert different functions. Also, differences between known as well as potentially unknown mouse and human isoforms or splice variants may affect its function and data derived from mouse studies may not be transferable to humans. So far, the only potential receptor of murine B7-H3 identified was Triggering receptor expressed on myeloid cell-like transcript 2 (TREM2) (124, 125). TREM2 is a modulator of innate and adaptive immune responses and its binding to B7-H3 lead to enhancement of CD8 T cell response (124, 125). However, later studies have disproved the engagement of human B7-H3 to this receptor (118). The binding partner of B7-H3 on immune cells remains elusive.

1.4.2 Non- immune function of B7-H3

Apart from the immune regulatory function, B7-H3 has been shown to have a non-immunological role in cancer progression. For the first time in 2008, downregulation of B7-H3 with siRNA resulted in up to 50% decrease of cell adhesion to fibronectin and up to 70% *in vitro* decrease of migration and invasion in melanoma and breast cancer cells (126). Further *in vitro* studies showed that silencing of B7-H3 lead to reduction of cell adhesion to fibronectin, migration and invasion in PCa (127). This was further validated *in vivo* by reduction of tumour metastasis in nude mice harbouring PDAC xenografts (108). Of note, a few studies have also associated B7-H3 with increased tumour proliferation *in vitro* (128, 129) and tumour growth in mouse orthografts (130).

Further studies identified regulation of matrix metalloproteases (MMPs) as one of the downstream pathways involved. In a melanoma study, stable knock out (KO) of B7-H3 decreased migration and invasion *in vitro* and metastasis in *in vivo* xenograft models (130). It also showed that B7-H3 KO reduced the expression of known key metastasis players, such as matrix metalloproteinases 2 (MMP2), phosphorylation of STAT3, secretion of IL-8 and increased the expression of

tissue inhibitors of metalloproteinase 1 & 2 (TIMP1&2) (130). A study using overexpression and silencing of B7-H3 in bladder cancer cell lines, showed B7-H3 promoted cell migration and invasion by upregulating MMP2 and MMP9, at least partly via the PI3K/AKT/STAT3 signalling pathway (131). B7-H3 overexpression in osteosarcoma was associated with poor prognosis, inversely correlated with CD8 T cell infiltration, promoted invasion *in vitro* and upregulated expression of MMP2 (132). B7-H3 also promoted migration and invasion in colorectal cancer *in vitro* and enhanced MMP9 expression by upregulation of Jak2/Stat3 pathway (133).

In other tumour types, modulation of epithelial to mesenchymal transition (EMT) markers appears to be the dominant downstream pathway of B7-H3 mediated functions. In hepatocellular carcinoma, B7-H3 overexpression correlated with metastasis and poorer survival, and silencing of B7-H3 significantly decreased migration and invasion *in vitro* (134). This was accompanied by decreased expression of MMP2, MMP9 and epithelial to mesenchymal transition (EMT) markers that could be attributed at least partially to a decreased phosphorylation of STAT3 and Jak2 (134). B7-H3 overexpression in NSCLC patients correlated with LN and distant metastasis, transient silencing of B7-H3 reduced *in vitro* cell proliferation, migration and invasion and expression of EMT markers (135). A study on colorectal cancer cells using overexpression and KO cell lines for B7-H3 showed that B7-H3 promoted *in vitro* and *in vivo* migration/invasion and EMT by activating the PI3K-AKT pathway and upregulating SMAD1 (136).

A few other possible downstream targets of the invasive phenotype associated with B7-H3 have been under investigation. A study focused on soluble B7-H3 (sB7-H3) and showed that pancreatic cancer cells released sB7-H3 according to their membranous bound levels. Exposure to sB7-H3 lead to an increase in migration and invasion through the TLR4/NF- κ B pathway and its downstream targets, IL-8 and Vascular endothelial growth factor (VEGF) (137). A study on gastric cancer human cell lines reported the direct interaction with the chemokine receptor CXCR4 and potential contribution of phosphorylation of AKT, ERK and Jak2/STAT3 (138).

B7-H3 is also shown to play a role in resistance to cancer chemotherapy drugs. B7-H3 silencing enhanced gemcitabine cytotoxicity *in vitro* and *in vivo* PDAC by inducing apoptosis and downregulating anti-apoptotic protein survivin (139). B7-H3 also induced sensitivity to paclitaxel *in vitro* and *in vivo* breast cancer, at least partially by regulating phosphorylation of the Jak2/Stat3 pathway and downstream targets Mcl-1 and survivin (140). In colon cancer cell lines, overexpression of B7-H3 inhibited drug-induced apoptosis and showed increased Jak2/STAT3 phosphorylation, upregulation of anti-apoptotic proteins bcl-2 and bcl-xl and down-regulation of pro-apoptotic protein Bax (128). Finally, in a recent study, B7-H3 increased chemoresistance of breast cancer cells by regulating stem cell enrichment through major vault protein mediated MEK activation (141). Summarising, the role of B7-H3 in cancer progression as well as in normal biologic functions extends far beyond its first reported immunoregulatory abilities.

1.4.3 B7-H3 immune checkpoint in prostate cancer

Assessment of B7-H3 expression in large cohort of 823 PCa patients treated with RP showed variable degree of B7-H3 expression in 93% of the tumours. High expression was present in 26% of cases and significantly associated with extracapsular extension, seminal vesicle invasion, cancer recurrence, and PCa related death (107). In a separate study of 338 men treated with RP, high B7-H3 expression significantly correlated with adverse pathological features and cancer progression after surgery (142). B7-H3 expression was maintained in bone metastases, even after ADT treatment (143) and its high expression correlated with biochemical recurrence after salvage radiation therapy (SRT) in recurrent PCa (144).

Chapter 2 Materials and methods

2.1 Reagents

The details of all reagents used in the following experiments are listed in Table 2.

Reagent	Cat number	Supplier
Xylene	X/0250/17	Fisher Chemicals
Ethanol absolute	20821.365	VWR Chemicals
Methanol	20846.326	VWR Chemicals
EDTA (Ethylenediaminetetraacetic acid)	D10700153	Thermo Fisher Scientific
Tri-sodium-citrate	S/3320/60	Thermo Fisher Scientific
Hematoxylin solution modified acc. to Gill III	105174	Merk
Hydrogen Peroxide 30-32% (w/w)	H/1800/15	Fisher Chemicals
Parafilm 'M'	PM-996	Bemis
RPMI-1640 medium	1640	Sigma-Aldrich
FBS (fetal bovine serum)	10270	Thermo Fisher Scientific
L-glutamine	25030	Thermo Fisher Scientific
Trypsin solution from porcine pancreas	T4549	Sigma-Aldrich
DMSO (dimethyl sulfoxide)	D/4121/PB08	Fisher Scientific
BSA (Bovine Serum Albumin)	A3059-506	Sigma
MOPS SDS running buffer	NP0001	Thermo Fisher Scientific
Immobilon-FL PVDF Membrane	IPFL00010	Merk
Amersham ECL Western Blotting Detection Reagent	RNP2106	GE Healthcare Life Sciences
Pierce ECL Plus Western Blotting Substrate	32132	Thermo Fisher Scientific
Halt™ Protease and Phosphatase Inhibitor Cocktail (100X)	78440	Thermo Fisher Scientific
PhosSTOP™ Phosphatase Inhibitor Cocktail	4906837001	Roche
Bradford Assay	5000006	Biorad
RNase Zap	AM9780	Invitrogen
2-mercaptoethanol	M-3148	Sigma
Opti-Mem	31985070	Thermo Fisher Scientific
Lipofectamine RNAiMAX	13778-150	Thermo Fisher Scientific
Matrigel	354234	Corning
Transwell Boydon Chamber	3422	Corning
Calcein AM	1430	Invitrogen

Table 2 Commonly used reagents

2.2 Solutions and buffers

The composition of buffers and solutions used in the following experiments are listed in Table 3. Tris Buffered Saline and Tween (TBST), Tris Buffered Saline (TBS) and Phosphate Buffered solution (PBS) buffers were provided by our core facility services at the Beatson Institute.

Solutions and buffers	Composition
Tris Buffered Saline and Tween (TBST)	25mM Tris-HCl pH7.4 137mM NaCl 5mM KCl 0.1% Tween-20
Tris Buffered Saline (TBS)	25mM Tris-HCl pH 7.4 137mM NaCl 5mM KCl
Phosphate Buffered solution (PBS)	170mM NaCl 3.3mM KCl 1.8mM Na ₂ HPO ₄ 10.6mM KH ₂ PO ₄ pH7.4
5% goat serum IHC blocking solution	5% goat serum (Dako) 1% BSA 0.1% Triton in TBS
RIPA Cell Lysis Buffer (for protein extraction)	Tris 1M pH7.6 NaCl 4M Triton 10% Deoxycholate 10% SDS 10% Sodium Orthovanadate 100mM Sodium Fluoride 0.5M Protease and phosphatase Inhibitor Cocktail PMSF 50mM PhosSTOP dH ₂ O

Table 3 Working solutions and buffers

2.3 Human tissue

2.3.1 Construction of intermediate/high risk discovery primary prostate cancer tissue microarray

Formalin-fixed, paraffin-embedded (FFPE) histologic sections from intermediate and high-risk PCa patients who underwent RP and extended regional lymphadenectomy with curative intent (half with and half without evidence of nodal disease) were retrospectively identified between 4th June, 2008 and 23rd January, 2018 at the Queen Elizabeth University Hospital in NHS Greater Glasgow and Clyde. I reviewed all H&E stained histologic sections and when necessary slides were double checked by a specialist Uropathologist (Dr J. Salmond). The index prostate cancer lesion was marked for each case and three 1 mm thick tissue cores were punched out and transferred onto a tissue microarray (TMA) format. PCa commonly has multiple distinct foci, the index lesion was selected as the largest focus according to the pathology report (7). The work described here is carried out in accordance with approval from the West of Scotland

Research Ethics Committee (REC) 4 granted to the NHSGGC Bio-repository and Pathology Tissue Resource II (REC reference: 16/WS/0207).

This format was chosen because TMAs have an inherent capacity to process hundreds of tumour specimens at once (145). Two hundred and eighty two cores were distributed among three blocks, each containing 94 tumour samples. There were 10 control tissue cores on each block including tissue from tonsil, lymph node, kidney, liver, skin, breast cancer, lung cancer and normal prostate tissue from two different patient samples. From the resultant TMA paraffin blocks, 3 μm serial histologic sections were prepared. The first set of sections was routinely stained with H&E and presence of cancer was confirmed. The cores were further analysed only when more than 60% of the core contained tumour glands.

The patients' selection for inclusion in the discovery TMA was based on their intermediate and high-risk status. Clinicopathological information were extracted from the pathology report including total number of excised lymph nodes at surgery, peak pre-operative PSA (ng/dl), age at diagnosis, pathological tumour stage (pT) according to the 7th edition of American Joint Committee on Cancer (AJCC), Gleason score and perineural invasion (PNI). Follow up information was retrieved from the medical records and included overall survival (OS), cancer-specific survival and relapse-free survival (RFS), defined as rise of PSA (≥ 0.2 ng/dl) in two consecutive measurements or presence of distant metastases. The first PSA value above or equal to 0.2 ng/mL was used to define the time of relapse. Patients without evidence of tumour relapse were censored at the last follow-up.

2.3.2 Validation intermediate/high risk primary prostate cancer tissue microarray

We established a collaboration with Professor George Thalmann (Department of Urology, University of Bern, Switzerland) and obtained an incidence primary prostate PCa TMA containing intermediate and high-risk tumours for validation of findings from the discovery TMA. This TMA included treatment naïve, newly diagnosed prostate cancer patients who underwent RP. Tissue cores of 0.6 μm were taken from the index prostate cancer lesion of each patient and were

distributed in one block. Four μm serial histologic sections were cut and sent to us alongside anonymised patient clinical information. The first set of sections was stained with H&E and cores were further analysed only when more than 60% was cancerous.

2.3.3 Low risk primary prostate cancer tissue microarray

We established a collaboration with Professor David Berman (Department of Pathology, Queen's University, Kingston, Ontario, Canada) and obtained a primary PCa TMA consisting of low risk tumours at the time of diagnosis. This included tissue cores from the index tumour lesion, surrounding PIN and benign tissue from RP specimens. Tissue cores of 0.6 μm were distributed in nine blocks. Three μm serial histologic sections were cut and sent to us alongside anonymised patient clinical information. Only the annotated index tumour cores were included in my analysis.

2.3.4 Benign prostatic hyperplasia tissue microarray

Transurethral resection of the prostate (TURP) specimens from 390 men with no evidence of prostate cancer were used to construct a benign prostatic hyperplasia (BPH) TMA previously by Dr Joanne Edwards (146). Three 0.6 μm cores were obtained from every patient and they were distributed in three slides. Already cut sections were available in our lab, with no clinical information attached to these patients.

2.4 Chromogenic immunohistochemistry

Chromogenic immunohistochemistry was performed manually after 1-2 hours oven incubation at 60°C the day before. Following antigen retrieval buffer and antibody concentration optimisation, the list of the primary antibodies used is presented in Table 4. These were incubated with appropriate secondary antibodies (EnVision System HRP labelled Polymer anti rabbit #K4003 or anti-mouse #K4001) and the staining was visualised using 3,3'-Diaminobenzidine (DAB) Quanto (TA-125-QHDX).

Antibody	Antigen retrieval	Dilution (v/v)	Catalogue number	Manufacturer
Anti-CD68	Citrate	1:400	76437	Cell Signalling
Anti-CD163	Citrate	1:50	93498	Cell Signalling
Anti-CD20	EDTA	1:400	60271-1	Proteintech
Anti-CD8	EDTA	1:200	70306	Cell Signalling
Anti-CD4	EDTA	1:100	ab133616	Abcam
Anti-FoxP3	Citrate	1:100	98377	Cell Signalling
Anti-PD-1	Citrate	1:200	86163	Cell Signalling
Anti-AE1/3 (PanCK)	EDTA	1:1	GA053	Dako
Anti-ERG (EPR3864)	EDTA	1:50	Ab92513	Abcam
Anti-PTEN (138G6)	Citrate	1:100	9559	Cell Signalling
Anti-Ki67 (MIB1)	EDTA	1:100	M7240	Dako
Anti- Collagen I	EDTA	1:100	ab138492	Abcam
Anti- Collagen III	Citrate	1:50	ab7778	Abcam
Anti- Fibronectin 1	Citrate	1:100	ab2413	Abcam
Anti- FAPa	EDTA	1:200	ab207178	Abcam
Anti-B7-H3	Citrate	1:100	14058	Cell Signalling

Table 4 Antibodies used for chromogenic immunohistochemistry

2.4.1 Chromogenic immunohistochemistry protocol

Step 1 - Deparaffinisation and rehydration: Slides were incubated in the following order: Xylene three times for 10 min, 100% Ethanol two times for 10 min, 95% Ethanol two times for 10 min, dH₂O two times for 5 min.

Step 2 - Antigen retrieval: Either 10 mM sodium citrate buffer (pH 6.0) or 1 mM EDTA buffer (pH 8.0) were made fresh on the day and pre-heated for 10 min in the microwave. Slides were added in the buffer in a pressure cooker for 3 min under pressure. The slides were then left to cool down at room temperature for 30 min, followed by three 5 min washes in dH₂O.

Step 3- Quenching of endogenous peroxidases: Slides were incubated with freshly made 3% H₂O₂ for 10 min. They were then washed in dH₂O three times for 5 min and in TBTS for 5 min.

Step 4 - Blocking of non-specific binding: Tissue containing areas were circled with a hydrophobic barrier PAP pen (R37622, Invitrogen) and incubated in 5% goat serum for 1 hour in a humid chamber.

Step 5 - Primary antibody incubation: The primary antibody was diluted in 5% goat serum in the appropriate concentration and left overnight at 4°C. This was followed by three 15 min washes in TBST the next day.

Step 6 - Secondary Antibody Incubation: Secondary anti-mouse or anti-rabbit antibody was added for an one hour incubation at room temperature, followed by three 15 min washes in TBST.

Step 7 - Substrate visualisation: DAB chromogen was applied for 5 min according to manufacturer's instructions.

Step 8 - Counterstain and mounting: Slides were then washed in water, counterstained with haematoxylin and coverslipped using Dibutylphthalate Polystyrene Xylene (DPX) mountant (CellPath, UK). Stained slides were then scanned with Leica Aperio AT2 bright field microscope, x 20 magnification for digital image recording.

2.4.2 Dual CD4-FoxP3 chromogenic immunohistochemistry protocol

For selected validation experiments, histologic slides were manually stained for dual CD4-FoxP3 immunohistochemistry. The same steps as in section 2.4.1 were followed up to DAB substrate visualisation for FoxP3 (1/100 v/v) and slides were washed in dH₂O for 1 min and TBST twice for 5 min. Horse serum (2.5%, v/v) was added for 1 hour and then slides were incubated with CD4 (1/100, v/v) for 1 hour at room temperature. The slides were then washed in TBTS twice for 5 min and incubated with ImmPRESS-Alkaline phosphatase Polymer Anti-Rabbit IgG Reagent (MP-5401, 1:1) for 30 min. Slides were washed again in TBST twice for 5 min and ImmPACT Vector Red Alkaline Phosphatase Substrate (SK-5105) was added according to manufacturer's instructions for 15 min. For counterstaining, slides were manually washed in dH₂O for 1 min, incubated in Mayer's Haematoxylin for 2 min, washed in dH₂O for 1min, incubated in Scotts Tap Water for 2 min and washed in in dH₂O for 1 min. Lastly, sections were dried in the oven at 60°C for 30 min and mounted with EcoMount (M897L).

2.4.3 HALO scoring

Digital images were analysed using the HALO™ Image Analysis Platform (v2.1.1637.6) to objectively quantify the number of positively stained cells within an area. The software enables tissue classification (epithelium vs stroma vs background) based on the morphological characteristics and the quantification of positively stained

cells in each of the tissue compartments. The number of cells positive for each marker within a tissue compartment was then expressed as tissue cell density (cells/mm²).

2.4.4 ERG, PTEN, Ki67 scoring

ERG scoring was based on visual scoring systems validated in previous studies, using endothelial and immune cell staining as internal control (26-28). For each tumour core, only nuclear staining was assessed and defined as negative or positive when there was immunoreactivity in at least 30% of tumour tissue. It was given an intensity score of 0-4 but for the subsequent analysis any degree of intensity staining was considered positive as there has been previously verified that there is no significant difference between ERG intensity staining and *ERG* gene rearrangement detected by FISH (27). A patient's tumour was defined as ERG positive if at least one core was defined as ERG positive and negative if all cores had no ERG staining.

PTEN scoring was based on the intensity of cytoplasmic and nuclear staining described in previous studies (18, 28, 31). In brief, if there was protein expression in >90% of malignant glands of a core that was considered PTEN intact. If the PTEN expression was absent in 100% of the glands that was regarded as homogeneous PTEN loss. If there was between 10% and 100% of PTEN immunoreactivity observed, the case was scored as having heterogeneous PTEN loss (focal loss). Benign prostate and stromal staining were used as internal positive controls and in their absence, the staining was considered ambiguous and the core was not given a PTEN score. Each patient was scored for the presence or absence of PTEN loss by summarising the scores of each individual TMA core. A patient's tumour was designated as having intact PTEN if all cores showed intact PTEN expression and homogeneous loss of PTEN if all cores showed complete absence of PTEN expression. A tumour was defined as having heterogeneous PTEN loss if there was at least one core showing heterogeneous PTEN loss (intracore heterogeneity), or alternatively, if at least one core showed intact PTEN and another one showed heterogeneous and/or homogeneous PTEN loss (intercore heterogeneity).

Ki67 scoring was defined as low ($\leq 10\%$), moderate (10-20%) and high ($\geq 20\%$) according to the fraction of tumour cells showing nuclear immunoreactivity (147).

2.4.5 Histoscore

Histoscore (H-score) was used to quantify B7-H3 expression on tumour cells. This is a well-established visual semi-quantitative assessment that uses intensity of staining (scored as: 0, no staining; 1, weak; 2, moderate; or 3, strong) multiplied by the percentage (%) of positive cells (148). The scoring range spans from 0 to 300.

2.5 In situ hybridisation for CXCL14

In situ-hybridisation for the detection of CXCL14 mRNA (using probe 425298 from Advanced Cell Diagnostics) was performed by Mr Colin Nixon, the Beatson Histology Laboratory. RNAscope 2.5 LS (Brown) detection kit (Advanced Cell Diagnostics) was used on a Leica Bond Rx autostainer according to the manufacturer's instructions (146). Positive staining was measured by brown punctate dots present within the nucleus and/or cytoplasm.

2.6 Second generation harmonic image acquisition and analysis for determination of collagen quantity and quality

Five μm FFPE TMA sections from the discovery TMA were deparaffinised manually, imaged using Second generation harmonic (SGH) and analysed by Ewan McGhee as described previously (149). In brief, collagen SGH images were collected using a LaVision Biotec Trimscope 1 system equipped with a Coherent Chameleon Ultra II femtosecond pulsed laser. A $500 \times 500 \times 30 \mu\text{m}$ z-stack was acquired at the centre of each TMA core and generated collagen stack images. Three slides from the discovery TMA were imaged.

Image analysis was performed using Image J. The UMB GLCM plugin (http://arken.nmbu.no/~kkvaal/eamtexplorer/imagej_plugins.html) was used. This removed the background noise and selected only the collagen SHG signal. The output of the plugin for each image was saved as a text data file and then

the data files were processed using another ImageJ macro, generating outputs for both the mean and individual values for each image. These were then imported into GraphPad Prism for plotting.

2.7 Multiplex immunofluorescence

2.7.1 Optimisation steps for multiplex immunofluorescence panel development

My aim was to develop a panel of antibodies paired with fluorophores in order to detect different immune cell populations on the same tissue slide. Initially, several optimisation steps for the multiplex immunofluorescence (mIF) panel development were performed manually in our facility. Sections from tonsil blocks were cut at 3 μm thickness and used for optimisation because of its immune cell abundance and well characterised immune cell spatial distribution. Antibodies were tested for each marker using chromogenic IHC in order to validate their sensitivity and specificity and also to determine their optimal concentration (Table 4). The antibodies were tested in different dilutions using the concentration for IHC recommended by the company as a reference and trialling concentrations above and below that. A negative control was used for each antibody and DAB chromogen staining was assessed visually with a light microscope. Not all commercially available antibodies claiming to work in human FFPE tissue showed a strong and/or specific staining. Such examples were CD4 (4SM95, 14-9766-82, Invitrogen), CD4 (CL03995, AMAb90754, sigma), CD68 (ab125212), Pan-Keratin (4545, Cell signalling).

For transition to immunofluorescence (IF) staining, some alterations were implemented to the chromogenic IHC protocol. There were changes in the reagents used, as primary antibodies were diluted in Signal stain antibody diluent (#8112) and Signal stain Boost IHC reagents (rabbit #8114, mouse #8125, Cell signalling) were used as secondary antibodies. After secondary antibody incubation, TSA conjugated fluorophores were added according to manufacturer's instructions and visualised under the confocal microscope for singleplex immunofluorescence (sIF) staining. For multiple marker staining, a microwaving step was performed after the addition of fluorophores (for primary and secondary antibody removal) and tissue was subsequently stained with the

next primary antibody (Figure 2). Slides were mounted with ProLong® Gold Antifade Reagent (#9071, Cell Signalling) for sIF and ProLong® Gold Antifade Reagent with DAPI (#8961, Cell Signalling) for multiplex staining.

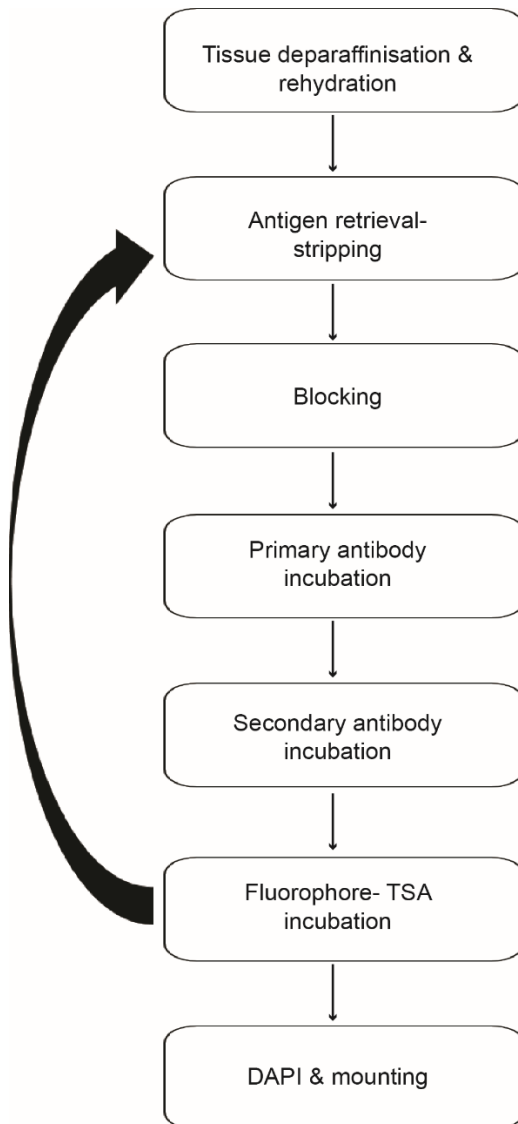


Figure 2 Multiplex immunofluorescence staining workflow

TSA: Tyramide signal amplification

Prior to conducting a multiplex experiment, the antibody concentration for each primary antibody was determined in the singleplex setting. After tonsil and prostate cancer whole tissue sections were stained with each marker, the slides were imaged in Zeiss 880 Airyscan Confocal Microscope. The optimal concentration was determined based on the assessment of highest signal

intensity in combination signal to noise ratio (Figure 3A). ZEN.2 software was used for these calculations. Once the optimal dilution for each antibody in the singleplex setting was determined, different antibody-fluorophore pairs were tested and the optimal combination was determined as before (Figure 3B). The aim of this was to balance signal intensities, generally pairing low abundance targets with the brightest fluorophores. Lastly, multiple rounds of heating can compromise the antigen integrity. For this reason, the order in which the antibody-fluorophore pairs will be added requires optimising. Each tissue section was stained only once and subjected to microwave heating the same amount of times irrespective of the labelling order (Figure 3C).

These data were used in a five marker multiplexing proof of principle experiment that confirmed the feasibility of this method (Figure 3D). The panel showed specific staining but there was fluorescence intensity variation between staining rounds and the tissue auto-fluorescence was pronounced in red blood cells, vessels, muscle and occasionally stromal areas. The manual staining of five antibodies was a five day protocol, susceptible to technical errors that were likely responsible for the batch variations. More importantly, there were limitations with image acquisition capabilities in our facility and I could not use confocal microscopes designed for high-resolution microscopy for whole slide imaging.

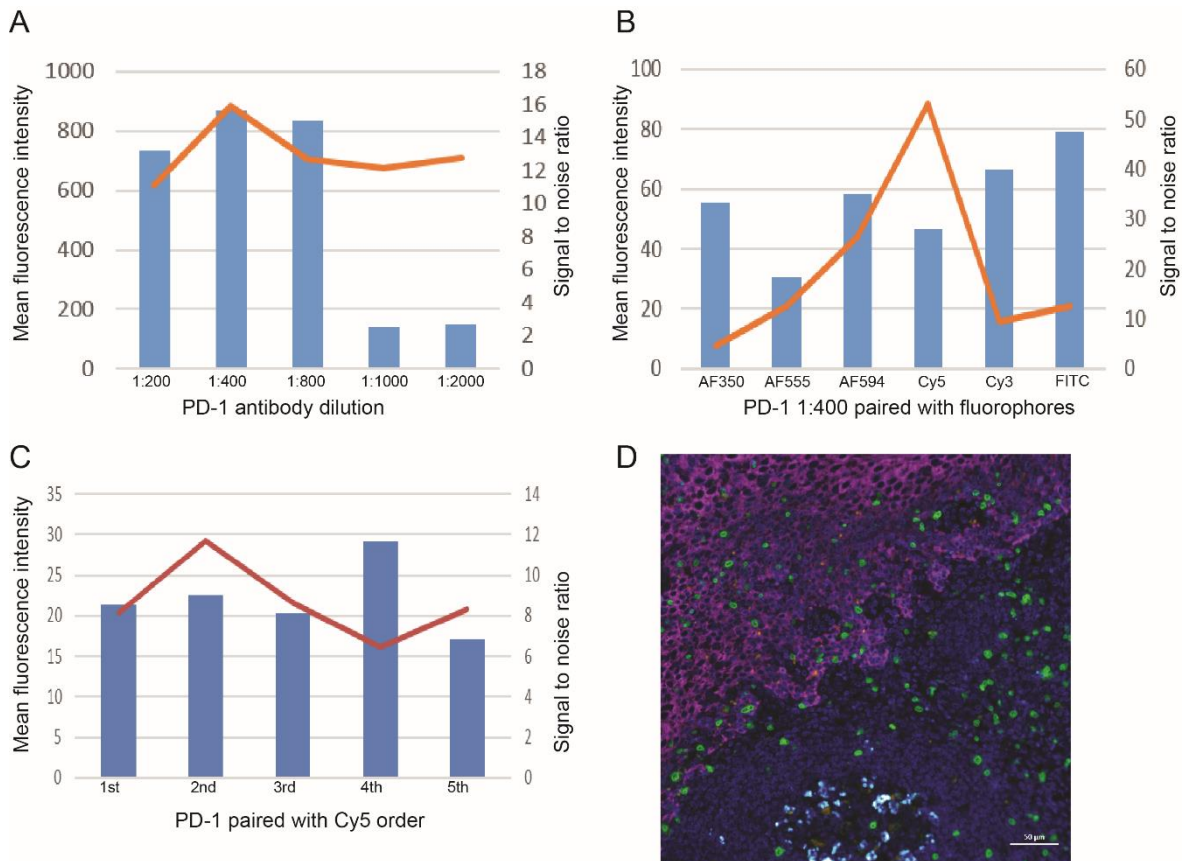


Figure 3 Manual multiplex immunofluorescence staining optimisation

(A) Representative example for PD-1 antibody optimal titration (1:400). (B) Representative example for PD-1 antibody fluorophore pairing comparison (Cy5). (C) Representative example for PD-1 antibody order optimisation. Positioning PD-1 in the second step was chosen. (A-C) Mean fluorescence intensity in blue bars and signal to noise ratio in red line. (D) Representative image of tonsil tissue stained manually with five antibodies using spectral unmixing with microscope airyscan zeiss 880. FoxP3 (1:200) paired with FITC in green, PD-1 (1:400) paired with Cy5 in cyan, CD68 (1:5000) paired with AF555 in yellow, AE1/3 (1:1) paired with AF350 in magenta and DAPI (1:1) in blue.

2.7.2 Automated multiplex immunofluorescence staining and image acquisition

Due to the difficulties mentioned above, we developed a collaboration with Dr John Le Quesne (Department of Pathology, University of Leicester; now at University of Glasgow). Dr Le Quesne's laboratory has already established protocols for simultaneous automated staining of multiple markers alongside the necessary imaging equipment (Vectra Polaris) and analysis software (InForm 2.4.2). My data were shared with his team in order to assist in their panel optimisation, however some antibodies were incompatible with their automated staining and were substituted accordingly. Also, they used the PerkinElmer Opal kit (Perkin-Elmer, Waltham, MA), therefore my fluorophore combinations were translated into their system. A prostate cancer test TMA that was created for

optimisation. This comprised of four 1 mm cores from four cases (16 cores in total) from old TURP blocks. The same optimisation steps were followed. All stainings were performed in Ventana Discovery Ultra.

Two mIF were developed, presented in Table 5. In detail, Panel 1 comprised of CD68 (macrophage marker, 1:200, #76437, Cell signalling) with Opal 520 (1:200), AE1/AE3 (epithelial marker, 1:250, #NCL-L-AE1/AE3, Leica) with Opal 650 (1:200), CD20 (B cell marker, 1:1, #760-2531, Ventana) with Opal 690 (1:150), CD163 (macrophage marker, 1:200, #NCL-L-CD163, Leica) with Opal 570 (1:550), discovery QD DAPI (#760-4196, Ventana). Panel 2 consisted of AE1/AE3 (1:250, #NCL-L-AE1/AE3, Leica) with Opal 620 (1:100), FoxP3 (regulatory T cell marker, 1:20, #ab20034, abcam) with Opal 690 (1:200), PD-1 (immune checkpoint, 1:1, clone NAT 105, #760-4895 Ventana) with Opal 650 (1:200), CD4 (helper T marker, 1:1, clone SP35, #790-4423, Ventana) with Opal 570 (1:150), CD8 (1:100, clone C8/144B, #70306, Cell signalling) with Opal 520 (1:100) and discovery QD DAPI. Slides were mounted with Prolong TM Diamond Antifade Mountant (#P36979, Invitrogen).

	Marker	Cell of interest
Macrophage and B cell panel (panel 1)	CD68	Macrophages
	CD163	Macrophages
	CD20	B-cells
	AE1/3 (PanCK)	Tumour epithelium
	DAPI	Nucleus
Lymphocytic T cell Panel (panel 2)	CD4	CD4 helper T cells
	CD8	CD8 T cells
	PD-1	Immune checkpoint
	FoxP3	Regulatory T cells
	AE1/3 (PanCK)	Tumour epithelium
	DAPI	Nucleus

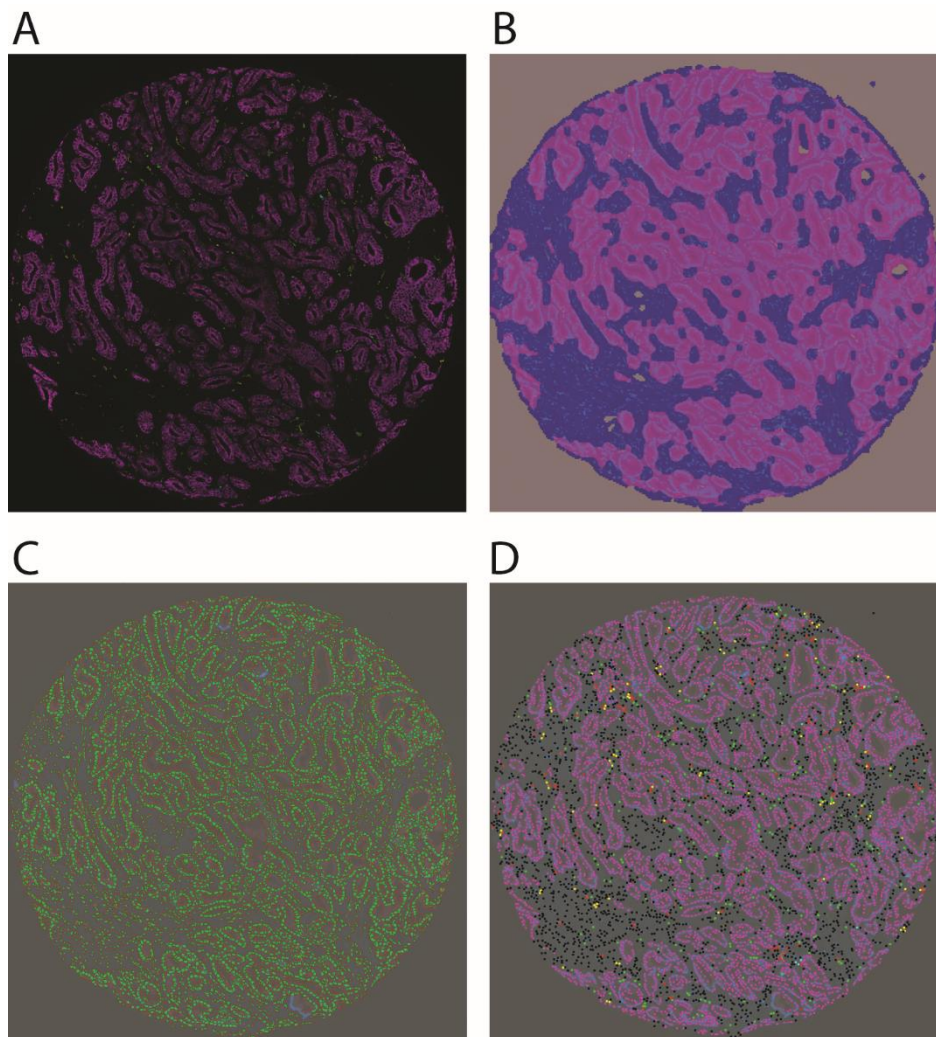
Table 5 Multiplex immunofluorescence panels developed and used for staining
PanCK= Pancytokeratin

The stained slides were scanned with 3.0 Vectra microscope system (PerkinElmer, MA) in 10x magnification. A spectral library was generated using each fluorophore signal and an unstained section for auto-fluorescence. Fluorescence bleed-through between different fluorophores was addressed by spectral unmixing of the multiplex image data after image acquisition. This

spectral library was the cornerstone of our marker quantitation, as the fluorescence intensity of each target was extracted from the multispectral data based on their specific spectral properties.

2.7.3 Multiplex immunofluorescence analysis

The InForm 2.4.2. software package was used for our analysis because of its unique pattern recognition based image analysis. The spectral library created from singlex IF staining (including auto-fluorescence) was used in order to un-mix the signal from each fluorophore in the multiplex image. By doing this, the fluorescent bleed-through was eliminated. The analysis comprised of three steps: tissue segmentation, cell segmentation and cell phenotyping (Figure 4). A selection of representative multispectral images was used for machine learning alongside a simulated 'brightfield' image that was produced from the software in order to facilitate tissue recognition with classic pathology views. This was an iterative process in which settings were refined with each round under my supervision until the output image met the desired criteria described in detail below. Only then were the settings saved within an algorithm which was used for automated batch analysis of the rest of the multispectral images.

**Figure 4 Multiplex immunofluorescence analysis workflow**

(A) Representative multiplex immunofluorescence image, spectrally unmixed. (B) Tissue Segmentation with magenta as epithelium, blue as stroma and grey as background. (C) Cell segmentation, nuclei shown in green and cytoplasmic membranes in orange. (D) Cell phenotyping in which each cell is given a colour coded identity. All images are from the same core.

Tissue segmentation was the first step which allowed for segmentation of the image in tissue compartments (epithelium vs stroma vs background) (Figure 4B). Thirteen representative multispectral images were used for training. Due to tissue heterogeneity, the accuracy of the segmentation was proportionate to the number of images used for training. However, the use of 14 images or more caused significant delays in each processing step and software crashes, therefore thirteen images were used as a compromise. PanCK staining was used as a 'mask' for the epithelial compartment to facilitate tissue segmentation. Acceptable tissue segmentation was arbitrarily defined as 80% of the entire core image. The outcome of tissue segmentation (epithelium vs stroma vs

background) for each core image was assessed visually and cores that did not meet the criteria were excluded from the analysis.

Cell segmentation was the second step which allowed for segmentation of the subcellular compartments (nucleus vs cytoplasm vs membrane), shown in Figure 4C. Nuclear identification was reliably conducted using DAPI staining for nuclei. However, occasional nuclei closely situated (without any intervening cytoplasm) were recognised as one large nucleus. This was addressed by several iterative rounds of segmentation fine-tuning the 'cell roundness' and 'distance to nucleus' parameters. Acceptable cell segmentation was arbitrarily defined as 90% of the entire core images with 10% poorly segmented area. It should be noted that more than 95% of cores had near perfect cell segmentation.

Cell phenotyping was the third step in which each cell can be given a phenotype identity (Figure 4D). The software was trained manually to identify several immunophenotypes based on tissue architecture, cell morphology and fluorophore staining of the cell. For panel 1 (Figure 5A), the cell phenotyping was: M1-like macrophages (CD68+ CD163-), M2-like macrophages (CD68- CD163+ and CD68+ CD163+), B cells (CD20+), epithelial cells (AE1/AE3+) and other cells (negative for all markers). In panel 2 (Figure 5B) cells were defined as: CD4 effector T cells (CD4+ FoxP3- PD-1-), CD4 regulatory T cells (CD4+ FoxP3+ PD-1-), PD-1 expressing CD4 T cells (CD4+ FoxP3- PD-1 +), CD8 effector T cells (CD8+ FoxP3- PD-1+), CD8 regulatory T cells (CD8+ FoxP3+ PD-1-), PD-1 expressing CD8 T cells (CD8+ FoxP3- PD1-), epithelial cells (AE1/AE3+) and other cells (negative for all markers). The 'other cells' comprised of fibroblasts, blood vessels, nerves, muscle etc. Acceptable cell phenotyping was arbitrarily defined as 90% of the entire core images with 10% poorly segmented area. All cores that did not meet this threshold were not included in the analysis.

After training was complete, the analysis algorithm was run on all images and automated identification and counting of each cell phenotype in each tissue compartment was performed. This output was available for each core in an excel format. Any cores with tissue folding, more than 5% artefact staining (such as unspecific staining of prostate crystalloids) or less than 60% malignant epithelium were excluded from the analysis.

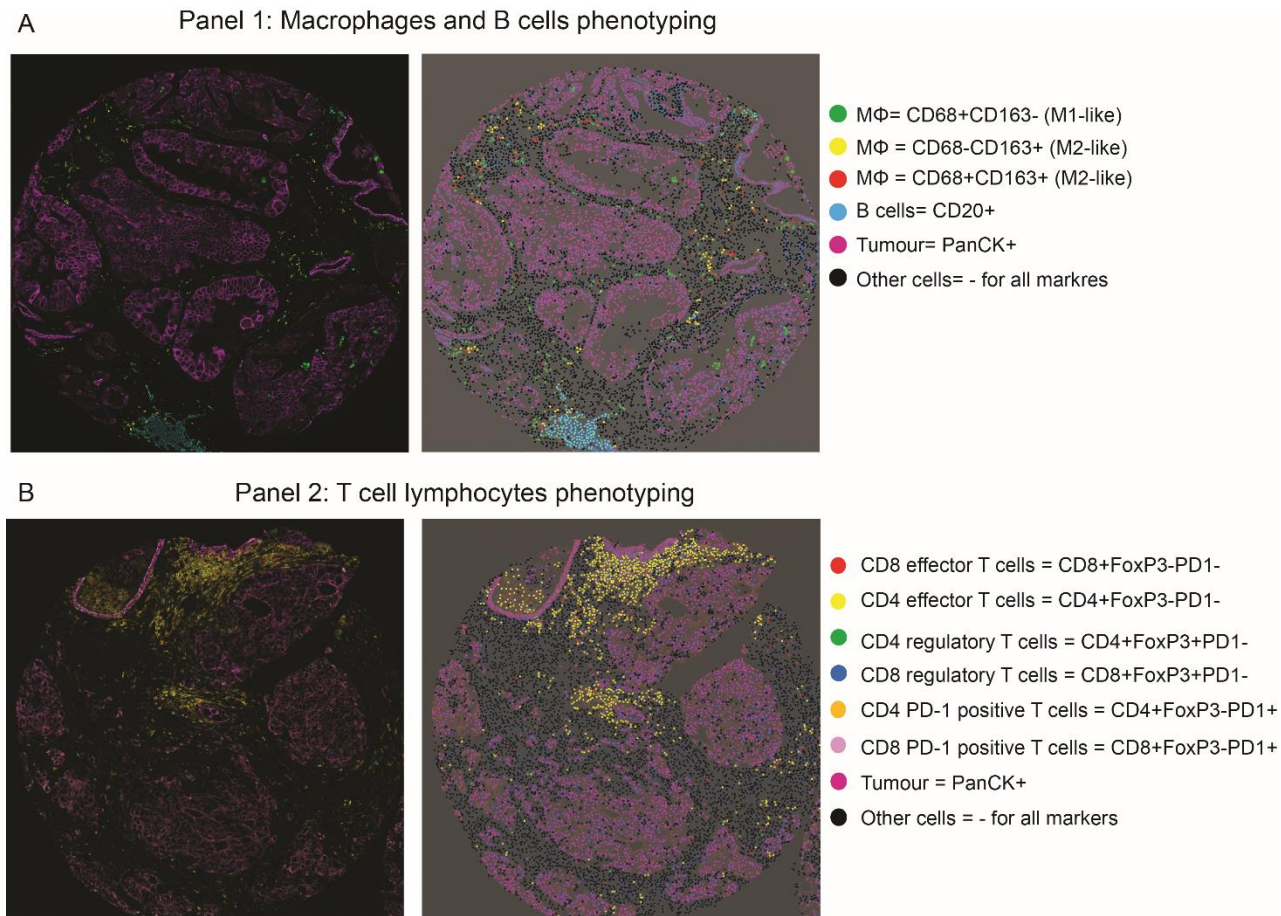


Figure 5 Multiplex immunofluorescence cell phenotyping

Cell phenotyping for the macrophage and B cell panel (A) and T cell lymphocyte panel (B). Spectrally unmixed images (left) with corresponding colour coded cell phenotypes (right).

2.8 Gene expression analysis of formalin fixed paraffin embedded tissue using HTG EdgeSeq Precision Immuno-Oncology Panel

The HTG EdgeSeq Immuno-Oncology Assay (HTG Molecular Diagnostics, Inc., Tucson, AZ) was performed in order to compare mRNA expression levels of multiple immune markers on FFPE prostate tissue biopsies. Forty-eight diagnostic biopsy cores from patients within the discovery TMA cohort were selected for gene expression analysis, including 24 without LN metastasis and 24 with LN metastasis respectively. This assay contained probes to measure the expression of 1,410 RNAs. Annotated H&E slides alongside an unstained 5 µm blank serial section were sent to HTG EdgeSeq Company (Tucson, Arizona). The samples were processed at HTG Molecular Diagnostics, Inc. (HTG), Tucson,

Arizona, USA. I performed the data analysis using the HTG reveal software. The processing steps that were undertaken are briefly described.

2.8.1 Sample preparation

The HTG EdgeSeq System chemistry workflow follows an automated procedure, thus avoiding common operating errors. The samples were randomly allocated on a 96-well plate and put on the HTG EdgeSeq processor. HTG EdgeSeq Lysis Buffer was added to lyse the sample making the RNA available. The lysed samples were transferred to another standard 96-well micro-titer plate. Then, functional DNA Nuclease Protection Probes (NPPs) were added in excess amounts and hybridised with target RNAs. S1 nuclease was subsequently added to digest excess non-hybridised RNA and NPP probes. NPPs were flanked with universal wing sequences which hybridised to universal DNA wingmen, preventing S1 nuclease digestion. This produced a 1:1 ratio of NNP detection probes to RNA initially present in the sample. The processed samples were then transferred to a 96-well micro-titer plate with a v-bottom, the stop plate. The S1 digestion step was terminated by termination solution followed by heat denaturation which released the NPPs from the DNA-RNA duplexes. Each processed NNP from the stop plate was used as a template to set up a PCR reaction.

2.8.2 Library preparation

The library was prepared using HTG EdgeSeq PCR processing. Specifically designed primers (referred to as tags) complementary to the 5'- and 3' end 'wing' sequences of the NPPs were added, along with common adaptors for cluster generation on an illumine sequencing platform. Each tag contained a unique barcode used for sample identification and multiplexing. No Template Control reactions (H₂O alone) were made for each master mix used during qPCR process as a test for no probe or qPCR reagent contamination. The library was subsequently prepared.

2.8.3 Library quantification and Normalisation

After the PCR amplification was finished, clean up was performed to remove unincorporated tags with HTG EdgeSeq AMPure cleanup of Illumina Sequencing Libraries. Following library preparation, all samples and controls were quantified

using HTG EdgeSeq KAPA Library Quantification for Illumina Sequencing in triplicate. The HTG EdgeSeq RUO library calculator was used for ensuring there was sufficient sample concentration for library pooling and determined the appropriate sample dilution for the library pool. All samples had sufficient levels of PCR product to be pooled for sequencing. It also determined the volume of denaturation reagents to be added to the library. In brief, 2M NaOH was added, samples were vortexed, spun down and incubated for 8' at room temperature. Then, cold HT1 buffer was added, followed by 2M HCl and the sample was vortexed and spun down. The PhiX control adaptor-ligated library was spiked at a concentration of 12.5 pM to the pooled library. The concentration of the pooled library loaded on the NextSeq flow cell was 3 pM. The library was vortexed, spun down, denatured for 4 min at 98°C and immediately chilled on ice for 5 min. The denatured library was loaded into the well of NextSeq sequencing cartridge.

2.8.4 Sequencing

The sequencing was performed on the Illumina NextSeq sequencer in accordance with HTG EdgeSeq Illumina NextSeq sequencing.

2.8.5 Data analysis

The sequencing data on mRNA expression of target genes were imported into HTG EdgeSeq parser software for alignment to previously defined target sequences. The HTG Reveal App (<https://reveal.htgmolecular.com/>) was used for quality check and data normalisation. Data from three samples that did not pass quality control (QC) metrics and were excluded from the analysis.

2.9 *In vitro* experiments

2.9.1 Cell Culture and Cell Storage

Human prostate cancer cell lines were acquired from the American Type Culture Collection (ATCC) and they were routinely tested six monthly for mycoplasma using an in-house MycoAlert™ Mycoplasma Detection Kit (Lonza, Switzerland), according to the manufacturer's instructions. All cell lines were grown in standard conditions containing 5% CO₂ at 37°C in a tissue culture class I

incubator. PC3M, C4-2, LNCaP and DU145 cells were grown in RPMI-1640 medium, 10% FBS and 1% L-Glutamine. All the reagents are listed in Table 2. Cells were passaged approximately every 3 to 4 days at 60-80% confluency depending on cell line growth rate. Medium was aspirated, cells were washed with PBS, and trypsin was added for 2-3 min incubation for cell detachment. Fresh medium was added to neutralise the trypsin and cells were counted using a CASY® counter (Innovatis) and seeded as required. Cell suspensions were transferred to new flasks/ plates.

Cell lines were stored using cryo-freezing. Cells were trypsinised and resuspended in fresh media. They were subsequently centrifuged at 300 rpm and cell pellets were resuspended in 90% (v/v) FBS and 10% (v/v) dimethyl sulphoxide (DMSO). 1 ml aliquots were transferred to cryotubes (Nunc) on dry ice wrapped in cotton wool. They were frozen overnight at -80°C and placed in liquid nitrogen for permanent storage the next day.

2.9.2 Protein extraction

RIPA lysis buffer was used for protein extraction. RIPA lysis buffer was added according to plate volume and cell confluency, e.g. 100 µl in 80% confluency in a 6 well plate. Cells were scraped off and placed on ice for 15 min. They were then centrifuged at 11,200 rpm for 15 min at 4°C. The supernatant was retained and samples were stored at -80°C.

2.9.3 Western Blot

Protein lysates were quantified by Bradford protein dye assay (protein assay dye reagent concentrate, Biorad) in a spectrophotometer. Western Blots were performed using 10 well pre-set gradient SDS-PAGE electrophoresis gels. Briefly, 20 µg of cell lysate were re-suspended into 6.25 µl sample reducing agent buffer with 2.5 µl NuPAGE loading dye and dH₂O (25 µl total volume). Samples were then loaded onto a 4-12% BIS-TRIS gel with MOPS running buffer and electrophoresed at 100 V for initially 15 min then increased to 130 V until the dye front reached the end of the gel. Proteins were then transferred to a PVDF membrane at 100 V for 1 hour in a transfer buffer of 10% methanol and 10% 10x blotting buffer in dH₂O. Membranes were then blocked with 5% milk in TBST for

1 hour. They were then probed with anti-B7-H3 primary antibody (14058, Cell Signalling) at 1:1000 (v/v) dilution in 5% bovine serum albumin (BSA) in TBST with 0.1% sodium azide overnight. The next day the membranes were washed with TBST on a shaker 3 times for 15 min and then a secondary goat anti-rabbit IgG HRP-linked antibody (7074, Cell signalling) was added at 1:5000 (v/v) dilution in 5% milk in TBST. Membranes were incubated for an hour and then washed with TBST on a shaker 3 times for 15 min. ECL or ECL Plus were added to the membrane according to manufacturer's instructions and chemiluminescence was imaged in Biorad ChemiDoc system. Anti-HSC 70 (sc-7298, Santa Cruz) was used as the loading control paired with secondary goat anti-mouse IgG HRP-linked antibody (7076, Cell signalling). Image analysis was performed using ADOBE photoshop.

2.9.4 RNA extraction and cDNA preparation

Total RNA was extracted from cell lines grown using the RNeasy mini kit (Qiagen) according to manufacturer instructions when cells reached approximately 60% confluency. The additional recommended step to remove genomic DNA using RNase-free DNase 1 (Qiagen) was included. RNA was eluted in 20 μ l of nuclease free water. The quality and quantity of the purified RNA was assessed using Nanodrop 2000/200c (Thermo Scientific).

cDNA was reverse transcribed using 2-4 μ g of the extracted RNA using the High Capacity cDNA Transcription Kit (Applied Biosystems) according to the manufacturer's instructions. The final reaction volume was 20 μ l, comprising of 10 μ l RNA, 2 μ l 10x RT buffer, 0.8 μ l 25 dNTP Mix, 2 μ l 10x RT Random Primers, 1 μ l Multiscribe Reverse Transcriptase and 4.2 μ l nuclease free water per reaction. This was placed in a thermocycler with the following successive thermal conditions: 25°C for 10 min, 37°C for 120 min, 85°C for 5 min, followed by 4°C until the samples were removed. Samples were subsequently stored at -80°C.

2.9.5 Quantitative Polymerase chain reaction (qPCR)

Roche universal probe library was used for all primer design (Table 6). qPCR was done using a 96 well plate with a 20 μ l reaction volume per well comprising of 10 μ l 2x Taqman® universal PCR Master Mix (Applied Biosystems), 0.2 μ l Universal

Library probe (Roche), 0.2 μ l of forward and reverse primers respectively, 2 μ l cDNA (routinely diluted 1/7) and 7.4 μ l nuclease free H₂O. Each sample was loaded in triplicate and the 96 well plate was sealed with microAmp optical adhesive film (Thermo Fisher Scientific) and spun prior to thermal cycling conditions to ensure the samples were at the bottom of the wells. The consecutive thermal cycling conditions were as follows: 50°C for 2 min, 95°C for 10 min, 40 cycles of denaturation at 95°C for 15 min and 60°C for 1 min (ThermoFisher Scientific Quant studio 3 Real-Time PCR System). *Casc3* was used as the housekeeping control for all genes examined.

Gene	Forward Primer (5'-3')	Reverse Primer (5'-3')	Probe
CASC-3	accaccgcctcatctgtatc	tggcggggttatagtaggt	25
B7-H3	tgcaaatggcacctacagc	cctcagggacctggacct	18
MMP2	ccccaaaacggacaaagag	cttcagcacaacagggttc	43
MMP3	gcagtttgctcagcctatcc	tttctctaacaactgtttcacatc	58
MMP9	gaaccaatctcaccgacagg	gccaccgagtgtaaccata	6
TIMP1	ctgttggctgtggctgat	aactggcctgatgacg	3
TIMP2	gaagagcctgaaccacaggt	cggggaggagatgtagcac	43
TIMP3	caccctcactgtggaa	tgacccaaccagaaccaac	3
CCL2	agtctctgccgcccttct	gtgactggggcattgattg	40
CCL26	ctgggtgcgaagctatgaat	tcttgcccttttgtagtgaa	32
CLDN1	cctatgaccccagcaatgc	acagcaaagtagggcacctc	20
CLDN7	cactgtgctgctcacctc	ccggcaagtccaaaagta	26
CLDN11	cccgggtggctaaagtacag	caacaagggcgagagag	20
CXCL1	cgaaaagatgctgaacagtg	gcctctgcagctgtgtctc	35
CXCL6	gtccttcgggctcctgt	cagcacagcagagacaggac	68
CXCL16	tgattgagtctctttatggaaaca	gaagccaggaatcacagtaagg	30
CXCL8	agacagcagagcacacaagc	Atggttccttccgggtgt	72
IL4R	gtgctcattcatttaacagagctt	actgaacacccttgacagc	16
IL11	ggacaggggaagggttaaagg	gctcagcacgaccaggac	37
IL33	ccaccaaaggccttcaact	aaggcaaagcactccacagt	27
MMP1	gctaacctttgatgctataactacga	tttgtgcatgtagaatctg	7
MMP10	ctgacgttggtcactcagc	gcaaatctggtgataattcacaatc	72

Table 6 Primers and probe pairs used

2.9.6 Transient silencing transfection using Lipofectamine RNAiMAX

Cells were seeded the day before transfection in a 6 well plate, typically 100,000 cells/well so that they were transfected at 60-80% the following day. On the day, Lipofectamine RNAiMAX was diluted in Opti-Mem medium (9 μ l in 150 μ l) and siRNAs (Table 7) were also diluted in Optimem medium (9 μ l in 150 μ l). The solutions were combined at a 1:1 ratio and left for 5 min at room temperature. 250 μ l were added to each well and cells were incubated for 24-48 hours.

siRNA name	Cat Number	Target sequence
ON-TARGETplus Human CD276 SMART pool siRNA (pool siRNA)	L-007813-01-0005	GAGUGAGACUUCAGACGUU GGUGGUGCUGGGUGCGAAU CUCCAAAGGAUGCGAUACA ACCAAAGACACGAUGCAUA
ON-TARGETplus Human CD276 siRNA (S1 siRNA)	J-007813-09-0005	GAGUGAGACUUCAGACGUU
ON-TARGETplus Human CD276 siRNA (S2 siRNA)	J-007813-10-0005	GGUGGUGCUGGGUGCGAAU
ON-TARGETplus Human CD276 siRNA (S3 siRNA)	J-007813-11-0005	CUCCAAAGGAUGCGAUACA
ON-TARGETplus Human CD276 siRNA (S4 siRNA)	J-007813-12-0005	ACCAAAGACACGAUGCAUA
ON-TARGETplus Non-targeting Control Pool (NT siRNA)	D-001810-10	Not disclosed

Table 7 List of siRNA sequences

2.9.7 Generation of stable cell clones with reduced levels of B7-H3 expression

Stable knock out (KO) clones for B7-H3 were generated using CRISPR/Cas9 plasmid specific to human B7-H3 sequence and homology directed repair (HDR) insertion plasmid (sc-402032) in PC3M and C4-2 cell lines. Amaxa Cell Line Nucleofector Kit V (VCA -1003, Lonza) was used for electroporating PC3M cells, and Amaxa Cell Line Nucleofector Kit R (VCA-1001, Lonza) was used for C4-2. Electroporation setting code T013 was used for PC3M cells and T009 for C4-2 cells. Scrambled CRISPR plasmid and an in-house Infra-Red Fluorescent Protein plasmid with puromycin resistance was used as control. 10 cm plates were prepared with 4 ml full media. Media was then changed every 5 days and puromycin was added to the media at 2 µg/mL for PC3M and 1.2 µg/ml for C4-2. After approximately 21 days for PC3M and 35 days for C4-2, clones were picked using selection disks soaked in trypsin. B7-H3 expression was checked with Western blotting and PCR. Four knock out (KO pool, KO4, KO10, KO13) B7-H3 clones were picked for PC3M cells, and five knock out (KO pool, KO2, KO3, KO10, KO18) B7-H3 clones were picked for C4-2 cells. For both, one control pool was picked. For both cell lines, two KO clones and one control pool (referred to as PC3M cntr and C4-2 cntr) were used in subsequent experiments.

2.9.8 *In vitro* Growth Assay

LNCaP B7-H3 pool siRNA (si B7-H3) and NT siRNA (siNT) controls were seeded in 6 well plates, 400,000 cells/well. PC3M si B7-H3 and si NT controls were seeded in

6 well plates, 200,000 cells/well. After 72 hours cells were counted in CASY® cell counter (Innovatis). All experiments were done in three biological and four technical replicates.

2.9.9 *In vitro* apoptosis assay

Cells were seeded in a 6 well plate and transfected with lipofectamine RNAiMAX as previously described. The plate was incubated for 72 hours at 37°C and stained with Annexin V and propidium iodide using the FITC Annexin V Apoptosis Detection Kit I (Cat: 556547, BD Biosciences) according to manufacturer's instructions. In brief, floating (in the media) and attached (trypsinised) cells from each well were put in one eppendorf and were spun down at 1000 rpm for 5 min. They were washed with cold PBS two times and spun down at 1000 rpm for 5 min. The cell pellet was resuspended in 200 µl of 1x binding buffer and 100 µl of the solution were transferred to a 5 ml FACS tube. 5 µl of Annexin V and 5 µl of propidium iodide were added and the solution was vortexed and incubated for 15 min in the dark at room temperature. An unstained sample was always used as a control. Another 300 µl of 1x binding buffer were added to each tube and proceeded to analysis by flow cytometry in the ATTUNE NxT flow cytometer (ThermoFisher Scientific). Three biological replicates with two technical replicates were used.

In the flow cytometer, cells were firstly visualised in a data plot of SSC-A and FSC-A in order to exclude cell debris. Then, they were visualised in a FSC-H and FCS-A plot in order to exclude any duplicate cells. The unstained sample was used for setting up the negative gates. The data were saved in excel format and further analysis was performed in FlowJo 10.

2.9.10 *In vitro* colony formation assay

Cells were seeded in 6 well plates in low numbers so that they could form discernible separate colonies. 500 cells per well were seeded and 3 wells were seeded for each cell condition (PC3M cntr, KO pool, KO10). Cells were left to grow for 3 weeks (this time frame has previously been optimised in our lab). Afterwards, they were fixed in 100% methanol for 30 min at -20°C and stained with 0.25% crystal violet (V5265 Sigma) for 10'. Cells were then washed in dH₂O

until there was no more dye to come off and plate was left to dry overnight. The next day, the plate was imaged in LI-COR (LI-COR Biosciences) with 700 wavelength, and Image Studio Lite Ver 5.2 was used for image analysis.

2.9.11 *In vitro* transwell migration assay

Cells were seeded in 6 well plates and when they reached 60%-80% confluency they were serum starved for 24 hours. Then cells were trypsinised and resuspended in full serum media to deactivate the trypsin. Cells were centrifuged at 1000 rpm for 5 min and re-suspended in serum free media. They were then counted using CASY® cell counter (Innovatis) and made up to a cell concentration of 1×10^5 /ml of serum free medium (unless otherwise stated). 750 μ l of full serum media was added to the bottom of each well of a 24 well plate and a transwell Boydon Chamber was inserted into each well. 500 μ l of the cell suspension was then added onto each chamber. This created a top to bottom cell migration flow resulting in migrating cells adhering to the lower surface of the boydon chamber membrane.

Cells were routinely incubated at 37°C for 48 hours. First the medium was removed from the upper chamber and each chamber was fixed at -20°C in 100% methanol for 30 min. Subsequently, methanol was removed and each chamber was placed in filtered haematoxylin for 30 min. Then, each chamber was washed in H₂O scrubbing off the cells attached to the upper membrane. They were then placed inverted at room temperature to dry for 15-20 min. Once dried, each membrane was detached using a scalpel and mounted onto a slide using DPX mountant. They were left to stabilise overnight and cells of each membrane were counted in a light microscope at x20 magnification.

2.9.12 *In vitro* scratch wound healing assay

Essen Bioscience 96 well ImageLock Microplates were seeded with 30,000 cells/well and incubated for 24 hours in a culture incubator. Once the cells reached 90-100% confluence, the WoundMaker™ was applied in order to create homogenous 700-800 μ m wide scratch wounds. The cells were then washed with PBS to wash away any floaters and cell debris and then 100 μ l of media was added. Cells were then placed in the IncuCyte within an incubator and two

hourly images were recorded for 72 hours. The output used for analysis was wound confluence/time, calculated using the IncuCyte software.

2.9.13 *In vitro* invasion assay

A Boydon Chamber was inserted into each well of a 24 well plate. 100 μ l of Matrigel was added in each chamber diluted 1:1 in ice cold PBS. The plate was incubated for 30 min at 37°C to allow matrigel to set. Suspensions of PC3M cells were prepared in RPMI supplemented with full serum at 5×10^5 cells/ml. Once the matrigel was set, the transwell chambers were inverted and 100 μ l of the cell suspension (5×10^4 cells) were placed onto the underside of the filter (which was now the uppermost). The inverted transwells were then covered carefully with the base of the 24 well plate such that the droplet of cell suspension was in contact with the base. The plate was incubated for 3 hours to allow cells to attach to the chamber. It was then turned again right-side-up and each transwell was washed in serum free RPMI three times and then left in it. On top of the matrigel, 100 μ l full serum RPMI was added. The plate was incubated at 37°C for 4 days. Each transwell chamber was then placed in 1 ml of 1:1000 (v/v) Calcein AM in serum free RPMI in a 24 well plate. The plate was incubated for 1 hour at 37°C and imaged using an Olympus FV100 confocal microscope the same day. Stained cells were visualised using a 20x objective. Optical sections (Z-stack) were taken at 15 μ m intervals moving up from the underside of the filter into the matrigel, producing a series of images. To quantify these, Image J software was used. For analysis, only cells in the 15 μ m section or above were considered invasive and quantified according to their pixel intensity. The sum of these values was calculated and normalised to the value obtained from the corresponding 0 μ m section as a “loading” control. It is important that the same pixel threshold was used for all the samples each experiment. Three biological replicates with two technical replicates were used.

2.9.14 RNA sequencing

RNA sequencing (RNA-seq) with poly-A-tailed mRNA selection based RNA-seq library preparation was performed by our Molecular Technology Services. RNA was extracted from PC3M cntr, KO pool and KO10 clone for B7-H3 using Qiagen kit as previously described, including the additional DNase step for genomic DNA.

For tapestation RNA quality control, 5 µl of 50 ng/µl per sample was required, and for library preparation 1 µg from each sample was used. Quality and quantity of the libraries were assessed on an Agilent 2100 Bioanalyser and Qubit (Thermo Fisher Scientific), respectively. The libraries were subsequently run on the Illumina Next Seq 500 using the High Output 75 cycles kit (2 × 36 cycles, paired-end reads, single index). Three biological replicates of each sample with three technical replicates were sequenced. Quality checks on the raw RNA-Seq data files were conducted by Mr William Clark (Core Sequencing Services, Beatson Institute) using fastqc (<https://www.bioinformatics.babraham.ac.uk/projects/fastqc/>). Analysis of the RNAseq data was carried out by Dr Ann Hedley (Informatician, Beatson Institute) using genes with an absolute fold change > 2 and an adjusted P value < 0.05 in Metacore.

2.10 Statistical methods

Statistical analyses were carried out with Graph Prism 8 and IBM SPSS statistics 25. Comparisons between groups were conducted using Mann-Whitney U test (unpaired, nonparametric, two-tailed), t-test (unpaired, parametric, two-tailed), ANOVA, Fisher's and Chi-square test where appropriate. Spearman correlation and Cohen's Kappa coefficient for agreement were performed to examine correlations between numerical and categorical values respectively. Kaplan Meier curves were compared with log-rank test. Multivariate logistic regression models were used to identify novel predictive factors of lymph node metastasis. Covariates consisted of peak preoperative PSA value, stage, Gleason Score and percentage of positive biopsy cores (when available). Receiver operative curve (ROC) analysis was performed and area under the curve (AUC) was used to quantify the predictive accuracy. For the targeted gene expression panel, HTG reveal software was used for statistical analysis using the DESeq2 test with an adjusted p value less than 0.05 and a log fold change value of greater than 1.5.

Chapter 3 Immune profiling of prostate cancer tumour microenvironment in the context of lymph node metastasis

Prostate cancer is known for its biological and clinical heterogeneity, with a large discrepancy observed between incidence and mortality rates (7). Identifying patients with a prostate tumour that grows slowly and does not metastasise is critical for patient treatment decision, including whether extended pelvic lymph node dissection is indicated at the time of radical surgery. During tumour progression, lymph nodes are often the first organs affected by metastases. The presence of lymph node metastasis increases the 15-year prostate cancer specific mortality risk from 0.8-1.5% for organ confined disease to 22-30% (150). All cancer staging systems, including the TNM staging system for prostate cancer, assess the presence or absence of lymph node involvement for the evaluation of patient prognosis (151). Therefore, metastasis to the lymph nodes has a big impact on patient outcomes.

Tumour immune evasion is one of the hallmarks of cancer and tumour infiltrating immune cells are decisive factors of cancer progression (33, 38). The immune landscape of prostate cancer has been surprising difficult to characterise with multiple conflicting results regarding clinical outcomes (67), likely due to study limitations as well as inherent tumour heterogeneity. It is therefore essential to comprehensively characterise the baseline immune status of well-defined patient cohorts in order to gain a better understanding of disease progression. I hypothesised that local immune cell infiltration shapes the local host anti-tumour response and influences the spread to regional lymph nodes. My objective was to provide additional novel biomarkers that could improve the current predictive nomograms of lymph node invasion.

I applied multiplex immunofluorescence to characterise the tumour immune microenvironment at the tissue level using specimens obtained from radical prostatectomy (RP) and extended pelvic lymphadenectomy. The discovery cohort included patients with pathologically confirmed regional lymph node metastases (LN+) and patients free from regional lymph node metastases (LN-). The identified immune signature of LN+ disease was validated in a comparable independent patient cohort. I further investigated for potential correlation

between key reported genetic alterations in PCa, such as *ERG* translocation and loss of PTEN expression, and the tumoural immune cell composition. Finally, I explored the potential for translating this immune signature in the clinic and its significance in low-risk prostate cancer patients.

3.1 Validation of multiplex immunofluorescence assay

Using chromogenic IHC and singleplex IF staining, serial sections of FFPE human tonsil tissue were stained. Tonsil was chosen because of its well-characterised tissue architecture and immune cell spatial distribution. Both techniques resulted in similar patterns of staining, as shown in Figure 6A-B. CD20 (B cell lymphocytes), CD68 (Macrophages-M1 like), CD163 (Macrophages-M2 like), CD4 (helper T cells), CD8 (cytotoxic T cells), FoxP3 (regulatory T cells), PD-1 (immune checkpoint) and AE1/3 (pan cytokeratin) had specific staining without significant background staining.

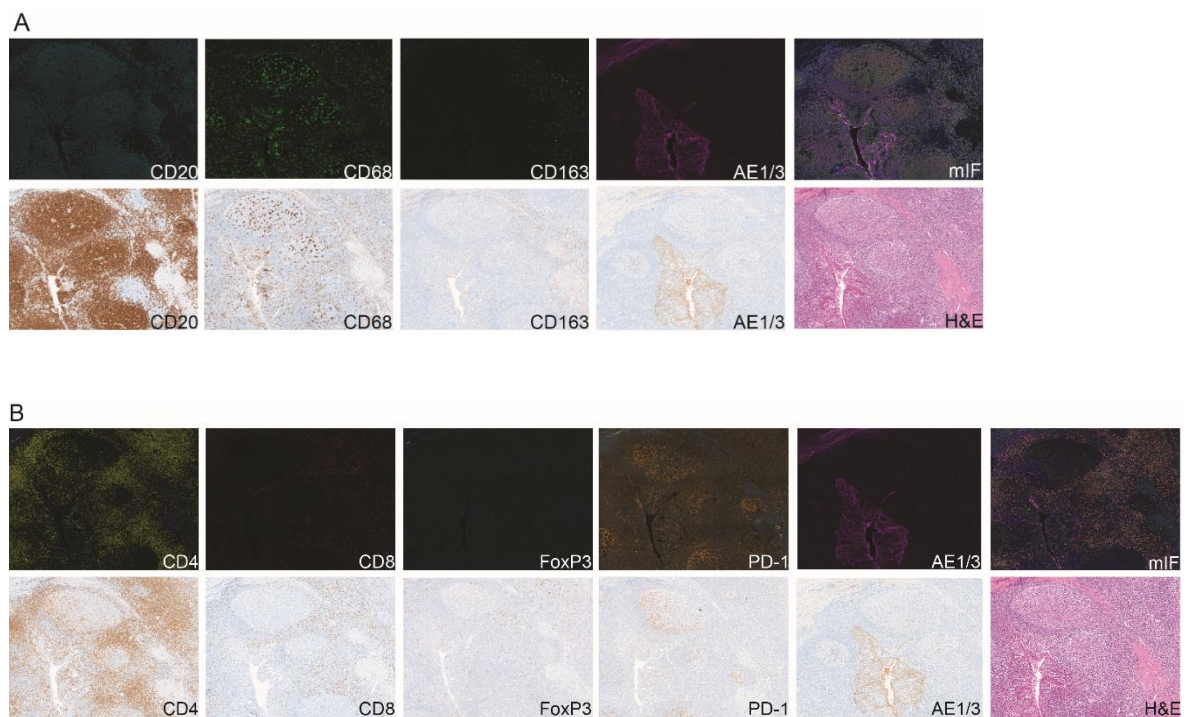


Figure 6 Photographs of representative examples of validation from IHC and H&E (bottom panels), uniplex and multiplex IF (top panels) in tonsil tissue

(A) Macrophage and B cell panel: CD20 (B cell lymphocytes), CD68 (Macrophages-M1 like), CD163 (Macrophages-M2 like), AE1/3 (cytokeratin positive epithelium). 10x magnification.

(B) T cell lymphocytic panel: CD4 (helper T cells), CD8 (cytotoxic T cell), FoxP3 (regulatory T cells), PD-1 (immune checkpoint) and AE1/3 (cytokeratin positive epithelium). 10x magnification.

3.1.1 Correlation between mIF and DAB chromogenic IHC

Serial sections from the discovery TMA were stained with the mIF panels and chromogenic DAB IHC for individual markers. Immune cell densities for each core were quantified using inForm and HALO automated scoring respectively. I compared mIF and individual IHC staining using Spearman r value for correlation. Overall, there was significant positive correlation between mIF and IHC stainings. CD68 ($r=0.67$, $p<0.0001$), CD163 ($r=0.46$, $p<0.0001$), CD20 ($r=0.31$, $p=0.02$), CD4 ($r=0.68$, $p<0.0001$), CD8 ($r=0.752$, $p<0.0001$), FoxP3 ($r=0.3$, $p=0.003$), PD-1 ($r=0.23$, $p=0.05$) showed significant positive correlations. PD-1 had the weakest, but significant, positive correlation, which was unsurprising due to the scarcity of this marker.

3.1.2 Co-localisation of markers

One of the main advantages of using mIF was the co-localisation of markers within individual cells (Figure 7), thus defining their specific cell phenotypes. We were able to identify M2-like macrophages (CD68+ CD163+), CD8 regulatory T cells (CD8+ FoxP3+), PD-1 positive CD8 T cells (CD8+ PD-1+), CD4 regulatory T cells (CD4+ FoxP3), PD-1 positive CD4 T cells (CD4+ PD-1+). Unexpectedly, we observed cells with double staining for CD4 and CD8 which has been observed before (91). The proportion of cells with double staining was minimal and they were not quantified further.

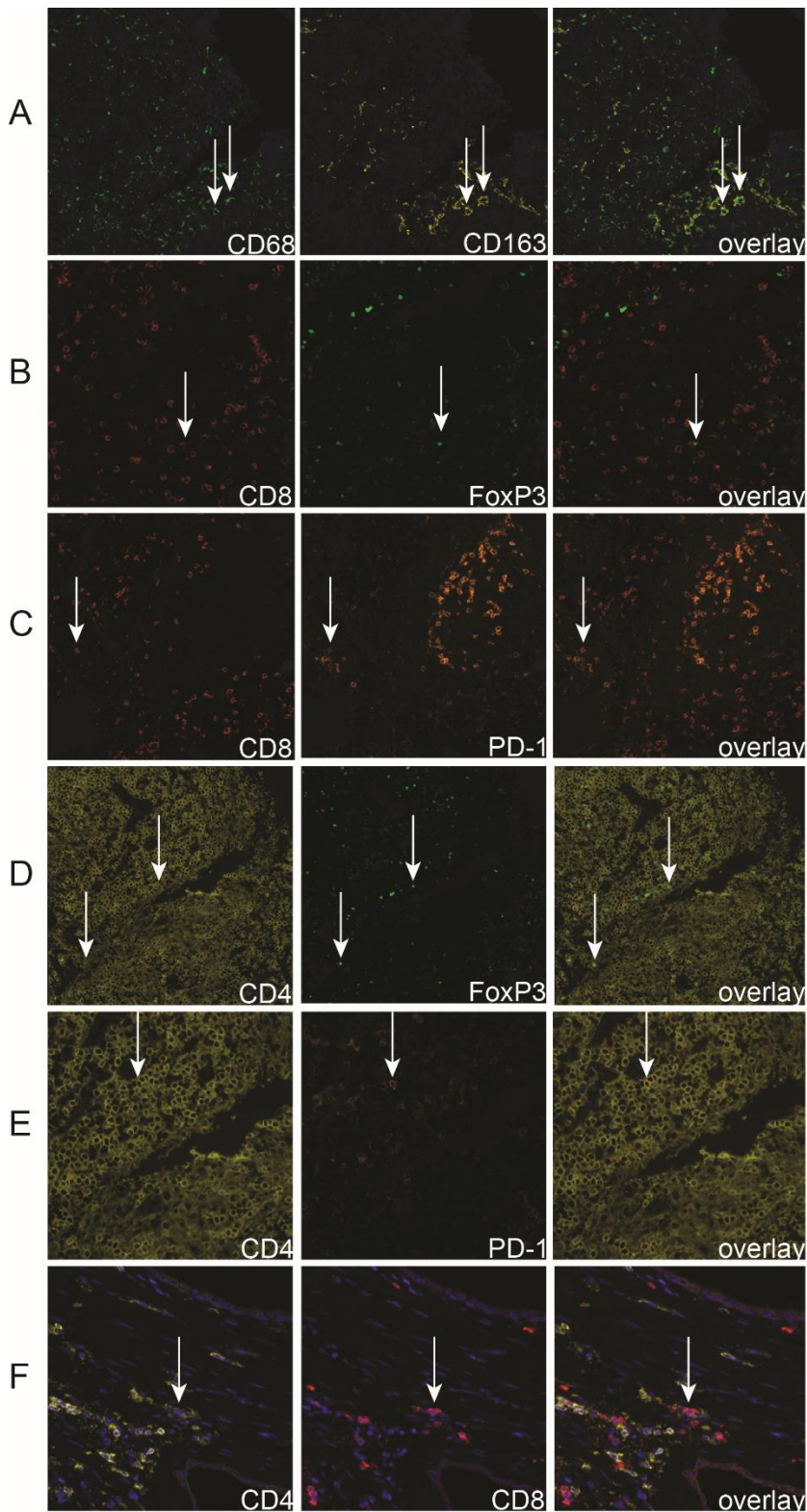


Figure 7 Representative examples of co-localisation of the cell markers

Representative image of M2-like macrophages (CD68+ CD163+) in (A), CD8 regulatory T cells (CD8+ FoxP3+) in (B), PD-1 positive CD8 T cells (CD8+ PD-1+) in (C), CD4 regulatory T cells (CD4+ FoxP3) in (D), PD-1 positive CD4 T cells (CD4+ PD-1+) in (E) and double CD4+ CD8+ cells in (F). White arrows indicate the co-localisation of markers.

3.2 Immune profiling of the discovery TMA cohort

3.2.1 Clinical characteristics of lymph node discovery TMA

Of the ninety-four patients that were identified, 50 had pathologically confirmed regional nodal metastasis (LN+) and 44 had no evidence of lymph node metastasis (LN-). Patient clinicopathological characteristics are presented in Table 1. All studied patients had newly diagnosed prostate cancer and had not received pre-operative chemotherapy or ADT. LN+ patients were younger than LN- patients (62 years vs 67 years, $p=0.0001$). The two groups were otherwise comparable in all clinicopathological parameters, including number of excised lymph nodes, pre-operative PSA levels, pT stage, Gleason score and presence of perineural invasion (PNI). There were 65 patients with Gleason score 7, 15 patients with 3+4 and 50 patients with 4+3. Due the small number of patients with Gleason score 3+4 (11 in LN+ and 4 in LN- groups), all patients with a sum of Gleason score 7 were grouped together in order to perform meaningful statistical analysis. Follow-up data were available for 91 patients, ranging from 33 to 70 months (median 41 months). Fifteen patients had disease relapse after surgery and four patients died during follow-up, two of them due to prostate cancer. These limited numbers prohibited any meaningful conclusions for overall or cancer specific survival, and relapse-free survival was used as surrogate for these events.

	Overall	Lymph node metastasis		
	N=94	LN-, n=44	LN+, n=50	p value
Age at diagnosis, median (95% CI)	65 (63-66)	67 (66 - 70)	62 (59-65)	0.0001
Number of lymph nodes excised, median (95%CI)	15 (13-17)	17 (14- 18)	13.5 (10-17)	0.0514
Peak PSA, median (95%CI)	14.8 (12.3-16.7)	15.5 (11.5- 17.7)	14.2 (11-17)	0.831
Stage, N (%)				0.089
pT2	34 (36.17)	20 (45.45)	14 (28)	
pT3-T4	60 (63.83)	24 (54.55)	36 (72)	
Gleason Score, N (%)				0.109
7	65 (69.15)	34 (77.27)	31 (62)	

>7 (8-9)	29 (30.85)	10 (22.73)	19 (38)	
PNI, N (%)				0.156
Negative	15 (15.96)	10 (22.73)	5 (10)	
Positive	79 (84.04)	34 (77.27)	45 (90)	

Table 8 Clinical and histopathological characteristics of discovery TMA of patients with (LN+) and without lymph node metastasis (LN-)

CI= Confidence interval, PSA: Prostate specific antigen, PNI: Perineural invasion. Mann-Whitney and Fisher's exact test used for statistical calculations.

3.2.2 Immune profiling of intermediate and high risk prostate cancer patients

Characterising the baseline immune status of intermediate and high-risk PCa is essential for understanding disease progression as well as planning targeted immunotherapies. I aimed to describe the frequencies as well as spatial localisation of macrophage and lymphocytic immune cell populations. The discovery TMA described previously was stained with mIF (1) Macrophage and B cell panel: CD68, CD163, CD20, PanCK and (2) T cell lymphocyte panel: CD4, CD8, FoxP3, PD-1, PanCK. The immune cell densities of different cell populations were quantified within the epithelial and stromal compartments separately using inForm 2.1 analysis software. The results are summarised in Table 9. Unsurprisingly, immune cell infiltration was more prominent within the stroma (232.9 cells/mm²) compared to epithelium (90.44 cells/mm²). Macrophages were the most prominent immune cell type irrespective of spatial compartment, 41.21 cells/mm² within epithelium and 130.4 cells/mm² within stroma. CD4 T cells were the second most frequent immune cell type within epithelium (35.42 cells/mm²) and within the stroma (90.29 cells/mm²). The most uncommon immune cell type overall were B cells. When encountered, they had formed tertiary germinal centres but that was present in very few cases (approx. 10 out of 282 cores).

Further characterisation of cellular subtypes showed that macrophages infiltrating the epithelium were polarised in M1 and M2 in comparable levels (19.02 cell/mm² and 18.07 cells/mm² respectively). Stromal macrophages had slightly more frequently M2-like phenotype (66.17 cells/mm²) compared to M1-like (52.23 cells/mm²). CD4 effector T cells, CD4 regulatory T cells and PD-1 positive T cells had median cell densities of 66.93 cells/mm², 6.68 cells/mm²

and 6.48 cells/mm² respectively within the stroma. Within the epithelium, CD4 T cell subtypes were present in lower densities, CD4 effector 21.6 cells/mm², CD4 regulatory 4.2 cells/mm² and CD4 PD-1 positive cells 6.2 cells/mm². Within the stroma, CD8 effector T cells had a median density of 29.85 cells/mm², CD8 regulatory T cells 0.51 cells/mm² and CD8 PD-1 positive 5.64 cells/mm². Intraepithelial cytotoxic CD8 T cells had a density of 6.33 cells/mm², CD8 regulatory T cells 2.85 cells/mm² and CD8 PD-1 positive T cells 3.65 cells/mm². It is noteworthy that CD8 regulatory cells were the scarcest immune subtype.

	N=94 total	Immune cell densities (cells/mm²)
Epithelium	91	90.44 (82.84-113.8)
Macrophages	83	41.21 (33.58-49.85)
M1-like macrophages	83	19.02 (16-22.84)
M2-like macrophages	83	18.07 (13.36-22.98)
B cells	83	1.8 (1.41-3.66)
CD4 T cells	66	35.42 (30.96-45.6)
CD4 effector T cells	66	21.6 (15.5-23)
CD4 regulatory T cells	66	4.2 (2.9-5.8)
CD4 PD-1 positive T cells	57	6.2 (4.5-13.1)
CD8 T cells	66	20.65 (14.6-24)
CD8 effector T cells	66	10.33 (3.9-12.8)
CD8 regulatory T cells	66	2.85 (1.3-4.1)
CD8 PD-1 positive T cells	66	3.65 (0-6.9)
Stroma	91	232.9 (202.9-269.8)
Macrophages	83	130.4 (106.5-155.4)
M1-like macrophages	83	52.23 (40.89-64.66)
M2-like macrophages	83	66.17 (60.3-77.21)
B cells	83	8.14 (5.46-12.3)
CD4 T cells	66	90.29 (50.2-102.5)
CD4 effector T cells	66	66.93 (34.31-82.77)
CD4 regulatory T cells	66	6.68 (5.35-7.78)
CD4 PD-1 positive T cells	66	6.48 (3.8-9.2)
CD8 T cells	66	39.37 (32.16-52.7)
CD8 effector T cells	66	29.85 (22.1-40.63)
CD8 regulatory T cells	66	0.51 (0.32-1.5)
CD8 PD-1 positive T cells	66	5.64 (3-8.55)

Table 9 Immune cell densities of intermediate and high-risk patients included in the Discovery cohort

Data are presented as median immune cell densities (cells/mm²) with 95% Confidence Intervals. N= number of cases with available data.

An interesting observation was that stromal CD4 effector T cells were predominantly located at the tumour-stromal interface. This led to a

collaboration with Dr Ian Powley (University of Leicester) who quantified the distance of CD4 effector T cells from epithelium using the phenoptr package in R software. Density plots were generated that showed the distance of CD4 effector T cells from the PanCK+ tumour cells (Figure 8). The median distance for all high-risk patients was 23.3 μm (20.6-27.3 95%CI), shown in Figure 8A. For LN+ and LN- patients the distance was similar, 25.85 μm (21.6-30 95%CI) and 20.65 μm (18.8-26.2 95%CI, $p=0.17$) respectively (Figure 8B).

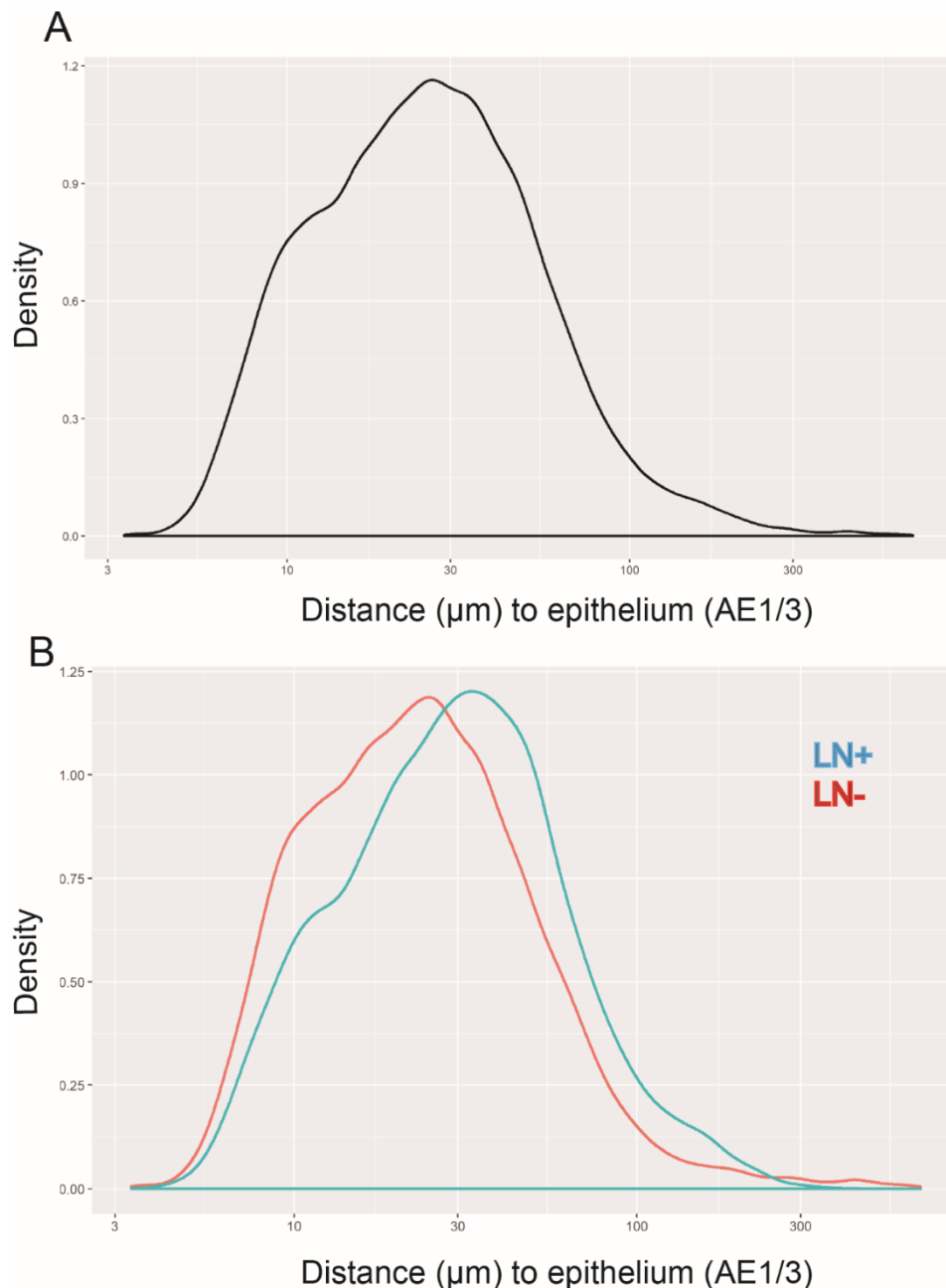


Figure 8 Spatial distribution of CD4 effector T cells (CD4+ FoxP3- PD-1-) in intermediate and high risk prostate cancer patients

Density plot graphic representation of CD4 effector T cells (CD4+ FoxP3- PD-1-) according to their distance from the nearest PanCK+ cancer cells for all PCa patients (top) and in patients with (LN+) vs without (LN-) lymph node metastasis (bottom).

3.2.3 Immune cell densities and ratios in discovery cohort patients with vs without lymph node metastasis

The discovery TMA was designed and constructed to detect differences pertaining to lymph node spread in prostate cancer patients. Comparisons of the epithelial and stromal compartment immune cell densities between patients with (LN+) and without (LN-) lymph node metastasis are presented in Table 10. Intraepithelial M1-like macrophages were decreased in patients with lymph node metastasis (16.2 cells/mm² vs 18.46 cells/mm², p=0.046) and intraepithelial CD8 cytotoxic T cells were also significantly decreased in the same patients (1.8 cells/mm² vs 12.6 cells/mm², p=0.001). Stromal M1-like macrophages were decreased in LN+ patients, 45.03 cells/mm² vs 64.04 cell/mm², p=0.047. Stromal CD4 effector T cells were also decreased in the same patients, 32.5 cells/mm² vs 91.35 cells/mm², p=0.0003. Lastly, CD8 effector T cells were decreased in LN+ patients, 22.7 cells/mm² vs 40.63 cells/mm² in LN- patients, p=0.008. There were no significant differences in M2-like macrophages, B-cells, CD4 and CD8 regulatory T cells, CD4 and CD8 PD-1 positive T cells between patient groups.

Biologically relevant immune cell density ratios were also calculated. The stromal ratio of M1/M2 macrophages was significantly lower in LN+ patients (0.56, 0.5-0.8 95%CI) compared to LN- patients (0.89, 0.6-1.1 95%CI, p=0.03). More intriguingly, the ratio of CD4 effector T cells to CD4 regulatory T cells within the stroma was also lower in LN+ patients (7.59, 1.7-16.2 95%CI) compared to LN- patients (18.76, 12.7-47 95%CI, p=0.0006). Lastly, the epithelium to stroma ratio of CD8 effector T cells was used as a surrogate for the CD8 cell infiltration within the tumours and was lower in LN+ patients (0.19, 0.04-0.2 95%CI) compared to LN- patients (0.29, 0.2-0.4 95%CI, p=0.01).

Immune cell densities	All N=94	Lymph node metastasis		
		Negative =44	Positive =50	p value
Epithelium				
M1-like macrophages	83	20.64 (17.07-27.45)	16.38 (11.01-21.15)	0.046
M2-like macrophages	83	18.46 (11.49-24.9)	16.2 (11.98-31.94)	0.895
B cells	83	2.807 (1.41-8.29)	1.7 (0.84-4.2)	0.205
CD4 effector T cells	66	23 (13.3-32.9)	18 (11.8-22)	0.093
CD4 regulatory T cells	66	3.250 (1-6.2)	1.5 (0-4.2)	0.159
CD4 PD-1 positive T cells	57	8.015 (0-18.7)	6.2 (5.87-12.7)	0.19
CD8 effector T cells	66	12.6 (6.5-21)	1.8 (0.68-5.7)	0.001
CD8 regulatory T cell	66	3.8 (0.41-5.69)	2.2 (0.5-4.8)	0.772
CD8 PD-1 positive T cells	66	5.3 (0-9.4)	0 (0-6.82)	0.277
Stroma				
M1-like macrophages	83	64.04 (39.11-89.31)	45.03 (39.7-55.3)	0.047
M2-like macrophages	83	65.32 (53.91-76.92)	73.83 (54.69-83.85)	0.7
B cells	83	8.9 (5.27-23.53)	7.05 (4.27-11.51)	0.193
CD4 effector T cells	66	91.35 (55.41-154.1)	32.5 (14.1-70.61)	0.0003
CD4 regulatory T cells	66	4.65 (1.6-7.94)	4.71 (3.6-5.4)	0.971
CD4 PD-1 positive T cells	66	7.74 (0-16.2)	8.73 (1.8-13.3)	0.597
CD8 effector T cells	66	40.63 (28.1-95.46)	22.7 (11.5-31.38)	0.008
CD8 regulatory T cells	66	0.56 (0.29-1.9)	0.51 (0.31-1.7)	0.9
CD8 PD-1 positive T cells	66	8.1 (2.9-16.3)	4.66 (0.7-7.9)	0.06

Table 10 Summary of discovery cohort immune cell densities stratified according to lymph node status

Comparison of intraepithelial and stromal immune cell densities in patients with vs without lymph node metastasis. Data presented as median immune cell densities with 95% Confidence interval (CI). N= number of cases with available data. Mann-Whitney test used for all statistical calculations.

3.2.4 Correlations between immune cell densities

Further investigation of the relationships between different immune cells revealed a positive correlation between stromal CD4 effector cells and stromal CD8 effector cells (Spearman $r = 0.648$, $p < 0.0001$), as well as intraepithelial CD8 effector T cells (Spearman $r = 0.256$, $p = 0.003$). Intraepithelial CD4 effector T cells positively correlated with intraepithelial CD8 effector T cells (Spearman $r = 0.4976$, $p < 0.001$) and M1-like macrophages (Spearman $r = 0.373$, $p = 0.004$). Stromal CD4 effector cells also correlated with stromal M1-like macrophages (Spearman $r = 0.346$, $p = 0.008$). Stromal CD8 effector T cells positively correlated with stromal M1-like (Spearman $r = 0.4$, $p = 0.001$) and M2-like (Spearman $r = 0.278$, $p = 0.003$) macrophages. This was not surprising as there was a positive association between stromal M1-like and M2-like macrophages (Spearman $r = 0.413$, $p = 0.0001$).

The positive correlation between CD4 effector cells with CD8 effector cells and M1-like macrophages within the epithelium and stroma, in combination with the significantly increased immune cell density in the patients without lymph node metastasis suggest a possible interaction between those immune cell subtypes in order to orchestrate their anti-tumour response.

3.2.5 Immune cell densities and clinicopathological characteristics

The next step was to investigate the relationship between different immune cell densities and patients' clinicopathological characteristics. Table 11-13 summarise the associations of different immune cell populations within epithelium and stroma with patient clinical parameters. More intraepithelial M1-like macrophages were associated with higher pT stage (14.45 vs 20.84, $p=0.036$), a finding somewhat counterintuitive (Table 11). Stromal CD4 effector T cells were increased in patients with lower pT stage (77.8 vs 36.46 cells/mm², $p=0.04$) showing an association with early staged disease (Table 12). There were no statistically significant differences among immune cell counts with Gleason score and presence of perineural invasion.

	M1-like macrophages			M2-like macrophages			B cells		
Epithelium									
	N	Median	p value	N	Median	p value	N	Median	p value
Stage			0.036			0.453			0.315
T2	28	14.45		28	19.6		28	2.9	
T3-T4	55	20.84		55	16.36		55	1.7	
Gleason score			0.122			0.235			0.620
=7	55	18.7		55	15.82		55	2.11	
>7(8-9)	28	20.17		28	24.59		28	1.75	
PNI			0.611			0.266			0.877
Absent	11	17.82		11	28.66		11	2.9	
Present	72	19.13		72	17.21		72	1.75	
Stroma									
Stage			0.226			0.898			0.484
T2	28	44.3		28	65.28		28	8.81	
T3-T4	55	55.3		55	69.2		55	7.94	
Gleason score			0.394			0.337			0.65
=7	55	47.09		55	63.16		55	7.94	
>7(8-9)	28	59.99		28	77.62		28	8.977	
PNI			0.861			0.657			0.853
Absent	11	52.15		11	94.86		11	4.92	
Present	72	52.3		72	65.87		72	8.35	

Table 11 Macrophage and B cell densities of discovery cohort stratified by clinicopathological parameters

Data are presented as median immune cell densities (cells/mm²). N= number of cases with available data. Mann-Whitney test used for all statistical calculations. CI= Confidence interval, PNI= Perineural invasion

	CD4 effector T cells			CD4 regulatory T cells			CD4 PD1+ T cells		
Epithelium									
	N	Median	p value	N	Median	p value	N	Median	p value
Stage			0.11			0.654			0.318
T2	22	30.1		21	2.6		20	8.01	
T3-T4	44	18.9		44	2		37	12.3	
Gleason score			0.97			0.446			0.406
=7	46	20.6		45	2.2		40	12.35	
>7(8-9)	20	20.9		20	2.1		17	8.57	
PNI			0.742			0.787			0.12
Absent	10	10.55		9	2.2		10	4.3	
Present	56	20.95		56	2.1		47	11.6	
Stroma									
Stage			0.045			0.328			0.665
T2	28	77.8		22	4.13		22	6.69	
T3-T4	57	36.46		44	4.84		44	8.8	
Gleason score			0.393			0.549			0.582
=7	46	63.78		36	4.64		46	7.99	
>7(8-9)	20	73.69		20	4.68		20	8.79	
PNI			0.411			0.66			0.752
Absent	10	78.61		10	2.94		10	10.17	
Present	56	63.78		56	4.68		56	8.48	

Table 12 CD4 T cell densities of discovery cohort stratified by clinicopathological parameters

Data are presented as median immune cell densities (cells/mm²). Mann-Whitney test used for all statistical calculations. N= number of cases with available data. CI= Confidence interval, PNI= Perineural invasion

	CD8 effector T cells			CD8 regulatory T cells			CD8 PD1+ T cells		
Epithelium									
	N	Median	p value	N	Median	p value	N	Median	p value
Stage			0.2			0.76			0.5
T2	22	10.6		22	3.2		22	1.9	
T3-T4	44	5.29		44	2.7		44	3.8	
Gleason score			0.09			0.92			0.24
=7	46	7.57		46	2.45		46	2.7	
>7(8-9)	20	1.95		20	3.25		20	5.85	
PNI			0.713			0.358			0.324
Absent	10	2.35		10	1.1		10	8.56	
Present	56	6.63		56	3.25		56	1.95	
Stroma									
Stage			0.641			0.997			0.541
T2	22	27.75		22	5.98		22	1.9	
T3-T4	44	30.64		44	5.34		44	3.8	
Gleason score			0.714			0.595			0.2
=7	46	31.59		46	0.53		46	5.16	
>7(8-9)	20	27.7		20	0.48		20	8.89	
PNI			0.07			0.388			0.504
Absent	10	44.99		10	0.37		10	9.6	
Present	56	28.18		56	0.59		56	5.16	

Table 13 CD8 T cell densities of discovery cohort stratified by clinicopathological parameters

Data are presented as median immune cell densities (cells/mm²). N= number of cases with available data. Mann-Whitney test used for all statistical calculations. CI= Confidence interval, PNI= Perineural invasion

In summary, comparison of different infiltrating immune cells with clinicopathological parameters revealed that tumours of higher pT stage (pT3-4) were associated with less stromal CD4 effector T cells and more intraepithelial M1-like macrophages.

3.3 Immune profiling of Validation cohort

3.3.1 Clinical characteristics of Validation cohort (Validation TMA)

A validation TMA of intermediate and high-risk patients was used to test whether our results were maintained in a larger, independent patient cohort from another institution. The validation cohort included 285 patients with primary PCa who underwent RP and regional lymph node dissection. Two hundred and

fifty-one patients had one 0.6 µm core and 34 patients had two 0.6 µm cores from the index lesions. The median age at diagnosis was 64.05 years (63.27-65.09 95% CI). The median follow-up time was 12.87 years (12.07-13.43 95%CI), during which 246 men developed biochemical recurrence, 145 men died (among whom, 70 men died from PCa). Table 14 presents the clinical characteristics of patients included in the validation cohort. A significant proportion of the cases were not informative due to complete lack of tissue samples, absence of cancer tissue and interpretable staining; however there was no significant difference between overall cohort and the informative cases.

	All patients (285)	Available for analysis (184)	p value
Age at diagnosis, median (95% CI)	64.05 (63.27-65.09)	63.93 (63.06-65.32)	0.557
Peak pre-op PSA, median (95% CI)	13.55 (12-15.6)	12 (10.2-15.3)	0.883
Gleason score, N (%)			0.98
≤6	216 (76%)	138 (75%)	
7	22 (8%)	16 (9%)	
≥8	45 (16%)	29 (16%)	
missing	2 (0%)	1 (0%)	
pT stage, N (%)			0.695
2	150 (53%)	90 (49%)	
3	128 (45%)	90 (49%)	
4	7 (2%)	4 (2%)	
missing	0 (0%)	0 (0%)	
pN status, N (%)			0.677
0	204 (72%)	128 (70%)	
1	81 (28%)	56 (30%)	
missing	0 (0%)	0 (0%)	
M status, N (%)			0.692
0	282 (99%)	183 (100%)	
1	2 (1%)	1 (0%)	
missing	1 (0%)	0 (0%)	

Table 14 Clinicopathological characteristics of the validation cohort

Of 285 patients with intermediate and high-risk disease, 184 were informative due to lack of interpretable tissue samples. Mann-Whitney and Chi-square test were used for statistical comparisons. CI= Confidence interval

3.3.2 Immune profiling of validation cohort patients in the context of lymph node metastasis

A summary of all the immune cell densities stratified by nodal status is presented in Table 15. Data from the T lymphocyte panel were available for 181 patients, 59 with and 122 without lymph node metastasis. CD4 effector T cells were significantly decreased in patients with lymph node metastasis (51.8 cells/mm² vs 100.5 cells/mm², p<0.0001), validating our previous observation.

There was no significant difference between the ratios of CD4 effector/ CD4 regulatory T cells within the stroma (18.18 vs 12.66, $p= 0.211$), likely due to the lack of CD4 regulatory T cell immune cells. There was a non-significant trend for increased intraepithelial CD8 effector T cells (28.7 cells/mm² vs 19 cells/mm², $p=0.063$), but there was no difference in the CD8 effector T cell density within the stroma which was previously observed. Lastly, from 184 informative cases (56 with and 128 without lymph node metastasis), there were no significant differences between the M1 macrophage densities within the epithelium or stroma, which does not replicate the earlier results from our discovery TMA. It is noteworthy that no CD4 PD-1 positive T cells were detected, however this is a rather rare immune population and it is conceivable that due to under sampling there were not any cells present. In addition, CD8 PD-1 positive T cells were detected therefore we are confident there were no technical problems with PD-1 staining.

Immune cell densities (95% CI)	N	LN status		
		Negative =128	Positive = 56	p
Epithelium				
M1-like macrophages	184	48.75 (38.3-58)	61.15 (51.5-76.2)	0.06
M2-like macrophages	184	28 (22.7-32.8)	26 (21.1-38.9)	0.607
B cells	184	0 (0-0)	0 (0-5)	0.65
CD4 effector T cell	181	22.2 (16-30.4)	25.25 (11-32)	0.966
CD4 regulatory T cells	181	0 (0-0)	0 (0-2)	0.935
CD4 PD-1 positive T cells	181	0 (0-0)	0 (0-0)	>0.99
CD8 effector T cells	181	28.7 (22.5-41.8)	19 (7.5-26.55)	0.063
CD8 regulatory T cells	181	0 (0-0)	0 (0-1.2)	0.986
CD8 PD-1 positive T cells	181	0 (0-0)	0 (0-0)	0.92
Stroma				
M1-like macrophages	184	104 (89.2-135)	122.2 (84-145)	0.801
M2-like macrophages	184	86.6 (75-106)	68(56.85-106)	0.293
B cells	184	3.9 (0-7.2)	2.5 (0-9.7)	0.18
CD4 effector T cells	181	100.5 (78.5-113)	51.8 (39.9-70.4)	<0.001
CD4 regulatory T cells	181	2.7 (1.8-4.1)	1.7 (0-3.1)	0.317
CD4 PD-1 positive T cells	181	0 (0-0)	0 (0-0)	>0.999
CD8 cytotoxic T cells	181	23 (18.2-27.3)	28.2 (20.2-37)	0.32
CD8 regulatory T cells	181	0 (0-1.05)	0 (0-1.4)	0.5
CD8 PD-1 positive T cells	181	0 (0-0.1)	0 (0-0)	0.633

Table 15 Summary of validation cohort immune cell densities stratified according to lymph node status

Comparison of intraepithelial and stromal immune cell densities in patients with and without lymph node metastasis. Data are presented as median immune cell densities (cells/mm²) with 95% Confidence interval (CI). N= number of cases with available data. Mann-Whitney test used for statistical comparisons.

Summarising, the key finding from mIF staining of the validation TMA was that stromal CD4 effector T cells were significantly reduced in the stroma of localised

prostate cancer tumours with regional lymph node metastasis. Furthermore, there was a trend for reduced CD8 effector T cells in the same patient group.

3.4 Prognostic value of tumour stromal CD4 effector T cells for lymph node metastasis

A crucial question was whether different immune cell infiltrates could be used as predictive biomarkers of lymph node invasion. Since stromal CD4 effector T cells were identified as the immune cell population reproducibly associated with the status of nodal involvement, I tested if high stromal CD4 effector T cell infiltrates could predict the presence of pelvic nodal disease. Firstly, univariate regression was performed in the discovery (OR=0.157, 0.05-0.49 95%CI, p=0.01) and validation cohort (OR=0.26, 0.13-0.51 95%CI, p<0.001). Then, multivariate regression analyses was performed on data from the discovery cohort, including standard of care clinicopathological factors (namely pT stage, Gleason score from RP, peak pre-operative PSA level and percentage of positive cores). Stromal CD4 effector T cell density remained an independent predictor of lymph node spread (OR=0.38, p=0.004; Table 16). Similarly, from the validation cohort, high stromal CD4 effector T cell density was confirmed to be a significant independent predictor of lymph node metastasis (OR=0.26, p<0.001; Table 16).

Multivariate regression analysis			
Discovery cohort			
	OR	95% CI	p value
pT stage	2.96	0.72-12.12	0.131
Gleason score	1.05	0.24-4.57	0.944
Peak pre-op PSA	0.99	0.94-1.03	0.719
Percentage of positive cores	1.01	0.99-1.03	0.175
High stromal CD4 effector T cells	0.15	0.04-0.53	0.004
Validation cohort			
	OR	95% CI	p value
pT stage	2.49	1.17-5.27	0.017
Gleason score	3.74	1.48-9.44	0.005
Peak pre-op PSA	1.04	1.02-1.05	0.0004
High stromal CD4 effector T cells	0.26	0.12-0.54	0.0004

Table 16 Multivariate regression analysis of stromal CD4 effector T cells with standard of care clinicopathological factors commonly used for the prediction of nodal metastasis

In the discovery cohort high density of stromal CD4 effector T cells (upper tertile) was an independent predictor of lymph node metastasis. In the validation cohort high density of stromal CD4 effector T cells (upper two tertiles) was an independent predictor of lymph node metastasis. OR= odds ratio, CI= confidence interval.

I then examined the receiver operator characteristic (ROC) curve in both patient cohorts to assess the benefit of adding stromal CD4 effector T cell density in a prediction model. In the discovery cohort (Figure 9A), the area under the curve (AUC) of a model with standard of care clinicopathological factors was 0.635 (0.49-0.78 95%CI, $p=0.07$), which was improved significantly to 0.768 (0.65-0.89 95%CI, $p<0.0001$) with the addition of stromal CD4 effector T cell density. Similarly, in the validation cohort (Figure 9B), the AUC increased from AUC=0.77 (0.7-0.84 95%CI, $p<0.0001$) to AUC=0.804 (0.73-0.87 95%CI, $p<0.0001$) when stromal CD4 effector T cell density is incorporated into the model. Even though the improvement observed in the validation cohort is not as impressive, this represents a significant confirmation of an association between decreased stromal effector CD4 T cell infiltration and nodal invasion.

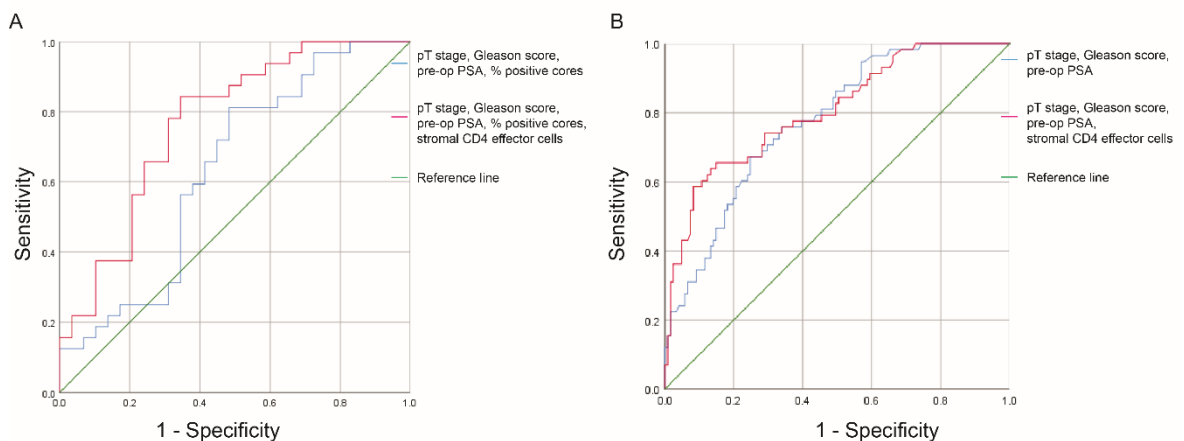


Figure 9 Clinical impact of stromal CD4 effector T cells in lymph node metastasis

Receiver Operator Curve (ROC) curves of the addition of stromal CD4 effector T cells to standard of care clinicopathological factors for predicting lymph node metastasis in the discovery (A) and validation (B) cohorts.

3.5 Prognostic value of stromal CD4 effector T cells in survival

During tumour progression, lymph node spread has a negative impact on patient survival (2, 150). Increased immune cell densities of stromal CD4 effector T cells (values were dichotomised into the upper tertile compared to the bottom two tertiles) were associated with improved relapse-free survival in the discovery cohort (log-rank test, $p=0.029$), as shown in Figure 10A. Increased stromal CD4

effector T cells (values were dichotomised into the upper two tertiles compared to bottom tertile) were also associated with improved relapse-free survival in the discovery cohort (log rank test, $p=0.045$), as shown in Figure 10B.

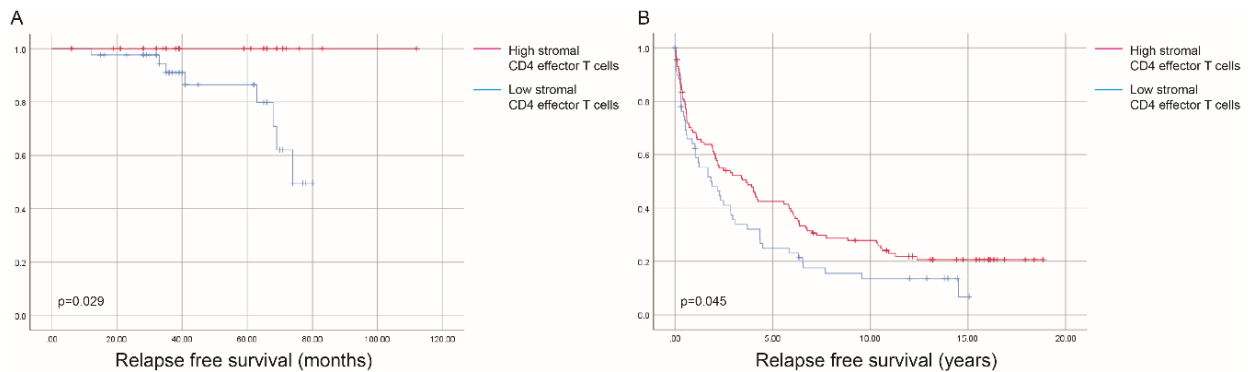


Figure 10 Clinical impact of stromal CD4 effector T cells in survival

Kaplan-Meier curves of prostate cancer patients in the discovery cohort (A) and validation cohort (B). Log rank test used for statistical comparison.

Furthermore, this finding was in agreement with the negative impact that lymph node metastasis bears in patient survival (150, 151), which was confirmed in both discovery (log-rank, $p=0.021$) and validation cohorts (log-rank, $p<0.001$), presented in Appendix Figure 1.

3.6 Prostate cancer common genetic alterations are not associated with immune cell infiltration

The tumour immune microenvironment plays an important role in the pathogenesis and progression of tumours and may be associated with somatic genomic alterations (22, 25). From the immune profiling results, patients with lymph node metastasis had decreased infiltration of effector CD8 T cells that are known to contribute to local cancer confinement and reduction of cell proliferation (42). Also, the same patients reproducibly showed significantly decreased infiltration of CD4 effector T cells. I therefore investigated whether the observed differences in tumour immune landscape were associated with common prostate cancer molecular alterations.

Previous studies have shown that *TMPRSS2/ETS* fusion gene fusions may be caused, at least in part, by increased local inflammation and oxidative stress (24). In addition, the generation of fusion genes can result in the formation of new amino acid sequences, potentially generating fusion proteins that can function as neoantigens (152). Furthermore, PCa tumours with ERG overexpression have been reported to be significantly associated with increased lymphocytic infiltration (25, 66). Therefore, I hypothesised that patients with decreased CD8 and CD4 T cells infiltration and lymph node metastasis may be associated with ERG negative tumours. Also, *PTEN* inactivation can influence immune cell infiltration and immunosuppression (22) and has been largely associated with metastasis and poor clinical outcome (17, 28). Therefore, patients with *PTEN* loss may be more frequently associated with nodal metastasis and *PTEN* status could potentially improve the CD4 effector T cell predictive ability. Lastly, I hypothesised that high tumour cell proliferation, measured by Ki67 proliferation index, will be present in patients with lymph node metastasis that lack anti-tumour lymphocytes.

ERG overexpression was used as a surrogate for *TMPRSS2/ERG* translocation (25, 153). Only nuclear positivity was assessed and endothelial cells and/or lymphocytes were used as positive controls (Figure 11A). Lack of *PTEN* expression was used as a surrogate for *PTEN* loss (18, 31). Nuclear and cytoplasmic positivity were assessed (Figure 11B). Background benign glands, fibromuscular stroma and nerves were used as a positive control. Ki67 scoring was used as proliferation index based on nuclear immunoreactivity (Figure 11C).

Thirty percent of the total cores were double scored by a specialist uropathologist (Dr Jonathan Salmond) for ERG, *PTEN* and Ki-67 staining, blinded to patient characteristics. There was almost perfect agreement in scoring for ERG ($\kappa=0.89$) and substantial agreement in scoring for *PTEN* ($\kappa=0.74$) and Ki67 ($\kappa=0.74$).

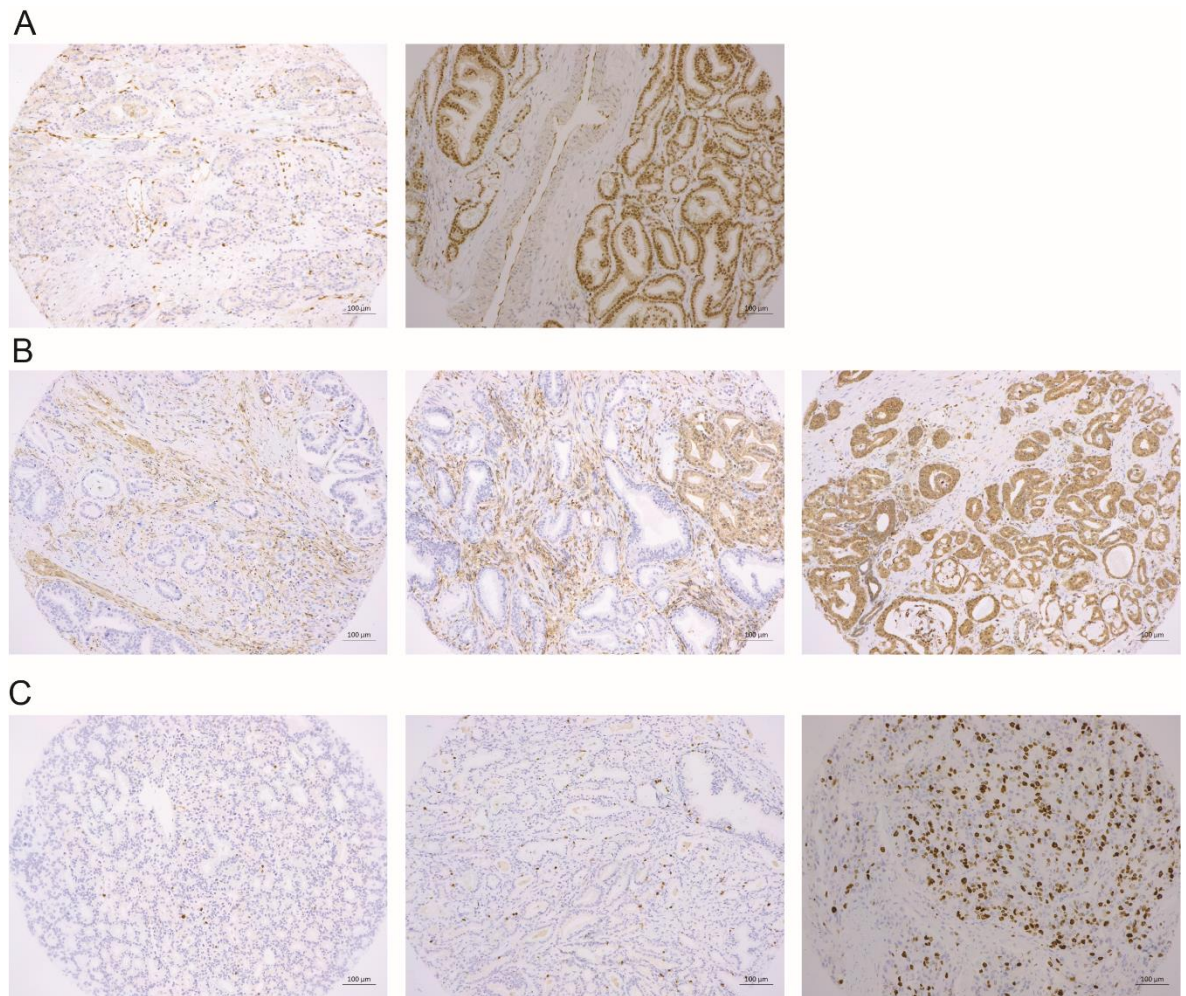


Figure 11 Representative images of ERG, PTEN and Ki67 staining

(A) Tissue cores with negative (left) and positive (right) ERG immunostaining. (B) Tissue cores with homogeneous PTEN loss (left), heterogeneous PTEN loss (middle) and intact PTEN (right). (C) Tissue cores with low (left), moderate (middle) and high (right) Ki67 nuclear immunoreactivity. (Scale bar = 100 µm)

3.6.1 Molecular characteristics in primary tumours of patients with vs without lymph node metastasis

Out of 94 patients in our TMA, 92, 91 and 89 had at least two out of three evaluable cores for ERG, PTEN and Ki67 staining by IHC respectively (Table 17). Of the tumours with assessable staining, 43/92 (47%) had positive ERG immunostaining which is in keeping with the incidence of *TMPRSS2/ERG* translocation previously reported (154, 155). There was no difference in ERG status according to the presence of nodal metastasis ($p = 0.836$). PTEN staining was detected in 52/91 (57%) patients. PTEN loss was significantly associated with nodal metastasis ($p=0.0001$), as previously described in the literature (17, 18).

Lastly, there was no association between Ki67 proliferation and lymph node spread.

	Overall N=94	Lymph node metastasis		
		Absent=44	Present=50	p value
<i>TMPRSS2/ERG</i> fusion (<i>ERG</i> overexpression), N (%)	92			
Positive	43 (47)	19 (21)	24 (26)	0.836
Negative	49 (53)	23 (25)	26 (28)	
PTEN status, N (%)	91			0.0001
Intact	52 (57)	33 (36)	19 (21)	
Loss	39 (43)	9 (10)	30 (33)	
Ki67 score, N (%)	89			0.573
Low ($\leq 10\%$)	43 (49)	19 (21)	24 (27)	
Moderate ($>10\%, \leq 20\%$)	19 (21)	11 (12)	8 (9)	
High ($>20\%$)	27 (30)	12 (14)	15 (17)	

Table 17 Molecular features of discovery cohort according to their lymph node status

N= number of cases with available data. Fisher's exact test and Chi-square test used for statistical comparisons.

3.6.2 *ERG*, PTEN and Ki67 are not associated with immune cell infiltration

There were no significant differences stratifying immune cell infiltrates by *ERG* status (Table 18). Similar results were obtained when immune cell densities were stratified according to PTEN status (Table 19) and Ki67 scoring (Table 20). Overall, these results support the notion that immune cell infiltration is not associated with the presence of *ETS* translocation, *PTEN* loss and differences in tumour cell proliferation.

Epithelium		ERG status		
Immune densities, median (95% CI)	All N=92	Positive = 43	Negative = 49	p value
M1-like macrophages	80	16.75 (11.01-22.89)	20.84 (14.45-25.67)	0.273
M2-like macrophages	81	14.66 (11.95-22.4)	19.85 (11.49-33.32)	0.437
B cells	81	1.66 (0.9-3.45)	2.6 (1-7.92)	0.571
CD4 effector T cells	66	21 (16-27.3)	16.2 (10.1-30.5)	0.572
CD4 regulatory T cells	63	3.5 (1-6.2)	1.18 (0-3.2)	0.092
CD4 PD-1 positive T cells	55	5.3 (8.16-16.4)	9.83 (1.3-16.9)	0.65
CD8 cytotoxic T cells	64	8.8 (4.2-14.5)	4.2 (0.85-6.8)	0.094
CD8 regulatory T cells	64	3.9 (1.3-5.6)	0.88 (0-3.2)	0.067
CD8 PD-1 positive T cells	64	3.5 (0-9.48)	0 (0-8.7)	0.72
Stroma				
M1 macrophages	80	48.85 (39.11-75.67)	52.15 (35.58-89.31)	0.954
M2 macrophages	81	65.28 (53.55-79.07)	66.48 (53.9-81.99)	0.745
B cells	81	8.49 (4.44-15.22)	6.74 (3.96-11.51)	0.491
CD4 effector T cells	66	40.81 (28.3-82.77)	75.83 (27.47-91.35)	0.769
CD4 regulatory T cells	63	4.71 (1.7-7.94)	4.58 (1.7-6.12)	0.603
CD4 PD-1 positive T cells	55	8.73 (1.7-17.7)	7.33 (0.84-11.2)	0.365
CD8 cytotoxic T cells	64	29.8 (21.7-50.6)	28.1 (14-39)	0.479
CD8 regulatory T cells	64	0.66 (0.34-1.9)	0.4 (0.28-1)	0.319
CD8 PD-1 positive T cells	64	4.66 (0.87-8.5)	6.23 (3-18.6)	0.182

Table 18 Immune cell densities of discovery cohort stratified by ERG status

Immune cell densities of prostate cancer patients presented as median with 95% CI. N= number of cases with available data. Mann Whitney test used for statistical comparisons. CI=confidence interval.

Epithelium		PTEN status		
Immune densities, median (95% CI)	All N=91	Intact = 52	Lost = 39	p value
M1-like macrophages	80	19.74 (16.8-25.4)	17.63 (10.45-22.89)	0.152
M2-like macrophages	81	18.07 (11.95-24.9)	15.02 (11.4-27.35)	0.702
B cells	81	2.11 (0.9-6.5)	1.7 (1-5)	0.703
CD4 effector T cells	64	21.7 (14.7-30.5)	20 (10.9-27.3)	0.653
CD4 regulatory T cells	64	1.5 (0.41-3.3)	3.65 (0.9-6.6)	0.208
CD4 PD-1 positive T cells	55	10.4 (6.59-1.7)	13.15 (0.8-18.8)	0.667
CD8 cytotoxic T cells	64	6.1 (4.2-12.6)	5.7 (0.68-13)	0.424
CD8 regulatory T cells	64	3.8 (0.88-4.3)	1.9 (0-8.4)	0.668
CD8 PD-1 positive T cells	64	5.3 (0-8.7)	1.9 (0-10.4)	0.555
Stroma				
M1-like macrophages	80	54.62 (40.04-81.78)	48.73 (36.49-76.35)	0.522
M2-like macrophages	81	66.17 (60.67-77.04)	62.97 (42.14-88.56)	0.704
B cells	81	8.75 (3.9-14.22)	7.35 (4.44-13.07)	0.687
CD4 effector T cells	64	64.72 (32.5-91.35)	47.92 (27.47-82.77)	0.756
CD4 regulatory T cells	64	5.14 (3.35-7.47)	3.8 (1.6-6.85)	0.331
CD4 PD-1 positive T cells	55	8.88 (1.3-16.3)	6.06 (0-12.6)	0.452
CD8 cytotoxic T cells	64	24.94 (14-40.19)	29.9 (21.7-46.18)	0.829
CD8 regulatory T cells	64	0.51 (0.32-1.5)	0.62 (0.26-1.8)	0.871
CD8 PD-1 positive T cells	64	8.1 (3.01-16.3)	4.66 (0.87-7.9)	0.177

Table 19 Immune cell densities of discovery cohort stratified by PTEN status

Immune cell densities of prostate cancer patients presented as median with 95% CI. N= number of cases with available data. Mann Whitney test used for statistical comparisons. CI=confidence interval.

Epithelium		Ki67 score			
		All N=89	Low=43	Moderate=19	High=27
Immune densities, median (95% CI)					
M1-like macrophages	79	19.3 (13.9-25.67)	18.57 (10.65-26.1)	18.5 (13-22.89)	0.837
M2-like macrophages	80	20.38 (15.4-28.6)	11.49 (9.68-40.2)	14.66 (10.95-31.94)	0.509
B cells	80	2.8 (1.09-8.33)	1.8 (0.43-8.29)	1.45 (1-5)	0.568
CD4 effector T cells	62	17.5 (9.5-32.9)	20 (8.26-32.4)	21.35 (13-31)	0.653
CD4 regulatory T cells	61	1.8 (0-5.2)	3 (0-8.84)	3.4 (1-4.63)	0.875
CD4 PD-1 positive T cells	53	11.8 (0-18.7)	10.08 (0-19.7)	6.25 (0-13.6)	0.812
CD8 cytotoxic T cells	62	3.9 (0-7.15)	8.8 (5.2-25.5)	10.5 (0.88-20.3)	0.557
CD8 regulatory T cells	62	3.2 (0-9.36)	1.3 (0-4.1)	4 (1.9-7.6)	0.425
CD8 PD-1 positive T cells	62	0 (0-15.6)	5.5 (0-17.6)	1.95 (0-6.9)	0.817
Stroma					
M1-like macrophages	79	48.85 (36.2-78.8)	81.78 (43.94-96.7)	48.42 (35.6-75.67)	0.586
M2-like macrophages	80	62.21 (50-81.99)	65.28 (42.95-88.7)	72.87 (58.12-92.37)	0.708
B cells	80	7.36 (4.7-13.07)	7.85 (2.67-19.85)	8.81 (3.64-23.53)	0.775
CD4 effector T cells	62	75.83 (21-91.35)	79.77 (11.1-105)	54.4 (21.7-92.7)	0.741
CD4 regulatory T cells	61	2.1 (1.1-7.55)	5.4 (3.6-13.5)	5.05 (3.8-8.09)	0.467
CD4 PD-1 positive T cells	53	8.25 (0.3-16.5)	9.65 (1.3-16.3)	5.52 (0-20.3)	0.86
CD8 cytotoxic T cells	62	32.08 (21.1-57.45)	40.19 (22.1-51.6)	23.65 (8.86-62.13)	0.571
CD8 regulatory T cells	62	0.34 (0.27-1.5)	0.82 (0.5-1.9)	1.6 (0.23-3.59)	0.27
CD8 PD-1 positive T cells	62	5.54 (2.8-14)	4.66 (0-20.8)	8.2 (1.4-11.8)	0.875

Table 20 Immune cell densities of discovery cohort stratified by Ki67 score

Immune cell densities of prostate cancer patients presented as median with 95% CI. N= number of cases with available data. Kruskal–Wallis test used for statistical comparisons. CI=confidence interval.

3.6.3 Combining PTEN and stromal CD4 effector T cells in predicting lymph node metastasis does not improve prognostic value

PTEN status was the only molecular feature that was associated with and predictive of lymph node spread with univariate regression. Intact PTEN had a negative predictive value, with OR= 0.173 (0.07- 0.44 95% CI, p=0.0002) in the discovery cohort and OR=0.44 (0.23- 0.83 95%CI, p=0.01) in the validation cohort. PTEN status remained a significant prognostic factor in the multivariate setting, including all currently used parameters for predicting nodal metastasis, as shown in Table 21.

Multivariate regression analysis			
Discovery cohort			
	OR	95% CI	p value
pT stage	1.61	0.52-4.97	0.406
Gleason score	1.7	0.54-5.28	0.357
Peak pre-op PSA	1.01	0.96-1.04	0.955
Percentage of positive cores	1.01	0.99-1.02	0.415
Intact PTEN	0.22	0.08-0.61	0.004
Validation cohort			
	OR	95% CI	p value
pT stage	2.6	1.23-5.49	0.012
Gleason score	4.23	1.69-10.592	0.002
Peak pre-op PSA	1.03	1.02-1.05	0.005
Intact PTEN	0.45	0.21-0.93	0.032

Table 21 Multivariate regression analysis of PTEN status with standard of care clinicopathological factors commonly used for the prediction of nodal metastasis

In the discovery cohort (top) and the validation cohort (bottom) PTEN status was an independent predictor of lymph node metastasis. OR= odds ratio, CI=confidence interval.

However, ROC curve analysis showed that the addition of PTEN status in the currently used parameters was inferior to the addition of stromal CD4 effector cells. In the discovery cohort addition of PTEN resulted in an AUC=0.67 (0.537-0.813 95%CI, p=0.022) whereas CD4 stromal effector T cells had AUC=0.75 (0.62-0.87 95%CI, p=0.001). In the validation cohort addition of PTEN resulted in AUC=0.76 (0.69-0.84 95%CI, p<0.0001) and CD4 stromal effector T cells had AUC=0.79 (0.71-0.86 95%CI, p<0.001). Combination of PTEN status with CD4 effector immune cell density did not carry a significant benefit. In the discovery cohort it resulted in an AUC=0.77 (0.65-0.89 95%CI, p<0.001) and in the validation AUC=0.79 (0.71-0.87 95%CI, p<0.0001), as shown in Figure 12.

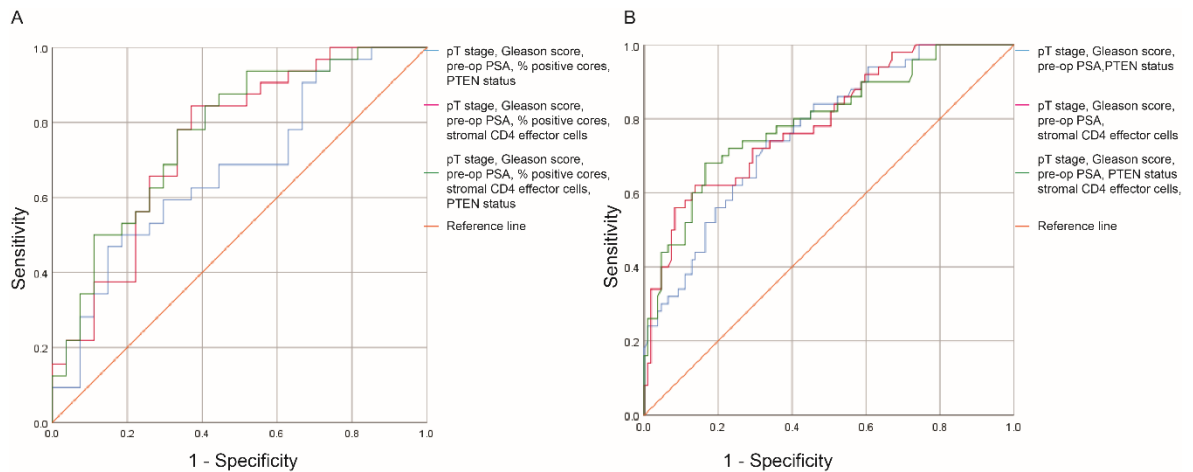


Figure 12 Clinical impact of PTEN and stromal CD4 effector T cells in lymph node metastasis

Receiver Operator Curve (ROC) curves of the addition of stromal PTEN and CD4 effector T cells to standard of care clinicopathological factors for predicting lymph node metastasis in the discovery (A) and validation (B) cohorts.

3.7 Optimisation of dual CD4-FoxP3 Immunohistochemistry

The data collected so far suggest an important role of stromal CD4 effector T cells (CD4+ FoxP3- PD-1-). A quantitative mIF platform was used for reasons described previously, however this methodology is not currently available at the clinical setting or every research laboratory. For this reason, I explored the potential of a method more easily implemented clinically, such as dual chromogenic IHC for CD4 and FoxP3. CD4 effector T cells were defined as CD4+FoxP3-PD1- with multiplex IF and the CD4+PD1+ cells were the least common within the stroma (0.07% in discovery and 0% in validation cohorts), so PD-1 staining was omitted.

Dual CD4-FoxP3 chromogenic IHC was successfully optimised, with CD4 stained with alkaline red and FoxP3 with DAB brown (Figure 13A). The discovery TMA was stained and analysed with HALO using a tissue classifier (epithelium vs stroma) based on the morphological characteristics, and the percentage of positively stained cells within the each area (cells/mm²) was quantified. There was a positive correlation between CD4 effector T cells detected by mIF and IHC within the stroma (Spearman's $r=0.37$, $p=0.002$), thus confirming the validity of the dual staining approach (Figure 9B).

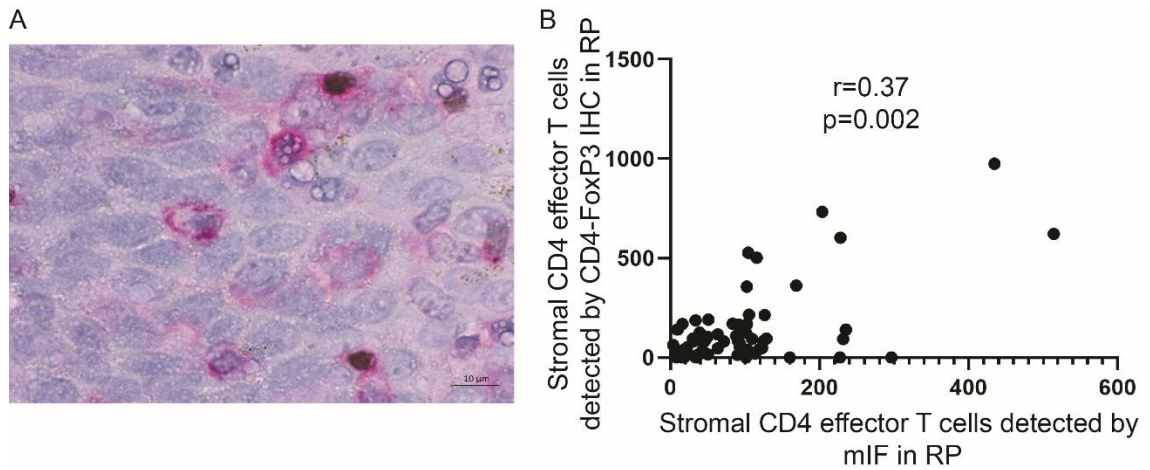


Figure 13 Optimisation of dual CD4- FoxP3 immunohistochemistry

(A) Representative image of dual CD4-FoxP3 staining. CD4 cells are shown in red (alkaline red) and FoxP3 in brown (DAB), scale bar 10 μ m. (B) Stromal CD4 effector T cells are presented as median immune cell densities (cells/mm²) derived from dual CD4-FoxP3 immunohistochemistry (IHC) staining and multiplex immunofluorescence (mIF) in the radical prostatectomy (RP) tissue (n=62). Spearman's correlation was used for statistical comparison.

3.8 Exploration of stromal CD4 effector T cells in low risk prostate cancer patients

Another question was whether stromal CD4 effector T cells had an impact on clinical outcomes in low risk prostate cancer. To explore this, we established a collaboration with Professor David Berman's lab in Queen's University in Kingston, Ontario, Canada. He provided a primary prostate cancer TMA of patients with low risk disease at diagnosis. I stained this TMA with dual CD4-FoxP3 IHC in order to assess the relationship of CD4 effector T cell density with relapse free survival in this patient cohort.

3.8.1 Low risk prostate cancer cohort

The low-risk patient cohort included 272 patients with three to five cores per patient. The median age of diagnosis 61 years (60-62 95%CI). The median peak pre-operative PSA level was 5.8 ng/ml (4.4-7.8 95%CI). Two hundred fourteen patients (78.7%) had pT2 stage disease and 58 (21.3%) had pT3 stage tumours. One hundred and thirty two patients had Gleason score 6 (48.5%) and 7 (48.5%) and eight patients had Gleason score >7 (3%). The median follow up was 4.92 years (4.7-5.1 95%CI) and 54 patients had biochemical relapse. Thirty-four patients were lost in follow-up.

3.8.2 Stromal CD4 effector T cells are not associated with survival in low risk prostate cancer patients

The low-risk prostate cancer cohort TMA was stained with dual CD4-FoxP3 IHC and scored with HALO as previously described. The overall stromal immune cell density was compared to data from the discovery cohort of high-risk disease. Interestingly, PCa patients diagnosed with more advanced (higher risk) disease had significantly higher overall stromal CD4 effector T cell density of 92.08 cells/mm² (62.7-117.1 95%CI) compared to low risk tumours, 8.53 cells/mm² (6.96 - 10.88 95%CI, $p < 0.0001$), shown in Figure 14A. Within the low-risk disease cohort, there was no significant difference in relapse-free survival in patients with high (above median) stromal CD4 effector T cell density ($p = 0.34$), shown in Figure 14B.

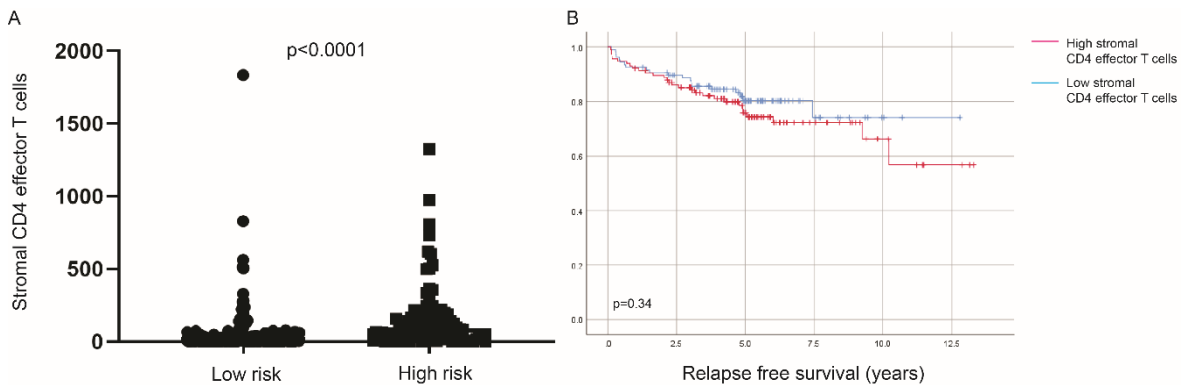


Figure 14 Stromal CD4 effector T cells in low risk prostate cancer

(A) Stromal CD4 effector T cell density is presented as median cells/mm² with 95% confidence interval in patients with low-risk (n=260) and high-risk (n=89) prostate cancer. (B) Kaplan-Meier curves of low-risk prostate cancer patients according to CD4 effector T cell infiltration. Log rank test used for statistical comparison.

3.9 Translation of stromal CD4 effector T cells detection in the clinical setting

3.9.1 Staining of prostate cancer diagnostic biopsies

The data collected so far support the use of stromal CD4 effector T cells in intermediate and high-risk disease in order to improve the current algorithms of nodal spread prediction. This would be applicable at the diagnostic biopsy stage

in order to spare patients from the unnecessary side effects of lymph node dissection.

For this reason, 31 diagnostic biopsies for the patients included in the discovery cohort were obtained from Glasgow Biorepository (16 LN+, 15 LN-). These were stained with dual CD4-FoxP3 IHC and analysed in HALO. Only tissue regions containing more than 70% cancer were analysed and CD4 effector (CD4+FoxP3-) T cells were quantified within stroma (Figure 15A-C). There was a positive correlation ($r=0.51$, $p=0.02$) between stromal CD4 effector T cells detected with IHC in diagnostic biopsies and detected with mIF in discovery TMA from index lesions from the same patient (Figure 15D). However, when the stromal CD4 effector immune cells detected in diagnostic biopsies were stratified according to nodal spread there was no significant difference (Figure 15E).

Apart from the small number of cases examined, which limits the conclusion that can be drawn, the nature of prostate biopsy tissue could explain this discrepancy. In biopsy material, the stromal CD4 effector T cells are in close proximity to cancerous prostate glands, as well as benign glands and PIN. The tumour stromal area examined is therefore more heterogeneous compared to the prostate cancer stroma derived from the index lesion that was used for the discovery TMA. This raises interesting questions regarding the scoring system that should be applied in biopsy tissue. For example, a more stringent threshold cut-off above 70%, e.g. 90%, would be more appropriate. Also, using MRI/US guidance for specific sampling of the index lesion and scoring only those cores could be another possible approach.

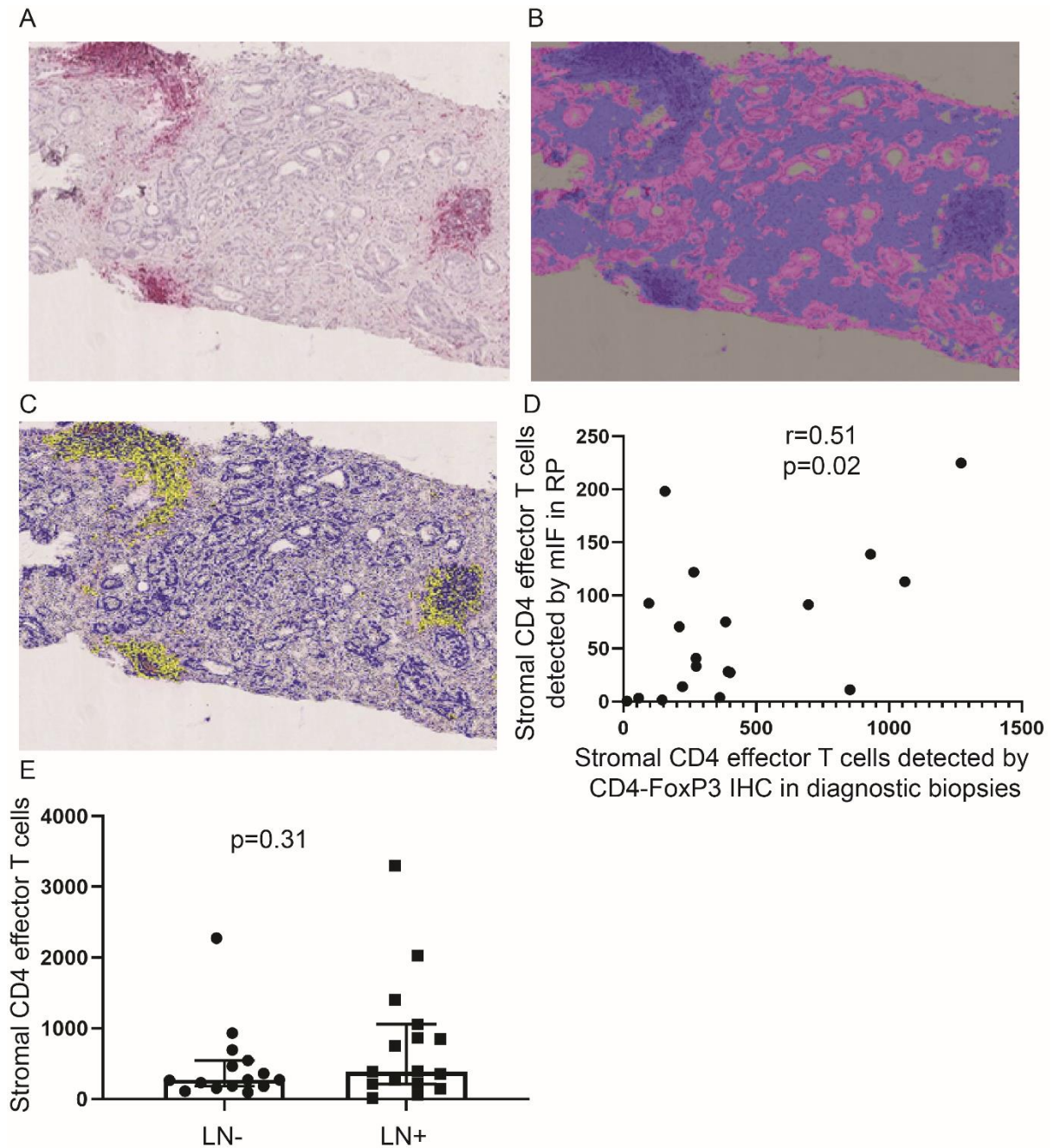


Figure 15 Staining of prostate cancer diagnostic biopsies with dual CD4-FoxP3 immunohistochemistry

Prostate cancer biopsy tissue stained with dual CD4-FoxP3 (A), classified in epithelium (magenta) and stroma (blue) (B), and scored using HALO (C), yellow indicating positively stained cells. (D) Stromal CD4 effector T cells are presented as median immune cell densities (cells/mm²) derived from dual CD4-FoxP3 staining of diagnostic biopsies and multiplex immunofluorescence (mIF) in the radical prostatectomy (RP) tissue, n=19. Spearman's correlation was used for the immune infiltration in the same patient. (F) Stromal CD4 effector T cells are presented as median immune cell densities (cells/mm²) derived from dual CD4-FoxP3 staining on diagnostic biopsies from patients with (LN+, n=16) vs without (LN-, n=15) lymph node metastasis. Error bars indicate 95% confidence interval. Mann-Whitney test used for statistical comparison.

3.10 Concluding summary

I aimed to dissect the clinical significance of the immune landscape in localised PCa patients. I explored the relationship of specific tumour infiltrating immune cells with malignant prostate epithelium to determine if this correlates with the ability of a tumour to metastasise to regional lymph nodes. For this reason, we successfully developed and applied a novel mIF methodology combining up to six antibodies on a single slide (Figure 6-7). Low CD4 effector T cell (CD4⁺ FoxP3⁻ PD-1⁻) density was significantly associated patients with lymph node metastasis (Table 9). Using multivariate analysis, we established a predictive model based on stromal CD4 T cell expression for predicting nodal spread and validated the model in a larger independent cohort of patients (Table 16). I additionally correlated subsets of tumour infiltrating immune cells with commonly present molecular alterations and found no associations with ERG overexpression or PTEN deletion (Table 18-20). The detection of stromal CD4 effector T cells by mIF was comparable to a simpler and easily transferable to the clinic dual CD4/FoxP3 IHC assay (Figure 13). However, its implementation on prostate biopsies requires further investigation (Figure 15). Lastly, we measured CD4 effector T cell (CD4⁺FoxP3⁻) density in a cohort of low risk prostate cancer patients and showed no impact on relapse-free survival (Figure 14).

It is challenging to replicate the complexity of human immune system with *in vitro* or *in vivo* experiments. Therefore, we used patient derived tissue in order to comprehensively characterise the immune tumour microenvironment. The exploration of the *in situ* immune cell composition of baseline, treatment-naïve, higher risk PCa patient samples offers critical insights into the complex and heterogeneous immune landscape associated with the growth and progression of this tumour, such as the reproducibly higher presence of CD4 effector T cells in patients without nodal metastasis. I generated a discovery TMA (Table 8) in order to examine a large number of patients at the same time, however this always carries the disadvantage of under sampling heterogeneous tumour immune infiltrates. I mitigated this issue by using three large cores (1 mm) from each tumour. Other limitations of this cohort are its retrospective nature of and the lack of long-term patient follow-up.

Flow cytometry is the most commonly used method for investigating lymphocytes and cytokines in cancer but the requirement to examine cell suspensions, the spatial context and the respective biologic relationships are inevitably lost. With mIF, spatial relationships are preserved, enabling the assessment of infiltrating cells in the context of the adjacent tumour and differentiating between stromal and intratumoural localisation. We used a TSA automated staining platform combined with slide scanning, multispectral imaging and a pattern recognition-based image analysis in order to extract maximum proteomic and morphometric information from our FFPE tissue samples.

Despite the overall validity of the data produced by mIF and multispectral imaging, some limitations should be mentioned. In terms of the immune cells subpopulations examined, CD68 is a recognised pan-macrophage marker, however low CD68 expression can be found on other monocytes, therefore our analysis likely contains a small proportion of non-macrophage cells. On the other hand, there is a risk that not all macrophages express CD68 or CD163 and we therefore might have missed small macrophage populations. It should also be noted that M1/M2-like is an oversimplified way of describing macrophage polarisation and I used those markers to describe macrophage phenotypic heterogeneity, not to define polarisation states. Lastly, due to limitations associated with the number of markers that can be used at the same time, we only investigated lymphocytic and macrophage populations. Using additional markers for T cell activation/exhaustion and other immune components, such as dendritic and natural killer cells will elucidate the PCa immune microenvironment further.

In patients with intermediate and high-risk localised prostate cancer, macrophages were the most abundant infiltrating immune cells, followed by CD4 T cells within stroma and epithelium (Table 9). CD4 regulatory T cells were proportionately distributed between stroma and epithelium, whereas CD8 T regulatory cells were scarce within epithelium. B cells were the least abundant immune cells. A previous study has shown that tertiary lymphoid follicles are commonly encountered in non-malignant areas surrounding the prostate cancer tissue (75). In my study I only looked into index lesions, therefore I cannot

exclude the role of B cells outside of the cancer mass lesions via non-cell contact mechanisms.

My initial hypothesis was that patients with lymph node metastasis would be associated with an immunosuppressive microenvironment, comprising M2-like macrophages (40), T regulatory cells (77), and PD-1 positive cells (78). Even though we cannot confidently exclude a non-cell contact effect of these cells (75), there were no differences in their abundance within index tumour lesions between LN+ and LN- patients (Table 10). Interestingly, there were significant differences between immune cell subtypes that are traditionally considered anti-tumorigenic (38). M1-like macrophages, and CD8 effector T cells were decreased in stromal and epithelial areas of LN+ patients (Table 10). In addition, stromal CD4 effector T cells that were consistently located at the interface between epithelium and stroma (Figure 8) were decreased in LN+ patients. Furthermore, the ratios stromal CD4 effector/CD4 regulatory T cells and epithelial/stromal CD8 effector T cells were lower in LN+ positive patients. These immune cells positively correlated with each other, consistent with potential functional interactions to determine host-tumour response. More importantly, stromal CD4 effector T cells, and to a lesser degree CD8 effector T cells, were reproducibly decreased in LN+ patients in an independent patient cohort (Table 10 and 15).

It is currently unknown if the lower number of tumoural effector T lymphocytes in LN+ patients is a primary or a secondary event. Although we are unable to describe a cell specific mechanism to explain this observation, these data provide evidence for a potentially clinically relevant role of CD4 effector T cells. A recent study of a humanised prostate cancer animal model is in agreement with my findings (156). Mice with human peripheral blood lymphocytes and DCs were unable to control PC3M tumour growth upon CD4 T cell depletion, whereas CD8 T cell depletion had no effect (156). In another large gene expression study of different tumour types, elevated Th1 and TH17 CD4 helper T cell expression was associated with an anti-tumourigenic phenotype (157). It is possible that CD4 effector T cells have a key role in prostate cancer tumour progression.

One possibility is that tumour in situ or regional nodal interactions between CD4 and CD8 cytotoxic T and other immune cell subsets is essential for mediating anti-tumour response and preventing lymph node metastasis by CD8 mediated

tumour cell killing at the primary tumour site (42, 158). While CD8 T cells are the key effector population that mediate tumour cell killing, they can be affected by the tumour immune environment to develop into regulatory and/or exhausted T cells in the absence of CD4 effector T cell help (42, 159). There is also some evidence that CD4 T cells can play an active role in tumour defence by themselves (160, 161). Even though cytotoxic potential of CD4 T cells is still controversial and not studied in the tumour context, there are seminal studies that confirm the cytotoxic capabilities of these cells in humans with chronic infections (160) and advanced age (161).

Better stratification of PCa patients is an urgent unmet need that would facilitate earlier intervention of aggressive, fast growing disease and avoidance of overtreatment for slow growing, latent disease. There has been significant progress in gene expression approaches to prostate cancer prognostication (162). However, there has been little advancement in protein-based approaches, even though dysregulated protein levels are more directly linked with a perturbed phenotype. My data suggest that the addition of stromal CD4 effector T cells immune cell density of intermediate and high-risk patients can improve the current algorithms of nodal spread prediction (Figure 9). Even though the quantitative mIF platform that we used is not currently used in the clinical setting, there was good concordance with dual FoxP3 and CD4 IHC (Figure 13). The main issue we discovered is interpreting this stromal immune signature on the prostate biopsy, due to close proximity between normal and malignant glands. This could potentially be addressed by radiology-guided sampling of the index lesion only. Prior to suggesting its use in the everyday clinical practice, external validation in larger prospective cohorts is necessary.

Distinct genomic alterations can shape the PCa immune microenvironment (22, 23). For example, immune cell composition of prostate cancer genetically engineered (GEMM) animal models was driven by the loss of the tumour suppressive gene *PTEN*, alone or in combination with other immunosuppresses at least partly due to different chemokine secretion (22). Therefore, I examined the association of common PCa genetic alterations with infiltrating immune cells. I stained the discovery cohort with ERG and PTEN IHC as surrogates for *TMPRSS2/ERG* fusion and *PTEN* loss respectively (Figure 11), and reassuringly

found the incidence of those alterations in agreement with the literature, reinforcing the generalisability of this patient cohort (Table 17). My hypothesis was that primary prostate tumours with absence of ERG gene translocation, presence of PTEN inactivation and high Ki67 would be associated with nodal metastasis. However, contrary to previous studies (25, 66) there was no association between immune cell densities and those features (Table 18-20). It is noteworthy that these previous studies included mixed patient cohorts with varying treatments (25, 66). Our study included only high-risk European PCa patients with localised disease, which may inherently have a rather homogeneous genetic background.

Prostate cancer is rather heterogeneous, comprising of a continuum of lower-risk, higher-risk and mCRPC patients (7). Our data do not contain androgen deprived or metastatic samples and are thus not applicable to mCRPC prostate cancer, which may have a very different immune microenvironment. I aimed to explore the presence of stromal CD4 effector T cells (CD4+FoxP3-) in a lower risk PCa cohort in a pilot experiment. Interestingly, lower-risk patients has significantly less infiltration of CD4 effector T cells compared to the discovery higher risk cohort (Figure 14A). It is possible that higher risk patients may have baseline levels of increased inflammation, contributing to oxidative stress mediated tumourigenesis and accelerated progression (24). Furthermore, there was no association with relapse free survival (Figure 14B), contrary to our findings in higher risk patients (Figure 10). This suggests a potentially different role of CD4 effector T cells in different stages of PCa progression and further work is needed in order to gain a better understanding.

The data collected so far do not address the function of infiltrating CD4 effector T cells or the impact they may have on the prostate tissue as this will require a more thorough phenotypic analysis of the lymphocytes. This could be ideally elucidated with single cell gene expression profiling of purified human infiltrating CD4 T cells that could reveal biologically relevant CD4 T cells subpopulations. While a basic understanding of the composition and phenotype of tumour immune microenvironment can only be derived from human tumours, there is a need to directly investigate mechanisms and interactions. For this, either humanised PCa or GEMM animal models could be used for studying the

impact of specific CD4 T cell subset (or other immune cells of the innate and adaptive immune system), to determine the contribution of such cells to PCa progression. Even though these studies were not feasible during the limited time of my PhD, they could be followed up in the future.

Summarising, our data associate stromal CD4 effector T cell infiltration with lymph node metastasis in PCa for the first time. Their specific localisation at the peritumoural border suggests that CD4 effector T cells within the direct vicinity of cancer cells could perform important biological functions, either by facilitating anti-tumour function of other cytotoxic cells or by directly lysing tumour cells themselves. While this is a reasonable hypothesis based on correlative observations, insights that are more mechanistic are necessary. Previous studies have highlighted the importance of functional orientation of different CD4 T cell immune cell subsets, with Th1 orientated CD4 T effector T cells collaborating with CD8 cytotoxic T cells and resulting in a better patient prognosis in colorectal cancer (163). Furthermore, the expression of specific chemokines and adhesion molecules were found to be critical for high densities of oligoclonal CD8 T cell subsets in colorectal cancer (164) and melanoma (165). Based on our results and those previous studies we next performed a targeted gene expression assay of immuno-oncology markers in order to explain the differences observed in immune cell infiltration between LN+ and LN- PCa patients.

Chapter 4 Phenotyping of prostate cancer using a targeted gene expression panel

In Chapter 3 of this thesis, I presented evidence that, in intermediate to high-risk PCa patients with regional lymph node metastasis, there was decreased infiltration of the tumour-stroma interface by CD4 effector T cells.

Intraepithelial CD8 effector T cells were also decreased and there was positive correlation between CD4 effector, CD8 effector and M1-like macrophages within tumour epithelium and stroma. These findings suggested a possible interaction between tumour and those immune cell subtypes in LN- patients in order to orchestrate an anti-tumour response which was absent in LN+ patients. The development of an effective anti-tumour immune response depends on the coordinated interactions of immunocompetent cells (e.g. CD8 cytotoxic and Th1 polarised CD4 helper T cells), whose spatial distributions are at least partly regulated by chemokines and adhesion molecules (38, 166).

I hypothesised that LN+ patients would have decreased tumour and stromal secreted cytokines (CXCL9 and CXCL10) and adhesion molecules (ICAM, VCAM) which contribute to recruitment of effector T cells (39, 166). I also expected a decreased Th-1 polarisation of CD4 effector T cells resulting in decreased cytotoxicity (granzymes, perforin) and tumour cell killing (39, 157) in LN+ cases. In order to confirm this hypothesis and explain the differences in immune cell infiltration we performed a targeted gene expression profiling of the tumours with a panel of immuno-oncology markers comparing PCa patients with and without lymph node metastasis.

Forty-eight diagnostic biopsy cores from patients within the discovery TMA cohort were selected for gene expression analysis, including 24 without LN metastasis and 24 with LN metastasis respectively. The patients had a median time interval of 113 days (81-151 range) between diagnosis and surgery. Each sample was macro-dissected to obtain tumour rich tissue with >70% tumour and <10% tumour necrosis. This methodology was selected because it was ideal for minimal tissue input (down to 6 mm² area) which is crucial for limited PCa biopsy material, and has also been proven to reproducibly detect low expressing genes which is essential for the occasionally sparse immune cell infiltrates in PCa FFPE tissue (167, 168).

The targets of HTG Immuno-Oncology Panel are shown in Appendix Table 1 and include immune related genes as well as genes related to common cancer signalling pathways. These include genes involved in apoptosis, cell cycle and adhesion, DNA repair, immunosuppressive pathways as well as cytokines and cytokine receptors, immunophenotyping and MHC and associated receptors. One probe was designed for each gene. A total of 1,410 probes were used, including 12 housekeeper control genes (DDX5, ATP5F1, EEF1G, NCL, OAZ1, PPIA, RPL38, RPL6, RPS7, SLC25A3, SOD1, YWHAZ), 4 positive process controls and 4 negative process controls. In addition, negative probes had sequences of non-human genes (Arabidopsis), while positive probes had sequences of targets that were mixed with all the probe mix (so these probes will hybridize with their targets during the hybridisation step).

Forty-eight samples were sent for sequencing. One of them was omitted from the analysis due to tissue damage, leaving forty-seven samples processed and successfully sequenced according to company's standards.

4.1 Post-sequencing quality control

Post-sequencing quality control metrics (QC0, QC1 and QC2) were performed using the HTG reveal software in order to detect three different sample failures (Figure 16). QC0 detected degraded RNA or poor quality RNA samples by assessing the percentage of overall reads being allocated to the positive process control for each sample; $\geq 40\%$ was considered as a failure. QC1 detected samples with insufficient read depth; read depth ≤ 1.5 million / sample was considered a failure. QC2 detected samples with minimal expression variability, which was determined by the relative standard deviation (RSD) of reads allocated to each probe within a sample; $RSD \leq 0.1$ was considered a failure. Five samples failed QC2 metric and were not included in further analysis. Failure of QC2 is commonly attributed to failure of the S1 digestion step of the sample processing according to the company's protocols.

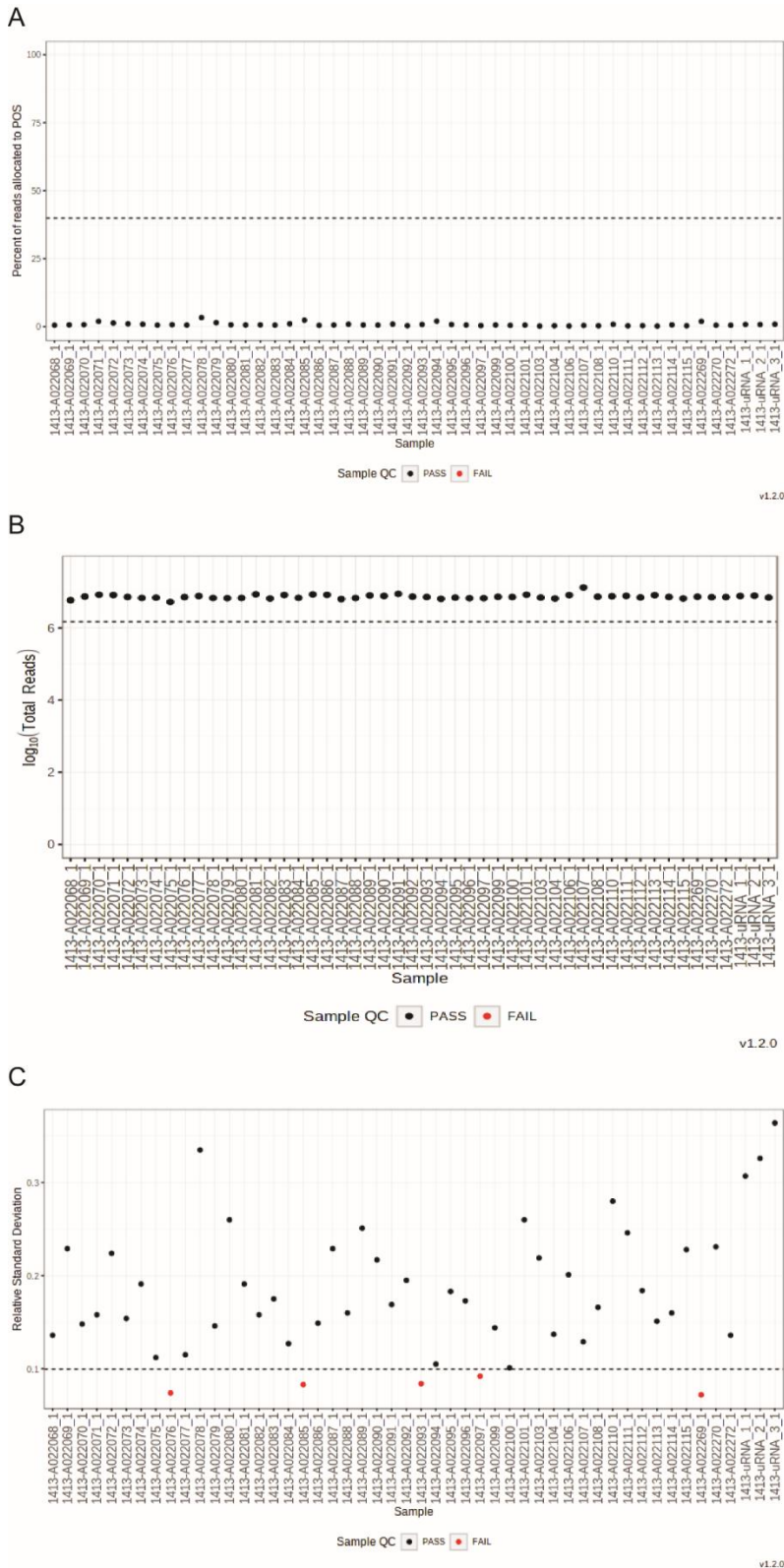


Figure 16 Post sequencing quality controls

Forty-seven samples were processed and underwent post-sequencing quality control metrics (QC0, QC1 and QC2) using the HTG reveal software. (A) QC0 plot represented the RNA quality by assessing the percentage of overall reads being allocated to the positive control for each sample. (B) QC1 plot represented the read depth. (C) QC2 plot represented the expression variability of each sample, which was determined by the relative standard deviation (RSD) of reads allocated to each probe within a sample. Five samples highlighted in red failed QC2 metric and were not included in further analysis.

4.2 Extracellular matrix components genes are upregulated in prostate cancer patients with nodal metastasis

We used the HTG EdgeSeq Immuno-Oncology panel to compare gene expression between primary prostate tumours from patients with and without pathologically confirmed pelvic lymph node metastasis (LN+ and LN- respectively). This was calculated using DESeq2 test with an adjusted p value less than 0.05 and a log fold change value of greater than 1.5. Nineteen genes were differentially expressed, 15 were upregulated and four were downregulated in LN+ cases, presented in Table 22.

My initial hypothesis was that patients with lymph node metastasis will have reduced expression of chemotactic and adhesion factors, resulting in the decreased infiltration of CD4 effector T cells that was observed. However, even though an extensive list of adhesion molecules, cytokines and cytokine receptors was included in our panel, there were no differences between patient groups. An interesting finding though was that the highest upregulated genes in LN+ cases were extracellular matrix (ECM) core proteins, namely collagen type I and III and fibronectin 1 (FN1), as well as the cancer associated fibroblast (CAF) proteins, fibroblast activation protein alpha (FAPa) and Chemokine ligand 14 (CXCL14) (Table 22).

ECM remodelling is one of the cancer hallmarks and abnormal, typically dense or fibrotic ECM affects cancer progression and metastasis, generating a tumour promoting tumour microenvironment (169-172). Tumour associated fibrosis is a well-established regulator of tumour progression but may also be a critical regulator of immune surveillance (173-176). Following on this growing body of evidence, I firstly aimed to address whether tumoural ECM components were increased at the protein level prostate cancer patients with nodal disease.

Gene	Full gene name	Fold Change LN + vs LN -	Adjusted p value
Upregulated			
CXCL14	C-X-C Motif Chemokine Ligand 14	2.56	2.50E-05
ISG15	Interferon-stimulated gene 15	2.14	4.20E-04
IFI6	Interferon Alpha Inducible Protein 6	1.85	0.0251
FAPa	Fibroblast Activation Protein Alpha	1.83	2.50E-05
LYZ	Lysozyme	1.8	0.0156
COL1A1	Collagen Type I Alpha 1 Chain	1.73	0.0156
FCGR3A_3B	Fc Fragment Of IgG Receptor IIIa	1.7	4.20E-04
FN1	Fibronectin 1	1.68	0.0392
OAS3	2'-5'-Oligoadenylate Synthetase 3	1.62	0.0029
COL3A1	Collagen Type III Alpha 1 Chain	1.6	0.0251
LAPTM5	Lysosomal Protein Transmembrane 5	1.58	0.0156
HLA-DRA	Major Histocompatibility Complex, Class II, DR Alpha	1.54	0.0405
FCGR2A_2C	Fc Fragment Of IgG Receptor IIa	1.53	0.0023
IGFBP3	Insulin growth factor binding pr 3	1.52	0.0425
TYROBP	TYRO Protein Tyrosine Kinase Binding Protein	1.51	0.0092
Downregulated			
PAGE3	Prostate-Associated Gene 3 Protein	-1.69	0.0452
CD244	CD244 Molecule	-1.68	0.0481
RND2	Rho Family GTPase 2	-1.65	0.0251
TCL1B	Activation Induced Cytidine Deaminase	-1.55	0.0478

Table 22 Differentially expressed genes in patients with vs without lymph node metastasis (LN+ vs LN-).

HTG RNA sequencing results showed 15 upregulated and 4 downregulated genes in patients with LN metastasis. Extracellular matrix genes (collagen type I & II and fibronectin 1) are highlighted in grey. DESeq2 test with fold change >1.5, adjusted p value < 0.05 used for statistical analysis

4.3 Extracellular matrix components are increased and disorganised in prostate cancer patients with lymph node metastasis

The gene expression analysis which showed increased ECM components was performed on the diagnostic biopsies of a fraction of patients (47 patients) included in the discovery TMA (94 patients). I then investigated the abundance of ECM components using the discovery TMA to study more cases with good tissue availability. More importantly, investigating the TMA cores would be more informative compared to diagnostic prostatic biopsy materials because needle biopsies tend to comprise of intermixed benign and malignant components in close proximity with associated stroma. Even though the presence of benign

glands can never be completely avoided, it was significantly reduced in the TMA due to sampling from the index lesion.

I used IHC for the detection of ECM components identified in the gene expression assay, specifically collagen I (Figure 17A), collagen III (Figure 17D) and FN 1 (Figure 17E). Even though FN1 and collagen III are primarily ECM components, they were also expressed in the tumour as well as in stromal cells, morphologically compatible with fibroblasts. Collagen I was restricted to stroma and in order to avoid confounding from the relative epithelial/stromal ratio in each core I quantified the presence of collagen I within the stromal compartment only, shown in Figure 17A-C. HALO image analysis was used to set up a tissue classifier (epithelium vs stroma) based on the morphological characteristics and to quantify the percentage of positively stained cells within the each area. Lastly, the same TMA was also investigated using multiphoton imaging and second harmonic generation (SHG) (performed and analysed by Ewan McGhee, Beatson Institute).

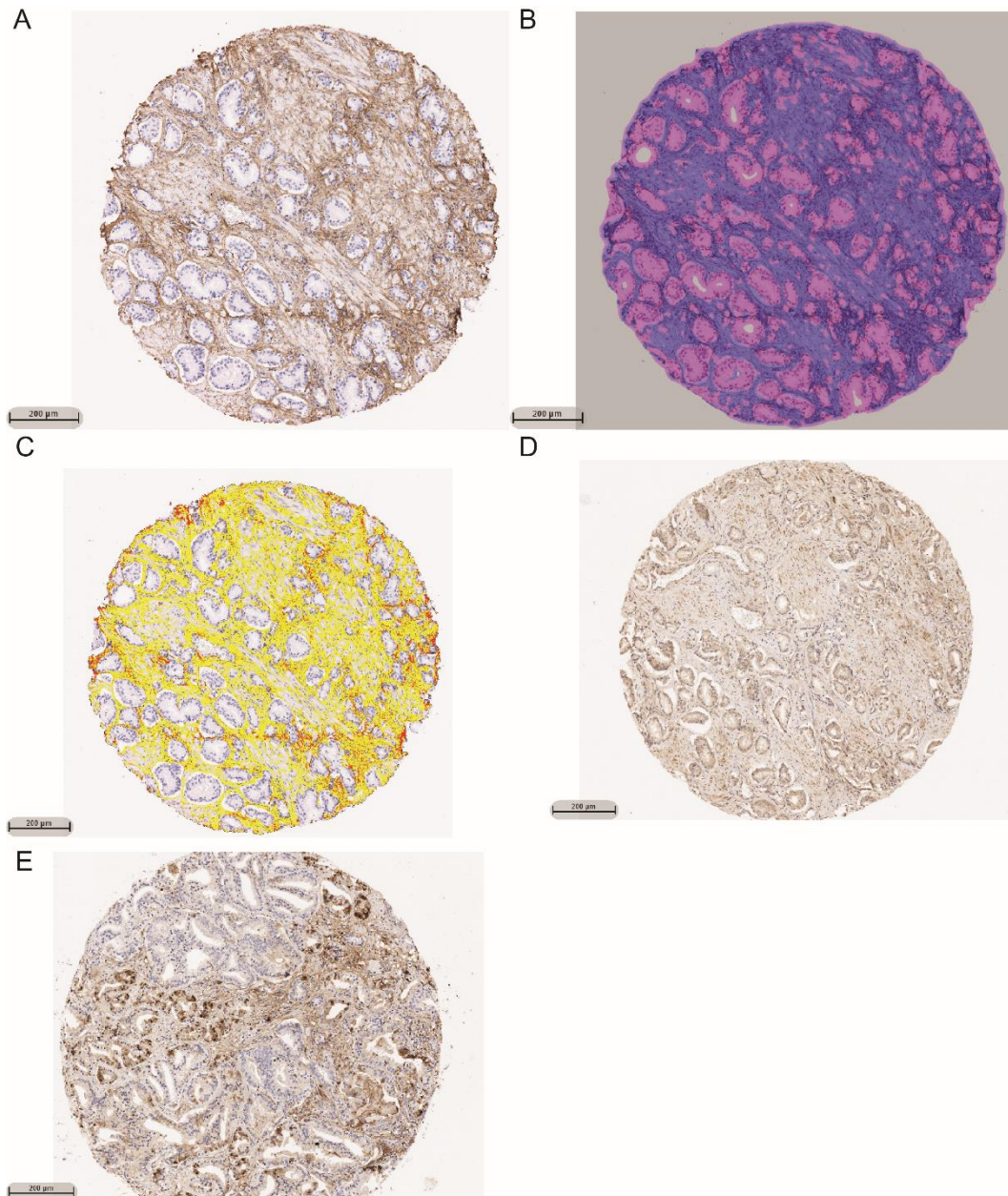


Figure 17 Extracellular matrix components staining

(A-C) Analysis for collagen I staining: (A) Representative image of collagen I staining. (B) Tissue classifier using HALO image analysis, epithelium annotated in magenta, stroma in blue. (C) Positive staining quantification shown in yellow, orange and red according to the staining intensity (low, medium and high respectively). All images are taken from the same core. (D) Representative images of collagen III and (E) fibronectin 1 staining. Scale bar=200µm.

The collagen score analysis derived from the mean decay distance of the SHG signal showed that collagen I was significantly associated with the presence of lymph node spread, 17.72 (11.52-34 IQR) in LN+ vs 13.43 (9.14-21.46 IQR) in LN-, $p=0.0003$ (Figure 18A). The percentage of collagen I positive staining within the stroma did not show any statistically significant differences within the two groups, 32.92 (29.89-37.95 95%CI) in LN+ vs 29.87 (21.8-37.49 95%CI) in LN-,

$p=0.189$ (Figure 18B). Tumours often display a fibrotic stroma with increased collagen deposition and altered organisation, such as increased collagen density and collagen fibre elongation (172, 177). While SHG collagen I density score in LN+ patients increased, the overall collagen abundance did not differ, eluding to a stroma with increased cross-linking and elongated fibres. This is reinforced by the fact that both analyses were performed on the same slide. The percentage of collagen III positive staining within epithelial and stromal compartments was significantly increased in LN+ 22.28 (15.93-23.79 95%CI) vs 16.11 (12.65-17.37 95%CI), $p=0.0056$ (Figure 18C). Lastly, the percentage of FN1 positive staining was significantly increased in LN+ patients, 26.36 (20.32-36.94 95%CI) vs 17.93 (10.83-24.23 95%CI), $p=0.0096$ (Figure 18D).

These results suggested that the generation of fibrillar collagen I, collagen III and FN1 are associated with PCa lymph node spread and as a direct consequence, disease progression. Our data revealed reduced migration of effector T cells to the tumour stromal compartment in LN+ patients. The relatively reduced infiltration by immune subpopulations in the progressing tumours can be mediated by lack of migratory cues, including chemokines and TCR stimulation (173). The gene expression analysis of primary PCa tumours investigated potential mediators for recruiting immune cells extensively but no difference was detected between LN+ and LN- patients. However, core ECM molecules were increased at both mRNA and protein levels in LN+ patients, thus supporting the importance of enhanced ECM deposition and remodelling in shaping the TME including immune infiltrates. The reduced immune cell infiltration of LN+ tumours is more likely associated with dense ECM, which can function as a physical barrier (175, 176, 178).

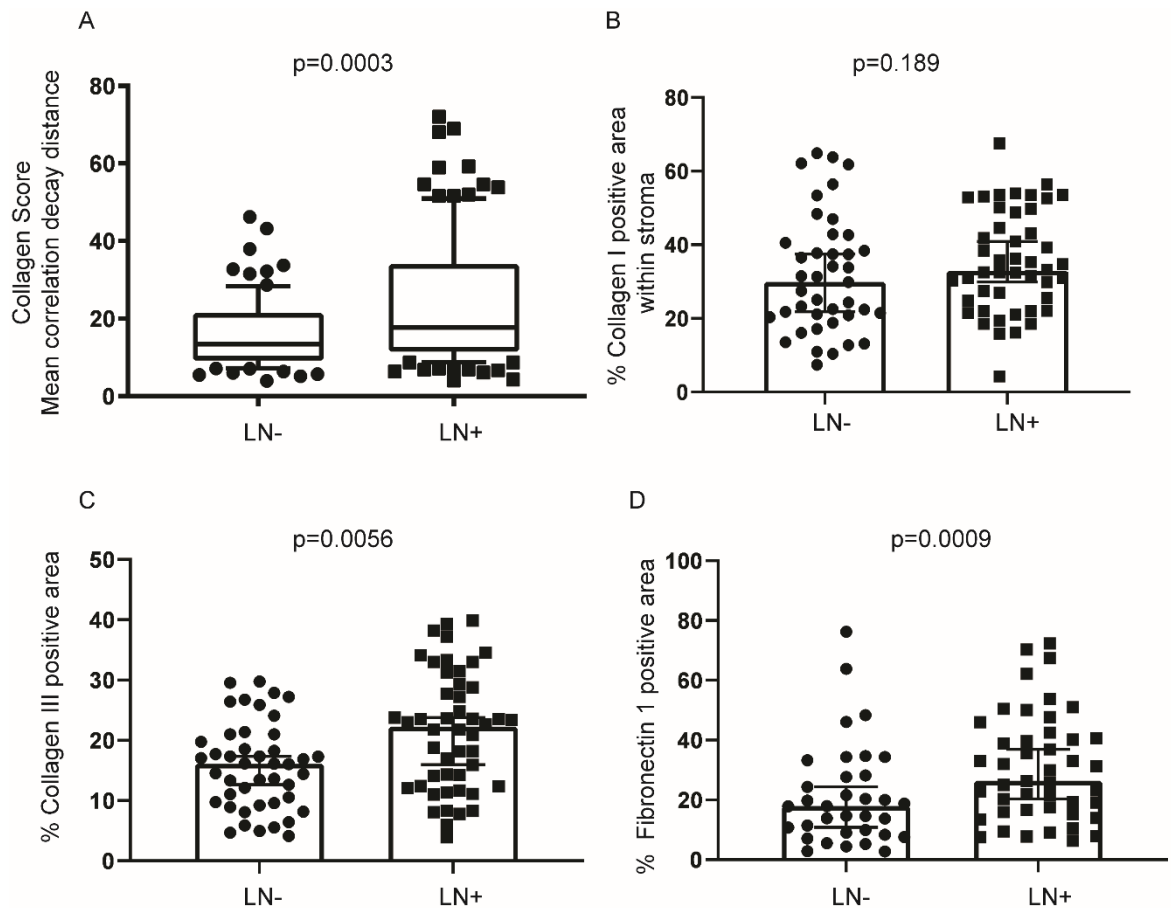


Figure 18 Enhanced collagen I, collagen III and fibronectin 1 in patients with lymph node metastasis

(A) Mean decay distance (collagen score) of the second harmonic generation (SHG) signal emitted by fibrillar collagen I. Mean decay distance is represented by boxplots showing the second and third quartile of the data with the whiskers indicating the maximum and minimum data points for LN- (n=89) and LN+(n=113) cores. Outliers are shown by individual data points. (B) Percentage (%) of stroma positive for collagen I staining is presented as median with 95% CI in LN- (n=41) and LN+ (n=46) patients. (C) Percentage (%) of collagen III staining is presented as median with 95% CI in LN- (n=44) and LN+ (n=47) patients. (D) Percentage (%) of fibronectin1 staining is presented as median with 95% CI in LN- (n=34) and LN+ (n=45) patients. Two-tailed Mann-Whitney test was used for all statistical comparisons presented in this figure.

4.4 Exploratory investigation of cancer associated fibroblast markers (CXCL14 and FAP α) in prostate cancer patients with nodal metastasis

The targeted gene expression analysis identified two more upregulated genes in patients with lymph node metastasis that were of interest, namely Chemokine ligand 14 (CXCL14) and Fibroblast Activation Protein alpha (FAP α). Cancer associated fibroblasts (CAFs) are the fibroblasts found in the stroma of human

cancers (169). CAFs are activated compared to their quiescent counterparts (α SMA⁺, FAP α ⁺) and have significant heterogeneity in marker expression leading to different CAF phenotypes (169). They also differ from normal fibroblasts in their increased collagen and ECM protein production and secretion of cytokines (CXCL14) (169, 179-181). Depletion of FAP⁺ CAFs in a PDAC mouse model decreased tumour growth and fibrosis and increased T-effector cell infiltration in a CXCL12/CXCR4 dependent manner (182). CXCL14, a pleiotropic cytokine, is expressed by CAFs and promotes epithelial to mesenchymal transition (EMT) and metastasis (183). I therefore explored whether LN⁺ patients who had decreased effector T cell infiltration were associated with increased FAP α ⁺ CAFs and CXCL14 expression.

CXCL14 IHC had been previously attempted in our Histology laboratory but no CXCL14 antibody tested showed specific staining (personal communication with Mr Colin Nixon, Beatson Institute). Therefore, I assessed RNA expression of CXCL14 using in situ hybridisation (ISH) on the discovery TMA. FAP α expression was assessed by IHC on another section from the discovery TMA. CXCL14 expression was mainly localised in the stroma, from cells morphologically consistent with fibroblasts (Figure 19A, arrows). In addition, scattered cells morphologically consistent with benign basal epithelial cells were also positive (Figure 19B, arrows). CXCL14 expression was quantified using an ISH probe copies counting module in HALO image analysis. FAP α expression was confined to stroma areas only (Figure 19C) and was quantified as percentage area positive within stroma using HALO image analysis as previously described.

Despite an apparent trend for higher probe copies in node positive cases, the observed average CXCL14 probe copies (per μm^2) were not significantly different between lymph node positive (61.33×10^5 , 24.4×10^5 - 129×10^5 95%CI) and lymph node negative patients (34.75×10^5 , 22.05×10^5 - 55.6×10^5 95%CI, $p=0.3853$), Figure 19D. However, when the tumours were dichotomised into high and low expressers of CXCL14 (above 400 probe copies $\times 10^5/\mu\text{m}^2$), there were 11 high expressers, 1 LN⁻ and 10 LN⁺ ($p<0.0001$, Fisher's exact test). FAP α expression was also not statistically different between lymph node positive (0.08, 0.04-0.12 95%CI) and lymph node negative group (0.04, 0.02- 0.04 95%CI, $p=0.06$), presented in Figure 19E.

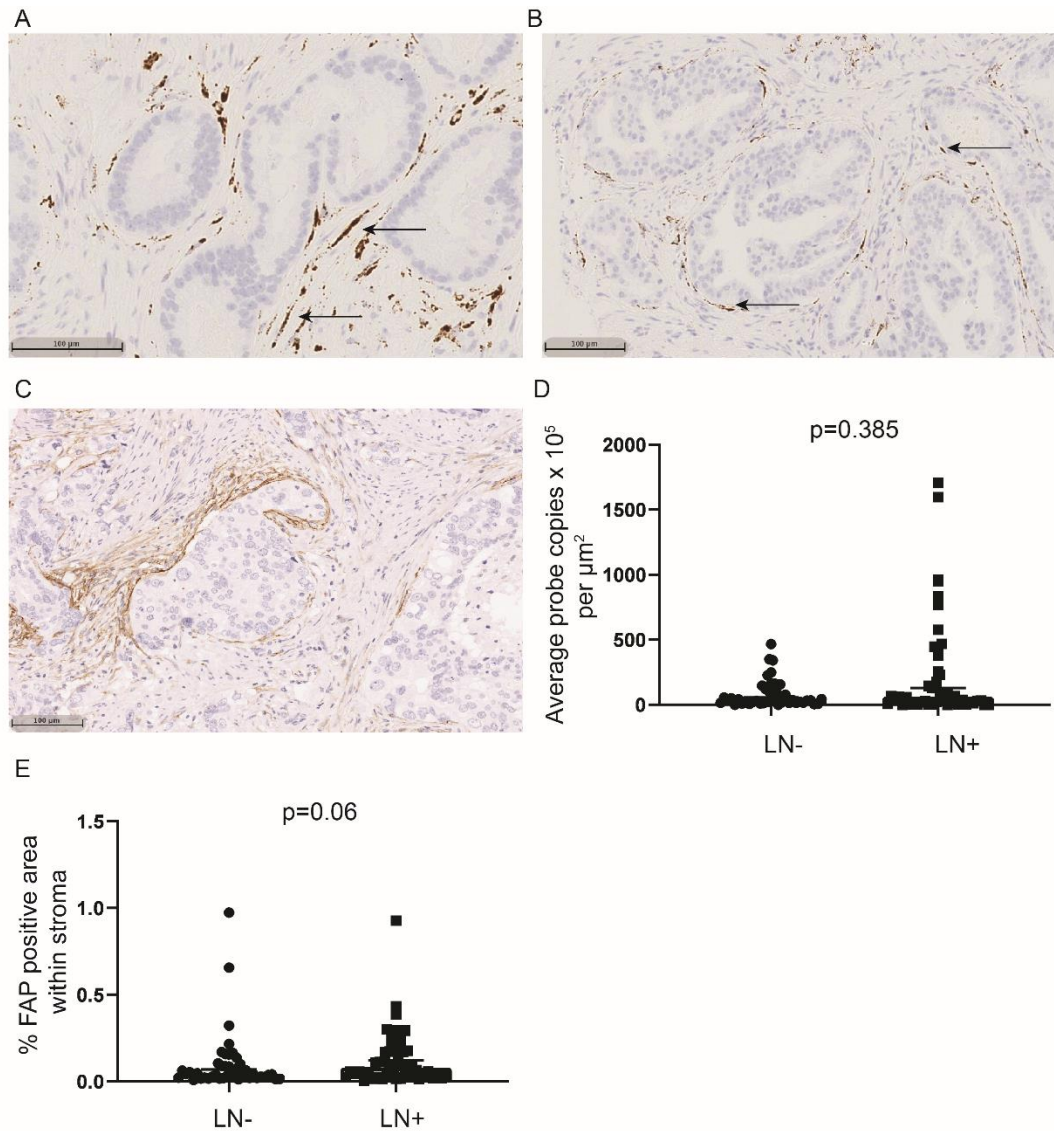


Figure 19 CXCL14 and FAPa expression in prostate cancer patients with nodal metastasis (A-B) Representative images of CXCL14 ISH (Scale bar = 100 μm). (C) Representative image of FAPa staining (Scale bar = 100 μm). (D) Average CXCL14 probe copies per μm² presented as median with 95% CI in LN- (n=42) and LN+ (n=48) patients. (E) Percentage (%) of stroma positive for FAPa staining is presented as median with 95% CI in LN- (n=44) and LN+ (n=50) patients. Two-tailed Mann-Whitney test was used for all statistical comparisons.

4.5 Concluding summary

Targeted transcriptomic analysis was performed to study potential genes that may mechanistically mediate the TME with the observation of reduced immune subpopulation infiltrates in patients with regional lymph node metastasis (LN+). Although this methodology carries obvious disadvantages, such as a limited probe panel and the use of a single probe per gene missing possible splice variants, the analysis was technically successful (Figure 16) and revealed ECM

changes (rather than chemokine or adhesion molecule imbalance) as important factors in developing nodal disease (Table 22). Increased ECM deposition and reorganisation was confirmed in LN+ patients using IHC and multi photon microscopy (Figure 18). I examined different tissue types (prostate biopsy cores and TMA from index lesion) with different methodologies (gene expression, IHC, SGH). Overall, my data point to a more disorganised and fibrotic stroma in LN+ patients.

CAFs are increasingly recognised as a diverse population with variable marker expression, such as α SMA and FAP α (169). Our gene expression analysis showed upregulation of FAP α gene in tumours associated with LN+ disease, which was however not confirmed at the protein level by IHC (Figure 19E). The inconsistency in these results could be attributed to the heterogeneity of CAF FAP α expression in different tissue areas that are detected using different methodologies. It is therefore difficult to draw definite a conclusion from these data. CXCL14 was the highest upregulated gene in LN+ patients (Table 22), and LN + patients were the highest expressers of CXCL14 ($p < 0.0001$, Fisher's exact test). Interestingly, it was expressed by both stromal (Figure 19A) and morphologically benign epithelial cells (Figure 19B), highlighting the importance of spatial context and cellular origin in gene expression. I attempted scoring of CXCL14 expression in epithelial and stromal compartment separately but due to staining at the interface between epithelium and stroma (basal cells) quantification of CXCL14 in the appropriate tissue compartment was not satisfactory. Even though the tumours with highest expression of CXCL14 were LN+, it was impossible to be certain whether this was due to stromal or benign epithelial expression and was not investigated further.

All epithelial tumours, including PCa, are a complex of malignant epithelial cells organised within a specialised microenvironment, referred to as tumour stroma or TME. TME includes CAFs, endothelial cells, immune cells and ECM (169). The ECM is an organised structure of extracellular proteins, such as collagens, glycoproteins (i.e. fibronectin 1) and proteoglycans (169, 177). The ECM serves as structural scaffold that provides tissue support but also provides biomechanical and biochemical signals that are major regulators of cell proliferation, survival, migration and invasion (172, 173). In the cancer context,

it is well established that tumour stroma becomes enriched with ECM proteins such as collagen type I and fibronectin (169, 171-173, 177). Besides these quantitative changes, qualitative modifications also take place, such as increased collagen cross-linking and orientation leading to ECM stiffening (170, 172, 173, 177). These structural ECM alterations have direct impact on tumour cell function and progression.

A plethora of studies demonstrate that deregulation of ECM is more than just a secondary outcome but instead plays a causative role in cancer pathogenesis and progression. Increased stromal collagen in mouse mammary tissue significantly increased tumour formation, invasiveness and metastasis (171). Furthermore, in a breast cancer mouse model, collagen crosslinking induction caused ECM stiffening, promoted focal adhesion kinases, enhanced PI3 kinase activity and promoted invasion (170). Collagen crosslinking is almost exclusively mediated by the lysyl oxydase (LOX) enzyme, which post-translationally modifies collagens and elastin in the ECM (149). Knockdown of LOX expression or suppression of its function by a blocking antibody reduced *in vivo* tumour invasion and metastasis of PDAC (149). However, it is noteworthy that abrogating stromal fibroblasts from PDAC tumours which reduced ECM stiffening actually promoted tumour progression (184). These data suggest that interaction between ECM and cancer cells is complex and biological outcome may be dependent on specific stromal cell components, different cancer type and heterogeneity of genetic background.

Apart from the intrinsic tumour cell properties, one of the cancer hallmarks is avoidance of immune destruction (33) and ECM can modulate critical immune functions, such as immune cell exclusion from tumour cells (174-176). ECM density and orientation have previously been shown to dictate T cell migration in *ex vivo* human lung and ovarian cancer tissue, with poor T cell infiltration and contact with tumour cells in dense ECM areas (174, 176). Furthermore, high collagen density functioned as a physical barrier of T cell infiltration in PDAC and was able to completely abolish chemokine-guided movement (175). These studies suggest that when chemokine responsive migrating T cells come in contact with tumour ECM, the actual recruitment of the immune cells are influenced by the structural properties of local ECM.

Tumour destruction by the immune system is a key physiological mechanism that suppresses local tumour progression and prevents tumour spread. This relies on the ability of cytotoxic immune cells to encounter the malignant cells. For example, CD8 cytotoxic T cells need to recognise foreign antigens displayed on transformed cells and thereafter induce their destruction through T-cell-mediated cell death (39, 42). Our data suggested that decreased immune cell infiltration of CD8 and CD4 effector T cells in particular could be associated with enhanced and abnormal ECM deposition in prostate cancer patients with lymph node metastasis, indicating that limiting T cell infiltration is a potential immune evasion mechanism. My current working model is that, in LN+ PCa patients, dense ECM prevents CD4 and CD8 T cells interacting with antigen presenting cells and tumour cells, contributing to the failure of an effective anti-tumour response.

Altogether, my data propose that the PCa-associated ECM has an overall negative influence on resident T cells, limiting their migration within the stroma. However, additional work needs to be done in order to advance our understanding of the mechanistic aspect of this event. The first experimental steps would be staining the PCa discovery TMA with Picrosirius red (PSR) special stain and LOX IHC. The former can be analysed under orthogonal and polarising light (170) in order to strengthen the finding of increased ECM density in LN+ patients. The latter could indicate a potential mechanism for this event. Developing a mIF panel that incorporates CD4, CD8, collagen I, collagen III and fibronectin as key markers would also be valuable in dissecting the associations between those different TME components.

My data showed that epithelial prostate cancer cells as well as stromal cells morphologically compatible with CAFs are expressing collagen III and FN 1. Both tumour cells and stromal cells have been shown to contribute to the tumour ECM production (185). The relative contribution to abnormal ECM development of epithelial and stromal cells needs to be determined. Furthermore, it is essential to decipher at which time points of tumourigenesis and progression that ECM stiffening occurs, whether at tumour initiation or later when disease disseminates. Analysis of ECM components in normal prostate and low-risk prostate cancer samples would help answer these questions.

Apart from the valuable information derived from human samples, further *in vitro* and *in vivo* work could advance our molecular understanding of ECM contribution in prostate cancer initiation and progression. Firstly, tumour derived or peripheral blood monocytes from PCa patients could be cultured in high and low density matrices in order to assess the effect on migration and proliferation of CD4 as well CD8 T cells according to different chemokine stimuli. Importantly, single cell transcriptomic analysis of those differently cultured T cells could elucidate the downstream transcriptional regulators of differing ECM stiffness. Finally, it is essential to determine whether dense ECM and decreased T cell infiltration is a correlative phenotype or a causative factor driving this event. To answer this, GEMM studies can be performed, crossing a mouse prostate cancer model with collagen I/III null mice in order to see the effect on immune cell infiltration and lymph node spread. Finally, this could be combined with specific immune cell depletion (such as CD4 or CD8 T cell depletion) in order to pin down the exact immune cell population driving this event.

Lastly, our data are in agreement with the general characterisation of PCa as an 'immune cold' tumour, but make an important further distinction of an immune-exclusion phenotype (35). This carries important clinical implications as the efficacy of immunotherapies in PCa have so far been unsuccessful (186, 187), reinforcing the perception that PCa is a poorly immunogenic tumour. Careful selection of PCa patients for immunotherapy in combination with stroma-modifying treatments targeting factors, such as LOX inhibitors (149), could potentially improve therapeutic outcomes. ECM density could be one of the causes of resistance to immunotherapy for PCa patients and therefore warrants further investigation.

Chapter 5 B7-H3 and prostate cancer

Despite significant advances in other cancer types, immunotherapy with immune checkpoint inhibitors against CTL4, PD-L1 and PD-1 have so far been disappointing in PCa (188). There is therefore an urgent need for discovery of novel immune checkpoints that may be at play in PCa. B7-H3 is a newly discovered member of the B7 family of checkpoint molecules, with aberrant expression observed in multiple solid malignancies, including prostate cancer (107, 142). Previous studies have shown that prostate cancer patients with high B7-H3 expression were more likely to have adverse pathologic features, such as extraprostatic extension and seminal vesicle invasion (107, 142). Furthermore, B7-H3 intensity was associated with cancer relapse after radical prostatectomy as well as poor survival outcomes (107, 142). I aimed to validate externally those results in the discovery high-risk cohort of prostate cancer patients, with a special focus on the association of B7-H3 with regional lymph node status that has not been thoroughly explored before.

B7-H3 has also been shown to promote tumour invasion and metastatic spread in different tumours (130, 131), including a single study in prostate cancer, in which human PC3 prostate cancer cells were transiently silenced for B7-H3 expression. PC3 cells with suppressed B7-H3 expression showed 50% reduction in migration ($p < 0.001$) and invasion ($p = 0.0005$) *in vitro* while cellular adhesion to fibronectin was impaired by 30% ($p = 0.003$) (127). I built on these observations and investigated the impact of silencing B7-H3 expression in a panel of human prostate cancer cell lines (namely PC3M, LNCaP, C4-2, DU145). Cell growth, apoptosis, migration and invasion were analysed by cell counting, flow cytometry, scratch wound and transwell assays. B7-H3 silencing had no effect on cell growth and apoptosis but showed a significant decrease in migration and invasion. Following that, I also generated stable knock out clones of C4-2 and PC3M cells and successfully replicated data from transient silencing of B7-H3 expression. Finally, I aimed to investigate the transcriptional changes following manipulation of B7-H3 expression in order to explore its potential downstream targets.

5.1 B7-H3 is overexpressed in prostate cancer and associated with worse clinicopathological features

5.1.1 B7-H3 staining of human tissue

B7-H3 staining was performed manually and histoscore was applied according to previous studies (107). The intensity score given was absent [0] for no staining, weak [1] for cytoplasmic staining, moderate [2] for incomplete membranous and cytoplasmic staining and strong [3] for complete, intense membranous staining. Prostatic cancer glands had strong B7-H3 membranous staining (Figure 20A) whilst benign prostatic glands showed mostly weak to moderate cytoplasmic staining (Figure 20B). Occasional inflammatory cells were also positive, particularly in germinal centres of lymph node tissue (Figure 20C), morphologically compatible with lymphocytes and dendritic cells. In primary prostate tissue, no inflammatory or endothelial cell staining was observed. All cases were evaluated by myself (CN) without knowledge of patient information. In addition, more than 10% of the total B7-H3 cases were reviewed by a second urologic pathologist (Jonathan Salmond, NHS Greater Glasgow and Clyde), yielding high interobserver agreement (Figure 20D, $r=0.85$, $p<0.001$, Spearman's correlation). Therefore, the B7-H3 expression histoscore was considered reproducible and easy to implement. The Benign Prostatic Hyperplasia (BPH) TMA as well as the discovery TMA of intermediate and high-risk prostate cancer patients were stained manually for B7-H3 (Figure 20E). Prostate cancer had significantly increased B7-H3 immunoreactivity, Histoscore median value of 183.3 (163.3-197.7 95%CI) compared to BPH with median Histoscore of 70 (63.33-76.67 95%CI), $p<0.0001$.

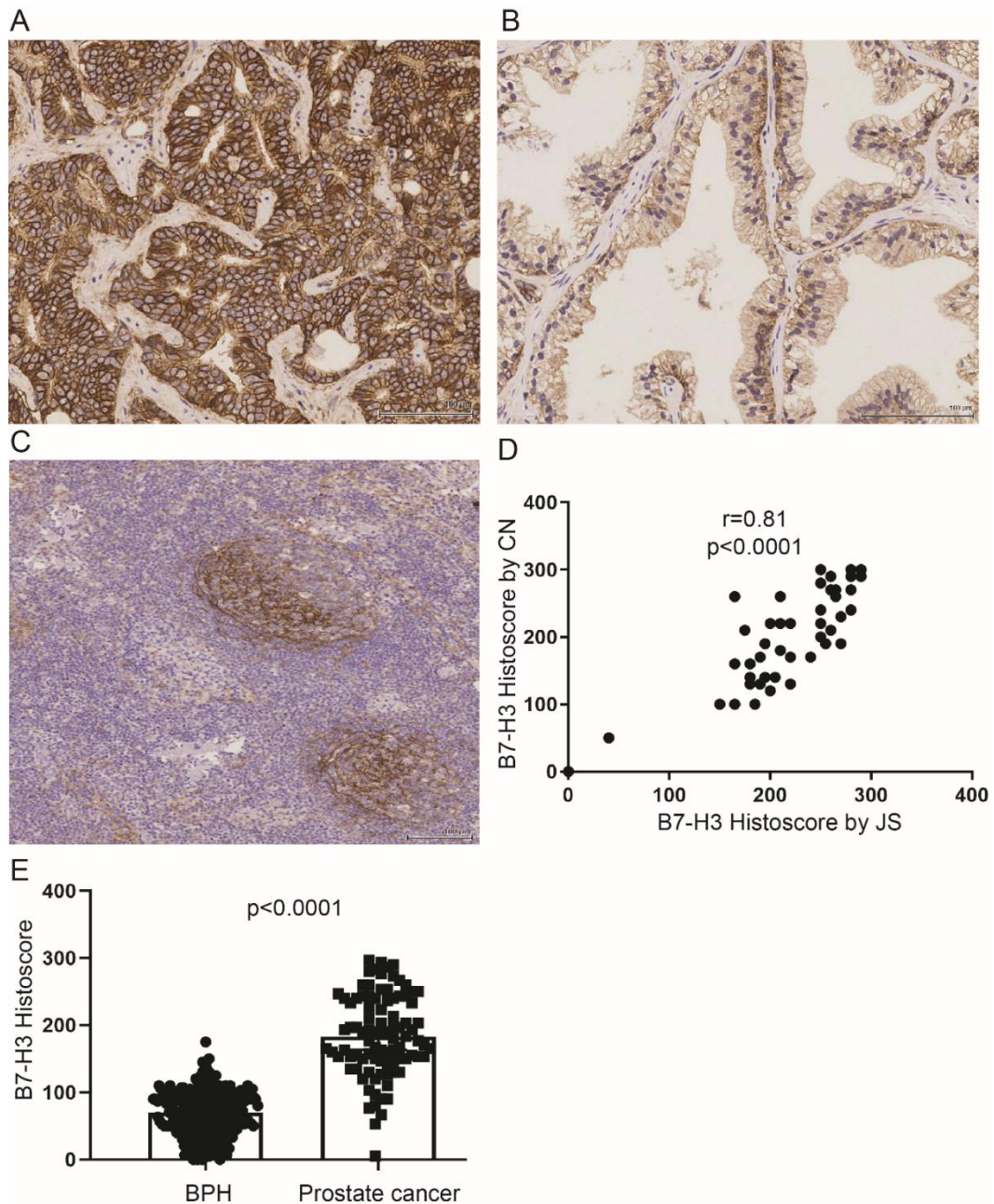


Figure 20 B7-H3 staining of human prostatic tissue and pelvic lymph nodes

(A) Representative image of strong B7-H3 staining in prostate cancer. Histoscore=300. (B) Representative image of weak B7-H3 staining in benign prostatic hyperplasia. Histoscore=100. (C) Representative image of strong B7-H3 staining observed in germinal centres of lymph node tissue. (D) B7-H3 Histoscore values (n=55) provided by two independent pathologists (Chara Ntala & Jonathan Salmond) compared by Spearman's correlation. (E) B7-H3 Histoscore values presented as median with 95% CI in benign prostatic hyperplasia (BPH, n=259) and prostate cancer patients (discovery cohort, n=94). Mann Whitney test used for statistical comparison. Scale bar=100 μ m.

5.1.2 High B7-H3 expression is associated with worse clinicopathological features in intermediate and high risk prostate cancer patients

Among the 94 patients within the discovery cohort, each case was represented by at least two tumour cores with informative B7-H3 staining. Tumours with high expression of B7-H3 were significantly more likely to have lymph node metastasis ($p=0.0006$, Figure 21A), however there was no difference between the number of involved lymph nodes ($p>0.99$, Figure 21B). Interestingly, B7-H3 expression was collectively retained in the regional lymph node metastatic foci compared to the primary tumour ($p=0.49$, Figure 21C-D). There was a lot of variation between cases, with some patients having comparable levels, some reduced and others increased expression of B7-H3 in the metastatic deposit compared to primary cancer (Figure 21C).

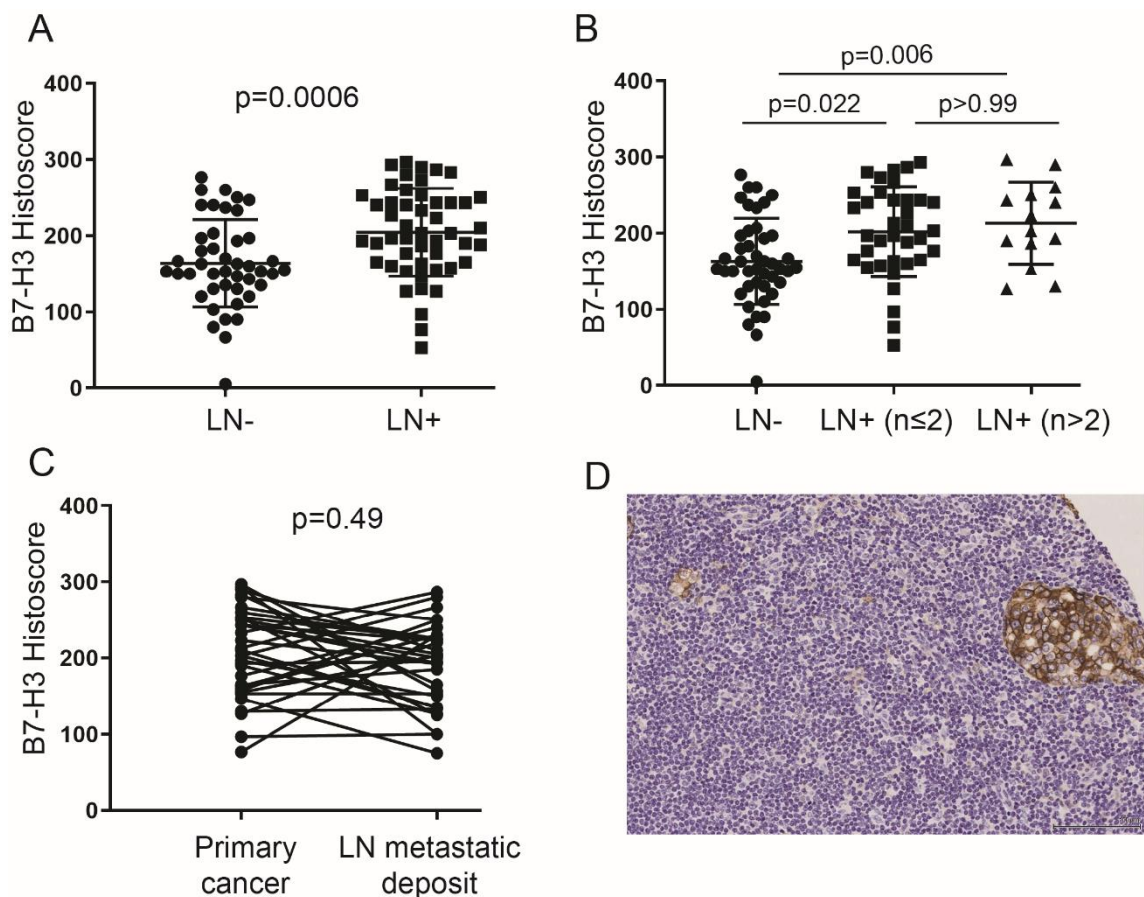


Figure 21 High B7-H3 expression is associated with lymph node metastasis

(A) B7-H3 Histoscore presented as median with 95% CI in patients without (LN-, $n=44$) and with (LN+, $n=50$) lymph node metastasis. Mann Whitney test used for statistical comparison. (B) B7-H3 Histoscore presented as median with 95% CI in LN- ($n=44$), patients with 2 or less positive nodes ($n=36$) and patients with more than 2 positive nodes ($n=14$). Kruskal-Wallis test used for statistical comparison. (C) B7-H3 Histoscore presented as median value in primary prostate cancer tissue and the metastatic deposit of the same patients ($n=35$). Wilcoxon matched-pairs signed rank test

used for statistical comparison. (D) Representative image of strong B7-H3 staining in metastatic deposit. H-score=280. Scale bar=100 μ m.

Furthermore, tumours with increased B7-H3 score were significantly associated with high pT stage ($p < 0.0001$, Figure 22A) and the presence of perineural invasion ($p = 0.044$, Figure 22B), but not Gleason score (Figure 22C). Given the short duration of post-treatment follow up, it is not surprising that there was no association between B7-H3 expression and the development of biochemical recurrence (Figure 22D).

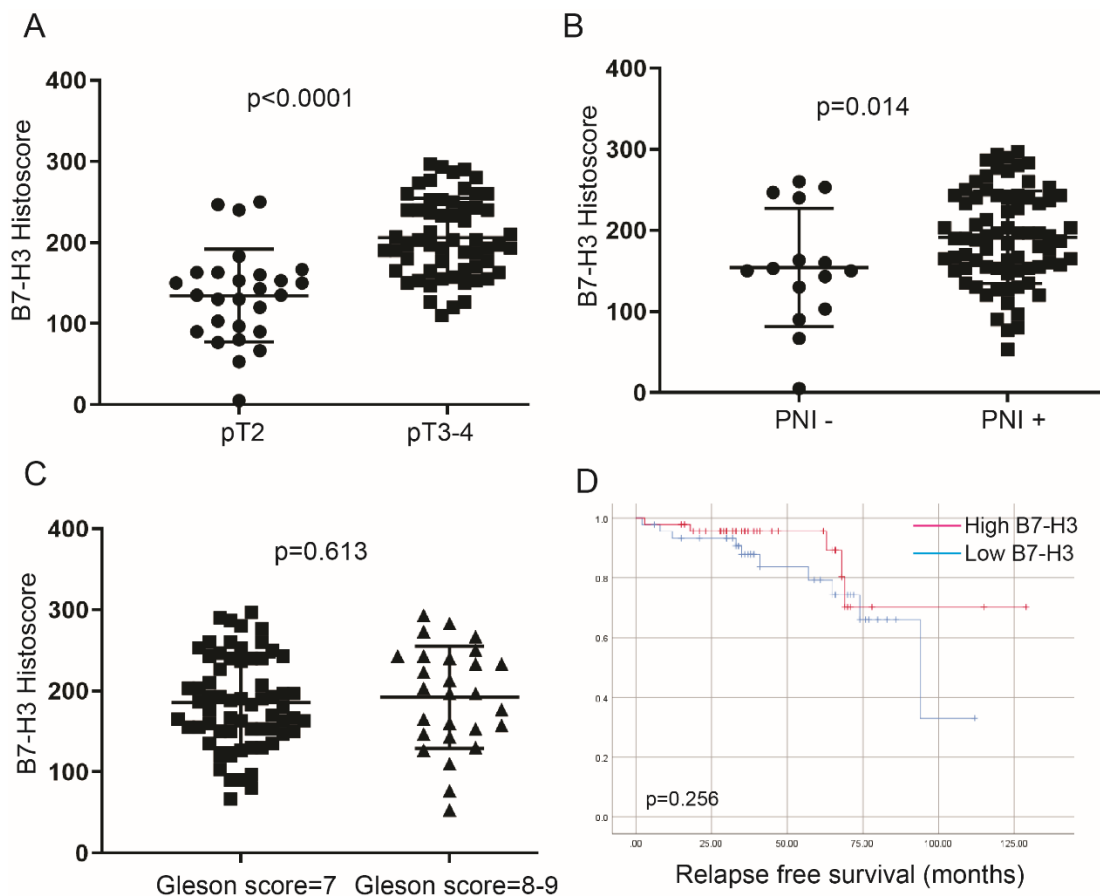


Figure 22 High B7-H3 expression is associated with worse clinicopathological features

(A) B7-H3 Histoscore presented as median with 95% CI in patients with pT2 ($n = 27$) and pT3-4 ($n = 59$) stage. (B) B7-H3 Histoscore presented as median with 95% CI in PNI- ($n = 15$) and PNI+ ($n = 76$). (C) B7-H3 Histoscore presented as median with 95% CI in patients with Gleason score=7 ($n = 65$) and Gleason score=8-9 ($n = 27$). (D) (A-C) Mann Whitney test used for statistical comparisons. (D) Kaplan Meier curves of PCa patients in the discovery cohort. High B7-H3 defined as \geq median. Log rank test used for statistical comparison. PNI: Perineural invasion.

5.1.3 B7-H3 expression inversely correlates with immune cell infiltration

I further explored the correlation between B7-H3 staining and immune cell infiltration. B7-H3 expression had a weak inverse correlation with epithelial CD8 effector T cells (Spearman's $r=-0.26$, $p=0.03$). Additionally there was a similar trend for stromal CD4 effector T cells (Spearman's $r=-0.21$, $p=0.08$) and stromal CD8 effector T cells (Spearman's $r=-0.22$, $p=0.06$). It should be noted that the stainings were not conducted in serial sections; therefore, even weak correlations were considered a strong indicator of potential association between these markers.

5.2 Transient silencing of B7-H3 expression in prostate cancer cell lines

Transient silencing of B7-H3 expression was performed on LNCaP, C4-2, PC3M and DU145 human prostate cancer cells using a pooled siRNA targeting B7-H3 (siB7-H3 pool). It was evident in all cell lines that mRNA (Figure 23A) expression of B7-H3 was markedly decreased 48 h after siRNA transfection compared to non-targeting control (siNT) based on quantitative polymerase chain reaction (qPCR). A similar decrease was found in protein expression 48 h after siB7-H3 pool transfection based on western blotting (Figure 23B). It was interesting that the baseline expression levels of B7-H3 varied between different cell lines, with LNCaP and C4-2 showing higher protein expression than PC3M and DU145 (Figure 23B).

Furthermore, I tested the efficiency of the singleton siRNA sequences (S1-S4) against B7-H3 within the siRNA pool in LNCaP and PC3M cells in an attempt to address any potential off-target effects with the use of pooled siRNA. All singleton siRNAs successfully decreased mRNA (Figure 23C) as well as protein (Figure 23D) levels of B7-H3. I used siB7-H3 pool and occasionally siB7H3 S1 and siB7H3 S4 for subsequent assays as their presence resulted in the largest decrease in B7-H3 expression.

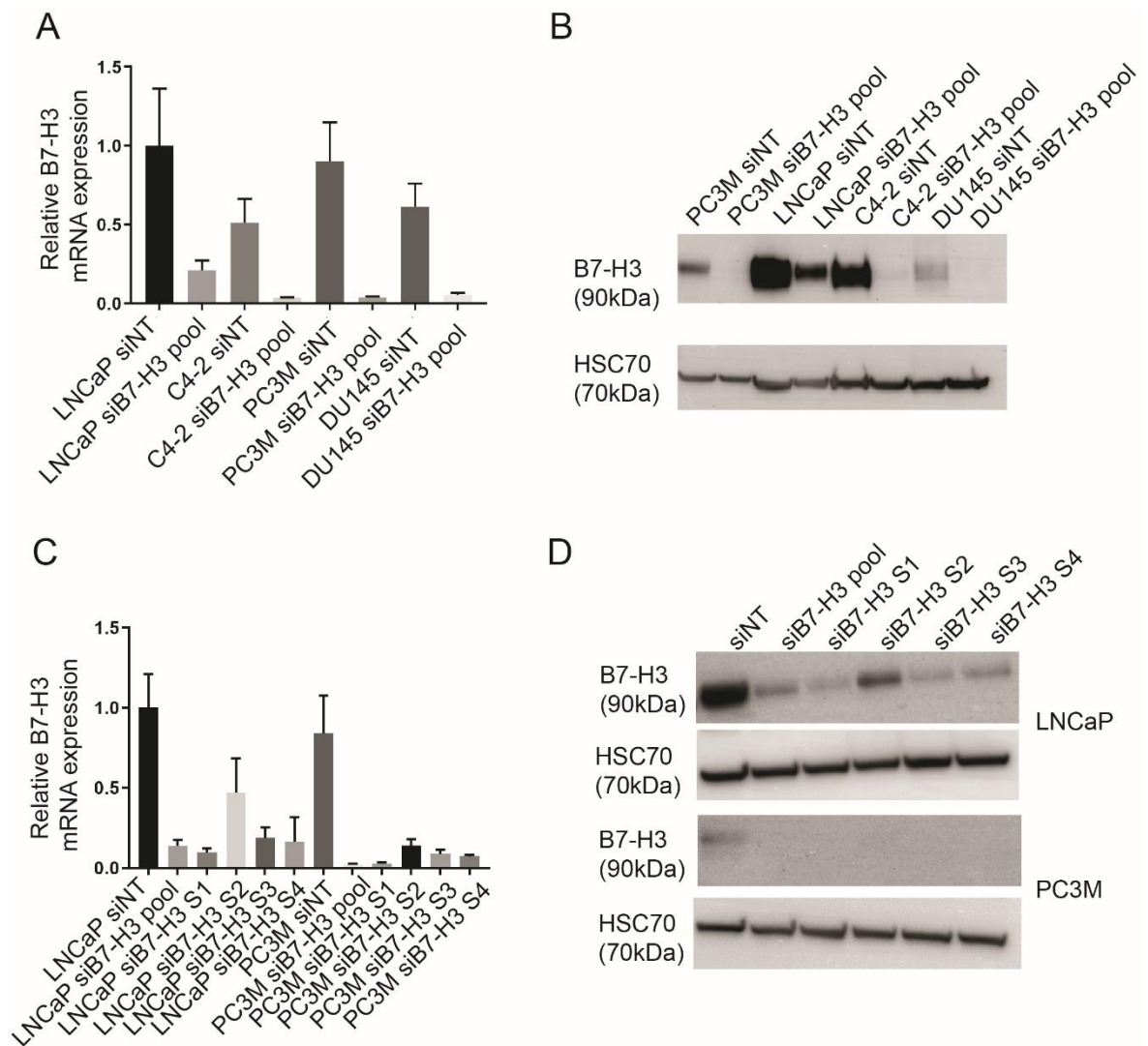


Figure 23 Transient silencing of B7-H3 in prostate cancer cell lines

(A) Quantitative polymerase chain reaction (qPCR) of B7-H3 mRNA expression in non-targeting control (siNT) and B7-H3 pool siRNA (siB7-H3 pool) transfected LNCaP, C4-2, PC3M and DU145 cells. Normalised to Casc 3 expression (house keeping gene). (B) Western blotting of whole cell lysates prepared from PC3M, LNCaP, C4-2 and DU145 human prostate cancer cell lines which had been transiently transfected with siNT or siB7-H3 pool using anti- B7-H3 antibody. HSC70 served as a loading control. (C) qPCR of B7-H3 mRNA expression in siNT, siB7-H3 pool, siB7-H3 S1 and siB7-H3 S4 (singleton siRNAs) transfected LNCaP and PC3M cells. (D) Western blotting of whole cell lysates prepared from LNCaP and PC3M cell lines which had been transiently transfected with siNT, siB7-H3 pool, siB7-H3 S1 and siB7-H3 S4 (singleton siRNAs) using anti- B7-H3 antibody. HSC70 served as a loading control. (A&C) Bars indicate mean values and error bars SD, n = 3 (technical replicates). (B&D) n=2 technical replicates.

5.2.1 Transient loss of B7-H3 expression does not affect prostate cancer cell growth or apoptosis *in vitro*

To investigate the role of B7-H3 in PCa cell growth, I measured cell proliferation by cell counting. There was no significant difference in cellular proliferation between control siNT and siB7-H3 pool in LNCaP (Figure 24A) and PC3M (Figure

24B) cells. Also, silencing of B7-H3 did not increase apoptosis in LNCaP (Figure 24C) or PC3M cells (Figure 24D), as measured by annexin V staining.

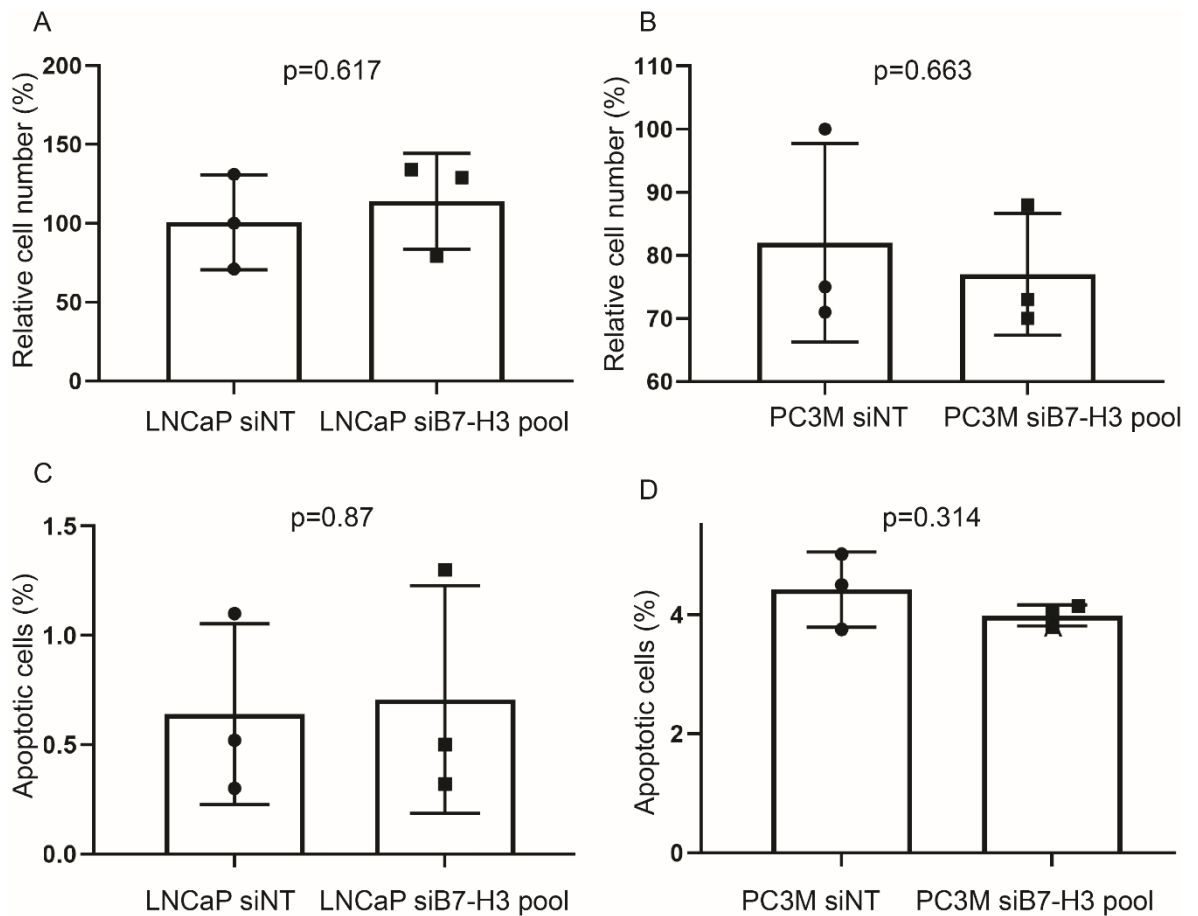


Figure 24 Transient loss of B7-H3 expression does not affect prostate cancer cell growth or apoptosis *in vitro*

(A) LNCaP and (B) PC3M cells were treated with control non-targeting siRNA (siNT) or pool siRNA directed against B7-H3 (siB7-H3 pool). The presented graphs show changes in cell proliferation by cell counting. (C) LNCaP and (D) PC3M cells were treated with siNT or siB7-H3 pool and stained with annexin V and analysed by flow cytometry. The presented graphs show percentage of apoptotic cells stained with annexin V. (A-D) n=3 (biological replicates), data in bar charts indicate the mean ± SD. t-test (unpaired, 2 tailed) was used for statistical analysis.

5.2.2 Transient loss of B7-H3 expression reduces prostate cancer cell migration *in vitro*

I conducted transwell migration assays to determine whether B7-H3 affects cell migration. Transient siRNA mediated silencing of B7-H3 expression significantly impaired migration in LNCaP (Figure 25A-B), C4-2 (Figure 25C-D) and PC3M (Figure 25E-F) cells, particularly pronounced in LNCaP and C4-2 cells, with >50% decreased migration.

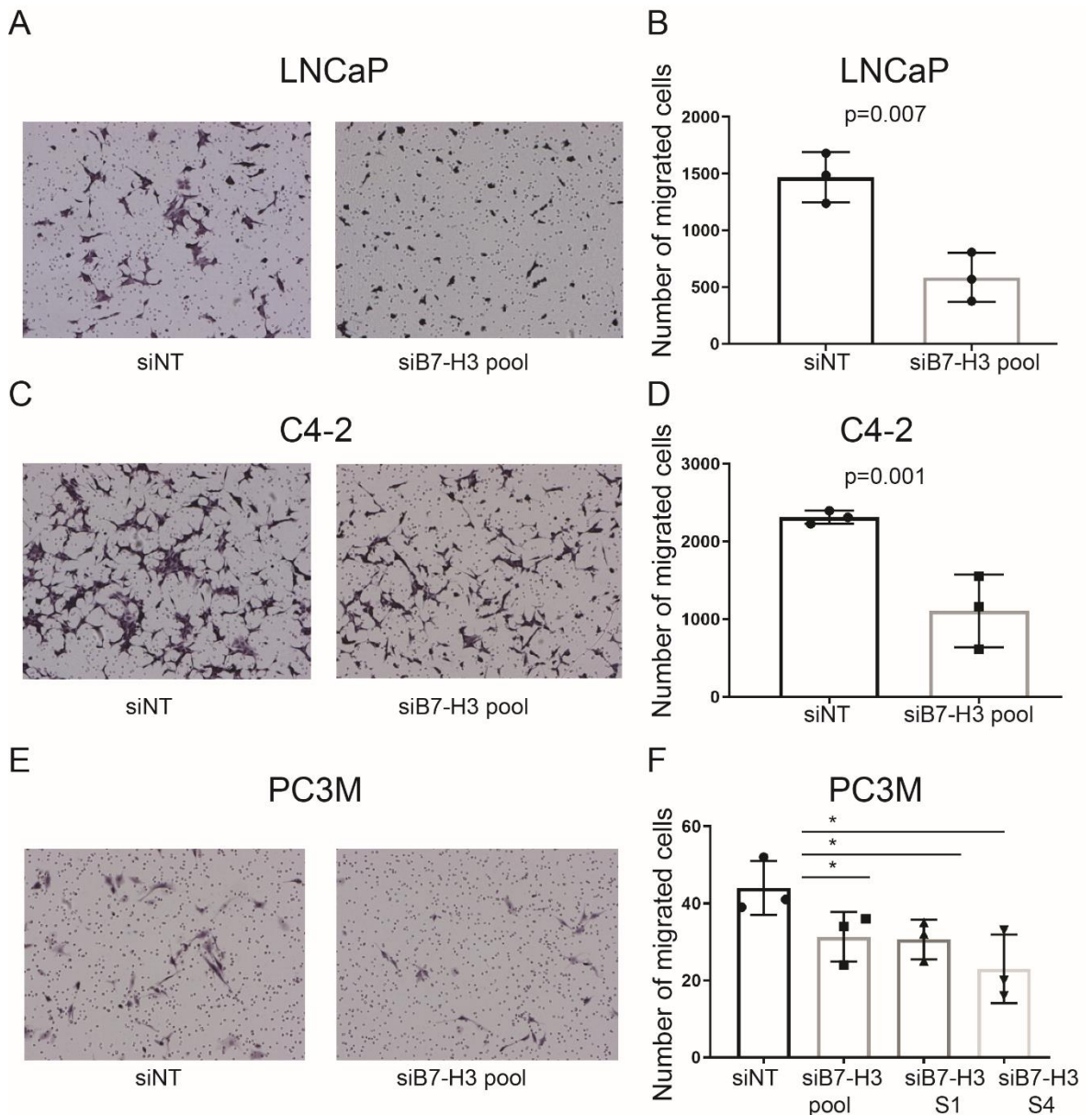


Figure 25 Transient loss of B7-H3 expression reduces prostate cancer cell migration in a transwell Boydon chamber assay

LNCaP (A-B), C4-2 (C-D) and PC3M (E-F) cells were silenced with control NT siRNA (siNT), pool siRNA (siB7-H3 pool) and/or two singleton siRNAs (S1, S4) directed against B7-H3 then subjected to transwell migration assay after 48 h incubation (n = 2 biological replicates for PC3M singleton B7-H3 siRNA's; n=3 for all other cell lines/conditions). A,C and D are representative images of migrated cells under light microscope (20x). In B,D,F graphs bar charts indicate the mean ± SD. t-test (unpaired, 2 tailed) and 2-way ANOVA were used for statistical analysis, * = p < 0.05.

Next, I sought to validate the observed effects of B7-H3 mediated cell migration using an additional *in vitro* methodology, namely a scratch wound healing assay. LNCaP and C4-2 wells could not be used in this assay due to their cell to cell adhesiveness that prevented the generation of a clean scratch wound and

resulted in detachment from the plastic in irregular shapes. Besides PC3M cells, DU145 cells were found to be suitable. B7-H3 silencing reduced PC3M (Figure 26A-B) and DU145 (Figure 26C-D) cell wound healing capacity, measured by Incucyte analysis. The maximum difference between siB7-H3 treated and control siNT was 12.47% (± 2.36 SD $p < 0.0001$) at 39 hours for PC3M and 13% (± 1.47 SD, $p < 0.0001$) at 40 hours for DU145 cells. These data combined with the previous data from transwell experiments suggested that B7-H3 could play an important role in cell migration.

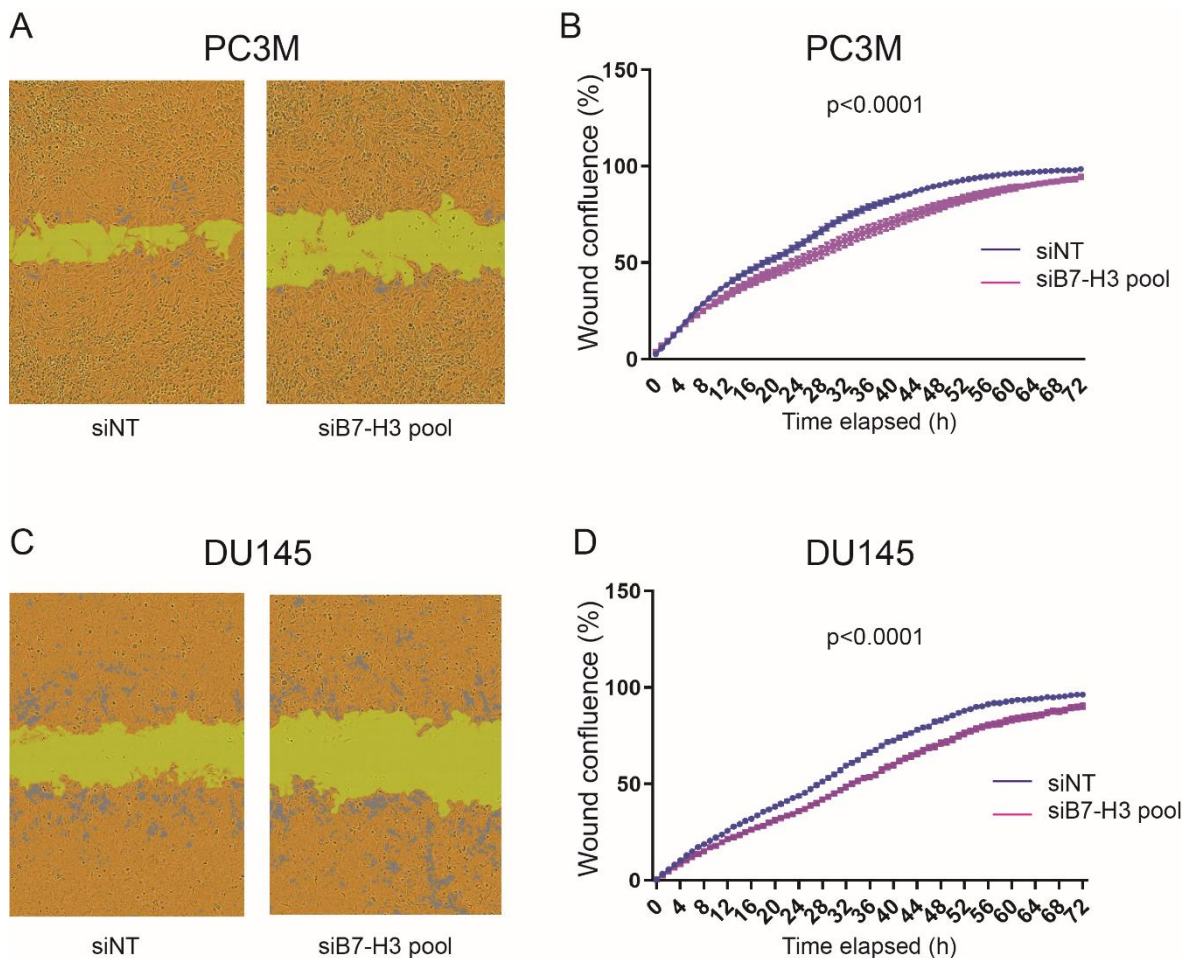


Figure 26 Transient loss of B7-H3 expression reduces prostate cancer cell migration shown by scratch wound assay

PC3M (A-B) and DU145 (C-D) cells were silenced with control NT siRNA (siNT) or pool siRNA directed against B7-H3 then subjected to scratch-wound assay using incucyte ($n = 3$ biological replicates). A and C are representative images taken by incucyte, migrating cells are shown as orange mask and scratch wound is shown as yellow mask. In B and D individual data indicate mean \pm SD wound confluence, 2-way ANOVA was used for statistical analysis.

5.2.3 Transient loss of B7-H3 expression reduces PC3M cell invasion *in vitro*

In order to assess the potential influence of B7-H3 on prostate cancer cell invasion, I conducted inverted transwell invasion assays. PC3M cells were used as suitable human prostate cancer cells capable of invading matrigel in an *in vitro* assay. Silencing of B7-H3 led to decreased invasion of PC3M cells compared to control (Figure 27). This was more pronounced using S4 singleton siRNA (21% reduction, $p=0.01$).

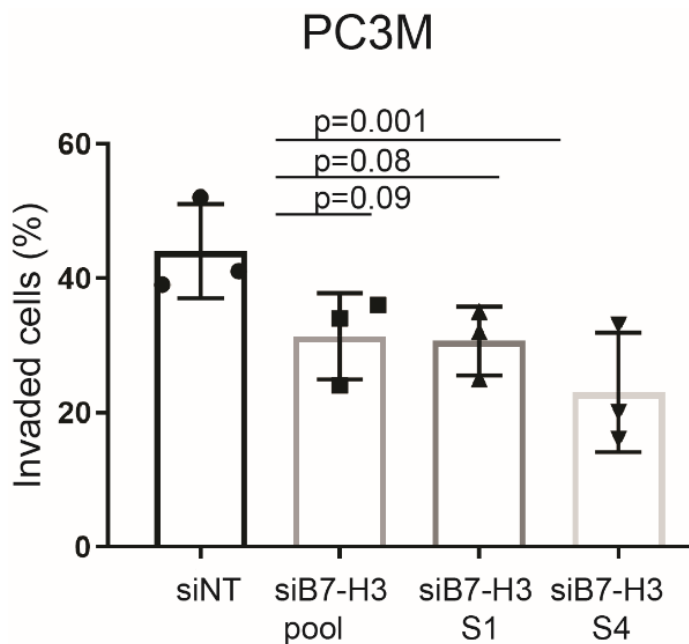


Figure 27 Transient loss of B7-H3 expression reduces PC3M prostate cancer cell invasion shown by inverted transwell Boydon chamber assay

PC3M cells were silenced with control NT siRNA or pool siRNA and/or two singleton siRNAs (S1, S4) directed against B7-H3 then subjected to transwell invasion assay ($n = 3$ biological replicates). Graphs bar charts indicate the mean \pm SD. 2-way ANOVA was used for statistical analysis.

In summary, *in vitro* assays with transient B7-H3 silencing showed no effect in prostate cancer cell lines proliferation and apoptosis, but a decrease in cell migration and invasion. Cell proliferation can be a confounding factor of migration assays, therefore I was confident that it had not contributed to the changes in migration observed.

5.3 Generation of stable knock out (KO) B7-H3 clones of PC3M and C4-2 cell lines

To validate the *in vitro* phenotype observed following transient silencing of B7-H3 expression, I generated stable knock out (KO) clones from PC3M and C4-2 parental prostate cancer cells. PC3M cells represent poorly differentiated prostate adenocarcinoma cells generated from a bone metastases from a patient with prostate cancer. C4-2 cells are derived from subcutaneous xenograft of LNCaP cells (isolated from a patient with lymph node metastasis) and are more aggressive and metastatic than LNCaP cells. These two human prostate cancer cell lines were selected due to their inherent capacity to migrate/invade as well as their potential for use in *in vivo* studies in the future.

B7-H3 was stably knocked out (KO) in PC3M cells using CRISPR Cas9 gene editing, generating four stable KO cell lines, namely, KO clone 10 (KO10), KO clone 4 (KO4) and KO clone 13 (KO13) and KO pool of different clones. As shown by Western blot, KO clones expressed very low levels of B7-H3 compared to parental and control transfection cells (Figure 28A). PC3M KO pool and KO10 clones were used in subsequent experiments. B7-H3 mRNA expression was also tested by qPCR in PC3M KO pool and KO10, confirming a significant reduction (Figure 28B).

Similarly, *B7-H3* was stably knocked out (KO) in C4-2 cells, generating five stable KO cell lines, namely KO pool, KO clone 2 (KO2), KO clone 3 (KO3), KO clone 4 (KO4), KO clone 10 (KO10) and KO clone 18 (KO18) (Figure 28C). Transfection control, KO pool and KO2 were selected for subsequent experiments. B7-H3 mRNA expression was also tested by qPCR and confirmed a significant decrease (Figure 28D).

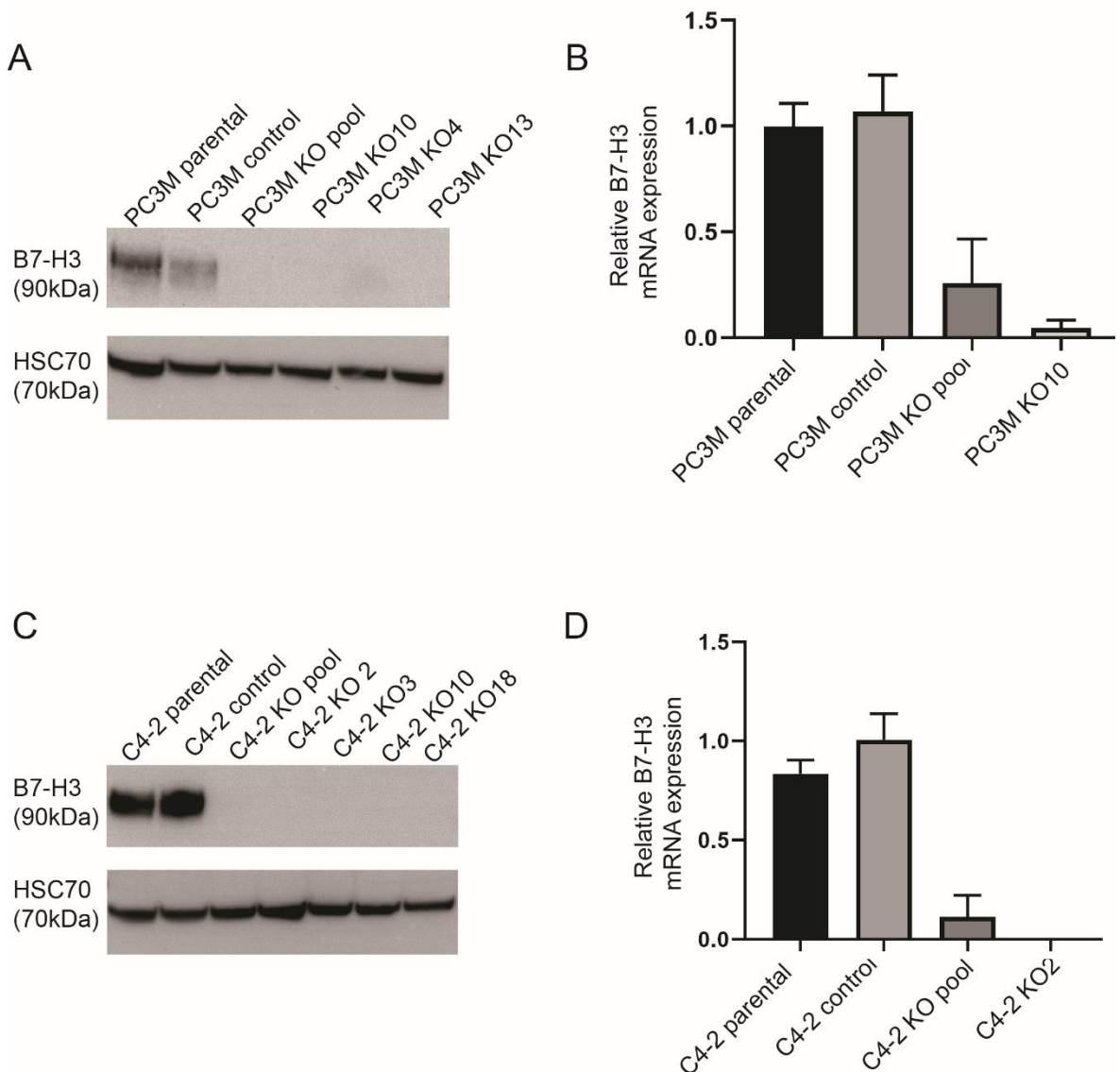


Figure 28 Generation of stable B7-H3 knock out (KO) clones of PC3M and C4-2 cells

(A) Western blotting of whole cell lysates prepared from PC3M prostate cancer cells which had been stably *B7-H3* knocked out (KO pool, KO10, KO4) using *CRISPR/Cas9*. A control pool was used as control (PC3M control). HSC70 served as a loading control. (B) qPCR of *B7-H3* mRNA expression in stable KO clones of PC3M compared to parental and control PC3M. Normalised to *Casc 3* expression (house keeping gene). (C) Western blotting of whole cell lysates prepared from C4-2 prostate cancer cell lines which had been stably *B7-H3* knocked out (KO pool, KO2, KO3, KO4, KO10, KO18) using *CRISPR/Cas9*. A control pool was used as control (C4-2 control). HSC70 served as a loading control. (D) qPCR of *B7-H3* mRNA expression in stable KO clones of C4-2 cells compared to parental and control C4-2. Normalised to *Casc 3* expression (house keeping gene). (B&D) Bars indicate mean values and error bars SD, n = 3 (technical replicates).

5.4 Stable knock out (KO) of B7-H3 does not affect survival and proliferation of PC3M cells

I applied the colony formation assay to investigate differences in survival and proliferation in stable *B7-H3* KO clones derived from human prostate cancer cells. This assay required very sparse seeding and C4-2 cells were unable to grow

in such low concentrations. The number of colonies developed from PC3M control cells was comparable to that of its KO pool and KO 10 derivatives (Figure 29). This suggests that suppressed B7-H3 expression did not alter the proliferation and survival of PC3M cells *in vitro*.

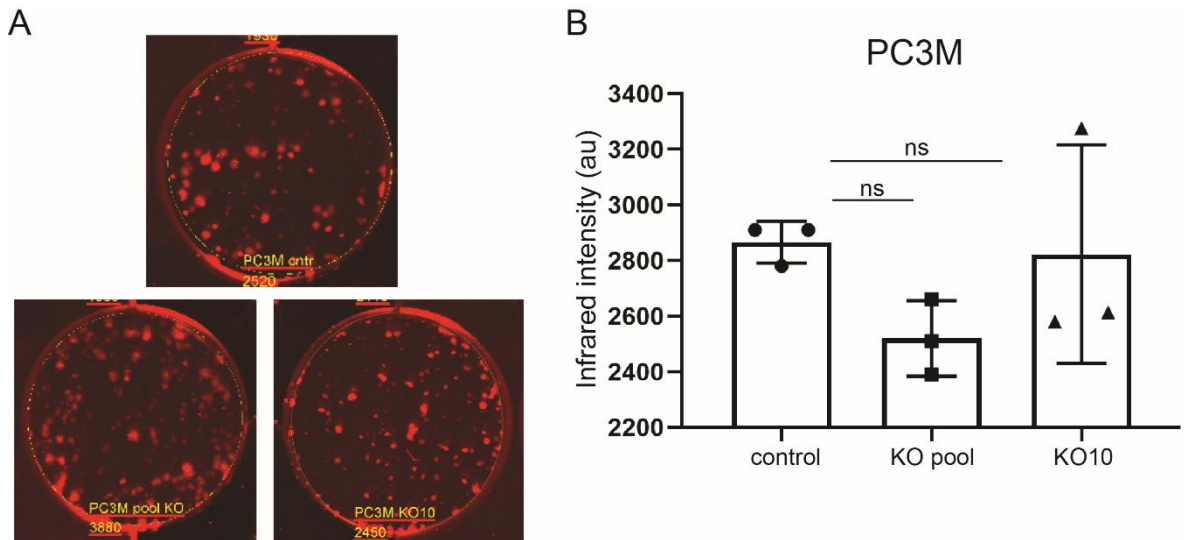


Figure 29 Stable knock out (KO) of B7-H3 does not affect survival and proliferation of PC3M cells

(A) Representative images of PC3M control (top), PC3M KO pool (bottom left) and PC3M KO10 (bottom right) stained with crystal violet and imaged in LI-COR with 700 wavelength. (B) Graph indicates colony numbers of each groups as mean \pm SD. 2-way ANOVA was used for statistical analysis (n=3 biological replicates). Au=arbitrary units, ns=not significant.

5.5 Stable knock out (KO) of B7-H3 reduces prostate cancer cell migration and invasion *in vitro*

To investigate whether B7-H3 affects prostate cancer cell migration, I performed transwell migration and scratch wound healing assay with the stable KO clones for B7-H3 expression. Both PC3M (Figure 30A) and C4-2 (Figure 30B) KO clones have significantly reduced migration (up to 50%). PC3M KO clones also showed significant decrease in wound healing capacity (Figure 30C). The maximum difference between KO pool and control was 16.2% (\pm 3.86 SD, $p < 0.0001$) and 34.91% (\pm 3.37 SD, $p < 0.0001$) for KO10 at 36 hours. In a transwell invasion assay, PC3M KO pool and KO 10 cell clones showed a significant decrease in invasive capacity when compared to the PC3M control cells (Figure 30D). These data reinforced the potential role of B7-H3 in regulating migration and invasion of prostate cancer cells.

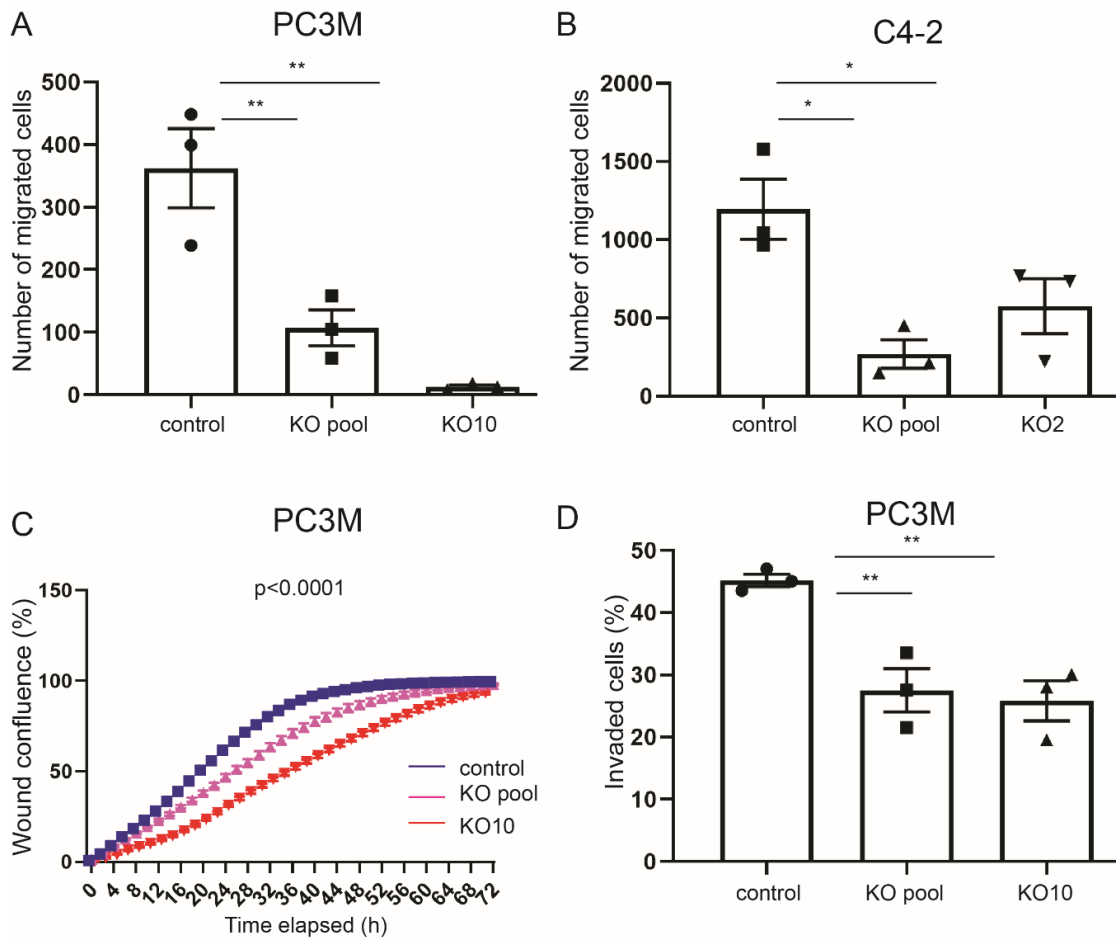


Figure 30 Stable knock out (KO) of B7-H3 reduces prostate cancer cell migration and invasion in vitro

(A) PC3M (control, KO pool and KO10 clones) and (B) C4-2 (control, KO pool and KO 2 clones) were subjected to transwell migration assay after 48 h incubation. Number of migrated cells are shown in A and B panels. (C) PC3M control, KO pool and KO 10 for B7-H3 were subjected to scratch-wound assay using incucyte. (D) PC3M control, KO pool and KO 10 for B7-H3 were subjected to transwell invasion assay. (A-D) Graph bar charts indicate the mean \pm SD. 2-way ANOVA was used for statistical analysis, * = <0.05 , ** = <0.01 (n = 3 biological replicates).

5.6 RNA sequencing and metacore pathway analysis reveals extracellular space cytokines are decreased in B7-H3 deficiency

Having established a decrease in migration and invasion associated with B7-H3 knock out, we performed RNA sequencing comparing PC3M pool KO and KO 10 with control PC3M cells (n=3 biological replicates) in order to gain a better understanding of the biological effect of B7-H3 loss. Principal component

analysis (PCA) showed good clustering between biological replicates and distance between PC3M control and KO clones (Figure 31A), confirming good reproducibility within each sample, and that loss of B7-H3 expression has an effect. KO pool and KO 10 did not cluster near each other, likely because KO10 is a single KO clone for B7-H3 whereas KO pool comprises of many different KO clones and has a larger heterogeneity. All genes that were differentially expressed in KO clones compared to control were defined to be significant if they have a fold change greater than 2 and an adjusted p value of <0.05 . Analysis was performed by Dr Ann Hedley, Bioinformatician, Beatson Institute. 368 genes were significantly changed in the same direction in both KO cells, 180 upregulated and 188 downregulated (Figure 31B). All significantly downregulated genes were used in Metacore analysis in order to identify involved pathways. The ten top pathways are shown in Figure 31C and included cytokines and their receptors (CCL2, CXCL1, CXCL6, CXCL8, CXCL16, IL13RA2, IL11, IL33, IL4RA,), complement (C3, C3a, C3b, C3c, C3dg, iC3b) and ECM remodelling (MMP1, MMP10, Collagen III) genes. These cytokines and MMPs are secreted molecules known to be involved in chemotaxis and matrix remodelling respectively, and have been implicated in migration, invasion and metastasis of different tumour types.

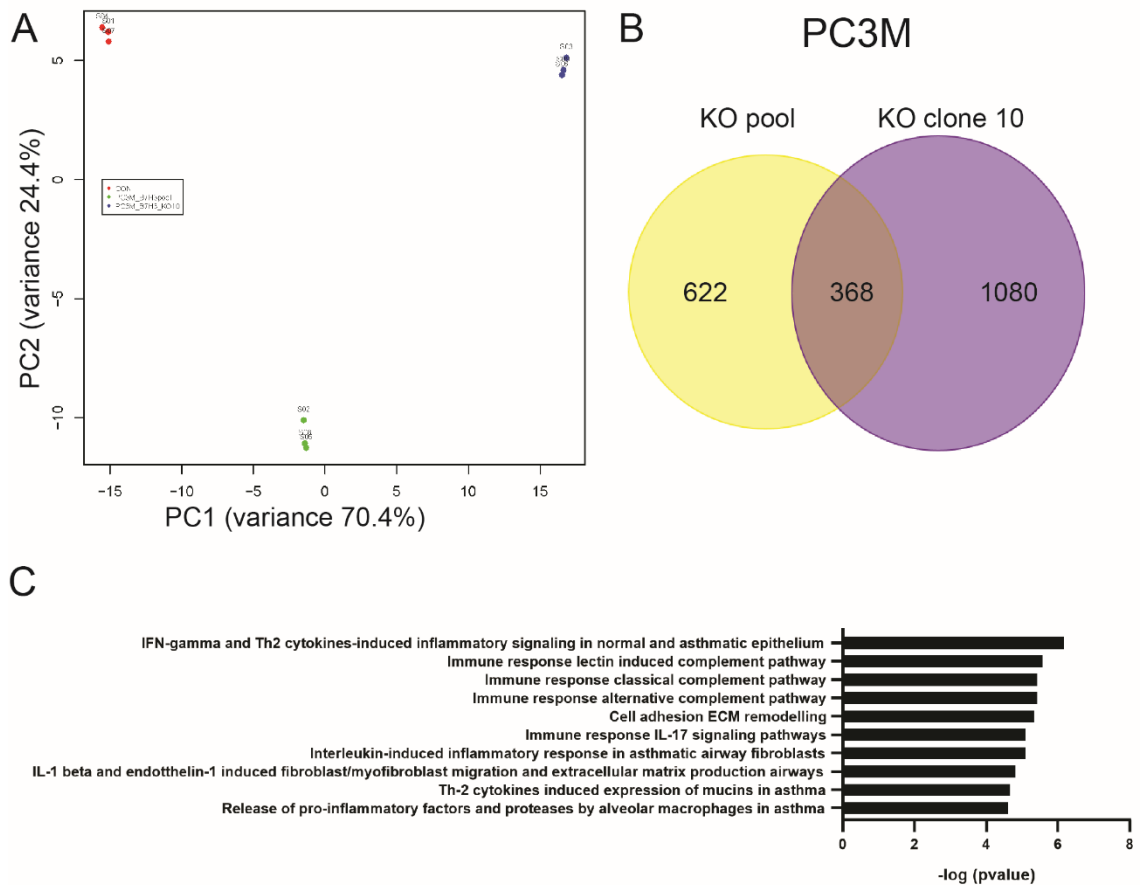


Figure 31 Metacore pathway analysis

(A) Principal component analysis (PCA) plot showing PC3M control (red), PC3M KO pool (green) and KO clone 10 (blue). (B) Venn diagram showing significantly changed genes in the same direction. Fold change >2, adj p value <0.05. (C) Top 10 significantly downregulated pathways in PC3M KO pool and KO10 compared to PC3M control using metacore pathway software analysis.

5.6.1 Differentially expressed genes from RNA sequencing validate in PC3M cells

The next step to confirm that the downregulated genes that were of most interest (i.e. cytokines and metalloproteinases) identified by the RNA sequencing could be validated with qPCR in PC3M cells (different biological replicates). CCL2, CXCL1, CXCL6, CXCL8, CXCL16, IL11, IL33, IL4R, MMP1 and MMP10 were significantly downregulated in PC3M KO pool and KO 10 for B7-H3 compared to PC3M control (Figure 32A-J). Interestingly, CXCL8 is the only one that so far been implicated in the metastatic potential of B7-H3 in melanoma (130) and pancreatic cancer (137).

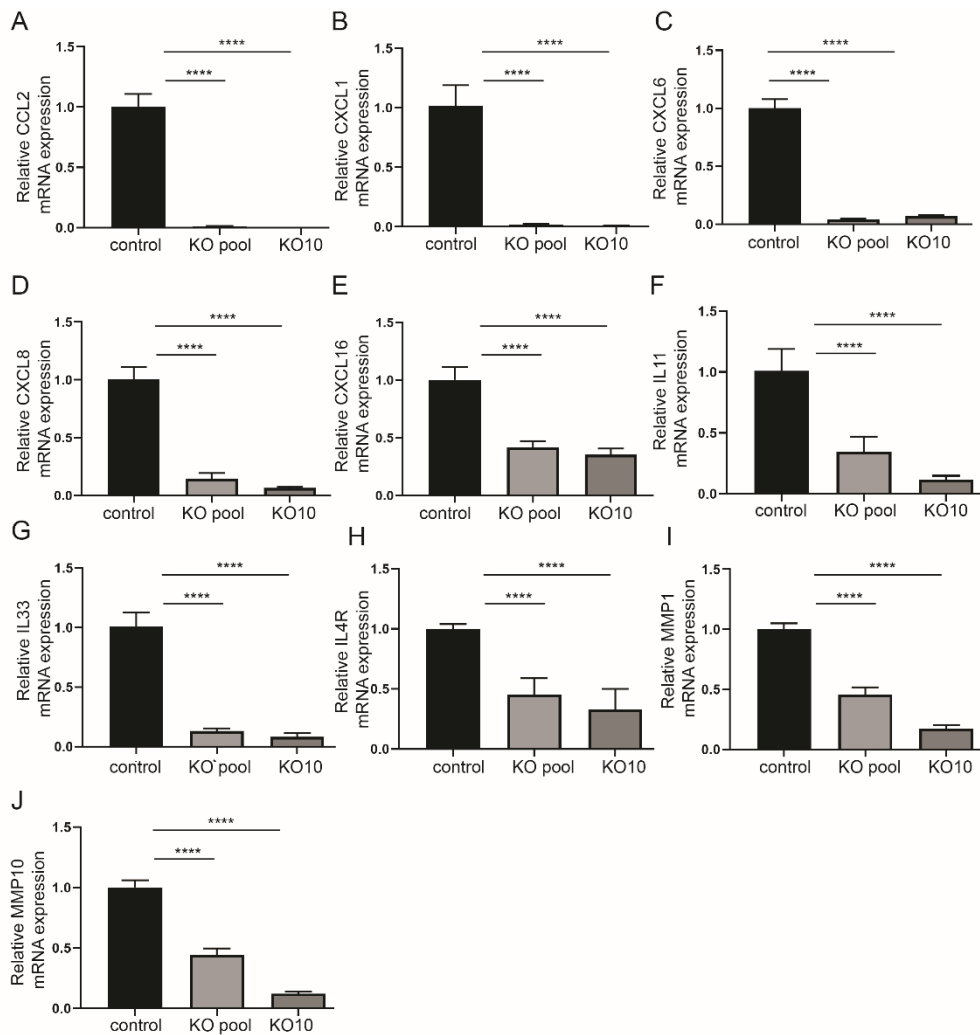


Figure 32 Differentially expressed genes from RNA sequencing validate in PC3M cells

(A-J) qPCR of mRNA expression of cytokine and metalloproteinase genes identified from RNA sequencing (performed in PC3M) in stable KO clones of PC3M compared to control PC3M. Normalised to Cas3 expression (house keeping gene). Bars indicate mean values and error bars SD, n = 2 (biological replicates). 2-way ANOVA was used for statistical analysis, * = <math><0.05</math>, ** = <math><0.01</math>, *** = <math><0.001</math>, **** = <math><0.0001</math>.

I next investigated whether any of the above target genes were also downregulated in C4-2 KO clones for B7-H3. However, none of these genes were significantly decreased in C4-2 B7-H3 KO clones when compared to C4-2 controls (Figure 33A-H). CXCL1, IL11 and IL4R genes were not expressed at all. Overall, the downregulated genes identified from RNA sequencing were robust for PC3M cells but do not show similar results in C4-2 cells, suggesting that there may be cell type differences in B7-H3 function.

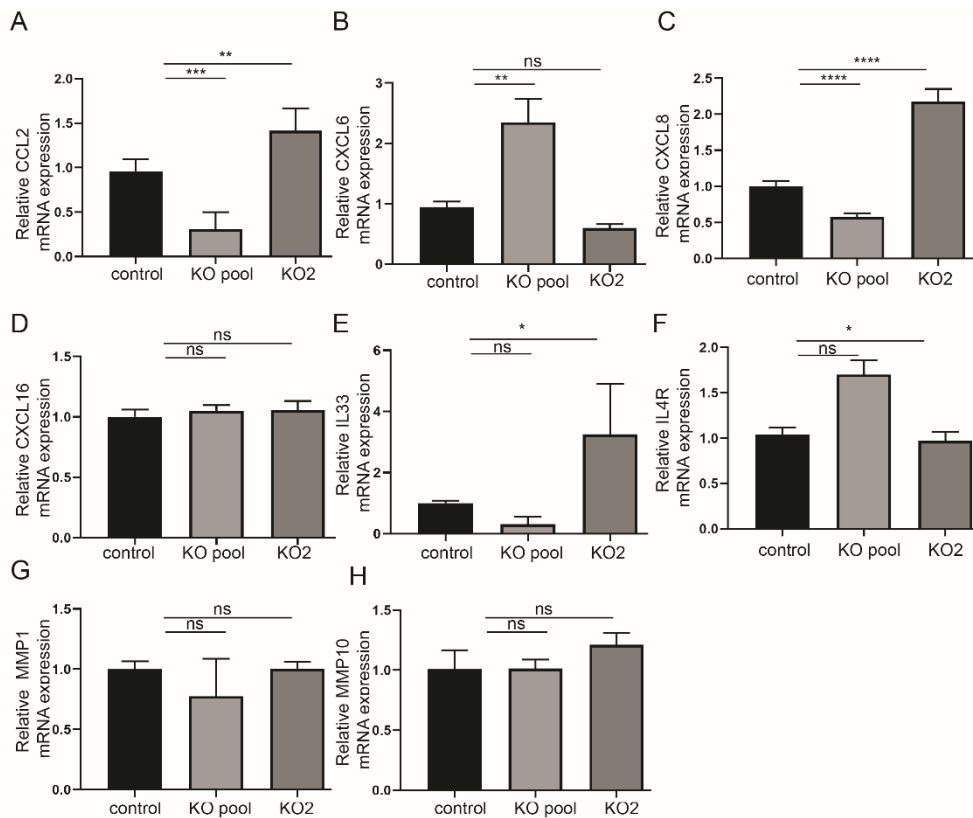


Figure 33 Differentially expressed genes from RNA sequencing do not validate in C4-2 cells (A-J) qPCR of mRNA expression of cytokine and metalloproteinase genes identified from RNA sequencing (performed in PC3M) in stable KO clones of C4-2 compared to control C4-2. Normalised to Casc 3 expression (house keeping gene). Bars indicate mean values and error bars SD, n = 2 (biological replicates). 2-way ANOVA was used for statistical analysis, * = <0.05, ** = <0.01, *** = <0.001, **** = <0.0001, ns= not significant).

5.7 Concluding summary

In summary, data presented in this chapter are consistent with the notion that B7-H3 may be involved in prostate cancer progression including metastasis. Firstly, B7-H3 chromogenic staining and histo-scoring is easy to implement and a reproducible methodology for B7-H3 protein quantification in FFPE tissue (Figure 20). A correlation between increased B7-H3 expression and poor prognosis has been previously established (107, 142), however a strong association with metastatic spread to the lymph nodes is shown for the first time in this thesis (Figure 21).

Furthermore, there were significant *in vitro* phenotypic changes related to B7-H3 loss across a panel of human prostate cancer cell lines (namely PC3M, C4-2,

LNCaP and DU145) (Figure 23, 28). Both transient and stable suppression of B7-H3 expression resulted in impaired cellular migration and invasion *in vitro*, in the absence of changes in proliferation or apoptosis (Figure 24-27, 29-33). These results are in agreement with the existing studies on non-immunoregulatory role of B7-H3 (127, 130, 189) in different cancer types. Our data confidently show that B7-H3 contributes to an invasive phenotype of different human prostate cell lines and raises interesting questions regarding the biological mechanisms involved and potential of B7-H3 therapeutic targeting.

We performed RNA sequencing on PC3M *B7-H3* KO and control clones in order to elucidate its downstream pathways, particularly in the context of its effects on migration and invasion (Figure 31). The top downregulated pathways identified in Metacore involved extracellular space chemotactic cytokines (CCL2, CXCL1, CXCL6, CXCL16, IL11, IL33, IL4R) and their receptors as well as metalloproteinases (MMP1, MMP10). Each of these targets deserves further investigation in the future, with CCL2 being one of the most promising candidates. CCL2, a known direct transcriptional target of NF- κ B, is a potent enhancer of PCa cell migration and acting at least in part, via activation of the PI3 kinase/AKT pathway (190-192).

Due to the finite time that was left during my PhD I did not investigate the above genes further. However, future experiments would include confirming that changes in the expression of candidate cytokine at the protein level following manipulation of B7-H3 expression in PC3M cells, perhaps using a targeted cytokine assay or secretome analysis since the majority of the top downregulated targets are extracellular molecules. Following that, a recombinant antibody for CCL2 (or other cytokines of interest) could be studied in *in vitro* migration/invasion assays to test whether the phenotypic changes could be rescued in KO *B7-H3* clones. Furthermore, the molecular cascade between B7-H3 loss and altered cytokine expression can be explored. For example, as NF- κ B is a major regulator of cytokine transcription (193), it would be interesting to test if NF- κ B function is suppressed in *B7-H3* KO clones. Evaluation of the role of B7-H3 in prostate cancer metastasis will require the use of *in vivo* metastasis models, for instance orthotopic xenograft model to assay for nodal disease using PC3M and/or C4-2 KO cell clones.

Chapter 6 Discussion and future directions

6.1 Identification and validation of novel TME signature to identify patients with nodal metastasis

Driven by the clinical unmet need for better PCa patient stratification I investigated the tumour immune microenvironment of a well-characterised intermediate and high-risk PCa patient cohort in order to identify novel prognostic biomarkers for lymph node metastasis. We developed and applied mIF panels for T lymphocytes (CD4, CD8, FoxP3, PD-1), B lymphocytes (CD20) and macrophages (CD68, CD163) to comprehensively characterise infiltrating immune cell subpopulations with spatial context. The primary tumours in patients with lymph node metastasis were less infiltrated by anti-tumourigenic immune cells, namely effector CD4 (CD4⁺ FoxP3⁻ PD-1⁻), effector CD8 (CD8⁺ FoxP3⁻ PD-1⁻) and M1-like macrophages (CD68⁺ CD163⁻). Stromal CD4 effector T cell density was similarly lower in an independent patient cohort and could independently predict pelvic lymph node spread. Importantly, addition of CD4 T cell density to the currently used nomograms improved their accuracy, showing promise as a future prognostic biomarker.

This highlighted the importance of spatial composition, as only the density of stromal CD4 effector T cells were reproducibly predictive of lymph node spread. In the literature, a distinction of immune cell density assessment between the central area of the tumour and the invasive margin has been used repeatedly for cancer prognosis (49, 52). Although conceptually this makes sense in cancers such as colon and breast, this is more difficult to implement in PCa due to the multifocality of the disease and confidently identifying the index lesions on diagnostic biopsies. I explored the possibility of translating CD4 effector stromal T cell density to the clinic using a simple co-staining protocol easily applied in the diagnostic biopsy setting. I stained a pilot cohort of diagnostic biopsies with dual CD4-FoxP3 and convincingly demonstrated technical feasibility. Given the small optimisation sample number, it was not surprising that I did not observe significant differences according to nodal status. This highlighted that further work is needed on how best to assess tumour infiltrating immune cells in biopsy tissue material in determining the appropriate cut-off criteria for scoring and the presence of index lesion with radiologic guidance.

A pending question was the biological underpinnings for the differences in immune cell infiltration between patients with and without nodal spread. Using a targeted gene expression analysis, we identified increased expression of ECM components in lymph node positive patients (collagen I, collagen III and fibronectin 1). Increased ECM abundance and perturbed organisation was identified in different tissues (TMA, diagnostic biopsies) using different methodologies (IHC, SGH), solidifying the presence of increased stromal fibrosis in lymph node positive patients. This finding suggested a fibrotic stroma could potentially function as a physical barrier and prevent anti-tumourigenic immune cell infiltration in these patients (immune exclusion).

A secondary project during my studies was the role of B7-H3 immune checkpoint molecule in PCa. Examining human tissue samples, I showed an association of B7-H3 expression and aggressive clinical features, including lymph node spread. *In vitro* experiments with acute and chronic loss of B7-H3 revealed an effect on migration and invasion without any changes in proliferation or apoptosis. RNA sequencing of *B7-H3* KO clones revealed downregulation of known pro-migratory molecules, such as extracellular secreted cytokines and MMPs.

The identification of prognostic markers of nodal metastasis will also facilitate development of radiation therapy in a precision medicine context. The decision to extend the radiation field to include the entire pelvis remains controversial and the practice ranges widely among oncologists. The incorporation of a prognostic signature as described here will support an evidence-based decision in the radiation field for treating patients with intermediate and high-risk prostate cancer.

6.2 B7-H3 checkpoint molecule immune function insights

The role of host immune system in cancer initiation and progression and how it can be exploited by immune therapies is currently a popular research topic (44). B7-H3 immune checkpoint molecule has a role in tumour progression that goes beyond its immune regulatory role (194), that was the focus of my experiments. However, some of my data provide useful insights into possible immune functions of B7-H3 in PCa. The primary tumour immune microenvironment is the location in which tumour cells interact with the host immune system for the first

time. Immune infiltrates with the TME may have pro-tumourigenic or anti-tumorigenic effects depending on the immune cell compositions. The phenotype of tumour immune evasion may at least be partly mediated by chemokines from tumour and stromal cells, and interactions with their cognate chemokine receptors in regulating the migration of certain immune populations into the TME as part of the host immune response to the tumour (195).

RNA sequencing identified cytokines and cytokine receptors as the highest downregulated genes in KO clones for *B7-H3* compared to control. In specific, CCL2, CXCL1 and CXCL8 are of particular interest due to their known role in promoting migration of pro-tumorigenic immune cells into the TME (196-198). Firstly, TAMs as well as MDSCs can be recruited to the TME via the CCL2-CCR2 axis to promote tumour metastasis (197). Similarly, CXCL1 tumour secretion results in increased infiltration of CXCR+ MDSCs and CXCL1 ablation can increase T cell infiltration and sensitivity to immunotherapy (198). CXCL8 expressed by tumour cells also regulates MDSCs and tumour associated neutrophil migration into the TME to promote tumour progression and metastasis (196). CXCL8 also targets endothelial cells and promotes angiogenesis (199). Therefore, these identified downstream potential targets of B7-H3 signalling may suggest an additional role in immune suppression via promoting pro-tumorigenic immune cell infiltration and require further investigation.

6.3 Future directions in tumour immune profiling

There is increasing need for comprehensive characterisation of the TME retaining spatial context as well as gaining information from minority immune cell populations that are lost with bulk sample analyses. This has led to the development of novel imaging technologies, such as mIF which was applied in this thesis. An alternative methodology is the use of quantum dot nanocrystals instead of fluorescent dyes for detection of the site of antibody-antigen binding. Quantum dots have some advantages over traditional fluorescent dyes, such as high stability and narrow fluorescence excitation and emission spectra resulting in less bleed through and theoretically larger capability of multiplexing (200). However, they also carry inherent limitations, such as inability to use antibodies from the same species hugely complicating the protocol.

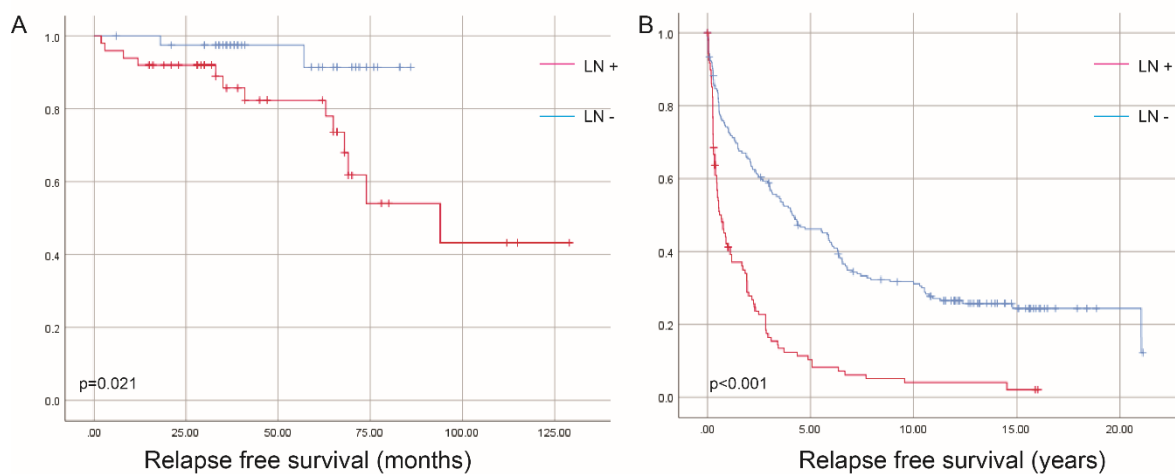
Another novel approach for tumour immune profiling which is constantly gaining popularity is tissue mass cytometry by time-of-flight (CyTOF). It combines traditional immunohistochemical methods of antigen-antibody binding with mass cytometry by measuring the abundance of metal isotopes with defined atomic mass tagged to antibodies (201). This approach can detect the metal-labelled antibodies in their exact tissue location using lasers or ion beams for subsequent mass spectrometry detection with one simultaneous antibody incubation and single step data acquisition and high-dimensional imaging (201, 202). Currently it has been validated to reliably image up to 32 markers on FFPE human tissue sections (201) and has the potential to increase to 100 due to the near zero crosstalk between metal labels. It can clearly provide much more information compared to every other method retaining spatial context. The main disadvantages lay in the limited number of antibodies currently suitable for this process, their relative instability which can cause alteration of the binding properties, the cumbersome analysis workflow, long processing times, specialised equipment and high cost of the mass spectrometer and destruction of the tissue after use. These limiting factors currently hinder this technology from widespread use but will likely be addressed in the near future.

It should be mentioned that all of these methods conducted on TMAs or representative tissue sections, suffer a key potential drawback, which is the risk of under-sampling. They examine only a fraction of the tumour tissue, missing information on tumour heterogeneity and rare events that may be present. However, in studies aiming to discover prognostic or predictive biomarkers, like the research presented here, the advantages of using mIF methodology on TMAs far out ways the drawbacks. The key benefit was that the patient tissue material used remained relatively intact and available for further examination in the clinic. Secondary considerations were the speed of biomarker analysis and decrease of cost and technical variability, as dozens of tissue samples were examined simultaneously. I aimed to address under sampling by using three large tissue cores (1mm) from each patient (routinely used size is 0.6 µm), but I recognise under sampling constituted an inevitable drawback of this screening high-throuput study.

6.4 Concluding summary

My PhD research thesis identified stromal CD4 effector T cell density as a promising prognostic biomarker for regional lymph node metastasis and highlighted the areas that necessitate future work before its adoption in the clinic (Chapter 3). It also showed increased stromal density as a key feature of lymph node positive PCa TME, presenting immune exclusion as a target for future studies (Chapter 4). Finally, it revealed the association of B7-H3 with nodal spread and aggressive clinicopathological features, as well as an *in vitro* pro-migratory and pro-invasive effect (Chapter 5).

Appendices



Appendix Figure 1 Clinical impact of lymph node metastasis in survival

Kaplan-Meier curves of prostate cancer patients in the discovery cohort (A) and validation cohort (B). Log rank test used for statistical comparison.

Gene	Description
A2M	alpha-2-macroglobulin
AADAT	aminoadipate aminotransferase
ABCB1	ATP binding cassette subfamily B member 1
ABCB11	ATP binding cassette subfamily B member 11
ABCC2	ATP binding cassette subfamily C member 2
ABCC6	ATP binding cassette subfamily C member 6
ABCF1	ATP binding cassette subfamily F member 1
ABCG2	ATP binding cassette subfamily G member 2 (Junior blood group)
ABHD1	abhydrolase domain containing 1
ABL1	ABL proto-oncogene 1, non-receptor tyrosine kinase
ABL2	ABL proto-oncogene 2, non-receptor tyrosine kinase
ACKR3	atypical chemokine receptor 3
ACP6	acid phosphatase 6, lysophosphatidic
ACTG2	actin, gamma 2, smooth muscle, enteric
ACTR3B	ARP3 actin related protein 3 homolog B
ADA	adenosine deaminase
ADAM17	ADAM metallopeptidase domain 17
ADCY1	adenylate cyclase 1
ADD2	adducin 2
ADGRE5	adhesion G protein-coupled receptor E5
ADORA2A	adenosine A2a receptor
ADORA2B	adenosine A2b receptor
ADRB2	adrenoceptor beta 2
AGER	advanced glycosylation end-product specific receptor
AHR	aryl hydrocarbon receptor
AICDA	activation induced cytidine deaminase
AIF1	allograft inflammatory factor 1
AKT1	AKT serine/threonine kinase 1
AKT3	AKT serine/threonine kinase 3
ALCAM	activated leukocyte cell adhesion molecule
ALOX15B	arachidonate 15-lipoxygenase, type B
ALOX5	arachidonate 5-lipoxygenase
ANAPC1	anaphase promoting complex subunit 1
ANKRD30A	ankyrin repeat domain 30A
ANLN	Anillin, actin binding protein
ANP32B	acidic nuclear phosphoprotein 32 family member B
ANPEP	alanyl aminopeptidase, membrane
ANXA1	annexin A1
APAF1	apoptotic peptidase activating factor 1
APC2	APC2, WNT signaling pathway regulator
APOE	apolipoprotein E

APP	amyloid beta precursor protein
ARG1	arginase 1
ARG2	arginase 2
ARHGAP11A	Rho GTPase activating protein 11A
ARHGAP11B	Rho GTPase activating protein 11B
ARHGDI1B	Rho GDP dissociation inhibitor beta
ARHGEF26	Rho guanine nucleotide exchange factor 26
ARMCX6	armadillo repeat containing, X-linked 6
AS3MT	arsenite methyltransferase
ASCL1	achaete-scute family bHLH transcription factor 1
ASF1A	anti-silencing function 1A histone chaperone
ASF1B	ASF1 anti-silencing function 1 homolog B
ASPM	Asp (abnormal spindle) homolog, microcephaly associated
ASRGL1	asparaginase like 1
ATF1	activating transcription factor 1
ATF2	activating transcription factor 2
ATF3_activating	activating transcription factor 3 (activating forms)
ATF3_repressing	activating transcription factor 3 (repressing forms)
ATG12	autophagy related 12
ATG16L1	autophagy related 16 like 1
ATG5	autophagy related 5
ATG7	autophagy related 7
ATM	ATM serine/threonine kinase
ATOH1	atonal bHLH transcription factor 1
ATP5F1	ATP synthase, H ⁺ transporting, mitochondrial Fo complex subunit B1
ATXN1	ataxin 1
AUNIP	aurora kinase A and ninein interacting protein
AURKA	Aurora kinase A
AURKB	Aurora kinase B
AXIN1	axin 1
AXIN2	axin 2
AXL	AXL receptor tyrosine kinase
B3GAT1	beta-1,3-glucuronyltransferase 1
BAGE	B melanoma antigen
BAGE_family	B melanoma antigen (family probe)
BAGE2_BAGE3	B melanoma antigen (members 2 and 3)
BAGE4_BAGE5	B melanoma antigen (members 4 and 5)
BATF	basic leucine zipper ATF-like transcription factor
BATF2	basic leucine zipper ATF-like transcription factor 2
BAX	BCL2 associated X, apoptosis regulator
BCL10	B-cell CLL/lymphoma 10
BCL2	BCL2, apoptosis regulator
BCL2L1	BCL2 like 1
BCL2L11	BCL2 like 11
BCL6	B-cell CLL/lymphoma 6
BEX1	brain expressed X-linked 1
BEX2	brain expressed X-linked 2

BID	BH3 interacting domain death agonist
BIRC5	baculoviral IAP repeat containing 5
BLK	BLK proto-oncogene, Src family tyrosine kinase
BLNK	B-cell linker
BMI1	BMI1 proto-oncogene, polycomb ring finger
BMP6	bone morphogenetic protein 6
BMP7	bone morphogenetic protein 7
BNC1	basonuclin 1
BORA	bora, aurora kinase A activator
BRCA1	BRCA1, DNA repair associated
BRCA2	BRCA2, DNA repair associated
BRIP1	BRCA1 interacting protein C-terminal helicase 1
BRMS1L	breast cancer metastasis-suppressor 1 like
BST2	bone marrow stromal cell antigen 2
BTK	Bruton tyrosine kinase
BTLA	B and T lymphocyte associated
BUB1	BUB1 mitotic checkpoint serine/threonine kinase
BUB1B	BUB1 mitotic checkpoint serine/threonine kinase B
C11orf71	chromosome 11 open reading frame 71
C17orf80	chromosome 17 open reading frame 80
C19orf66	chromosome 19 open reading frame 66
C1orf56	chromosome 1 open reading frame 56
C1QA	complement C1q A chain
C1QB	complement C1q B chain
C20orf24	C20orf24
C3	complement C3
C3AR1	complement C3a receptor 1
C4A_C4B	complement C4A/C4B (Chido blood group)
C5	complement C5
CA4	carbonic anhydrase 4
CALML3	calmodulin like 3
CAMP	cathelicidin antimicrobial peptide
CARD11	caspase recruitment domain family member 11
CASP1	caspase 1
CASP10	caspase 10
CASP3	caspase 3
CASP4	caspase 4
CASP5	caspase 5
CASP8	caspase 8
CAV1	caveolin 1
CBLB	Cbl proto-oncogene B
CCDC138	coiled-coil domain containing 138
CCL1	C-C motif chemokine ligand 1
CCL11	C-C motif chemokine ligand 11
CCL13	C-C motif chemokine ligand 13
CCL14	C-C motif chemokine ligand 14
CCL15	C-C motif chemokine ligand 15

CCL16	C-C motif chemokine ligand 16
CCL17	C-C motif chemokine ligand 17
CCL18	C-C motif chemokine ligand 18
CCL19	C-C motif chemokine ligand 19
CCL2	C-C motif chemokine ligand 2
CCL20	C-C motif chemokine ligand 20
CCL21	C-C motif chemokine ligand 21
CCL22	C-C motif chemokine ligand 22
CCL23	C-C motif chemokine ligand 23
CCL24	C-C motif chemokine ligand 24
CCL25	C-C motif chemokine ligand 25
CCL26	C-C motif chemokine ligand 26
CCL27	C-C motif chemokine ligand 27
CCL28	C-C motif chemokine ligand 28
CCL3	C-C motif chemokine ligand 3
CCL4	C-C motif chemokine ligand 4
CCL5	C-C motif chemokine ligand 5
CCL7	C-C motif chemokine ligand 7
CCL8	C-C motif chemokine ligand 8
CCNA2	Cyclin A2
CCNB1	Cyclin B1
CCNB2	cyclin B2
CCND1	cyclin D1
CCND3	cyclin D3
CCNE1	Cyclin E1
CCNE2	Cyclin E2
CCNF	Cyclin F
CCR1	C-C motif chemokine receptor 1
CCR10	C-C motif chemokine receptor 10
CCR2	C-C motif chemokine receptor 2
CCR3	C-C motif chemokine receptor 3
CCR4	C-C motif chemokine receptor 4
CCR5	C-C motif chemokine receptor 5 (gene/pseudogene)
CCR6	C-C motif chemokine receptor 6
CCR7	C-C motif chemokine receptor 7
CCR8	C-C motif chemokine receptor 8
CCR9	C-C motif chemokine receptor 9
CCRL2	C-C motif chemokine receptor like 2
CCT5	chaperonin containing TCP1 subunit 5
CD14	CD14 molecule
CD160	CD160 molecule
CD163	CD163 molecule
CD180	CD180 molecule
CD19	CD19 molecule
CD1A	CD1a molecule
CD1B	CD1b molecule
CD1C	CD1c molecule

CD1D	CD1d molecule
CD1E	CD1e molecule
CD2	CD2 molecule
CD200	CD200 molecule
CD209	CD209 molecule
CD22	CD22 molecule
CD226	CD226 molecule
CD24	CD24 molecule
CD244	CD244 molecule
CD247	CD247 molecule
CD27	CD27 molecule
CD274	CD274 molecule
CD276	CD276 molecule
CD28	CD28 molecule
CD33	CD33 molecule
CD34	CD34 molecule
CD37	CD37 molecule
CD38	CD38 molecule
CD3D	CD3d molecule
CD3E	CD3e molecule
CD3G	CD3g molecule
CD4	CD4 molecule
CD40	CD40 molecule
CD40LG	CD40 ligand
CD44	CD44 molecule (Indian blood group)
CD47	CD47 molecule
CD48	CD48 molecule
CD5	CD5 molecule
CD52	CD52 molecule
CD53	CD53 molecule
CD55	CD55 molecule (Cromer blood group)
CD58	CD58 molecule
CD59	CD59 molecule (CD59 blood group)
CD5L	CD5 molecule like
CD6	CD6 molecule
CD63	CD63 molecule
CD68	CD68 molecule
CD69	CD69 molecule
CD7	CD7 molecule
CD70	CD70 molecule
CD72	CD72 molecule
CD74	CD74 molecule
CD79A	CD79a molecule
CD79B	CD79b molecule
CD80	CD80 molecule
CD83	CD83 molecule
CD84	CD84 molecule

CD86	CD86 molecule
CD8A	CD8a molecule
CD8B	CD8b molecule
CD96	CD96 molecule
CD99	CD99 molecule (Xg blood group)
CDC20	Cell division cycle 20
CDC25A	Cell division cycle 25A
CDC25C	cell division cycle 25C
CDC45	Cell division cycle 45
CDC6	Cell division cycle 6
CDC7	cell division cycle 7
CDCA2	Cell division cycle associated 2
CDCA3	Cell division cycle associated 3
CDCA5	Cell division cycle associated 5
CDCA8	Cell division cycle associated 8
CDH1	cadherin 1
CDH15	cadherin 15
CDH5	cadherin 5
CDK1	cyclin dependent kinase 1
CDK4	cyclin dependent kinase 4
CDK6	cyclin dependent kinase 6
CDKN1A	cyclin dependent kinase inhibitor 1A
CDKN1B	cyclin dependent kinase inhibitor 1B
CDKN2A	cyclin dependent kinase inhibitor 2A
CDKN3	cyclin dependent kinase inhibitor 3
CDT1	Chromatin licensing and DNA replication factor 1
CEACAM1	carcinoembryonic antigen related cell adhesion molecule 1
CEACAM5	carcinoembryonic antigen related cell adhesion molecule 5
CEACAM6	carcinoembryonic antigen related cell adhesion molecule 6
CEACAM8	carcinoembryonic antigen related cell adhesion molecule 8
CEBPB	CCAAT/enhancer binding protein beta
CENPA	Centromere protein A
CENPE	Centromere protein E, 312kDa
CENPF	centromere protein F
CENPH	Centromere protein H
CENPI	Centromere protein I
CENPL	Centromere protein L
CENPU	centromere protein U
CENPW	Centromere protein W
CEP250	centrosomal protein 250
CEP55	Centrosomal protein 55kDa
CES1	carboxylesterase 1
CGREF1	cell growth regulator with EF-hand domain 1
CHDH	choline dehydrogenase
CHGA	chromogranin A
CHIT1	chitinase 1
CHMP4B	charged multivesicular body protein 4B

CHRM2	cholinergic receptor muscarinic 2
CHRM3	cholinergic receptor muscarinic 3
CHST10	carbohydrate sulfotransferase 10
CHUK	conserved helix-loop-helix ubiquitous kinase
CIITA	class II major histocompatibility complex transactivator
CIP2A	cell proliferation regulating inhibitor of protein phosphatase 2A
CKAP2	Cytoskeleton associated protein 2
CKAP2L	Cytoskeleton associated protein 2-like
CKLF	chemokine like factor
CLCA2	chloride channel accessory 2
CLDN3	claudin 3
CLEC12A	C-type lectin domain family 12 member A
CLEC2B	C-type lectin domain family 2 member B
CLEC4A	C-type lectin domain family 4 member A
CLEC4C	C-type lectin domain family 4 member C
CLEC5A	C-type lectin domain family 5 member A
CLEC6A	C-type lectin domain containing 6A
CLEC7A	C-type lectin domain containing 7A
CLEC9A	C-type lectin domain containing 9A
CLSPN	Claspin
CMA1	chymase 1
CMKLR1	chemerin chemokine-like receptor 1
CNNM1	cyclin and CBS domain divalent metal cation transport mediator 1
CNTLN	centlein
COCH	cochlin
COL1A1	collagen type I alpha 1 chain
COL1A2	collagen type I alpha 2 chain
COL3A1	collagen type III alpha 1 chain
CORO1A	coronin 1A
CPA3	carboxypeptidase A3
CPE	carboxypeptidase E
CR1	complement C3b/C4b receptor 1 (Knops blood group)
CR2	complement C3d receptor 2
CREB1	cAMP responsive element binding protein 1
CREB5	cAMP responsive element binding protein 5
CREBBP	CREB binding protein
CRISPLD1	cysteine rich secretory protein LCCL domain containing 1
CRMP1	collapsin response mediator protein 1
CRP	C-reactive protein
CRTAM	cytotoxic and regulatory T-cell molecule
CSF1	colony stimulating factor 1
CSF1R	colony stimulating factor 1 receptor
CSF2	colony stimulating factor 2
CSF2RA	colony stimulating factor 2 receptor alpha subunit
CSF2RB	colony stimulating factor 2 receptor beta common subunit
CSF3	colony stimulating factor 3
CSF3R	colony stimulating factor 3 receptor

CSK	C-src tyrosine kinase
CT45_family	cancer testis antigen family 45
CT47_family	cancer testis antigen family 47
CTAG1A_1B	cancer/testis antigen 1A and 1B
CTAG2	cancer/testis antigen 2
CTBP1	C-terminal binding protein 1
CTLA4	cytotoxic T-lymphocyte associated protein 4
CTNNB1	catenin beta 1
CTRC	chymotrypsin C
CTSG	cathepsin G
CTSH	cathepsin H
CTSL	cathepsin L
CTSS	cathepsin S
CX3CL1	C-X3-C motif chemokine ligand 1
CX3CR1	C-X3-C motif chemokine receptor 1
CXCL1	C-X-C motif chemokine ligand 1
CXCL10	C-X-C motif chemokine ligand 10
CXCL11	C-X-C motif chemokine ligand 11
CXCL12	C-X-C motif chemokine ligand 12
CXCL13	C-X-C motif chemokine ligand 13
CXCL14	C-X-C motif chemokine ligand 14
CXCL16	C-X-C motif chemokine ligand 16
CXCL2	C-X-C motif chemokine ligand 2
CXCL3	C-X-C motif chemokine ligand 3
CXCL5	C-X-C motif chemokine ligand 5
CXCL6	C-X-C motif chemokine ligand 6
CXCL8	C-X-C motif chemokine ligand 8
CXCL9	C-X-C motif chemokine ligand 9
CXCR1	C-X-C motif chemokine receptor 1
CXCR2	C-X-C motif chemokine receptor 2
CXCR3	C-X-C motif chemokine receptor 3
CXCR4	C-X-C motif chemokine receptor 4
CXCR5	C-X-C motif chemokine receptor 5
CXCR6	C-X-C motif chemokine receptor 6
CYBB	cytochrome b-245 beta chain
CYLD	CYLD lysine 63 deubiquitinase
CYP27A1	cytochrome P450 family 27 subfamily A member 1
DAPK2	death associated protein kinase 2
DAPL1	death associated protein like 1
DBF4	DBF4 homolog (<i>S. cerevisiae</i>)
DCLRE1A	DNA cross-link repair 1A
DCN	decorin
DDIAS	DNA damage induced apoptosis suppressor
DDX5	DEAD-box helicase 5
DDX58	DExD/H-box helicase 58
DEFB1	defensin beta 1
DEPDC1	DEP domain containing 1

DGAT2	diacylglycerol O-acyltransferase 2
DGKA	diacylglycerol kinase alpha
DHX40	DEAH-box helicase 40
DIAPH3	Diaphanous homolog 3 (Drosophila)
DLAT	dihydrolipoamide S-acetyltransferase
DLD	dihydrolipoamide dehydrogenase
DLGAP5	Discs, large (Drosophila) homolog-associated protein 5
DLX6	distal-less homeobox 6
DMBT1	deleted in malignant brain tumors 1
DNAH14	dynein axonemal heavy chain 14
DNMT1	DNA methyltransferase 1
DOCK9	dedicator of cytokinesis 9
DONSON	Downstream neighbor of SON
DPP4	dipeptidyl peptidase 4
DPYSL4	dihydropyrimidinase like 4
DSC3	desmocollin 3
DSE	dermatan sulfate epimerase
DSG3	desmoglein 3
DST	dystonin
DTL	Denticleless E3 ubiquitin protein ligase homolog (Drosophila)
DUSP4	dual specificity phosphatase 4
DUSP6	dual specificity phosphatase 6
E2F2	E2F transcription factor 2
E2F7	E2F transcription factor 7
EBF4	early B-cell factor 4
EBI3	Epstein-Barr virus induced 3
ECT2	Epithelial cell transforming sequence 2 oncogene
EEF1G	eukaryotic translation elongation factor 1 gamma
EEF2	eukaryotic translation elongation factor 2
EFNA4	ephrin A4
EFNB3	ephrin B3
EGFR	epidermal growth factor receptor
EGR1	early growth response 1
EGR2	early growth response 2
EGR3	early growth response 3
EHD2	EH domain containing 2
EIF2A	eukaryotic translation initiation factor 2A
EIF2AK2	eukaryotic translation initiation factor 2 alpha kinase 2
ELK1	ETS transcription factor
ELL3	Elongation factor RNA polymerase II-like 3
EME1	Essential meiotic endonuclease 1 homolog 1 (S. pombe)
EMP1	epithelial membrane protein 1
EMX2	empty spiracles homeobox 2
ENG	endoglin
ENO1	enolase 1
ENTPD1	ectonucleoside triphosphate diphosphohydrolase 1
EOMES	eomesodermin

EP300	E1A binding protein p300
EPCAM	epithelial cell adhesion molecule
EPHX3	epoxide hydrolase 3
EPSTI1	epithelial stromal interaction 1
ERBB2	erb-b2 receptor tyrosine kinase 2
ERBB3	erb-b2 receptor tyrosine kinase 3
ERCC6L	Excision repair cross-complementing rodent repair deficiency, complementation group 6-like
ESCO2	Establishment of cohesion 1 homolog 2 (<i>S. cerevisiae</i>)
ESPL1	extra spindle pole bodies like 1, separase
ESYT2	extended synaptotagmin 2
ETS1	ETS proto-oncogene 1, transcription factor
ETS2	ETS proto-oncogene 2, transcription factor
ETV1	ETS variant 1
ETV4	ETS variant 4
EWSR1	EWS RNA binding protein 1
EXO1	Exonuclease 1
EYS	eyes shut homolog (<i>Drosophila</i>)
EZH2	enhancer of zeste 2 polycomb repressive complex 2 subunit
F13A1	coagulation factor XIII A chain
F2RL1	F2R like trypsin receptor 1
FABP4	fatty acid binding protein 4
FADD	Fas associated via death domain
FAM111B	Family with sequence similarity 111, member B
FAM122B	family with sequence similarity 122B
FAM161A	family with sequence similarity 161 member A
FAM222A	family with sequence similarity 222 member A
FAM69B	family with sequence similarity 69 member B
FAM72_family	family with sequence similarity 72 (family probe)
FAM83B	family with sequence similarity 83 member B
FANCA	Fanconi anemia, complementation group A
FANCD2	Fanconi anemia, complementation group D2
FANCI	Fanconi anemia, complementation group I
FAP	fibroblast activation protein alpha
FAS	Fas cell surface death receptor
FASLG	Fas ligand
FBLN1	fibulin 1
FCAR	Fc fragment of IgA receptor
FCER1G	Fc fragment of IgE receptor Ig
FCER2	Fc fragment of IgE receptor II
FCGR1A_FCGR1B	Fc fragment of IgG receptor Ia and 1b
FCGR2A_2C	Fc fragment of IgG receptor IIa and IIc
FCGR2B	Fc fragment of IgG receptor IIb
FCGR3A_3B	Fc fragment of IgG receptor IIIa and IIIb
FCMR	Fc fragment of IgM receptor
FCRL2	Fc receptor like 2
FCRLA	Fc receptor like A

FEN1	Flap structure-specific endonuclease 1
FEZ1	fasciculation and elongation protein zeta 1
FGD6	FYVE, RhoGEF and PH domain containing 6
FGFR3	fibroblast growth factor receptor 3
FICD	FIC domain containing
FLI1	Fli-1 proto-oncogene, ETS transcription factor
FLT1	fms related tyrosine kinase 1
FLT3	fms related tyrosine kinase 3
FLT3LG	fms related tyrosine kinase 3 ligand
FLVCR1	feline leukemia virus subgroup C cellular receptor 1
FMO5	flavin containing monooxygenase 5
FN1	fibronectin 1
FOLH1	folate hydrolase 1
FOS	Fos proto-oncogene, AP-1 transcription factor subunit
FOXA1	forkhead box A1
FOXG1	forkhead box G1
FOXJ1	forkhead box J1
FOXM1	forkhead box M1
FOXO1	forkhead box O1
FOXP1	forkhead box P1
FOXP3	forkhead box P3
FOXRED2	FAD dependent oxidoreductase domain containing 2
FPR1	formyl peptide receptor 1
FPR2	formyl peptide receptor 2
FRYL	FRY like transcription coactivator
FUT4	fucosyltransferase 4
FUT5	fucosyltransferase 5
FXRD5	FXRD domain containing ion transport regulator 5
FYB1	FYN binding protein 1
FYN	FYN proto-oncogene, Src family tyrosine kinase
FZD3	frizzled class receptor 3
G6PD	glucose-6-phosphate dehydrogenase
GABRA5	gamma-aminobutyric acid type A receptor alpha5 subunit
GAD1	glutamate decarboxylase 1
GADD45GIP1	GADD45G interacting protein 1
GAGE_family	G antigen (family probe)
GATA2	GATA binding protein 2
GATA3	GATA binding protein 3
GBP1	guanylate binding protein 1
GBP5	guanylate binding protein 5
GCK_liver_T2	glucokinase (liver specific)
GCK_Pan_T2	glucokinase (pancreas specific)
GCK	glucokinase (all isoforms)
GDF15	growth differentiation factor 15
GGT7	gamma-glutamyltransferase 7
GINS4	GINS complex subunit 4 (Sld5 homolog)
GLB1L2	galactosidase beta 1 like 2

GLIPR1	GLI pathogenesis related 1
GNLY	granulysin
GPI	glucose-6-phosphate isomerase
GPR18	G protein-coupled receptor 18
GPR19	G protein-coupled receptor 19
GPRIN1	G protein regulated inducer of neurite outgrowth 1
GRAP2	GRB2-related adaptor protein 2
GSDME	gasdermin E
GTF3C1	general transcription factor IIIC subunit 1
GTSE1	G-2 and S-phase expressed 1
GUSB	glucuronidase beta
GZMA	granzyme A
GZMB	granzyme B
GZMH	granzyme H
GZMK	granzyme K
GZMM	granzyme M
H2AFZ	H2A histone family member Z
HASPIN	histone H3 associated protein kinase
HAVCR2	hepatitis A virus cellular receptor 2
HCAR1	hydroxycarboxylic acid receptor 1
HCAR2	hydroxycarboxylic acid receptor 2
HDC	histidine decarboxylase
HELLS	helicase, lymphoid specific
HERC6	HECT and RLD domain containing E3 ubiquitin protein ligase family member 6
HES1	hes family bHLH transcription factor 1
HES5	hes family bHLH transcription factor 5
HEXIM2	hexamethylene bisacetamide inducible 2
HEY1	hes related family bHLH transcription factor with YRPW motif 1
HEY2	hes related family bHLH transcription factor with YRPW motif 2
HEYL	hes related family bHLH transcription factor with YRPW motif-like
HGF	hepatocyte growth factor
HHLA2	HERV-H LTR-associating 2
HIF1A	hypoxia inducible factor 1 alpha subunit
HIST1H2BH	Histone cluster 1, H2bh
HJURP	Holliday junction recognition protein
HK1	hexokinase 1
HK2	hexokinase 2
HLA-A	major histocompatibility complex, class I, A
HLA-B	major histocompatibility complex, class I, B
HLA-C	major histocompatibility complex, class I, C
HLA-DMA	major histocompatibility complex, class II, DM alpha
HLA-DMB	major histocompatibility complex, class II, DM beta
HLA-DOA	major histocompatibility complex, class II, DO alpha
HLA-DOB	major histocompatibility complex, class II, DO beta
HLA-DPA1	major histocompatibility complex, class II, DP alpha 1
HLA-DPB1	major histocompatibility complex, class II, DP beta 1
HLA-DQA1	major histocompatibility complex, class II, DQ alpha 1

HLA-DQA2	major histocompatibility complex, class II, DQ alpha 2
HLA-DQB1	major histocompatibility complex, class II, DQ beta 1
HLA-DQB2	major histocompatibility complex, class II, DQ beta 2
HLA-DRA	major histocompatibility complex, class II, DR alpha
HLA-DRB1	major histocompatibility complex, class II, DR beta 1
HLA-E	major histocompatibility complex, class I, E
HLA-F	major histocompatibility complex, class I, F
HLA-G	major histocompatibility complex, class I, G
HLF	HLF, PAR bZIP transcription factor
HMBS	hydroxymethylbilane synthase
HMGB1	high mobility group box 1
HMGCS2	3-hydroxy-3-methylglutaryl-CoA synthase 2
HMMR	Hyaluronan-mediated motility receptor
HMOX1	heme oxygenase 1
HMX2	H6 family homeobox 2
HNF1A	HNF1 homeobox A
HNF1B	HNF1 homeobox B
HORMAD1	HORMA domain containing 1
HORMAD2	HORMA domain containing 2
HPDL	4-hydroxyphenylpyruvate dioxygenase like
HPN	hepsin
HRAS	HRas proto-oncogene, GTPase
HSD11B1	hydroxysteroid 11-beta dehydrogenase 1
HSP90B1	heat shock protein 90 beta family member 1
HSPA1A	heat shock protein family A (Hsp70) member 1A
IBSP	integrin binding sialoprotein
ICAM1	intercellular adhesion molecule 1
ICAM2	intercellular adhesion molecule 2
ICAM3	intercellular adhesion molecule 3
ICAM4	intercellular adhesion molecule 4 (Landsteiner-Wiener blood group)
ICOS	inducible T-cell costimulator
ICOSLG	inducible T-cell costimulator ligand
ID2	inhibitor of DNA binding 2
ID3	inhibitor of DNA binding 3, HLH protein
ID4	inhibitor of DNA binding 4, HLH protein
IDH1	isocitrate dehydrogenase (NADP(+)) 1, cytosolic
IDH2	isocitrate dehydrogenase (NADP(+)) 2, mitochondrial
IDO1	indoleamine 2,3-dioxygenase 1
IDO2	indoleamine 2,3-dioxygenase 2
IFI16	interferon gamma inducible protein 16
IFI27	interferon alpha inducible protein 27
IFI35	interferon induced protein 35
IFI44L	interferon induced protein 44 like
IFI6	interferon alpha inducible protein 6
IFIH1	interferon induced with helicase C domain 1
IFIT1	interferon induced protein with tetratricopeptide repeats 1
IFIT2	interferon induced protein with tetratricopeptide repeats 2

IFIT3	interferon induced protein with tetratricopeptide repeats 3
IFIT5	interferon induced protein with tetratricopeptide repeats 5
IFITM1	interferon induced transmembrane protein 1
IFITM2	interferon induced transmembrane protein 2
IFITM3	interferon induced transmembrane protein 3
IFNA_Family	interferon alpha (family probe)
IFNAR1	interferon alpha and beta receptor subunit 1
IFNAR2	interferon alpha and beta receptor subunit 2
IFNB1	interferon beta 1
IFNG	interferon gamma
IFNGR1	interferon gamma receptor 1
IFNL1	interferon lambda 1
IFNL2	interferon lambda 2
IFNL3	interferon lambda 3
IFNL4	interferon lambda 4 (gene/pseudogene)
IFNLR1	interferon lambda receptor 1
IGF1R	insulin like growth factor 1 receptor
IGF2R	insulin like growth factor 2 receptor
IGFBP3	insulin like growth factor binding protein 3
IGSF6	immunoglobulin superfamily member 6
IHH	indian hedgehog
IKBKB	inhibitor of nuclear factor kappa B kinase subunit beta
IKBKG	inhibitor of nuclear factor kappa B kinase subunit gamma
IKZF1	IKAROS family zinc finger 1
IKZF2	IKAROS family zinc finger 2
IKZF3	IKAROS family zinc finger 3
IKZF4	IKAROS family zinc finger 4
IL10	interleukin 10
IL10RA	interleukin 10 receptor subunit alpha
IL10RB	interleukin 10 receptor subunit beta
IL11	interleukin 11
IL11RA	interleukin 11 receptor subunit alpha
IL12A	interleukin 12A
IL12B	interleukin 12B
IL12RB1	interleukin 12 receptor subunit beta 1
IL12RB2	interleukin 12 receptor subunit beta 2
IL13	interleukin 13
IL13RA1	interleukin 13 receptor subunit alpha 1
IL13RA2	interleukin 13 receptor subunit alpha 2
IL15	interleukin 15
IL15RA	interleukin 15 receptor subunit alpha
IL16	interleukin 16
IL17A	interleukin 17A
IL17B	interleukin 17B
IL17C	interleukin 17C
IL17D	interleukin 17D
IL17F	interleukin 17F

IL17RA	interleukin 17 receptor A
IL17RB	interleukin 17 receptor B
IL18	interleukin 18
IL18BP	interleukin 18 binding protein
IL18R1	interleukin 18 receptor 1
IL19	interleukin 19
IL1A	interleukin 1 alpha
IL1B	interleukin 1 beta
IL1R1	interleukin 1 receptor type 1
IL1R2	interleukin 1 receptor type 2
IL1RAP	interleukin 1 receptor accessory protein
IL1RL1	interleukin 1 receptor like 1
IL1RL2	interleukin 1 receptor like 2
IL1RN	interleukin 1 receptor antagonist
IL2	interleukin 2
IL20	interleukin 20
IL20RA	interleukin 20 receptor subunit alpha
IL20RB	interleukin 20 receptor subunit beta
IL21	interleukin 21
IL21R	interleukin 21 receptor
IL22	interleukin 22
IL22RA1	interleukin 22 receptor subunit alpha 1
IL22RA2	interleukin 22 receptor subunit alpha 2
IL23A	interleukin 23 subunit alpha
IL23R	interleukin 23 receptor
IL24	interleukin 24
IL25	interleukin 25
IL26	interleukin 26
IL27	interleukin 27
IL2RA	interleukin 2 receptor subunit alpha
IL2RB	interleukin 2 receptor subunit beta
IL2RG	interleukin 2 receptor subunit gamma
IL3	interleukin 3
IL31	interleukin 31
IL32	interleukin 32
IL33	interleukin 33
IL34	interleukin 34
IL3RA	interleukin 3 receptor subunit alpha
IL4	interleukin 4
IL4R	interleukin 4 receptor
IL5	interleukin 5
IL5RA	interleukin 5 receptor subunit alpha
IL6	interleukin 6
IL6R	interleukin 6 receptor
IL6ST	interleukin 6 signal transducer
IL7	interleukin 7
IL7R	interleukin 7 receptor

IL9	interleukin 9
IL9R	interleukin 9 receptor
IMPG2	interphotoreceptor matrix proteoglycan 2
INSM1	INSM transcriptional repressor 1
IQGAP3	IQ motif containing GTPase activating protein 3
IRAK1	interleukin 1 receptor associated kinase 1
IRAK2	interleukin 1 receptor associated kinase 2
IRAK3	interleukin 1 receptor associated kinase 3
IRAK4	interleukin 1 receptor associated kinase 4
IRF1	interferon regulatory factor 1
IRF2	interferon regulatory factor 2
IRF3	interferon regulatory factor 3
IRF4	interferon regulatory factor 4
IRF5	interferon regulatory factor 5
IRF7	interferon regulatory factor 7
IRF8	interferon regulatory factor 8
IRF9	interferon regulatory factor 9
IRGM	immunity related GTPase M
IRS1	insulin receptor substrate 1
ISG15	ISG15 ubiquitin-like modifier
ISG20	interferon stimulated exonuclease gene 20
ITGA1	integrin subunit alpha 1
ITGA2	integrin subunit alpha 2
ITGA3	integrin subunit alpha 3
ITGA4	integrin subunit alpha 4
ITGA5	integrin subunit alpha 5
ITGA6	integrin subunit alpha 6
ITGAE	integrin subunit alpha E
ITGAL	integrin subunit alpha L
ITGAM	integrin subunit alpha M
ITGAX	integrin subunit alpha X
ITGB1	integrin subunit beta 1
ITGB2	integrin subunit beta 2
ITGB3	integrin subunit beta 3
ITGB4	integrin subunit beta 4
ITGB7	integrin subunit beta 7
ITK	IL2 inducible T-cell kinase
ITLN2	intelectin 2
ITPKC	inositol-trisphosphate 3-kinase C
JAK1	Janus kinase 1
JAK2	Janus kinase 2
JAK3	Janus kinase 3
JAKMIP3	Janus kinase and microtubule interacting protein 3
JAML	junction adhesion molecule like
JCHAIN	joining chain of multimeric IgA and IgM
KCNA1	potassium voltage-gated channel subfamily A member 1
KCNH2	potassium voltage-gated channel subfamily H member 2

KCNK5	potassium two pore domain channel subfamily K member 5
KDM5B	lysine demethylase 5B
KDR	kinase insert domain receptor
KHDRBS2	KH RNA binding domain containing, signal transduction associated 2
KHK	Ketohexokinase (fructokinase)
KIF14	Kinesin family member 14
KIF15	Kinesin family member 15
KIF18B	Kinesin family member 18B
KIF20A	Kinesin family member 20A
KIF23	Kinesin family member 23
KIF2C	Kinesin family member 2C
KIF4A	Kinesin family member 4A
KIF5C	kinesin family member 5C
KIFC1	Kinesin family member C1
KIR2DL1	killer cell immunoglobulin like receptor, two Ig domains and long cytoplasmic tail 1
KIR2DL1_2DL2	killer cell immunoglobulin like receptor, two Ig domains and long cytoplasmic tail 1 and 2
KIR2DL3	killer cell immunoglobulin like receptor, two Ig domains and long cytoplasmic tail 3
KIR2DL4	killer cell immunoglobulin like receptor, two Ig domains and long cytoplasmic tail 4
KIR2DL5A_5B	killer cell immunoglobulin like receptor, two Ig domains and long cytoplasmic tail 5A and 5B
KIR2DS2_2DS4	killer cell immunoglobulin like receptor, two Ig domains and short cytoplasmic tail 2 and 4
KIR2DS4	killer cell immunoglobulin like receptor, two Ig domains and short cytoplasmic tail 4
KIR2DSx	killer cell immunoglobulin like receptor, two Ig domains and short cytoplasmic tail (all isoforms)
KIR3DL1	killer cell immunoglobulin like receptor, three Ig domains and long cytoplasmic tail 1
KIR3DL2	killer cell immunoglobulin like receptor, three Ig domains and long cytoplasmic tail 2
KIR3DL3	killer cell immunoglobulin like receptor, three Ig domains and long cytoplasmic tail 3
KIR3DS1	killer cell immunoglobulin like receptor, three Ig domains and short cytoplasmic tail 1
KIR-panL	killer cell immunoglobulin like receptor, pan long forms
KIR-panS	killer cell immunoglobulin like receptor, pan short forms
KIT	KIT proto-oncogene receptor tyrosine kinase
KLF2	Kruppel like factor 2
KLHDC9	kelch domain containing 9
KLRB1	killer cell lectin like receptor B1
KLRD1	killer cell lectin like receptor D1
KLRF1	killer cell lectin like receptor F1
KLRG1	killer cell lectin like receptor G1
KLRK1	killer cell lectin like receptor K1
KNL1	kinetochore scaffold 1
KPNA2	Karyopherin alpha 2 (RAG cohort 1, importin alpha 1)
KREMEN1	kringle containing transmembrane protein 1
KRT13	keratin 13
KRT16	keratin 16

KRT17	keratin 17
KRT18	keratin 18
KRT19	keratin 19
KRT34	Keratin 34
KRT5	keratin 5
KRT6A	keratin 6A
KRT7	keratin 7
KRT8	keratin 8
KRTCAP3	keratinocyte associated protein 3
KSR2	Kinase suppressor of ras 2
L1CAM	L1 cell adhesion molecule
LAG3	lymphocyte activating 3
LAIR2	leukocyte associated immunoglobulin like receptor 2
LAMC3	Laminin, gamma 3
LAMP1	lysosomal associated membrane protein 1
LAMP3	lysosomal associated membrane protein 3
LAPTM5	lysosomal protein transmembrane 5
LAT	linker for activation of T cells
LCK	LCK proto-oncogene, Src family tyrosine kinase
LCN2	lipocalin 2
LCP1	lymphocyte cytosolic protein 1
LEXM	lymphocyte expansion molecule
LGALS1	galectin 1
LGALS3	galectin 3
LGALS9	galectin 9
LGSN	lengsin, lens protein with glutamine synthetase domain
LIF	leukemia inhibitory factor
LILRA4	leukocyte immunoglobulin like receptor A4
LILRB1	leukocyte immunoglobulin like receptor B1
LILRB2	leukocyte immunoglobulin like receptor B2
LIMA1	LIM domain and actin binding 1
LIPE	lipase E, hormone sensitive type
LMNA	lamin A/C
LMNB1	Lamin B1
LOXL1	lysyl oxidase like 1
LOXL2	lysyl oxidase like 2
LRBA	LPS responsive beige-like anchor protein
LRG1	leucine rich alpha-2-glycoprotein 1
LRP1	LDL receptor related protein 1
LST1	leukocyte specific transcript 1
LTA	lymphotoxin alpha
LTB	lymphotoxin beta
LTB4R	leukotriene B4 receptor
LTBP1	latent transforming growth factor beta binding protein 1
LTBR	lymphotoxin beta receptor
LTK	leukocyte receptor tyrosine kinase
LY86	lymphocyte antigen 86

LY9	lymphocyte antigen 9
LY96	lymphocyte antigen 96
LYN	LYN proto-oncogene, Src family tyrosine kinase
LYVE1	lymphatic vessel endothelial hyaluronan receptor 1
LYZ	lysozyme
M6PR	mannose-6-phosphate receptor, cation dependent
MAB21L2	mab-21 like 2
MAD2L1	MAD2 mitotic arrest deficient-like 1 (yeast)
MADCAM1	mucosal vascular addressin cell adhesion molecule 1
MAF	MAF bZIP transcription factor
MAGEA1	MAGE family member A1
MAGEA10	MAGE family member A10
MAGEA12	MAGE family member A12
MAGEA3_A6	MAGE family member A3/A6
MAGEA4	MAGE family member A4
MAGEB2	MAGE family member B2
MAGEC1	MAGE family member C1
MAGEC2	MAGE family member C2
MAP2K1	mitogen-activated protein kinase kinase 1
MAP2K2	mitogen-activated protein kinase kinase 2
MAP2K4	mitogen-activated protein kinase kinase 4
MAP2K6	Mitogen-activated protein kinase kinase 6
MAP2K7	mitogen-activated protein kinase kinase 7
MAP3K1	mitogen-activated protein kinase kinase kinase 1
MAP3K5	mitogen-activated protein kinase kinase kinase 5
MAP3K7	mitogen-activated protein kinase kinase kinase 7
MAP4	Microtubule-associated protein 4
MAP4K1	mitogen-activated protein kinase kinase kinase kinase 1
MAPK1	mitogen-activated protein kinase 1
MAPK11	mitogen-activated protein kinase 11
MAPK14	mitogen-activated protein kinase 14
MAPK3	mitogen-activated protein kinase 3
MAPK8	mitogen-activated protein kinase 8
MAPKAPK2	mitogen-activated protein kinase-activated protein kinase 2
MARCO	macrophage receptor with collagenous structure
MBL2	mannose binding lectin 2
MCM10	Minichromosome maintenance complex component 10
MCM2	minichromosome maintenance complex component 2
MCM6	Minichromosome maintenance complex component 6
MCM7	minichromosome maintenance complex component 7
MECOM	MDS1 and EVI1 complex locus
MEF2C	myocyte enhancer factor 2C
MELK	maternal embryonic leucine zipper kinase
MERTK	MER proto-oncogene, tyrosine kinase
MGA	MAX dimerization protein
MICA	MHC class I polypeptide-related sequence A
MICB	MHC class I polypeptide-related sequence B

MIF	macrophage migration inhibitory factor (glycosylation-inhibiting factor)
MKI67	marker of proliferation Ki-67
MLANA	melan-A
MLF1	myeloid leukemia factor 1
MME	membrane metalloendopeptidase
MMP11	matrix metalloproteinase 11
MMP12	matrix metalloproteinase 12
MMP2	matrix metalloproteinase 2
MMP9	matrix metalloproteinase 9
MND1	Meiotic nuclear divisions 1 homolog (<i>S. cerevisiae</i>)
MNDA	myeloid cell nuclear differentiation antigen
MOB3A	MOB kinase activator 3A
MPO	myeloperoxidase
MPPED1	metallophosphoesterase domain containing 1
MR1	major histocompatibility complex, class I-related
MRAP2	melanocortin 2 receptor accessory protein 2
MRC1	mannose receptor C-type 1
MS4A1	membrane spanning 4-domains A1
MS4A2	membrane spanning 4-domains A2
MS4A4A	membrane spanning 4-domains A4A
MSH2	mutS homolog 2
MSH3	mutS homolog 3
MSH4	mutS homolog 4
MSH5	mutS homolog 5
MSH6	mutS homolog 6
MSR1	macrophage scavenger receptor 1
MST1R	macrophage stimulating 1 receptor
MT2A	metallothionein 2A
MTDH	metadherin
MTFR2	Mitochondrial fission regulator 2
MTOR	mechanistic target of rapamycin kinase
MUC1	mucin 1, cell surface associated
MX1	MX dynamin like GTPase 1
MXD3	MAX dimerization protein 3
MYBL2	V-myb myeloblastosis viral oncogene homolog (avian)-like 2
MYC	v-myc avian myelocytomatosis viral oncogene homolog
MYD88	myeloid differentiation primary response 88
MYH10	myosin heavy chain 10
MYH11	myosin heavy chain 11
MYH9	myosin heavy chain 9
MYO1B	Myosin IB
MYO5C	myosin VC
MYOCD	myocardin
MYOF	myoferlin
NCAM1	neural cell adhesion molecule 1
NCAPG	Non-SMC condensin I complex, subunit G
NCAPG2	Non-SMC condensin II complex, subunit G2

NCAPH	Non-SMC condensin I complex, subunit H
NCF1	neutrophil cytosolic factor 1
NCK1	NCK adaptor protein 1
NCL	nucleolin
NCR1	natural cytotoxicity triggering receptor 1
NCR3	natural cytotoxicity triggering receptor 3
NCR3LG1	natural killer cell cytotoxicity receptor 3 ligand 1
NDC1	NDC1 transmembrane nucleoporin (also called TMEM48)
NDC80	NDC80 kinetochore complex component
NECTIN2	nectin cell adhesion molecule 2
NEFL	neurofilament light
NEIL3	nei like DNA glycosylase 3
NEK2	NIMA-related kinase 2
NFATC1	nuclear factor of activated T-cells 1
NFATC3	nuclear factor of activated T-cells 3
NFATC4	nuclear factor of activated T cells 4
NFKB1	nuclear factor kappa B subunit 1
NFKB2	nuclear factor kappa B subunit 2
NFKBIA	NFKB inhibitor alpha
NGFR	nerve growth factor receptor
NKG7	natural killer cell granule protein 7
NKX2-1	NK2 homeobox 1
NLRC5	NLR family CARD domain containing 5
NLRP3	NLR family pyrin domain containing 3
NMRAL1	NmrA like redox sensor 1
NOD1	nucleotide binding oligomerization domain containing 1
NOD2	nucleotide binding oligomerization domain containing 2
NOS2	nitric oxide synthase 2
NOS3	nitric oxide synthase 3
NOTCH1	notch 1
NOTCH3	notch 3
NOX1	NADPH oxidase 1
NPM1	nucleophosmin 1
NPR3	natriuretic peptide receptor 3
NRL	neural retina leucine zipper
NRP1	neuropilin 1
NT5E	5'-nucleotidase ecto
NTN3	netrin 3
NTRK2	neurotrophic receptor tyrosine kinase 2
NUDT1	Nudix (nucleoside diphosphate linked moiety X)-type motif 1
NUF2	NUF2, NDC80 kinetochore complex component, homolog (<i>S. cerevisiae</i>)
NUP107	nucleoporin 107
NUSAP1	Nucleolar and spindle associated protein 1
OAS1	2'-5'-oligoadenylate synthetase 1
OAS2	2'-5'-oligoadenylate synthetase 2
OAS3	2'-5'-oligoadenylate synthetase 3
OAZ1	ornithine decarboxylase antizyme 1

OCLN	occludin
OIP5	Opa interacting protein 5
OLR1	oxidized low density lipoprotein receptor 1
OPTN	Optineurin
ORC1	Hs.17908
ORC6	Origin recognition complex, subunit 6
OSM	oncostatin M
PAGE1	PAGE family member 1
PAGE2	PAGE family members 2 and 2B
PAGE3	PAGE family member 3
PAGE4	PAGE family member 4
PAGE5	PAGE family member 5
PATZ1	POZ (BTB) and AT hook containing zinc finger 1
PAX5	paired box 5
PBK	PDZ binding kinase
PBX1	PBX homeobox 1
PCLAF	PCNA clamp associated factor
PCNA	proliferating cell nuclear antigen
PDCD1	programmed cell death 1
PDCD1LG2	programmed cell death 1 ligand 2
PDGFC	platelet derived growth factor C
PDGFRB	platelet derived growth factor receptor beta
PDHA1	pyruvate dehydrogenase E1 alpha 1 subunit
PDHA2	pyruvate dehydrogenase E1 alpha 2 subunit
PDHB	pyruvate dehydrogenase E1 beta subunit
PDHX	pyruvate dehydrogenase complex component X
PDK1	pyruvate dehydrogenase kinase 1
PDK2	pyruvate dehydrogenase kinase 2
PDK3	pyruvate dehydrogenase kinase 3
PDK4	pyruvate dehydrogenase kinase 4
PDLIM1	PDZ and LIM domain 1
PDLIM3	PDZ and LIM domain 3
PDP1	pyruvate dehydrogenase phosphatase catalytic subunit 1
PECAM1	platelet and endothelial cell adhesion molecule 1
PF4	platelet factor 4
PFKFB3	6-phosphofructo-2-kinase/fructose-2,6-biphosphatase 3
PFKFB4	6-phosphofructo-2-kinase/fructose-2,6-biphosphatase 4
PGF	placental growth factor
PHF10	PHD finger protein 10
PIF1	PIF1 5'-to-3' DNA helicase homolog (<i>S. cerevisiae</i>)
PIK3CA	phosphatidylinositol-4,5-bisphosphate 3-kinase catalytic subunit alpha
PIK3CD	phosphatidylinositol-4,5-bisphosphate 3-kinase catalytic subunit delta
PIK3CG	phosphatidylinositol-4,5-bisphosphate 3-kinase catalytic subunit gamma
PIMREG	PICALM interacting mitotic regulator
PKLR	pyruvate kinase L/R
PKM	pyruvate kinase M1/2
PKMYT1	Protein kinase, membrane associated tyrosine/threonine 1

PKP1	plakophilin 1
PLA2G6	phospholipase A2 group VI
PLA2G7	phospholipase A2 group VII
PLAU	plasminogen activator, urokinase
PLAUR	plasminogen activator, urokinase receptor
PLEKHG4	pleckstrin homology and RhoGEF domain containing G4
PLEKHG6	pleckstrin homology and RhoGEF domain containing G6
PLK1	Polo-like kinase 1
PLK4	Polo-like kinase 4
PMCH	pro-melanin concentrating hormone
PMEL	premelanosome protein
PML	Promyelocytic leukemia
PNOC	prepronociceptin
POC1A	POC1 centriolar protein homolog A (Chlamydomonas)
PODXL2	podocalyxin like 2
POLQ	Polymerase (DNA directed), theta
POLR2A	RNA polymerase II subunit A
POU2AF1	POU class 2 associating factor 1
POU2F2	POU class 2 homeobox 2
POU5F1	POU class 5 homeobox 1 and 1B
PPARD	peroxisome proliferator activated receptor delta
PPARG	peroxisome proliferator activated receptor gamma
PPBP	pro-platelet basic protein
PPIA	peptidylprolyl isomerase A
PPM1E	Protein phosphatase, Mg ²⁺ /Mn ²⁺ dependent, 1E
PRAME	preferentially expressed antigen in melanoma
PRC1	Protein regulator of cytokinesis 1
PRDM1	PR/SET domain 1
PRDM6	PR/SET domain 6
PRF1	perforin 1
PRG2	proteoglycan 2, pro eosinophil major basic protein
PRKCD	protein kinase C delta
PRKCE	protein kinase C epsilon
PRR11	Proline rich 11
PRR15L	proline rich 15 like
PSEN1	presenilin 1
PSEN2	presenilin 2
PSMB10	proteasome subunit beta 10
PSMB5	proteasome subunit beta 5
PSMB6	proteasome subunit beta 6
PSMB7	proteasome subunit beta 7
PSMB8	proteasome subunit beta 8
PSMB9	proteasome subunit beta 9
PSMD7	proteasome 26S subunit, non-ATPase 7
PSRC1	Proline/serine-rich coiled-coil 1
PTEN	phosphatase and tensin homolog
PTGDR2	prostaglandin D2 receptor 2

PTGER1	prostaglandin E receptor 1
PTGER2	prostaglandin E receptor 2
PTGER3	prostaglandin E receptor 3
PTGER4	prostaglandin E receptor 4
PTGS1	prostaglandin-endoperoxide synthase 1
PTGS2	prostaglandin-endoperoxide synthase 2
PTK7	protein tyrosine kinase 7 (inactive)
PTPN11	protein tyrosine phosphatase, non-receptor type 11
PTPN6	protein tyrosine phosphatase, non-receptor type 6
PTPN7	protein tyrosine phosphatase, non-receptor type 7
PTPRC	protein tyrosine phosphatase, receptor type C
PTPRCAP	protein tyrosine phosphatase, receptor type C associated protein
PVR	poliovirus receptor
PVT1	Pvt1 oncogene (non-protein coding)
PXYLP1	2-phosphoxylose phosphatase 1
PYCARD	PYD and CARD domain containing
PYCR1	pyrroline-5-carboxylate reductase 1
PYGL	glycogen phosphorylase L
RAC1	Rac family small GTPase 1
RACGAP1	Rac GTPase activating protein 1
RAD51	RAD51 homolog (<i>S. cerevisiae</i>)
RAD51AP1	RAD51 associated protein 1
RAD54L	RAD54-like (<i>S. cerevisiae</i>)
RAG1	recombination activating 1
RB1	RB transcriptional corepressor 1
RBM24	RNA binding motif protein 24
RBX1	ring-box 1
RDM1	RAD52 motif 1
REL	REL proto-oncogene, NF-kB subunit
RELA	RELA proto-oncogene, NF-kB subunit
RELB	RELB proto-oncogene, NF-kB subunit
REPS1	RALBP1 associated Eps domain containing 1
REV3L	REV3 like, DNA directed polymerase zeta catalytic subunit
RFC4	replication factor C subunit 4
RGS20	regulator of G protein signaling 20
RHOG	ras homolog family member G
RIC8A	Resistance to inhibitors of cholinesterase 8 homolog A (<i>C. elegans</i>)
RIPK2	receptor interacting serine/threonine kinase 2
RMI2	RMI2, RecQ mediated genome instability 2, homolog (<i>S. cerevisiae</i>)
RNASEH2A	ribonuclease H2 subunit A
RND2	Rho family GTPase 2
RNF149	ring finger protein 149
RNF4	ring finger protein 4
RNFT2	Ring finger protein, transmembrane 2
ROR2	receptor tyrosine kinase like orphan receptor 2
RORC	RAR related orphan receptor C
RPL38	ribosomal protein L38

RPL6	ribosomal protein L6
RPS19	ribosomal protein S19
RPS6	ribosomal protein S6
RPS7	ribosomal protein S7
RPSA	ribosomal protein SA
RRAD	Ras related glycolysis inhibitor and calcium channel regulator
RRAS2	Related RAS viral (r-ras) oncogene homolog 2
RRM1	Ribonucleotide reductase M1
RRM2	Ribonucleotide reductase M2
RTN1	reticulon 1
RUNX1	runt related transcription factor 1
RUNX3	runt related transcription factor 3
S100A12	S100 calcium binding protein A12
S100A8	S100 calcium binding protein A8
S100A9	S100 calcium binding protein A9
S100B	S100 calcium binding protein B
SALL2	spalt like transcription factor 2
SAMD12	sterile alpha motif domain containing 12
SAMD9	sterile alpha motif domain containing 9
SAMHD1	SAM and HD domain containing deoxynucleoside triphosphate triphosphohydrolase 1
SCAMP5	secretory carrier membrane protein 5
SCG3	secretogranin III
SDHA	succinate dehydrogenase complex flavoprotein subunit A
SELE	selectin E
SELL	selectin L
SELPLG	selectin P ligand
SEMA4D	semaphorin 4D
SERINC2	serine incorporator 2
SERPINA1	serpin family A member 1
SERPINB2	serpin family B member 2
SERPINB5	serpin family B member 5
SERPINB7	serpin family B member 7
SERPINE1	serpin family E member 1
SGO1	shugoshin 1
SGO2	shugoshin 2
SH2D1A	SH2 domain containing 1A
SH2D1B	SH2 domain containing 1B
SHCBP1	SHC SH2-domain binding protein 1
SIGIRR	single Ig and TIR domain containing
SIGLEC5	sialic acid binding Ig like lectin 5
SIT1	signaling threshold regulating transmembrane adaptor 1
SKA1	Spindle and kinetochore associated complex subunit 1
SKA3	Spindle and kinetochore associated complex subunit 3
SKAP2	src kinase associated phosphoprotein 2
SKP2	S-phase kinase-associated protein 2, E3 ubiquitin protein ligase
SLAMF1	signaling lymphocytic activation molecule family member 1
SLAMF6	SLAM family member 6

SLAMF7	SLAM family member 7
SLAMF8	SLAM family member 8
SLC11A1	solute carrier family 11 member 1
SLC25A3	solute carrier family 25 member 3
SLC25A5-AS1	SLC25A5 antisense RNA 1
SLC27A2	solute carrier family 27 member 2
SLC2A1	solute carrier family 2 member 1
SLC31A2	solute carrier family 31 member 2
SLC35B1	solute carrier family 35 member B1
SLFN11	schlafen family member 11
SMAD2	SMAD family member 2
SMAD3	SMAD family member 3
SMAD7	SMAD family member 7
SMPD3	sphingomyelin phosphodiesterase 3
SMPDL3B	sphingomyelin phosphodiesterase acid like 3B
SNAI1	snail family transcriptional repressor 1
SNAI2	snail family transcriptional repressor 2
SOCS1	suppressor of cytokine signaling 1
SOCS3	suppressor of cytokine signaling 3
SOCS5	suppressor of cytokine signaling 5
SOD1	superoxide dismutase 1
SOX2	SRY-box 2
SOX9	SRY-box 9
SP100	SP100 nuclear antigen
SP110	SP110 nuclear body protein
SPANXACD	sperm protein associated with the nucleus, X-linked, family members A1, A2, C, and D
SPANXB1	SPANX family member B1
SPANXN1	SPANX family member N1
SPANXN3	SPANX family member N3
SPANXN4	SPANX family member N4
SPANXN5	SPANX family member N5
SPC24	SPC24, NDC80 kinetochore complex component, homolog (<i>S. cerevisiae</i>)
SPC25	SPC25, NDC80 kinetochore complex component, homolog (<i>S. cerevisiae</i>)
SPDL1	Spindle apparatus coiled-coil protein 1
SPI1	Spi-1 proto-oncogene
SPIB	Spi-B transcription factor
SPIN4	Spindlin family, member 4
SPINK1	serine peptidase inhibitor, Kazal type 1
SPINK5	serine peptidase inhibitor, Kazal type 5
SPN	sialophorin
SPOP	speckle type BTB/POZ protein
SPP1	secreted phosphoprotein 1
SPTLC3	serine palmitoyltransferase long chain base subunit 3
SRGN	serglycin
SSX1	synovial sarcoma X (SSX) breakpoint protein
SSX2	SSX family member 2 and 2B
ST6GAL1	ST6 beta-galactoside alpha-2,6-sialyltransferase 1

STAT1	signal transducer and activator of transcription 1
STAT2	signal transducer and activator of transcription 2
STAT3	signal transducer and activator of transcription 3
STAT4	signal transducer and activator of transcription 4
STAT5A	signal transducer and activator of transcription 5A
STAT5B	signal transducer and activator of transcription 5B
STAT6	signal transducer and activator of transcription 6
STIL	SCL/TAL1 interrupting locus
STK32A	serine/threonine kinase 32A
STOX2	storkhead box 2
SUSD3	sushi domain containing 3
SUZ12	SUZ12 polycomb repressive complex 2 subunit
SV2A	synaptic vesicle glycoprotein 2A
SVIL	supervillin
SYCP1	synaptonemal complex protein 1
SYK	spleen associated tyrosine kinase
SYT17	synaptotagmin 17
SYT4	synaptotagmin 4
TAB1	TGF-beta activated kinase 1 (MAP3K7) binding protein 1
TACC3	Transforming, acidic coiled-coil containing protein 3
TACSTD2	tumor associated calcium signal transducer 2
TAGAP	T-cell activation RhoGTPase activating protein
TAGLN	transgelin
TAGLN3	transgelin 3
TAL1	TAL bHLH transcription factor 1, erythroid differentiation factor
TAP1	transporter 1, ATP binding cassette subfamily B member
TAP2	transporter 2, ATP binding cassette subfamily B member
TAPBP	TAP binding protein
TARP	TCR gamma alternate reading frame protein
TBK1	TANK binding kinase 1
TBX21	T-box 21
TCF12	transcription factor 12
TCF19	Transcription factor 19
TCF7	transcription factor 7 (T-cell specific, HMG-box)
TCL1A	T-cell leukemia/lymphoma 1A
TCL1B	T cell leukemia/lymphoma 1B
TDO2	tryptophan 2,3-dioxygenase
TEDC2	tubulin epsilon and delta complex 2
TEK	TEK receptor tyrosine kinase
TESC	tescalcin
TEX14	testis expressed 14, intercellular bridge forming factor
TFF1	trefoil factor 1
TFRC	transferrin receptor
TGFB1	transforming growth factor beta 1
TGFB2	transforming growth factor beta 2
TGFBI	transforming growth factor beta induced
TGFBR1	transforming growth factor beta receptor 1

TGFBR2	transforming growth factor beta receptor 2
TGIF2	TGFB induced factor homeobox 2
THAP11	THAP domain containing 11
THBD	thrombomodulin
THBS1	thrombospondin 1
THY1	Thy-1 cell surface antigen
TICAM1	toll like receptor adaptor molecule 1
TICAM2	toll like receptor adaptor molecule 2
TIGIT	T-cell immunoreceptor with Ig and ITIM domains
TIMP1	TIMP metalloproteinase inhibitor 1
TIRAP	TIR domain containing adaptor protein
TK1	Thymidine kinase 1, soluble
TLDC1	TBC/LysM-associated domain containing 1
TLR1	toll like receptor 1
TLR10	toll like receptor 10
TLR2	toll like receptor 2
TLR3	toll like receptor 3
TLR4	toll like receptor 4
TLR5	toll like receptor 5
TLR6	toll like receptor 6
TLR7	toll like receptor 7
TLR8	toll like receptor 8
TLR9	toll like receptor 9
TMBIM1	transmembrane BAX inhibitor motif containing 1
TMEM173	transmembrane protein 173
TMEM246	transmembrane protein 246
TMPO	Thymopoietin
TNF	tumor necrosis factor
TNFAIP3	TNF alpha induced protein 3
TNFAIP8	TNF alpha induced protein 8
TNFRSF10A	TNF receptor superfamily member 10a
TNFRSF10B	TNF receptor superfamily member 10b
TNFRSF10C	TNF receptor superfamily member 10c
TNFRSF10D	TNF receptor superfamily member 10d
TNFRSF11A	TNF receptor superfamily member 11a
TNFRSF11B	TNF receptor superfamily member 11b
TNFRSF12A	TNF receptor superfamily member 12A
TNFRSF13B	TNF receptor superfamily member 13B
TNFRSF13C	TNF receptor superfamily member 13C
TNFRSF14	TNF receptor superfamily member 14
TNFRSF17	TNF receptor superfamily member 17
TNFRSF18	TNF receptor superfamily member 18
TNFRSF19	TNF receptor superfamily member 19
TNFRSF1A	TNF receptor superfamily member 1A
TNFRSF1B	TNF receptor superfamily member 1B
TNFRSF21	TNF receptor superfamily member 21
TNFRSF25	TNF receptor superfamily member 25

TNFRSF4	TNF receptor superfamily member 4
TNFRSF8	TNF receptor superfamily member 8
TNFRSF9	TNF receptor superfamily member 9
TNFSF10	tumor necrosis factor superfamily member 10
TNFSF11	TNF superfamily member 11
TNFSF12	TNF superfamily member 12
TNFSF13	TNF superfamily member 13
TNFSF13B	tumor necrosis factor superfamily member 13b
TNFSF14	tumor necrosis factor superfamily member 14
TNFSF15	TNF superfamily member 15
TNFSF18	tumor necrosis factor superfamily member 18
TNFSF4	tumor necrosis factor superfamily member 4
TNFSF8	tumor necrosis factor superfamily member 8
TNFSF9	TNF superfamily member 9
TOLLIP	toll interacting protein
TOP2A	DNA topoisomerase II alpha
TP53	tumor protein p53
TP63	tumor protein p63
TPSAB1	tryptase alpha/beta 1
TPX2	TPX2, microtubule nucleation factor
TRABD2A	TraB domain containing 2A
TRAF2	TNF receptor associated factor 2
TRAF3	TNF receptor associated factor 3
TRAF6	TNF receptor associated factor 6
TRAP1	TNF receptor associated protein 1
TRAT1	T cell receptor associated transmembrane adaptor 1
TREM1	triggering receptor expressed on myeloid cells 1
TREM2	triggering receptor expressed on myeloid cells 2
TRIM21	tripartite motif containing 21
TRIM22	tripartite motif containing 22
TRIM29	tripartite motif containing 29
TRIM59	tripartite motif containing 59
TRIP13	thyroid hormone receptor interactor 13
TROAP	trophinin associated protein
TSG101	tumor susceptibility 101
TTK	TTK protein kinase
TUBB	tubulin beta class I
TWIST1	twist family bHLH transcription factor 1
TWIST2	twist family bHLH transcription factor 2
TXLNA	taxilin alpha
TXNIP	thioredoxin interacting protein
TYK2	tyrosine kinase 2
TYMS	Thymidylate synthetase
TYROBP	TYRO protein tyrosine kinase binding protein
UBA6	ubiquitin like modifier activating enzyme 6
UBE2C	Ubiquitin-conjugating enzyme E2C
UBE2T	ubiquitin conjugating enzyme E2 T

UBE3A	ubiquitin protein ligase E3A
UHRF1	Ubiquitin-like with PHD and ring finger domains 1
ULBP1	UL16 binding protein 1
UNC5D	unc-5 netrin receptor D
UPK2	uroplakin 2
UPK3A	uroplakin 3A
USP9Y	ubiquitin specific peptidase 9, Y-linked
VAV1	vav guanine nucleotide exchange factor 1
VCAM1	vascular cell adhesion molecule 1
VEGFA	vascular endothelial growth factor A
VEGFC	vascular endothelial growth factor C
VSIR	chromosome 10 open reading frame 54
VSNL1	visinin like 1
VTCN1	V-set domain containing T-cell activation inhibitor 1
VWDE	von Willebrand factor D and EGF domains
VWF	von Willebrand factor
WARS	tryptophanyl-tRNA synthetase
WASHC4	WASH complex subunit 4
WDHD1	multiple N-terminal WD40 domains and a C-terminal high mobility group (HMG) box
WDR60	WD repeat domain 60
WDR76	WD repeat domain 76
WNK2	WNK lysine deficient protein kinase 2
WNT5A	Wnt family member 5A
WNT7B	Wnt family member 7B
XAF1	XIAP associated factor 1
XAGE1B_1E	X antigen family member 1B and 1E
XAGE2	X antigen family member 1A
XAGE3	X antigen family member 3
XAGE5	X antigen family member 5
XCL1	X-C motif chemokine ligand 1
XCL1_XCL2	X-C motif chemokine ligand 1 and 2
XCR1	X-C motif chemokine receptor 1
YWHAZ	tyrosine 3-monooxygenase/tryptophan 5-monooxygenase activation protein zeta
ZAP70	zeta chain of T cell receptor associated protein kinase 70
ZBTB46	zinc finger and BTB domain containing 46
ZEB1	zinc finger E-box binding homeobox 1
ZIC5	Zic family member 5
ZNF14	zinc finger protein 14
ZNF205	zinc finger protein 205
ZNF74	zinc finger protein 74
ZWILCH	Zwilch kinetochore protein
ZYX	Zyxin

Appendix Table 1 Annotated Gene List of HTG EdgeSeq Precision Immuno-Oncology Panel

List of References

1. Rosai J. Male reproductive system: Prostate and seminal vesicles, Testis, Testicular adnexa, Penis and scrotum, Rosai and Ackerman's Surgical Pathology, 10th Edition. 2011.
2. Salji MJ, Ahmad I, Slater S, Poon F-W, Alhasso A, Melquiot NV, et al. Prostate Neoplasm, Blandy's Urology, Third Edition.2019.
3. Cancer research UK <http://www.cancerresearchuk.org/health-professional/cancer-statistics/statistics-by-cancer-type/prostate-cancer#heading-zero>, accessed 05/2019.
4. Cancer research UK <http://www.cancerresearchuk.org/health-professional/cancer-statistics/statistics-by-cancer-type/prostate-cancer#heading-three>, accessed 05/2019.
5. Siegel RL, Miller KD, Jemal A. Cancer statistics, 2020. CA: a cancer journal for clinicians. 2020;70(1):7-30.
6. Cancer research UK <http://www.cancerresearchuk.org/health-professional/cancer-statistics/statistics-by-cancer-type/prostate-cancer#heading-one>, accessed 05/2019.
7. Attard G, Parker C, Eeles RA, Schröder F, Tomlins SA, Tannock I, et al. Prostate cancer. The Lancet. 2016;387(10013):70-82.
8. Mottet N, Bellmunt J, Bolla M, Briers E, Cumberbatch MG, De Santis M, et al. EAU-ESTRO-SIOG Guidelines on Prostate Cancer. Part 1: Screening, Diagnosis, and Local Treatment with Curative Intent. European Urology. 2017;71(4):618-29.
9. Drake CG. Prostate cancer as a model for tumour immunotherapy. Nature reviews Immunology. 2010;10(8):580-93.
10. Briganti A, Chun FK, Salonia A, Suardi N, Gallina A, Da Pozzo LF, et al. Complications and other surgical outcomes associated with extended pelvic lymphadenectomy in men with localized prostate cancer. Eur Urol. 2006;50(5):1006-13.
11. Briganti A, Larcher A, Abdollah F, Capitanio U, Gallina A, Suardi N, et al. Updated nomogram predicting lymph node invasion in patients with prostate cancer undergoing extended pelvic lymph node dissection: the essential importance of percentage of positive cores. Eur Urol. 2012;61(3):480-7.
12. Bivalacqua TJ, Pierorazio PM, Gorin MA, Allaf ME, Carter HB, Walsh PC. Anatomic extent of pelvic lymph node dissection: impact on long-term cancer-specific outcomes in men with positive lymph nodes at time of radical prostatectomy. Urology. 2013;82(3):653-8.
13. Yuh BE, Ruel NH, Mejia R, Wilson CM, Wilson TG. Robotic extended pelvic lymphadenectomy for intermediate- and high-risk prostate cancer. Eur Urol. 2012;61(5):1004-10.
14. Rodrigues DN, Boysen G, Sumanasuriya S, Seed G, Marzo AM, de Bono J. The molecular underpinnings of prostate cancer: impacts on management and pathology practice. The Journal of pathology. 2017;241(2):173-82.
15. Cancer Genome Atlas Research N. The Molecular Taxonomy of Primary Prostate Cancer. Cell. 2015;163(4):1011-25.
16. Grasso CS, Wu YM, Robinson DR, Cao X, Dhanasekaran SM, Khan AP, et al. The mutational landscape of lethal castration-resistant prostate cancer. Nature. 2012;487(7406):239-43.
17. Lotan TL, Wei W, Morais CL, Hawley ST, Fazli L, Hurtado-Coll A, et al. PTEN Loss as Determined by Clinical-grade Immunohistochemistry Assay Is Associated with Worse Recurrence-free Survival in Prostate Cancer. European urology focus. 2016;2(2):180-8.

18. Lotan TL, Gurel B, Sutcliffe S, Esopi D, Liu W, Xu J, et al. PTEN protein loss by immunostaining: analytic validation and prognostic indicator for a high risk surgical cohort of prostate cancer patients. *Clin Cancer Res*. 2011;17(20):6563-73.
19. Carver BS, Tran J, Gopalan A, Chen Z, Shaikh S, Carracedo A, et al. Aberrant ERG expression cooperates with loss of PTEN to promote cancer progression in the prostate. *Nature Genetics*. 2009;41:619.
20. Robinson D, Van Allen EM, Wu YM, Schultz N, Lonigro RJ, Mosquera JM, et al. Integrative clinical genomics of advanced prostate cancer. *Cell*. 2015;161(5):1215-28.
21. The Molecular Taxonomy of Primary Prostate Cancer. *Cell*. 2015;163(4):1011-25.
22. Bezzi M, Seitzer N, Ishikawa T, Reschke M, Chen M, Wang G, et al. Diverse genetic-driven immune landscapes dictate tumor progression through distinct mechanisms. *Nature medicine*. 2018;24(2):165-75.
23. Guedes LB, Antonarakis ES, Schweizer MT, Mirkheshti N, Almutairi F, Park JC, et al. MSH2 Loss in Primary Prostate Cancer. *Clin Cancer Res*. 2017;23(22):6863-74.
24. Mani RS, Amin MA, Li X, Kalyana-Sundaram S, Veeneman BA, Wang L, et al. Inflammation-Induced Oxidative Stress Mediates Gene Fusion Formation in Prostate Cancer. *Cell Rep*. 2016;17(10):2620-31.
25. Kaur HB, Guedes LB, Lu J, Maldonado L, Reitz L, Barber JR, et al. Association of tumor-infiltrating T-cell density with molecular subtype, racial ancestry and clinical outcomes in prostate cancer. *Mod Pathol*. 2018;31(10):1539-52.
26. Minner S, Luebke AM, Kluth M, Bokemeyer C, Janicke F, Izbicki J, et al. High level of Ets-related gene expression has high specificity for prostate cancer: a tissue microarray study of 11 483 cancers. *Histopathology*. 2012;61(3):445-53.
27. Minner S, Enodien M, Sirma H, Luebke AM, Krohn A, Mayer PS, et al. ERG status is unrelated to PSA recurrence in radically operated prostate cancer in the absence of antihormonal therapy. *Clin Cancer Res*. 2011;17(18):5878-88.
28. Ahearn TU, Pettersson A, Ebot EM, Gerke T, Graff RE, Morais CL, et al. A Prospective Investigation of PTEN Loss and ERG Expression in Lethal Prostate Cancer. *Journal of the National Cancer Institute*. 2016;108(2).
29. Reid AH, Attard G, Ambroisine L, Fisher G, Kovacs G, Brewer D, et al. Molecular characterisation of ERG, ETV1 and PTEN gene loci identifies patients at low and high risk of death from prostate cancer. *British journal of cancer*. 2010;102(4):678-84.
30. Tosoian JJ, Almutairi F, Morais CL, Glavaris S, Hicks J, Sundi D, et al. Prevalence and Prognostic Significance of PTEN Loss in African-American and European-American Men Undergoing Radical Prostatectomy. *Eur Urol*. 2017;71(5):697-700.
31. Lotan TL, Wei W, Ludkovski O, Morais CL, Guedes LB, Jamaspishvili T, et al. Analytic validation of a clinical-grade PTEN immunohistochemistry assay in prostate cancer by comparison with PTEN FISH. *Mod Pathol*. 2016;29(8):904-14.
32. Berger MF, Lawrence MS, Demichelis F, Drier Y, Cibulskis K, Sivachenko AY, et al. The genomic complexity of primary human prostate cancer. *Nature*. 2011;470:214.
33. Hanahan D, Weinberg RA. Hallmarks of cancer: the next generation. *Cell*. 2011;144(5):646-74.
34. Hanahan D, Coussens LM. Accessories to the crime: functions of cells recruited to the tumor microenvironment. *Cancer Cell*. 2012;21(3):309-22.

35. Chen DS, Mellman I. Elements of cancer immunity and the cancer-immune set point. *Nature*. 2017;541(7637):321-30.
36. Dunn GP, Bruce AT, Ikeda H, Old LJ, Schreiber RD. Cancer immunoediting: from immunosurveillance to tumor escape. *Nature immunology*. 2002;3(11):991-8.
37. Binnewies M, Roberts EW, Kersten K, Chan V, Fearon DF, Merad M, et al. Understanding the tumor immune microenvironment (TIME) for effective therapy. *Nature medicine*. 2018;24(5):541-50.
38. Fridman WH, Pages F, Sautes-Fridman C, Galon J. The immune contexture in human tumours: impact on clinical outcome. *Nature reviews Cancer*. 2012;12(4):298-306.
39. Gajewski TF, Schreiber H, Fu YX. Innate and adaptive immune cells in the tumor microenvironment. *Nature immunology*. 2013;14(10):1014-22.
40. Qian BZ, Pollard JW. Macrophage diversity enhances tumor progression and metastasis. *Cell*. 2010;141(1):39-51.
41. Chen DS, Mellman I. Oncology meets immunology: the cancer-immunity cycle. *Immunity*. 2013;39(1):1-10.
42. Bevan MJ. Helping the CD8(+) T-cell response. *Nature reviews Immunology*. 2004;4(8):595-602.
43. Coussens LM, Zitvogel L, Palucka AK. Neutralizing tumor-promoting chronic inflammation: a magic bullet? *Science (New York, NY)*. 2013;339(6117):286-91.
44. Palucka AK, Coussens LM. The Basis of Oncoimmunology. *Cell*. 2016;164(6):1233-47.
45. DeNardo DG, Barreto JB, Andreu P, Vasquez L, Tawfik D, Kolhatkar N, et al. CD4(+) T cells regulate pulmonary metastasis of mammary carcinomas by enhancing protumor properties of macrophages. *Cancer Cell*. 2009;16(2):91-102.
46. Teng MW, Ngiow SF, Ribas A, Smyth MJ. Classifying Cancers Based on T-cell Infiltration and PD-L1. *Cancer research*. 2015;75(11):2139-45.
47. Galon J, Angell Helen K, Bedognetti D, Marincola Francesco M. The Continuum of Cancer Immunosurveillance: Prognostic, Predictive, and Mechanistic Signatures. *Immunity*. 2013;39(1):11-26.
48. Galon J, Mlecnik B, Bindea G, Angell HK, Berger A, Lagorce C, et al. Towards the introduction of the 'Immunoscore' in the classification of malignant tumours. *The Journal of pathology*. 2014;232(2):199-209.
49. Galon J, Costes A, Sanchez-Cabo F, Kirilovsky A, Mlecnik B, Lagorce-Pages C, et al. Type, density, and location of immune cells within human colorectal tumors predict clinical outcome. *Science (New York, NY)*. 2006;313(5795):1960-4.
50. Pages F, Galon J, Dieu-Nosjean MC, Tartour E, Sautes-Fridman C, Fridman WH. Immune infiltration in human tumors: a prognostic factor that should not be ignored. *Oncogene*. 2010;29(8):1093-102.
51. Pagès F, Berger A, Camus M, Sanchez-Cabo F, Costes A, Molidor R, et al. Effector memory T cells, early metastasis, and survival in colorectal cancer. *The New England journal of medicine*. 2005;353(25):2654-66.
52. Bindea G, Mlecnik B, Tosolini M, Kirilovsky A, Waldner M, Obenauf AC, et al. Spatiotemporal dynamics of intratumoral immune cells reveal the immune landscape in human cancer. *Immunity*. 2013;39(4):782-95.
53. Geissler K, Fornara P, Lautenschlager C, Holzhausen HJ, Seliger B, Riemann D. Immune signature of tumor infiltrating immune cells in renal cancer. *Oncoimmunology*. 2015;4(1):e985082.

54. Guo C, Zhao H, Wang Y, Bai S, Yang Z, Wei F, et al. Prognostic Value of the Neo-Immunoscore in Renal Cell Carcinoma. *Front Oncol.* 2019;9:439.
55. Li L, Sun R, Miao Y, Tran T, Adams L, Roscoe N, et al. PD-1/PD-L1 expression and interaction by automated quantitative immunofluorescent analysis show adverse prognostic impact in patients with diffuse large B-cell lymphoma having T-cell infiltration: a study from the International DLBCL Consortium Program. *Mod Pathol.* 2019;32(6):741-54.
56. Carstens JL, Correa de Sampaio P, Yang D, Barua S, Wang H, Rao A, et al. Spatial computation of intratumoral T cells correlates with survival of patients with pancreatic cancer. *Nat Commun.* 2017;8:15095.
57. Masugi Y, Abe T, Ueno A, Fujii-Nishimura Y, Ojima H, Endo Y, et al. Characterization of spatial distribution of tumor-infiltrating CD8+ T cells refines their prognostic utility for pancreatic cancer survival. *Modern Pathology.* 2019;32(10):1495-507.
58. Kruger JM, Wemmert C, Sternberger L, Bonnas C, Dietmann G, Gancarski P, et al. Combat or surveillance? Evaluation of the heterogeneous inflammatory breast cancer microenvironment. *The Journal of pathology.* 2013;229(4):569-78.
59. Huang Y-K, Wang M, Sun Y, Di Costanzo N, Mitchell C, Achuthan A, et al. Macrophage spatial heterogeneity in gastric cancer defined by multiplex immunohistochemistry. *Nature Communications.* 2019;10(1):3928.
60. Lee HJ, Seo JY, Ahn JH, Ahn SH, Gong G. Tumor-associated lymphocytes predict response to neoadjuvant chemotherapy in breast cancer patients. *Journal of breast cancer.* 2013;16(1):32-9.
61. Brown JR, Wimberly H, Lannin DR, Nixon C, Rimm DL, Bossuyt V. Multiplexed Quantitative Analysis of CD3, CD8, and CD20 Predicts Response to Neoadjuvant Chemotherapy in Breast Cancer. *Clinical Cancer Research.* 2014;20(23):5995-6005.
62. Hou Y, Nitta H, Wei L, Banks PM, Parwani AV, Li Z. Evaluation of Immune Reaction and PD-L1 Expression Using Multiplex Immunohistochemistry in HER2-Positive Breast Cancer: The Association With Response to Anti-HER2 Neoadjuvant Therapy. *Clinical Breast Cancer.* 2017.
63. Brück O, Blom S, Dufva O, Turkki R, Chheda H, Ribeiro A, et al. Immune cell contexture in the bone marrow tumor microenvironment impacts therapy response in CML. *Leukemia.* 2018;32(7):1643-56.
64. Feng Z, Puri S, Moudgil T, Wood W, Hoyt CC, Wang C, et al. Multispectral imaging of formalin-fixed tissue predicts ability to generate tumor-infiltrating lymphocytes from melanoma. *J Immunother Cancer.* 2015;3:47.
65. Tsujikawa T, Kumar S, Borkar RN, Azimi V, Thibault G, Chang YH, et al. Quantitative Multiplex Immunohistochemistry Reveals Myeloid-Inflamed Tumor-Immune Complexity Associated with Poor Prognosis. *Cell Reports.* 2017;19(1):203-17.
66. Flammiger A, Bayer F, Cirugeda-Kuhnert A, Huland H, Tennstedt P, Simon R, et al. Intratumoral T but not B lymphocytes are related to clinical outcome in prostate cancer. *APMIS : acta pathologica, microbiologica, et immunologica Scandinavica.* 2012;120(11):901-8.
67. Strasner A, Karin M. Immune Infiltration and Prostate Cancer. *Front Oncol.* 2015;5:128.
68. Saltz J, Gupta R, Hou L, Kurc T, Singh P, Nguyen V, et al. Spatial Organization and Molecular Correlation of Tumor-Infiltrating Lymphocytes Using Deep Learning on Pathology Images. *Cell Rep.* 2018;23(1):181-93.e7.

69. Erlandsson A, Carlsson J, Lundholm M, Falt A, Andersson SO, Andren O, et al. M2 macrophages and regulatory T cells in lethal prostate cancer. *The Prostate*. 2019;79(4):363-9.
70. Gollapudi K, Galet C, Grogan T, Zhang H, Said JW, Huang J, et al. Association between tumor-associated macrophage infiltration, high grade prostate cancer, and biochemical recurrence after radical prostatectomy. *American journal of cancer research*. 2013;3(5):523-9.
71. Lanciotti M, Masieri L, Raspollini MR, Minervini A, Mari A, Comito G, et al. The role of M1 and M2 macrophages in prostate cancer in relation to extracapsular tumor extension and biochemical recurrence after radical prostatectomy. *BioMed research international*. 2014;2014:486798.
72. Nonomura N, Takayama H, Nakayama M, Nakai Y, Kawashima A, Mukai M, et al. Infiltration of tumour-associated macrophages in prostate biopsy specimens is predictive of disease progression after hormonal therapy for prostate cancer. *BJU international*. 2011;107(12):1918-22.
73. Shimura S, Yang G, Ebara S, Wheeler TM, Frolov A, Thompson TC. Reduced infiltration of tumor-associated macrophages in human prostate cancer: association with cancer progression. *Cancer research*. 2000;60(20):5857-61.
74. Miller AM, Lundberg K, Ozenci V, Banham AH, Hellstrom M, Egevad L, et al. CD4+CD25high T cells are enriched in the tumor and peripheral blood of prostate cancer patients. *Journal of immunology (Baltimore, Md : 1950)*. 2006;177(10):7398-405.
75. Ebelt K, Babaryka G, Frankenberger B, Stief CG, Eisenmenger W, Kirchner T, et al. Prostate cancer lesions are surrounded by FOXP3+, PD-1+ and B7-H1+ lymphocyte clusters. *European journal of cancer (Oxford, England : 1990)*. 2009;45(9):1664-72.
76. Sfanos KS, Bruno TC, Maris CH, Xu L, Thoburn CJ, DeMarzo AM, et al. Phenotypic analysis of prostate-infiltrating lymphocytes reveals TH17 and Treg skewing. *Clin Cancer Res*. 2008;14(11):3254-61.
77. Kuniwa Y, Miyahara Y, Wang HY, Peng W, Peng G, Wheeler TM, et al. CD8+ Foxp3+ regulatory T cells mediate immunosuppression in prostate cancer. *Clin Cancer Res*. 2007;13(23):6947-58.
78. Sfanos KS, Bruno TC, Meeker AK, De Marzo AM, Isaacs WB, Drake CG. Human prostate-infiltrating CD8+ T lymphocytes are oligoclonal and PD-1+. *The Prostate*. 2009;69(15):1694-703.
79. Martin AM, Nirschl TR, Nirschl CJ, Francica BJ, Kochel CM, van Bokhoven A, et al. Paucity of PD-L1 expression in prostate cancer: innate and adaptive immune resistance. *Prostate cancer and prostatic diseases*. 2015;18(4):325-32.
80. Haffner MC, Guner G, Taheri D, Netto GJ, Palsgrove DN, Zheng Q, et al. Comprehensive Evaluation of Programmed Death-Ligand 1 Expression in Primary and Metastatic Prostate Cancer. *Am J Pathol*. 2018;188(6):1478-85.
81. McArdle PA, Canna K, McMillan DC, McNicol AM, Campbell R, Underwood MA. The relationship between T-lymphocyte subset infiltration and survival in patients with prostate cancer. *British journal of cancer*. 2004;91(3):541-3.
82. Ness N, Andersen S, Valkov A, Nordby Y, Donnem T, Al-Saad S, et al. Infiltration of CD8+ lymphocytes is an independent prognostic factor of biochemical failure-free survival in prostate cancer. *The Prostate*. 2014;74(14):1452-61.
83. Vesalainen S, Lipponen P, Talja M, Syrjanen K. Histological grade, perineural infiltration, tumour-infiltrating lymphocytes and apoptosis as determinants of long-term prognosis in prostatic adenocarcinoma. *European journal of cancer (Oxford, England : 1990)*. 1994;30a(12):1797-803.

84. Woo JR, Liss MA, Muldong MT, Palazzi K, Strasner A, Ammirante M, et al. Tumor infiltrating B-cells are increased in prostate cancer tissue. *J Transl Med.* 2014;12:30.
85. Flammiger A, Weisbach L, Huland H, Tennstedt P, Simon R, Minner S, et al. High tissue density of FOXP3+ T cells is associated with clinical outcome in prostate cancer. *European Journal of Cancer.* 2013;49(6):1273-9.
86. Davidsson S, Ohlson AL, Andersson SO, Fall K, Meisner A, Fiorentino M, et al. CD4 helper T cells, CD8 cytotoxic T cells, and FOXP3(+) regulatory T cells with respect to lethal prostate cancer. *Mod Pathol.* 2013;26(3):448-55.
87. Watanabe M, Kanao K, Suzuki S, Muramatsu H, Morinaga S, Kajikawa K, et al. Increased infiltration of CCR4-positive regulatory T cells in prostate cancer tissue is associated with a poor prognosis. *The Prostate.* 2019;79(14):1658-65.
88. Fox SB, Launchbury R, Bates GJ, Han C, Shaida N, Malone PR, et al. The number of regulatory T cells in prostate cancer is associated with the androgen receptor and hypoxia-inducible factor (HIF)-2alpha but not HIF-1alpha. *The Prostate.* 2007;67(6):623-9.
89. Brunnstrom H, Johansson A, Westbom-Fremer S, Backman M, Djureinovic D, Patthey A, et al. PD-L1 immunohistochemistry in clinical diagnostics of lung cancer: inter-pathologist variability is higher than assay variability. *Mod Pathol.* 2017;30(10):1411-21.
90. Taylor CR, Levenson RM. Quantification of immunohistochemistry--issues concerning methods, utility and semiquantitative assessment II. *Histopathology.* 2006;49(4):411-24.
91. Parra ER, Uraoka N, Jiang M, Cook P, Gibbons D, Forget MA, et al. Validation of multiplex immunofluorescence panels using multispectral microscopy for immune-profiling of formalin-fixed and paraffin-embedded human tumor tissues. *Scientific reports.* 2017;7(1):13380.
92. Stack EC, Wang C, Roman KA, Hoyt CC. Multiplexed immunohistochemistry, imaging, and quantitation: A review, with an assessment of Tyramide signal amplification, multispectral imaging and multiplex analysis. *Methods.* 2014;70(1):46-58.
93. Pivetta E, Capuano A, Scanziani E, Minoli L, Andreuzzi E, Mongiat M, et al. Multiplex staining depicts the immune infiltrate in colitis-induced colon cancer model. *Scientific reports.* 2019;9(1):12645.
94. Sorrelle N, Ganguly D, Dominguez ATA, Zhang Y, Huang H, Dahal LN, et al. Improved Multiplex Immunohistochemistry for Immune Microenvironment Evaluation of Mouse Formalin-Fixed, Paraffin-Embedded Tissues. *The Journal of Immunology.* 2018:ji1800878.
95. Mezheyeuski A, Bergsland CH, Backman M, Djureinovic D, Sjoblom T, Bruun J, et al. Multispectral imaging for quantitative and compartment-specific immune infiltrates reveals distinct immune profiles that classify lung cancer patients. *The Journal of pathology.* 2018;244(4):421-31.
96. Huang W, Henrick K, Drew S. A colorful future of quantitative pathology: validation of Vectra technology using chromogenic multiplexed immunohistochemistry and prostate tissue microarrays. *Human pathology.* 2013;44(1):29-38.
97. Gorris MAJ, Halilovic A, Rabold K, van Duffelen A, Wickramasinghe IN, Verweij D, et al. Eight-Color Multiplex Immunohistochemistry for Simultaneous Detection of Multiple Immune Checkpoint Molecules within the Tumor Microenvironment. *Journal of immunology (Baltimore, Md : 1950).* 2017.
98. Zhang W, Hubbard A, Jones T, Racolta A, Bhaumik S, Cummins N, et al. Fully automated 5-plex fluorescent immunohistochemistry with tyramide signal

- amplification and same species antibodies. *Laboratory investigation; a journal of technical methods and pathology*. 2017;97(7):873-85.
99. Lim JCT, Yeong JPS, Lim CJ, Ong CCH, Wong SC, Chew VSP, et al. An automated staining protocol for seven-colour immunofluorescence of human tissue sections for diagnostic and prognostic use. *Pathology*. 2018;50(3):333-41.
 100. Feng Z, Jensen SM, Messenheimer DJ, Farhad M, Neuberger M, Bifulco CB, et al. Multispectral Imaging of T and B Cells in Murine Spleen and Tumor. *Journal of immunology (Baltimore, Md : 1950)*. 2016;196(9):3943-50.
 101. Ijsselsteijn ME, Brouwer TP, Abdulrahman Z, Reidy E, Ramalheiro A, Heeren AM, et al. Cancer immunophenotyping by seven-colour multispectral imaging without tyramide signal amplification. *The journal of pathology Clinical research*. 2019;5(1):3-11.
 102. Blom S, Paavolainen L, Bychkov D, Turkki R, Mäki-Teeri P, Hemmes A, et al. Systems pathology by multiplexed immunohistochemistry and whole-slide digital image analysis. *Scientific reports*. 2017;7(1):15580.
 103. Saylor J, Ma Z, Goodridge HS, Huang F, Cress AE, Pandol SJ, et al. Spatial Mapping of Myeloid Cells and Macrophages by Multiplexed Tissue Staining. *Frontiers in immunology*. 2018;9:2925.
 104. Chapoval AI, Ni J, Lau JS, Wilcox RA, Flies DB, Liu D, et al. B7-H3: a costimulatory molecule for T cell activation and IFN-gamma production. *Nature immunology*. 2001;2(3):269-74.
 105. Zhou YH, Chen YJ, Ma ZY, Xu L, Wang Q, Zhang GB, et al. 4IgB7-H3 is the major isoform expressed on immunocytes as well as malignant cells. *Tissue antigens*. 2007;70(2):96-104.
 106. Seaman S, Zhu Z, Saha S, Zhang XM, Yang MY, Hilton MB, et al. Eradication of Tumors through Simultaneous Ablation of CD276/B7-H3-Positive Tumor Cells and Tumor Vasculature. *Cancer Cell*. 2017;31(4):501-15.e8.
 107. Zang X, Thompson RH, Al-Ahmadie HA, Serio AM, Reuter VE, Eastham JA, et al. B7-H3 and B7x are highly expressed in human prostate cancer and associated with disease spread and poor outcome. *Proceedings of the National Academy of Sciences of the United States of America*. 2007;104(49):19458-63.
 108. Yamato I, Sho M, Nomi T, Akahori T, Shimada K, Hotta K, et al. Clinical importance of B7-H3 expression in human pancreatic cancer. *British journal of cancer*. 2009;101(10):1709-16.
 109. Arigami T, Narita N, Mizuno R, Nguyen L, Ye X, Chung A, et al. B7-h3 ligand expression by primary breast cancer and associated with regional nodal metastasis. *Annals of surgery*. 2010;252(6):1044-51.
 110. Steinberger P, Majdic O, Derdak SV, Pfistershammer K, Kirchberger S, Klauser C, et al. Molecular characterization of human 4Ig-B7-H3, a member of the B7 family with four Ig-like domains. *Journal of immunology (Baltimore, Md : 1950)*. 2004;172(4):2352-9.
 111. Sun M, Richards S, Prasad DV, Mai XM, Rudensky A, Dong C. Characterization of mouse and human B7-H3 genes. *Journal of immunology (Baltimore, Md : 1950)*. 2002;168(12):6294-7.
 112. Sun X, Vale M, Leung E, Kanwar JR, Gupta R, Krissansen GW. Mouse B7-H3 induces antitumor immunity. *Gene Ther*. 2003;10(20):1728-34.
 113. Lupu CM, Eisenbach C, Lupu AD, Kuefner MA, Hoyler B, Stremmel W, et al. Adenoviral B7-H3 therapy induces tumor specific immune responses and reduces secondary metastasis in a murine model of colon cancer. *Oncology reports*. 2007;18(3):745-8.
 114. Kreyborg K, Haak S, Murali R, Wei J, Waitz R, Gasteiger G, et al. Ablation of B7-H3 but Not B7-H4 Results in Highly Increased Tumor Burden in a

- Murine Model of Spontaneous Prostate Cancer. *Cancer immunology research*. 2015;3(8):849-54.
115. Lee YH, Martin-Orozco N, Zheng P, Li J, Zhang P, Tan H, et al. Inhibition of the B7-H3 immune checkpoint limits tumor growth by enhancing cytotoxic lymphocyte function. *Cell research*. 2017;27(8):1034-45.
116. Yonesaka K, Haratani K, Takamura S, Sakai H, Kato R, Takegawa N, et al. B7-H3 Negatively Modulates CTL-Mediated Cancer Immunity. *Clin Cancer Res*. 2018;24(11):2653-64.
117. Du H, Hirabayashi K, Ahn S, Kren NP, Montgomery SA, Wang X, et al. Antitumor Responses in the Absence of Toxicity in Solid Tumors by Targeting B7-H3 via Chimeric Antigen Receptor T Cells. *Cancer Cell*. 2019;35(2):221-37.e8.
118. Leitner J, Klauser C, Pickl WF, Stockl J, Majdic O, Bardet AF, et al. B7-H3 is a potent inhibitor of human T-cell activation: No evidence for B7-H3 and TREM2 interaction. *European journal of immunology*. 2009;39(7):1754-64.
119. Schneider T, Hoffmann H, Dienemann H, Schnabel PA, Enk AH, Ring S, et al. Non-small cell lung cancer induces an immunosuppressive phenotype of dendritic cells in tumor microenvironment by upregulating B7-H3. *Journal of thoracic oncology : official publication of the International Association for the Study of Lung Cancer*. 2011;6(7):1162-8.
120. Ma J, Ma P, Zhao C, Xue X, Han H, Liu C, et al. B7-H3 as a promising target for cytotoxicity T cell in human cancer therapy. *Oncotarget*. 2016;7(20):29480-91.
121. Ma W, Ma J, Ma P, Lei T, Zhao M, Zhang M. Targeting immunotherapy for bladder cancer using anti-CD3x B7-H3 bispecific antibody. *Cancer medicine*. 2018;7(10):5167-77.
122. Loo D, Alderson RF, Chen FZ, Huang L, Zhang W, Gorlatov S, et al. Development of an Fc-enhanced anti-B7-H3 monoclonal antibody with potent antitumor activity. *Clin Cancer Res*. 2012;18(14):3834-45.
123. Powderly J, Cote G, Flaherty K, Szmulewitz RZ, Ribas A, Weber J, et al. Interim results of an ongoing Phase I, dose escalation study of MGA271 (Fc-optimized humanized anti-B7-H3 monoclonal antibody) in patients with refractory B7-H3-expressing neoplasms or neoplasms whose vasculature expresses B7-H3. *Journal for Immunotherapy of Cancer*. 2015;3(Suppl 2):O8-O.
124. Hashiguchi M, Kobori H, Ritprajak P, Kamimura Y, Kozono H, Azuma M. Triggering receptor expressed on myeloid cell-like transcript 2 (TLT-2) is a counter-receptor for B7-H3 and enhances T cell responses. *Proceedings of the National Academy of Sciences of the United States of America*. 2008;105(30):10495-500.
125. Kobori H, Hashiguchi M, Piao J, Kato M, Ritprajak P, Azuma M. Enhancement of effector CD8+ T-cell function by tumour-associated B7-H3 and modulation of its counter-receptor triggering receptor expressed on myeloid cell-like transcript 2 at tumour sites. *Immunology*. 2010;130(3):363-73.
126. Chen YW, Tekle C, Fodstad O. The immunoregulatory protein human B7H3 is a tumor-associated antigen that regulates tumor cell migration and invasion. *Current cancer drug targets*. 2008;8(5):404-13.
127. Yuan H, Wei X, Zhang G, Li C, Zhang X, Hou J. B7-H3 over expression in prostate cancer promotes tumor cell progression. *The Journal of urology*. 2011;186(3):1093-9.
128. Zhang T, Jiang B, Zou ST, Liu F, Hua D. Overexpression of B7-H3 augments anti-apoptosis of colorectal cancer cells by Jak2-STAT3. *World journal of gastroenterology*. 2015;21(6):1804-13.

129. Chen L, Chen J, Xu B, Wang Q, Zhou W, Zhang G, et al. B7-H3 expression associates with tumor invasion and patient's poor survival in human esophageal cancer. *American journal of translational research*. 2015;7(12):2646-60.
130. Tekle C, Nygren MK, Chen YW, Dybsjord I, Nesland JM, Maelandsmo GM, et al. B7-H3 contributes to the metastatic capacity of melanoma cells by modulation of known metastasis-associated genes. *International journal of cancer*. 2012;130(10):2282-90.
131. Li Y, Guo G, Song J, Cai Z, Yang J, Chen Z, et al. B7-H3 Promotes the Migration and Invasion of Human Bladder Cancer Cells via the PI3K/Akt/STAT3 Signaling Pathway. *J Cancer*. 2017;8(5):816-24.
132. Wang L, Zhang Q, Chen W, Shan B, Ding Y, Zhang G, et al. B7-H3 is Overexpressed in Patients Suffering Osteosarcoma and Associated with Tumor Aggressiveness and Metastasis. *PloS one*. 2013;8(8):e70689.
133. Liu F, Zhang T, Zou S, Jiang B, Hua D. B7H3 promotes cell migration and invasion through the Jak2/Stat3/MMP9 signaling pathway in colorectal cancer. *Molecular medicine reports*. 2015;12(4):5455-60.
134. Kang FB, Wang L, Jia HC, Li D, Li HJ, Zhang YG, et al. B7-H3 promotes aggression and invasion of hepatocellular carcinoma by targeting epithelial-to-mesenchymal transition via JAK2/STAT3/Slug signaling pathway. *Cancer cell international*. 2015;15:45.
135. Yu T-T, Zhang T, Lu X, Wang R-Z. B7-H3 promotes metastasis, proliferation, and epithelial-mesenchymal transition in lung adenocarcinoma. *OncoTargets and therapy*. 2018;11:4693-700.
136. Jiang B, Zhang T, Liu F, Sun Z, Shi H, Hua D, et al. The co-stimulatory molecule B7-H3 promotes the epithelial-mesenchymal transition in colorectal cancer. *Oncotarget*. 2016;7(22):31755-71.
137. Xie C, Liu D, Chen Q, Yang C, Wang B, Wu H. Soluble B7-H3 promotes the invasion and metastasis of pancreatic carcinoma cells through the TLR4/NF-kappaB pathway. *Scientific reports*. 2016;6:27528.
138. Li Y, Yang X, Wu Y, Zhao K, Ye Z, Zhu J, et al. B7-H3 promotes gastric cancer cell migration and invasion. *Oncotarget*. 2017;8(42):71725-35.
139. Zhao X, Zhang G-B, Gan W-J, Xiong F, Li Z, Zhao H, et al. Silencing of B7-H3 increases gemcitabine sensitivity by promoting apoptosis in pancreatic carcinoma. *Oncol Lett*. 2013;5(3):805-12.
140. Liu H, Tekle C, Chen YW, Kristian A, Zhao Y, Zhou M, et al. B7-H3 silencing increases paclitaxel sensitivity by abrogating Jak2/Stat3 phosphorylation. *Molecular cancer therapeutics*. 2011;10(6):960-71.
141. Liu Z, Zhang W, Phillips JB, Arora R, McClellan S, Li J, et al. Immunoregulatory protein B7-H3 regulates cancer stem cell enrichment and drug resistance through MVP-mediated MEK activation. *Oncogene*. 2019;38(1):88-102.
142. Roth TJ, Sheinin Y, Lohse CM, Kuntz SM, Frigola X, Inman BA, et al. B7-H3 ligand expression by prostate cancer: a novel marker of prognosis and potential target for therapy. *Cancer research*. 2007;67(16):7893-900.
143. Chavin G, Sheinin Y, Crispen PL, Boorjian SA, Roth TJ, Rangel L, et al. Expression of immunosuppressive B7-H3 ligand by hormone-treated prostate cancer tumors and metastases. *Clin Cancer Res*. 2009;15(6):2174-80.
144. Parker AS, Heckman MG, Sheinin Y, Wu KJ, Hilton TW, Diehl NN, et al. Evaluation of B7-H3 expression as a biomarker of biochemical recurrence after salvage radiation therapy for recurrent prostate cancer. *International journal of radiation oncology, biology, physics*. 2011;79(5):1343-9.

145. Ilyas M, Grabsch H, Ellis IO, Womack C, Brown R, Berney D, et al. Guidelines and considerations for conducting experiments using tissue microarrays. *Histopathology*. 2013;62(6):827-39.
146. Loveridge CJ, Slater S, Campbell KJ, Nam NA, Knight J, Ahmad I, et al. BRF1 accelerates prostate tumourigenesis and perturbs immune infiltration. *Oncogene*. 2020;39(8):1797-806.
147. Minner S, Jessen B, Stiedenroth L, Burandt E, Kollermann J, Mirlacher M, et al. Low level HER2 overexpression is associated with rapid tumor cell proliferation and poor prognosis in prostate cancer. *Clin Cancer Res*. 2010;16(5):1553-60.
148. Wallace TJ, Qian J, Avital I, Bay C, Man YG, Wellman LL, et al. Technical Feasibility of Tissue Microarray (TMA) Analysis of Tumor-Associated Immune Response in Prostate Cancer. *J Cancer*. 2018;9(12):2191-202.
149. Miller BW, Morton JP, Pinese M, Saturno G, Jamieson NB, McGhee E, et al. Targeting the LOX/hypoxia axis reverses many of the features that make pancreatic cancer deadly: inhibition of LOX abrogates metastasis and enhances drug efficacy. *EMBO molecular medicine*. 2015;7(8):1063-76.
150. Eggener SE, Scardino PT, Walsh PC, Han M, Partin AW, Trock BJ, et al. Predicting 15-Year Prostate Cancer Specific Mortality After Radical Prostatectomy. *The Journal of urology*. 2011;185(3):869-75.
151. Amin MB, Edge, S., Greene, F., Byrd, D.R., Brookland, R.K., Washington, M.K., Gershenwald, J.E., Compton, C.C., Hess, K.R., Sullivan, D.C., Jessup, J.M., Brierley, J.D., Gaspar, L.E., Schilsky, R.L., Balch, C.M., Winchester, D.P., Asare, E.A., Madera, M., Gress, D.M., Meyer, L.R. (Eds.). *AJCC Cancer Staging Manual (8th edition)*. 2017.
152. Kalina JL, Neilson DS, Lin Y-Y, Hamilton PT, Comber AP, Loy EMH, et al. Mutational Analysis of Gene Fusions Predicts Novel MHC Class I-Restricted T-Cell Epitopes and Immune Signatures in a Subset of Prostate Cancer. *Clinical cancer research : an official journal of the American Association for Cancer Research*. 2017;23(24):7596-607.
153. Kiflemariam S, Mignardi M, Ali MA, Bergh A, Nilsson M, Sjoblom T. In situ sequencing identifies TMPRSS2-ERG fusion transcripts, somatic point mutations and gene expression levels in prostate cancers. *The Journal of pathology*. 2014;234(2):253-61.
154. Gopalan A, Leversha MA, Satagopan JM, Zhou Q, Al-Ahmadie HA, Fine SW, et al. TMPRSS2-ERG gene fusion is not associated with outcome in patients treated by prostatectomy. *Cancer research*. 2009;69(4):1400-6.
155. Demichelis F, Fall K, Perner S, Andren O, Schmidt F, Setlur SR, et al. TMPRSS2:ERG gene fusion associated with lethal prostate cancer in a watchful waiting cohort. *Oncogene*. 2007;26(31):4596-9.
156. Roth MD, Harui A. Human tumor infiltrating lymphocytes cooperatively regulate prostate tumor growth in a humanized mouse model. *J Immunother Cancer*. 2015;3:12.
157. Thorsson V, Gibbs DL, Brown SD, Wolf D, Bortone DS, Ou Yang T-H, et al. The Immune Landscape of Cancer. *Immunity*. 2018;48(4):812-30.e14.
158. Binnewies M, Mujal AM, Pollack JL, Combes AJ, Hardison EA, Barry KC, et al. Unleashing Type-2 Dendritic Cells to Drive Protective Antitumor CD4(+) T Cell Immunity. *Cell*. 2019;177(3):556-71.e16.
159. Antony PA, Piccirillo CA, Akpınarli A, Finkelstein SE, Speiss PJ, Surman DR, et al. CD8+ T Cell Immunity Against a Tumor/Self-Antigen Is Augmented by CD4+ T Helper Cells and Hindered by

- Naturally Occurring T Regulatory Cells. *The Journal of Immunology*. 2005;174(5):2591.
160. Appay V, Zaunders JJ, Papagno L, Sutton J, Jaramillo A, Waters A, et al. Characterization of CD4(+) CTLs ex vivo. *Journal of immunology (Baltimore, Md : 1950)*. 2002;168(11):5954-8.
161. Hashimoto K, Kouno T, Ikawa T, Hayatsu N, Miyajima Y, Yabukami H, et al. Single-cell transcriptomics reveals expansion of cytotoxic CD4 T cells in supercentenarians. *Proceedings of the National Academy of Sciences of the United States of America*. 2019;116(48):24242-51.
162. Peng Z, Skoog L, Hellborg H, Jonstam G, Wingmo IL, Hjalms-Eriksson M, et al. An expression signature at diagnosis to estimate prostate cancer patients' overall survival. *Prostate cancer and prostatic diseases*. 2014;17(1):81-90.
163. Tosolini M, Kirilovsky A, Mlecnik B, Fredriksen T, Mauger S, Bindea G, et al. Clinical impact of different classes of infiltrating T cytotoxic and helper cells (Th1, th2, treg, th17) in patients with colorectal cancer. *Cancer research*. 2011;71(4):1263-71.
164. Mlecnik B, Tosolini M, Charoentong P, Kirilovsky A, Bindea G, Berger A, et al. Biomolecular network reconstruction identifies T-cell homing factors associated with survival in colorectal cancer. *Gastroenterology*. 2010;138(4):1429-40.
165. Harlin H, Meng Y, Peterson AC, Zha Y, Tretiakova M, Slingluff C, et al. Chemokine expression in melanoma metastases associated with CD8+ T-cell recruitment. *Cancer research*. 2009;69(7):3077-85.
166. Franciszkiewicz K, Boissonnas A, Boutet M, Combadière C, Mami-Chouaib F. Role of chemokines and chemokine receptors in shaping the effector phase of the antitumor immune response. *Cancer research*. 2012;72(24):6325-32.
167. Knudsen ES, Vail P, Balaji U, Ngo H, Botros IW, Makarov V, et al. Stratification of Pancreatic Ductal Adenocarcinoma: Combinatorial Genetic, Stromal, and Immunologic Markers. *Clin Cancer Res*. 2017;23(15):4429-40.
168. Girard L, Rodriguez-Canales J, Behrens C, Thompson DM, Botros IW, Tang H, et al. An Expression Signature as an Aid to the Histologic Classification of Non-Small Cell Lung Cancer. *Clin Cancer Res*. 2016;22(19):4880-9.
169. Kalluri R. The biology and function of fibroblasts in cancer. *Nature reviews Cancer*. 2016;16(9):582-98.
170. Levental KR, Yu H, Kass L, Lakins JN, Egeblad M, Ertler JT, et al. Matrix crosslinking forces tumor progression by enhancing integrin signaling. *Cell*. 2009;139(5):891-906.
171. Provenzano PP, Inman DR, Eliceiri KW, Knittel JG, Yan L, Rueden CT, et al. Collagen density promotes mammary tumor initiation and progression. *BMC medicine*. 2008;6:11.
172. Lu P, Weaver VM, Werb Z. The extracellular matrix: a dynamic niche in cancer progression. *The Journal of cell biology*. 2012;196(4):395-406.
173. Jiang H, Hegde S, DeNardo DG. Tumor-associated fibrosis as a regulator of tumor immunity and response to immunotherapy. *Cancer immunology, immunotherapy : CII*. 2017;66(8):1037-48.
174. Salmon H, Franciszkiewicz K, Damotte D, Dieu-Nosjean MC, Validire P, Trautmann A, et al. Matrix architecture defines the preferential localization and migration of T cells into the stroma of human lung tumors. *The Journal of clinical investigation*. 2012;122(3):899-910.
175. Hartmann N, Giese NA, Giese T, Poschke I, Offringa R, Werner J, et al. Prevailing role of contact guidance in intrastromal T-cell trapping in human pancreatic cancer. *Clin Cancer Res*. 2014;20(13):3422-33.

176. Bougherara H, Mansuet-Lupo A, Alifano M, Ngo C, Damotte D, Le Frere-Belda MA, et al. Real-Time Imaging of Resident T Cells in Human Lung and Ovarian Carcinomas Reveals How Different Tumor Microenvironments Control T Lymphocyte Migration. *Frontiers in immunology*. 2015;6:500.
177. Peranzoni E, Rivas-Caicedo A, Bougherara H, Salmon H, Donnadieu E. Positive and negative influence of the matrix architecture on antitumor immune surveillance. *Cellular and molecular life sciences : CMLS*. 2013;70(23):4431-48.
178. Van Goethem E, Poincloux R, Gauffre F, Maridonneau-Parini I, Le Cabec V. Matrix architecture dictates three-dimensional migration modes of human macrophages: differential involvement of proteases and podosome-like structures. *Journal of immunology (Baltimore, Md : 1950)*. 2010;184(2):1049-61.
179. Augsten M, Sjöberg E, Frings O, Vorrink SU, Frijhoff J, Olsson E, et al. Cancer-associated fibroblasts expressing CXCL14 rely upon NOS1-derived nitric oxide signaling for their tumor-supporting properties. *Cancer research*. 2014;74(11):2999-3010.
180. Augsten M, Hagglof C, Olsson E, Stolz C, Tsagozis P, Levchenko T, et al. CXCL14 is an autocrine growth factor for fibroblasts and acts as a multi-modal stimulator of prostate tumor growth. *Proceedings of the National Academy of Sciences of the United States of America*. 2009;106(9):3414-9.
181. Lo A, Wang LS, Scholler J, Monslow J, Avery D, Newick K, et al. Tumor-Promoting Desmoplasia Is Disrupted by Depleting FAP-Expressing Stromal Cells. *Cancer research*. 2015;75(14):2800-10.
182. Feig C, Jones JO, Kraman M, Wells RJ, Deonaraine A, Chan DS, et al. Targeting CXCL12 from FAP-expressing carcinoma-associated fibroblasts synergizes with anti-PD-L1 immunotherapy in pancreatic cancer. *Proceedings of the National Academy of Sciences of the United States of America*. 2013;110(50):20212-7.
183. Sjöberg E, Meyrath M, Milde L, Herrera M, Lövrot J, Hägerstrand D, et al. A Novel ACKR2-Dependent Role of Fibroblast-Derived CXCL14 in Epithelial-to-Mesenchymal Transition and Metastasis of Breast Cancer. *Clinical Cancer Research*. 2019;25(12):3702.
184. Ozdemir BC, Pentcheva-Hoang T, Carstens JL, Zheng X, Wu CC, Simpson TR, et al. Depletion of Carcinoma-Associated Fibroblasts and Fibrosis Induces Immunosuppression and Accelerates Pancreas Cancer with Reduced Survival. *Cancer Cell*. 2015;28(6):831-3.
185. Naba A, Clauser KR, Lamar JM, Carr SA, Hynes RO. Extracellular matrix signatures of human mammary carcinoma identify novel metastasis promoters. *eLife*. 2014;3:e01308.
186. Brahmer JR, Tykodi SS, Chow LQM, Hwu W-J, Topalian SL, Hwu P, et al. Safety and Activity of Anti-PD-L1 Antibody in Patients with Advanced Cancer. *New England Journal of Medicine*. 2012;366(26):2455-65.
187. Topalian SL, Hodi FS, Brahmer JR, Gettinger SN, Smith DC, McDermott DF, et al. Safety, activity, and immune correlates of anti-PD-1 antibody in cancer. *The New England journal of medicine*. 2012;366(26):2443-54.
188. Comiskey MC, Dallos MC, Drake CG. Immunotherapy in Prostate Cancer: Teaching an Old Dog New Tricks. *Current oncology reports*. 2018;20(9):75.
189. Zhang G, Hou J, Shi J, Yu G, Lu B, Zhang X. Soluble CD276 (B7-H3) is released from monocytes, dendritic cells and activated T cells and is detectable in normal human serum. *Immunology*. 2008;123(4):538-46.
190. Loberg RD, Day LL, Harwood J, Ying C, St John LN, Giles R, et al. CCL2 is a potent regulator of prostate cancer cell migration and proliferation. *Neoplasia (New York, NY)*. 2006;8(7):578-86.

191. Maolake A, Izumi K, Shigehara K, Natsagdorj A, Iwamoto H, Kadomoto S, et al. Tumor-associated macrophages promote prostate cancer migration through activation of the CCL22-CCR4 axis. *Oncotarget*. 2017;8(6):9739-51.
192. Wang J, Cai Y, Shao L-J, Siddiqui J, Palanisamy N, Li R, et al. Activation of NF- κ B by TMPRSS2/ERG Fusion Isoforms through Toll-Like Receptor-4. *Cancer research*. 2011;71(4):1325-33.
193. Taniguchi K, Karin M. NF-kappaB, inflammation, immunity and cancer: coming of age. *Nature reviews Immunology*. 2018;18(5):309-24.
194. Flem-Karlsen K, Fodstad O, Tan M, Nunes-Xavier CE. B7-H3 in Cancer - Beyond Immune Regulation. *Trends in cancer*. 2018;4(6):401-4.
195. Nagarsheth N, Wicha MS, Zou W. Chemokines in the cancer microenvironment and their relevance in cancer immunotherapy. *Nature reviews Immunology*. 2017;17(9):559-72.
196. Najjar YG, Rayman P, Jia X, Pavicic PG, Jr., Rini BI, Tannenbaum C, et al. Myeloid-Derived Suppressor Cell Subset Accumulation in Renal Cell Carcinoma Parenchyma Is Associated with Intratumoral Expression of IL1B, IL8, CXCL5, and Mip-1 α . *Clin Cancer Res*. 2017;23(9):2346-55.
197. Qian BZ, Li J, Zhang H, Kitamura T, Zhang J, Campion LR, et al. CCL2 recruits inflammatory monocytes to facilitate breast-tumour metastasis. *Nature*. 2011;475(7355):222-5.
198. Li J, Byrne KT, Yan F, Yamazoe T, Chen Z, Baslan T, et al. Tumor Cell-Intrinsic Factors Underlie Heterogeneity of Immune Cell Infiltration and Response to Immunotherapy. *Immunity*. 2018;49(1):178-93.e7.
199. Gabellini C, Trisciuglio D, Desideri M, Candiloro A, Ragazzoni Y, Orlandi A, et al. Functional activity of CXCL8 receptors, CXCR1 and CXCR2, on human malignant melanoma progression. *European journal of cancer (Oxford, England : 1990)*. 2009;45(14):2618-27.
200. Dixon AR, Bathany C, Tsuei M, White J, Barald KF, Takayama S. Recent developments in multiplexing techniques for immunohistochemistry. *Expert review of molecular diagnostics*. 2015;15(9):1171-86.
201. Gerdes MJ, Sevinsky CJ, Sood A, Adak S, Bello MO, Bordwell A, et al. Highly multiplexed single-cell analysis of formalin-fixed, paraffin-embedded cancer tissue. *Proceedings of the National Academy of Sciences of the United States of America*. 2013;110(29):11982-7.
202. Angelo M, Bendall SC, Finck R, Hale MB, Hitzman C, Borowsky AD, et al. Multiplexed ion beam imaging of human breast tumors. *Nature medicine*. 2014;20(4):436-42.